Nonlinear convection in sea ice and other mushy layers



James Parkinson

Jesus College

University of Oxford

A thesis submitted for the degree of

Doctor of Philosophy

Trinity 2019

Acknowledgements

I am incredibly grateful to Andrew Wells for his seemingly limitless positivity and enthusiasm, which was more than a match for the torrent of problems I brought to our meetings each week. I have also been fortunate to work with Dan Martin and Rich Katz for much of this project, and thank Dan and the rest of the Chombo group at LBNL for their warm hospitality in Berkeley. Thanks to David Rees Jones for co-supervising my masters project on mushy layers, to Joe Hitchen for many helpful discussions (and for leaving this project for me to work on), and to Kevin Thielen for helping me keep the department supplied with coffee and biscuits. Thanks to NERC, The Royal Society, and Jesus College, whose generous financial contributions made this work possible. I would also like to thank my parents, without whom I doubt I would have started this PhD in the first place, and who restrained themselves from asking too many times whether I had finished the thesis yet. Thanks also to all my friends for their welcome distractions. Finally, and most importantly, I thank Helen for her immeasurable support and encouragement.

Abstract

The polar regions are changing dramatically. The Arctic ocean has seen an increasing fraction of young seasonal sea ice, which contains a relatively high fraction of liquid brine inclusions, and decreasing fraction of older multi-year ice. The binary mixture of solid ice crystals and liquid brine which forms sea ice is both porous and reactive, and can be classified as a *mushy layer*. Convection within porous sea ice rejects dense brine into the underlying ocean, where it provides an important buoyancy forcing, and circulates nutrients within the ice with consequences for the local biogeochemistry.

In this thesis I aim to build understanding of convective processes within sea ice and other mushy layers. I develop a code for direct numerical simulations in two and three dimensions, which uses adaptive mesh refinement to efficiently resolve the key dynamical features across multiple scales by solving mesoscopic conservation equations. This code is then applied to a variety of settings, whilst focussing on the relatively unexplored *far-from eutectic* limit which is particularly relevant to sea ice.

In this *far-from eutectic* limit the porosity is small except for a narrow porous layer near the mush-liquid boundary. New scaling laws are found for steady-state growth, where the convection is confined to this porous layer whilst the mush-liquid solute flux scales sublinearly with the Rayleigh number - a dimensionless parameter which characterises the ratio of buoyancy to dissipative forces. Simulations of transient growth from a fixed boundary provide new insights into the dynamics and spacing of brine channels, and I find that flow in 3-D is qualitatively similar to 2-D. Meanwhile, I find evidence that convection within warming sea ice may lead to periods of intense salt fluxes into the ocean. These results have important geophysical implications for the dynamics and biogeochemistry of the polar regions.

Contents

1 Introduction **1**

1.1 Thesis structure and aims . . . 3
1.2 Introduction to sea ice . . . 4
1.2.1 Sea ice formation . . . 4
1.2.2 Sea ice is a mushy layer . . . 6
1.2.3 The concentration ratio . . . 8
1.3 Natural convection in sea ice and other mushy layers . . . 9
1.3.1 Field observations of convection in sea ice . . . 12
1.3.2 Sea ice in the laboratory . . . 14
1.3.3 Theoretical approaches . . . 16
1.3.4 Numerical simulations and nonlinear solutions . . . 18
1.3.5 Parametrising convection in sea ice . . . 20
1.3.6 Wider implications of brine transport in sea ice . . . 21
1.4 Summary . . . 23

2 Sea ice model **25**

2.1 Governing equations for thermodynamics and flow in sea ice . . . 25
2.1.1 Mass conservation . . . 27
2.1.2 Energy conservation . . . 28
2.1.3 Salt conservation . . . 28
2.1.4 Momentum conservation . . . 29
2.1.5 Permeability . . . 30
2.1.6 Equation of state . . . 32
2.1.7 Phase diagram . . . 32
2.1.8 Directional solidification . . . 38
2.2 Initial and boundary conditions . . . 38
2.2.1 Atmospheric boundary conditions . . . 39
2.2.2 Ocean boundary conditions . . . 40
2.2.3 Side boundaries . . . 41
2.3 Nondimensionalisation . . . 41
2.3.1 Phase diagram . . . 44
2.3.2 Other comparisons with previous studies . . . 45
2.4 Summary . . . 46

3 Method **49**

3.1 Introduction . . . 49
3.1.1 Initial scaling analysis . . . 50
3.1.2 Introduction to adaptive mesh refinement . . . 53
3.1.3 Previous numerical approaches . . . 55
3.2 Numerical method . . . 56

3.2.1 AMR structure and notation . . . 57
3.2.2 AMR update . . . 58
3.2.3 Single level update . . . 60
3.2.4 Synchronisation . . . 64
3.2.5 Stability of the freestream preservation correction . . . 66
3.2.6 Initialisation . . . 68
3.2.7 Refinement . . . 68
3.2.8 Algorithm for Darcy flow . . . 69
3.3 Code validation . . . 70
3.3.1 Diffusive solidification . . . 71
3.3.2 Convection in a porous medium . . . 72
3.3.3 Convection in a mushy layer . . . 75
3.4 Additional model capabilities . . . 79
3.4.1 Variable fluid viscosity . . . 79
3.4.2 Biogeochemical tracers . . . 80
3.4.3 Nonlinear boundary conditions . . . 81
3.5 Summary . . . 83

A Numerical methods **85**
A.1 Discretisation . . . 85
A.2 Multigrid . . . 86
A.3 Godunov's method . . . 88

4 Steady state growth **91**
4.1 Mushy layer growth with Darcy flow . . . 94
4.1.1 Stability and bifurcation structure . . . 97
4.1.2 Convection in the optimal state . . . 101
4.1.3 Scalings for small concentration ratio . . . 104
4.1.4 Comparison with numerical results . . . 113
4.1.5 Comparison with experimental observations of transient growth 115
4.1.6 Discussion . . . 118
4.2 Mushy layer growth with Darcy-Brinkman flow . . . 121
4.2.1 Comparison between Darcy and Darcy-Brinkman flow . . . 122
4.2.2 Channel dynamics with solute diffusion . . . 123
4.3 Summary . . . 127

5 Growth from a fixed boundary **131**
5.1 Sea ice growth . . . 132
5.1.1 Phenomenology of transient growth . . . 134
5.1.2 Rate of ice growth . . . 136
5.1.3 Salt rejection . . . 139
5.1.4 Onset of convection . . . 146
5.1.5 Channel spacing . . . 147

5.2 Variation with concentration ratio . . . 152
5.2.1 Onset of convection . . . 153
5.2.2 Phenomenology of convection . . . 162
5.2.3 Mushy layer properties . . . 165
5.2.4 Comparison with steady state scaling . . . 169
5.2.5 Channel dynamics . . . 172
5.3 Comparing 3-D and 2-D simulations . . . 178
5.3.1 Experimental design . . . 179
5.3.2 Results for flow in 2-D and 3-D . . . 180
5.4 Summary . . . 186

6 Salt Release from Warming Sea Ice 189
6.1 Experimental design . . . 190
6.1.1 Initial state . . . 191
6.1.2 Spin up . . . 192
6.1.3 Control run . . . 194
6.2 Atmospheric warming . . . 195
6.2.1 Response timescale . . . 195
6.2.2 Sea ice response to warming . . . 198
6.2.3 Dynamics of full depth convection . . . 204
6.3 Ocean warming . . . 207
6.3.1 Initial warming . . . 208
6.3.2 Consequences of ice melt . . . 210
6.3.3 Full depth convection . . . 213
6.4 Comparison with other studies . . . 217
6.4.1 Observations . . . 217
6.4.2 Theory and 1-D models . . . 220
6.5 Summary . . . 222

7 Discussion and conclusions 225
7.1 Key results and their implications . . . 226
7.1.1 Modelling mushy layer convection with Adaptive Mesh Refinement 226
7.1.2 Steady state convection . . . 227
7.1.3 Convection during transient growth . . . 229
7.1.4 Convection in warming sea ice . . . 233
7.2 Opportunities for further investigation . . . 235

Bibliography 239

x

1

Introduction

Despite the recent rapid decline of sea ice (Cavalieri and Parkinson, 2012), vast areas of the polar oceans still freeze each year. With a typical thickness of order several metres (Haas, 2010), sea ice is a natural barrier which constrains the transport of heat, momentum and chemicals between the ocean and atmosphere (Struthers et al., 2011; Vihma, 2014). Sea ice is a porous material composed of fresh ice crystals and salty brine; a *mushy layer* (Worster, 1992a). Flow of salty brine through the ice can lead to a rich array of phenomena, with important consequences for both the local and global climate and biogeochemical systems (Hunke et al., 2011). Motivated by a desire to understand these processes, this thesis will investigate problems involving fluid flow and phase change within mushy layers whose properties reflect those of sea ice.

Whilst fresh water ice is present around the world from the poles to the equator, sea ice is only found at high latitudes. For sea ice to form the ocean must be cooled below approximately -2°C, the exact temperature depending on salinity. This constraint restricts the location of sea ice both spatially and temporally. Only in the polar regions is the atmospheric cooling sufficiently strong to form sea ice, and even here the seasonal variability results in highly variable ice coverage (Stroeve and Meier, 2017). Indeed, accounting for both the Arctic and Antarctic, around 24 million km^2 of open ocean is frozen (and then melted) every year (Fetterer et al., 2017) - an area the same size as North America - and therefore the mechanism by which sea ice forms is an important physical process to understand.

Sea ice interacts with the earth system through a wide variety of mechanisms (see Overeem, 2006, for a detailed review, with pertinent concepts summarised below). In contrast to fresh water ice, sea ice is white and relatively opaque. It absorbs significantly less radiative energy than the darker ocean which it covers, giving rise to

the ice-albedo feedback which has a destabilising effect on the ice cover (e.g. Curry et al., 1995; Moon and Wettlaufer, 2011). The difference in optical properties can be explained by the presence of sub-millimetre sized liquid inclusions in sea ice, which remain unfrozen due to the presence of impurities - primarily sodium chloride - in sea water (Petrich and Eicken, 2010). Due to chemical segregation during freezing of ocean water, these impurities can exist in far higher concentrations in sea ice than the ocean, stimulating intense primary production in the summer months (Arrigo et al., 1997). The impurities are transported through the network of liquid inclusions making sea ice an active component of the global biogeochemical cycle (Vancoppenolle et al., 2013). Where dissolved impurities become highly concentrated, they can have particularly significant effects. Halogens exposed to the atmosphere may explain ozone depletion events (Lieb-Lappen and Obbard, 2015), whilst accumulated microplastics can alter the optical properties of sea ice (Geilfus et al., 2019).

Whilst highly concentrated in the liquid brine, when averaged over both solid and liquid phases the impurities in sea ice represent just a fraction of those that are present in the ocean water from which it forms. The average bulk salinity of mature first year sea ice is often of order 5–10 g/kg (Nakawo and Sinha, 1981; Notz and Worster, 2008), whilst the average salinity at the surface of the polar oceans is around 30-34 g/kg (Pilson, 2013). The salt which is not trapped within sea ice is rejected into the ocean, with observed rates of up to 2 $\mathrm{kg\,m^{-2}}$ per day (Notz and Worster, 2008). This increases the density of the cold surface waters that sink to form the deep water masses which make up a crucial component of the global overturning circulation (Backhaus et al., 1997; Abernathey et al., 2016). Additionally, dense salty plumes have been suggested as an explanation for the formation of the Arctic halocline (Nguyen et al., 2009). The halocline, at a depth of around $50 - 200$ m, suppresses upward heat fluxes from the warm Atlantic water below, significantly enhancing ice production at the surface (Cottier et al., 2007).

Many of these phenomena are related to the porous nature of sea ice. Internal fluid flow can enhance the transport of heat, salt, and dissolved chemicals throughout the ice and into the ocean below (Lake and Lewis, 1970; Eide and Martin, 1975; Wettlaufer et al., 1997a; Jardon et al., 2013). Such processes occur over scales smaller than 1 m,

involving nonlinear feedbacks between fluid and thermodynamics, and are currently not fully understood (Hunke et al., 2011).

1.1 Thesis structure and aims

In this thesis, I will investigate fluid flow in porous sea ice driven by natural convection. This area has been studied previously using a range of methods, including environmental observations, experiments, numerical simulations and theoretical analysis (see Wells et al., 2019, for a recent review). Here I will develop and implement a new method for numerically simulating fluid flow in mushy layers, and then use this to explore new scenarios and parameter regimes which are of particular relevance to sea ice.

This chapter will give an introduction to the physics of sea ice and describe how the thermo- and hydrodynamics of porous ice can be modelled. In § 1.2 I introduce how sea ice can be modelled as a mushy layer, then in § 1.3 I explain the mechanism behind convection within sea ice and review relevant studies of this process. Finally I summarise the contents of this chapter in § 1.4, and set out the key scientific questions that will be addressed in the remainder of the thesis.

In chapter 2 I introduce the model of thermodynamics and flow in porous sea ice that will be used in thesis, then in chapter 3 I present the new numerical method developed to solve this model. I then describe the results from a wide variety of numerical simulations over the course of three chapters. In chapter 4 I consider growth from a cold boundary in a thin Hele-Shaw cell, which is translated at a fixed speed. In this setting, I compute steady-state solutions for a periodic array of convection cells whilst systematically varying the key system parameters, and derive scaling laws to explain the results. Chapter 5 explores transient growth from a fixed boundary, with a particular focus on the properties of the narrow channels which form. In chapter 6 I investigate the conditions under which sudden atmospheric or oceanic warming may trigger convection within a layer of sea ice. Finally, I summarise the most significant results in chapter 7.

1.2 Introduction to sea ice

The behaviour of sea ice varies across a wide range of temporal and spatial scales. On a microscopic level the properties of sea ice are dictated by its crystal structure, which consists of water (H_2O) molecules arranged tetrahedrally in a formation which is highly resistant to the inclusion of other components such as sodium chloride (Petrich and Eicken, 2010). In contrast, on a global scale sea ice forms a thin film covering the polar oceans with a strong seasonal cycle. In this section I will explain how sea ice forms, and how the properties of sea ice on length scales of centimetres to metres are well described by mushy layer theory.

1.2.1 Sea ice formation

The transition from open ocean to mature sea ice occurs through a series of distinct stages (see e.g. Petrich and Eicken, 2010). The first ice crystals to form are known as *frazil ice*. In still conditions these will predominantly form at the surface, whilst wind and wave action mixes the upper cold layer of the ocean within which frazil can form (Martin, 1981). Either way, the ice crystals are buoyant and eventually accumulate into a soupy surface layer of *grease ice*.

In the absence of significant wind, grease ice then solidifies into smooth, thin, sheets of *nilas* (< 10 cm thick and dark in colour) before thickening into greyish-white *sheet ice*. Turbulent conditions and significant wave activity can prevent the formation of nilas, the grease ice instead forming small (of order metre wide) circular discs known as *pancake ice*. These discs are pushed against each other by the wind and waves and eventually coalesce to form sheet ice with a much rougher appearance than that which forms in still conditions (Petrich and Eicken, 2010).

Sheet ice can be further classified based on whether it is attached to a shoreline (*fast ice*) or not (*drift ice*), and by its age. Ice which has survived one or more melt seasons is notably different from first year ice. During the summer, fresh melt water percolates down from the surface, 'flushing' salty brine out into the ocean (Untersteiner, 1968) and filling brine channels with fresher water which will freeze more completely in the following winter. Consequently, multiyear ice is less saline and less porous

than first year ice. Additionally, multiyear ice can continue to grow by accumulating mass at the surface, through snow precipitation, and at the base through additional freezing. Hence multiyear ice is usually thicker than younger ice (Haas, 2010), although mechanical deformation also contributes to thickness changes.

Sheet ice, and particularly drift ice, is highly heterogeneous in all three spatial dimensions. Divergent stresses imposed by the wind and ocean can cause the ice cover to break apart, forming areas of open water known as *leads* or *polynyas*. In these regions the ocean is directly exposed to the cold atmosphere leading to intense heat loss and rapid ice growth (see Morales Maqueda et al., 2004, for a review of polynyas). Meanwhile, convergent stresses may force ice floes together. When thin floes meet, one may slide over the over in a process known as *rafting*. When larger floes collide, ice may be forced downwards at the interface forming linear features called *pressure ridges* which extend up to 10 m into the ocean (Haas, 2010).

On a global scale, and over timescales of weeks to months, the deformation of the ice pack is often described by models which treat it as a thin elastic-plastic or viscous-plastic material (Feltham, 2008), which grows and melts due to thermal conduction in the vertical direction (e.g Maykut and Untersteiner, 1971). Such models attempt to describe deformation which arises due to internal and imposed stresses, such as the fracturing and ridging of the ice cover, and the overall growth and melt of the ice cover. On a local scale of centimetres to metres, and on far shorter timescales of seconds to hours, a different dynamical regime exists in which the key physical processes are the transport of heat, salt, and momentum in both the horizontal and vertical directions. To study processes on this mesoscopic scale, as is the goal of this thesis, a common approach is to model sea ice as a *mushy layer* (Hunke et al., 2011). The striking under-ice topography such as pressure ridges which were discussed above are the consequence of wind and ocean driven collisions between well developed ice floes (Haas, 2010). Hence, on scales which are far smaller than size of individual ice floes, and during the early stages of ice growth, it is reasonable to consider an approximately planar ice-ocean interface (Petrich and Eicken, 2010).

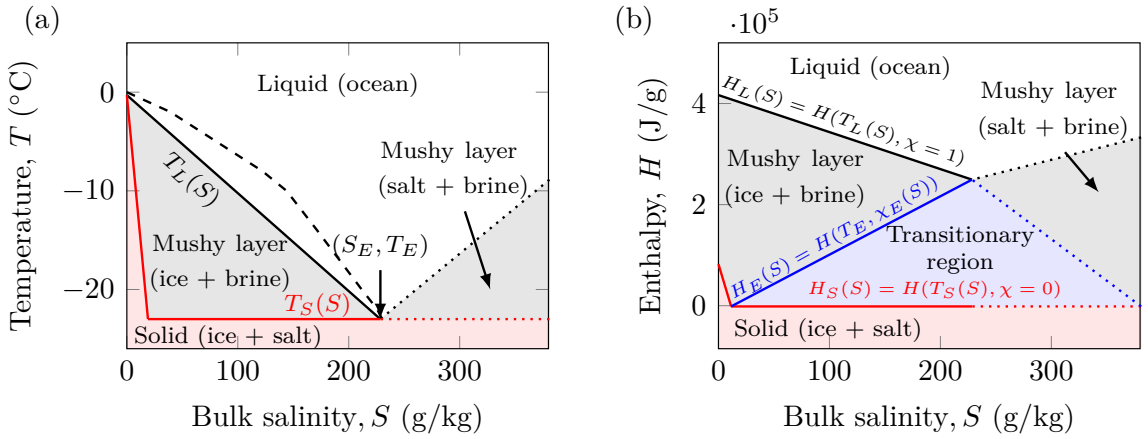


Figure 1.1: Idealised equilibrium phase diagram for salt water in (a) (temperature-salinity) space and (b) (enthalpy-salinity) space for salinities up to 350 g/kg and at constant pressure of 1 atm, using the physical properties given in table 2.1. The full phase diagram, which extends up to 1000 g/kg, is not shown as sea ice does not reach values above the eutectic salinity S_E. Above the liquidus (black, $T = T_L(S)$) the mixture is entirely liquid. For convenience, the liquidus for salt water – indicated by a black dashed line in (a) – will be linearised (black solid line). Below the solidus (red, $T = T_S(S)$) it is entirely solid. In between, the two phases co-exist in thermal equilibrium. The eutectic solid phase is formed at a fixed temperature $T = T_E$ so is not visible in $T - S$ space, the difference in enthalpy across it results from the latent heat release due to phase change at the (non zero) eutectic porosity χ_e. Note that the gradient of the solidus between $T = 0$ and $T = T_E$ has been exaggerated so that it is visible; in reality it is around $\partial T_s/\partial S = -10^3$ °C/ $\left(\mathrm{g\,kg^{-1}}\right)$ so the solidus would be indistinguishable from a vertical line drawn at $S = 0$. Data from Richardson (1976) has been added for the nonlinear liquidus (black dashed line) for comparison to the approximation of a linear liquidus.

1.2.2 Sea ice is a mushy layer

The porous structure of sea ice results initially from the consolidation of frazil ice crystals, and more generally from morphological instability. For pure ice growth into a saline ocean cooled from above, a planar ice-ocean interface is unstable to small perturbations, leading to dendritic growth (Mullins and Sekerka, 1964). This gives sea ice an incredibly complicated microscopic structure with an ice matrix bathed in liquid brine (Petrich and Eicken, 2010). In order to study this process numerically and theoretically, it is helpful to restrict ourselves to scales larger than the very fine microstructural features and treat sea ice as a *mushy layer* using a phase-averaged approach. It is often assumed that the solid and liquid phases are in local thermodynamic equilibrium. This approach is well established theoretically (Feltham et al., 2006; Worster, 1997) and has been used to explain observations of sea ice made in the field (e.g. Wettlaufer et al., 2000)

and in the laboratory (e.g. Wettlaufer et al., 1997a).

We here consider mushy layers consisting of two chemical components. The leading order behaviour of sea ice can be understood by considering a mixture entirely composed of H_2O and NaCl (Petrich and Eicken, 2010; Vancoppenolle et al., 2019). However the underlying theory has broader utility (e.g. to metallurgy and the dynamics of the Earth's inner core) so we use a generic formulation. The phase diagram for such a binary eutectic material is shown in fig. 1.1 for the temperature T, bulk phase-averaged salinity S, and enthalpy H. Above the *liquidus temperature* $T = T_L(S)$ mushy layers are simply liquid solutions (here, salt water) with a porosity or liquid volume fraction χ equal to 1. Below the *eutectic temperature* T_E they are entirely solid, with $\chi = 0$. Between these two regimes there exists a mixture of solid and liquid phases. The *eutectic salinity* S_E marks the transition between systems where ice solidifies ($S < S_E$) and salt solidifies ($S > S_E$) and is sufficiently large that terrestrial sea ice always remains in the former regime. The solute (NaCl) is rejected from the solid phase (ice) during sea ice growth, becoming more concentrated in the surrounding fluid and decreasing its freezing point. This allows liquid inclusions to exist at temperatures well below the freezing point of standard ocean water.

This simplified phase diagram ignores the host of other impurities present in sea ice, which include potassium chloride (KCl), sodium sulphate (Na_2SO_4), and magnesium chloride ($MgCl_2$). Fortunately, these other components have a sufficiently small mass fraction relative to sodium chloride to be neglected to a good approximation (Assur, 1960). The liquidus and solidus are therefore typically surfaces in a higher dimensional space (Assur, 1960), but we assume them to be linear functions of the bulk salinity. The generality of mushy layer theory means that any results we arrive at will be applicable to a range of other geophysical problems involving solidification. Equally, the use of mushy layer theory allows us to draw parallels between experiments conducted with different chemical systems, such as ammonium chloride solutions (NH_4Cl-H_2O), and sea ice. Mushy layer theory also applies to systems with more than two components (e.g. see Aitta et al., 2001), which can lead to complicated convective dynamics (Anderson and Guba, 2020) but the study of these systems will not be pursued here.

1.2.3 The concentration ratio

In addition to other parameters defined later, the properties of a mushy layer are highly dependent on the dimensionless *concentration ratio*,

$$\mathscr{C} = \frac{S_i - S_S}{\Delta S}, \tag{1.1}$$

which describes the ratio of the initial fluid concentration before solidification, S_i, minus the solid composition S_S, to the characteristic range of concentrations $\Delta S = |S_E - S_i|$. This ratio lies in the range $0 \leq \mathscr{C} \leq \infty$.

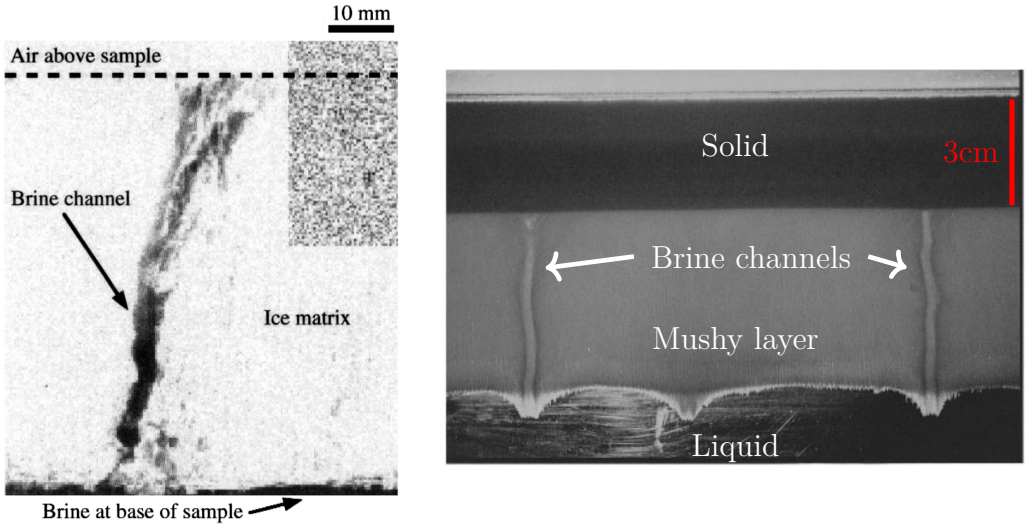
Physically, it can be helpful to think of the concentration ratio as a measure of the increase in liquid concentration during solidification relative to typical variations of the liquid concentration. In this sense, $\mathscr{C}$ is the solutal analogue to the Stefan number which describes the release of latent heat during solidification. Large values of $\mathscr{C}$ are known as the *near eutectic* limit and correspond to systems where the bulk solute concentration is typically large and close to S_E. Such systems release relatively more solute upon solidification than in the opposite *far-eutectic* limit (where $\mathscr{C} \ll 1$). As the presence of solute depresses the freezing point of the fluid, the enhanced release of solute in near eutectic systems acts as a barrier to further solidification and ensures that the liquid fraction typically remains high, with $\chi \approx 1$. In contrast, systems in the far-eutectic limit have a larger range of porosity.

Sea water has a salinity far below the eutectic salinity for salt water, so sea ice (with $S_i \approx 30$ g/kg, $S_E \approx 230$ g/kg, and $S_S \approx 0$ g/kg) has a relatively small concentration ratio, $\mathscr{C} \approx 0.15$. As we will see later, previous theoretical studies have predominantly focussed on systems in the near-eutectic limit - such as metallic alloys - where the governing equations are more analytically tractable but may be less relevant to the dynamics of sea ice. A key focus of this thesis will be the exploration of systems in the far-from eutectic limit, where $\mathscr{C} \ll 1$.

1.3 Natural convection in sea ice and other mushy layers

Once a consolidated mass of sheet ice has formed, further basal growth can occur as long as the net surface flux to the atmosphere continues to extract heat. The net surface heat flux is determined by several components, whose contributions vary with both the time of year and the thickness of the ice (Maykut, 1978). These include incoming thermal and solar radiation from the atmosphere, and outgoing thermal emission from the ice. It is through this final stage that most sea ice forms, extending the ice depth from around 10 cm to a few metres (Petrich and Eicken, 2010). During this process, an unstable density stratification arises in the pore fluid due to the salinity and temperature gradients through the ice. The density of salt water increases with salinity and decreases with temperature, with the salinity dependence being roughly 20 times stronger (Worster and Rees Jones, 2015). Salt is not included in the ice crystals which form during ice growth, but remains in the surrounding liquid whose salinity is therefore increased. Without fluid flow, the liquid density would usually be highest at the top of the ice, where temperatures are usually colder and the volume fraction of ice is higher. The lowest density of interstitial brine is found at the base of the porous ice layer. Once the stratification is sufficiently unstable the dense fluid sinks though the porous ice into the ocean, being replaced with warmer fresher water from below.

Buoyancy driven convection of interstitial brine results in a net flux of salt from the ice into the ocean, and this so-called gravity drainage is the dominant desalinisation mechanism during the winter freezing season (Notz and Worster, 2009). A curious consequence of this convection is the formation of brine channels (Eide and Martin, 1975; Worster, 1997), entirely liquid conduits with diameters much larger than the size of individual pores (see fig. 1.2). Brine channels, first observed by Bennington (1967), are the most striking example of the heterogeneous porosity field formed by convection within sea ice (Worster, 1997). When highly saline brine sinks, it finds itself out of thermodynamic equilibrium with its warmer and fresher surroundings. Salt diffuses much slower than heat, so the salt concentration returns to a state of local equilibrium by dissolving ice crystals, reducing the salinity of the surrounding liquid. By reducing



(a) **(b)**

Figure 1.2: (a) Vertical profile of a brine channel captured by Magnetic Resonance Imaging (MRI) in a 0.14 m deep sample. The top right corner has been enhanced to show the relative size of liquid pores (black) within the ice (image from Eicken et al., 2000).
(b) Mushy layer grown in an experiment from an ammonium chloride solution, highlighting the spacing between channels relative to their width. The salt solidifies out of the solution at room temperature leaving behind a buoyant liquid, in contrast to sodium chloride where the residual solution is relatively dense, so the original image has been inverted vertically here to yield a dynamical analogy with the geometry of sea ice. (image adapted from Schulze and Worster, 1998).

the volume fraction of ice, this process increases the porosity and permeability in regions of downwelling, which permits a stronger fluid flow. This drives a feedback process where eventually the flow is focussed into entirely liquid vertical channels - the brine channels - which dominate the salt and heat fluxes from the ice to the ocean.

Natural convection, and in particular the formation of vertical liquid channels, can occur during the solidification of any mushy layer with a statically unstable density gradient. This typically arises in cases where the buoyancy of the interstitial fluid is a function of its composition. Whilst this thesis is particularly concerned with this phenomena in the context of sea ice, it is often useful to consider the behaviour of similar analogue systems. Common examples of mushy layers are listed in table table 1.1; of these, ammonium chloride is particularly well studied as it solidifies at temperatures which are readily achieved and controlled in the laboratory.

In most cases, including sea ice and ammonium chloride, the density of the interstitial fluid is dominated by compositional rather than thermal variations. In the case of sea

System	Primary components	Reference
Sea ice	H_2O - NaCl	Worster and Wettlaufer (1997)
Ammonium chloride	H_2O - NH_4Cl	Katz and Worster (2008)
Isopropanol solution	H_2O - C_3H_8O	Worster (1997)
Sucrose solution	H_2O - $C_{12}H_{22}O_{11}$	Aussillous et al. (2006)
Metallic alloys	Pb-Sn, Pb-Sb, and Pb-Sn-Sb	Sarazin and Hellawell (1988)

Table 1.1: Summary of some of the mushy layer systems that have been studied in experiments.

ice, the density of the interstitial fluid increases as salt is rejected during solidification and hence an unstable stratification occurs when ice grows downwards from a cold surface - as happens in the polar oceans. For some other systems, such as ammonium chloride, the density decreases during solidification as salt crystallises to leave a lower concentration melt. For convection to be possible, growth must be upwards from a cold boundary. Such differences are relatively superficial in settings where thermal convection is relatively insignificant, and different experiments may be compared by simply reversing the direction of gravity where necessary.

When considering the convective stability of a mushy layer a key factor is the ratio of buoyancy to dissipative mechanisms, which is known as the *mushy Rayleigh number* and given by

$$Rm = \frac{\rho_l g \beta \, \Delta S \, h \, K_0}{\kappa_l \, \eta}, \tag{1.2}$$

where ρ_l is the reference density of the liquid in a linearised equation of state, g is acceleration due to gravity, β is the solutal expansion coefficient, h is a characteristic length scale, K_0 is the characteristic permeability, κ_l is the thermal diffusivity in the liquid and η is the dynamic viscosity of the fluid. Systems with a larger value of Rm will be more unstable. Physically, the mushy Rayleigh number can be thought of as a ratio between the buoyancy timescale and the diffusive timescale (Worster and Rees Jones, 2015), i.e.

$$Rm = \frac{\tau_B}{\tau_D} = \frac{\rho_l g \beta \, \Delta S \; K_0/(\eta h)}{\kappa_l / h^2}. \tag{1.3}$$

Parcels of fluid move through the ice matrix with a timescale τ_B, whilst at the same time they begin to equilibrate with their surroundings over a timescale τ_D. For convection to occur, particles must move sufficiently quickly that they remain buoyant, i.e. the ratio $Rm = \tau_B/\tau_D$ must be sufficiently large. The buoyancy differences within a system, characterised by $\Delta B = \rho_l g \beta \Delta S$, will drive flow and therefore increasing ΔB will increase Rm (Worster, 1997). Reducing the permeability K_0 makes it more difficult for flow to pass through the porous matrix and hence reduces Rm (e.g. see Aussillous et al., 2006). Similarly, increasing the fluid viscosity restricts fluid flow (Tait and Jaupart, 1992).

In this section, I will review some of the previous work on convection in sea ice and relevant analogue mushy layers.

1.3.1 Field observations of convection in sea ice

Field observations are a vital method for studying sea ice, with ice coring being a common method. This typically involves taking cores from a designated region of ice, say 100×100 m, at specific time intervals and dividing them into sections which are melted to enable measurement of their chemical constituents (e.g. Nakawo and Sinha, 1981; Eicken, 1992). Results from these studies reveal the typical "C-shaped" salinity profile within sea ice: high salinity at the top and the base, lower salinity in the interior (Cox and Weeks, 1974). However the sampling errors associated with this technique are large, due particularly to brine draining out of the bottom of cores (Notz, 2005). It is also not possible to directly observe convection within the ice by taking one dimensional samples like these. Wakatsuchi and Saito (1985) considered the horizontal variation in samples with cross-sectional area 45×45 cm and found that the spatial density of brine channels increased with the ice growth rate. A particularly methodical approach was employed by Cottier and Wadhams (1999), who divided sea ice samples of approximate size $30 \times 40 \times 20$ cm into individual 1 cm^3 cubes and then determined the salinity of each cube by melting it. Their data clearly reveals the highly variable brine distribution within sea ice, including the existence of regions of very high salinity where brine channels were observed. Meanwhile, Zhou et al. (2013) took ice cores within the same region of ice over a period of 4 months and found that the bulk salinity varies over a range of timescales from days to months.

Lake and Lewis (1970) made in situ measurements by freezing thermistors into growing sea ice, detecting horizontal temperature gradients and therefore convection within the ice. Furthermore, they took vertical cross sections of sea ice which revealed a vertical network of channels through which the brine drains into the underlying ocean. More recently Notz and Worster (2008) used a series of horizontal wires, vertically separated by a few centimetres, to measure the electrical impedance and temperature and hence infer the porosity and salinity profiles within sea ice. Their results confirmed the presence of an unstable brine density gradient which drives continuous salt loss, although the actively convecting region becomes restricted to the bottom of the ice as growth progresses.

Wakatsuchi and Ono (1983) directly measured brine release from growing sea ice by placing a funnel and expandable balloon a small distance below the ice. Meanwhile, various authors have measured the ocean salinity at high latitudes near to ice formation sites (e.g. in the Okhotsk sea; Shcherbina et al. (2003), the Japan sea; Talley et al. (2003), and the Canada Basin; Timmermans (2015)). These observations demonstrate that brine rejection during sea ice formation is important for ocean dynamics, via bottom water formation and ventilation.

Brine fluxes from ice have also been observed during the spring, as the atmosphere and the ocean begins to warm (Widell et al., 2006; Jardon et al., 2013; Peterson, 2018). In some cases, salt fluxes have been observed despite melting at the base of the ice (Widell et al., 2006; Peterson, 2018), where a flux of fresh water would be expected. Ice cores suggest that these brine fluxes are likely associated with desalination of the full depth of ice (Peterson, 2018), which may have been made possible by an increase in the permeability of the warming ice.

Sea ice is involved in the transport of other chemicals in the polar oceans. Evans and Nishioka (2018) observed that brine release is a key mechanism in the distribution of trace metals such as iron, with potential implications for biological production. Within sea ice nutrients are rejected into the liquid phase where they can be found in far higher concentrations than elsewhere in the polar regions. Coupled with the availability of sunlight this can lead to regions of intense biogeochemical activity within the porous ice (see Vancoppenolle et al., 2013, for a review).

1.3.2 Sea ice in the laboratory

A primary limitation of the observations described above is their spatial and/or temporal sparsity. In situ measurements sample a very small subset of the vast polar oceans, whilst the data collected typically either spans only a few weeks (Widell et al., 2006; Jardon et al., 2013; Talley et al., 2003), or is temporally sparse (Zhou et al., 2013). Laboratory experiments offer a more controlled environment in which to study sea ice and mushy layer processes; an extensive review of many of these experiments can be found in Zhong et al. (2012). I here summarise the findings most relevant to the problems studied in this thesis.

Thin Hele-Shaw cells provide a useful tool for observing convection due to their tendency to promote quasi-two-dimensional flow. Eide and Martin (1975) froze sea water in a 3 mm thick cell whilst injecting dye to reveal the drainage features, which provided further evidence of the tall and narrow geometry of brine channels and broader return flow between channels. Niedrauer and Martin (1979) used a thinner cell - with a gap width of 1.6 mm - and observed brine channels which were typically orientated at between 30° to 60° to the horizontal and which moved through the ice in both the vertical and horizontal directions. Middleton et al. (2016) grew sea ice in a Hele-Shaw cell of gap width 3 mm, and observed that the spacing between brine channels increases with ice depth whilst convection through individual channels was intermittent over timescales of minutes to hours. Eide and Martin (1975) observed oscillatory flow in the brine channels, where downflow out of the channel was followed by flow up into the channel. Unfortunately, Middleton et al. (2016) were not able to determine whether the intermittent 'on-off' behaviour they observed involved an upwards return flow like that seen by Eide and Martin (1975).

Whilst Hele-Shaw cells make observation of the sea ice easier, they are not entirely representative of the three dimensional nature of ice formation. Wakatsuchi and Ono (1983) collected the brine rejected from sea ice grown in the laboratory, and found that salt flux decreased as the growth rate decreased. Meanwhile, Wakatsuchi and Saito (1985) also grew sea ice in the laboratory and found that the density of brine channels decreases as the ice growth rate decreases. Wettlaufer et al. (1997b) grew ice from salt water in a rectangular container and measured the concentration of the liquid

region. The concentration was constant until the ice reached a critical thickness and convection began, at which point it increased linearly with ice thickness. The idea of a critical thickness, related to a critical Rayleigh number, is supported by theoretical linear stability analyses (as discussed later in § 1.3.3).

Some authors have considered solidification of other solutions, most commonly ammonium chloride (NH_4Cl). Chen and Chen (1991) grew mushy layers in an ammonium chloride solution, and found that convection within the mushy layer was possible once the local Rayleigh number exceeded a critical value. Tait and Jaupart (1992) observed channels whose diameter and spacing increased with increasing fluid viscosity whilst solidifying NH_4Cl from a fixed cold boundary. In 3-D, Tait et al. (1992) found that convection forms in roughly hexagonal cells with channels at each node for sufficiently strong flow. Solomon and Hartley (1998) measured the temperature field during NH_4Cl growth in a Hele-Shaw cell using thermochronic liquid crystal paints, and observed that the number of active channels typically decreased over time. Neufeld and Wettlaufer (2008b) investigated the stability of a mushy layer to shear flow, and found that there is a critical flow speed below which the mushy layer is unaffected by the flow. Using a different analogue solution (sucrose–water) Aussillous et al. (2006) observed significant branching of channels, whilst the channels were confined near the mush-liquid interface to regions where a local Rayleigh number was sufficiently large. Zhong et al. (2012) found that the convective instability is affected by the horizontal width λ of the apparatus within which a mushy layer is grown. If λ is below a critical value, which varies with the system properties, then convection does not occur. Recently, Ding et al. (2019a,b) considered solidification of ammonium chloride from a boundary whose temperature varied periodically which results in damped thermal waves propagating throughout the mushy layer.

Other authors have considered solidification of NH_4Cl in the context of *directional solidification*; a material sample is translated vertically at a steady speed V between two heat exchangers, which makes the analytic problem more tractable and hence allows for easier comparison between results (e.g. Copley et al., 1970; Katz and Worster, 2008; Whiteoak et al., 2008). Chen (1995) used dye to visualise flow, and X-ray tomography to measure the solid fraction within the mushy layer, finding that the solid fraction

decreases unexpectedly near the eutectic interface. Peppin et al. (2008) found that convection is suppressed with increasing solidification speed V, which effectively reduces the relevant length scale $h \sim \kappa_l/V$ in the dimensionless mushy Rayleigh number (eq 1.2).

Geophysical interest in mushy layers is partly motivated by the possibility of mushy layer convection in the Earth's inner core (Bergman and Fearn, 1994), motivating several further experimental studies. Bergman et al. (1997) considered directional solidification of a Pb-Sn solution and found that small interfacial channels can form at a lower mushy Rayleigh number than channels which penetrate into the interior of the mushy layers. Huguet et al. (2016) considered crystallisation of an ammonium chloride solution in hypergravity conditions (up to 1300 g) and found that the spacing between channels decreases as gravity is increased, which is consistent with the channel spacing decreasing as the mushy Rayleigh number is increased. O'Rourke et al. (2012) also studied the effect of the strength of gravity on solidification of ammonium chloride. They found that under microgravity conditions buoyancy forces become weaker, reducing the mushy Rayleigh number, and as a result convection was suppressed.

Solidification of metallic mushy layers also has industrial applications to metal casting (Copley et al., 1970), motivating other studies. Sarazin and Hellawell (1988) investigated solidification of a range of lead-based metallic alloys and found that sustained channel flow required a sufficiently permeable mushy layer, with the permeability being partly controlled by the composition of the alloy. Channels were observed to propagate through the mushy layer and interact, decreasing their density. Hellawell et al. (1993) compared lead-based metallic alloys with aqueous ammonium chloride, and an organic succinonitrile-ethanol mixture, and found that in all three cases the channels had similar dimensions though the strength of flow out of the channels varied by several orders of magnitude.

1.3.3 Theoretical approaches

Theoretical models of convection rely on mushy layer theory, which was well established by the time geophysicists applied it to sea ice. Metallurgists had long referred to binary alloys as 'mushy' (Smith, 1868) and have more recently explained the formation of liquid chimneys (analogous to the brine channels seen in sea ice) which result from

compositionally driven convection (Copley et al., 1970). Convection in mushy layers share many similarities with convection in non-reactive porous media (e.g. see Hitchen, 2017, for a comprehensive review). Here, I will restrict the discussion to the aspects of convection in mushy layers which is most relevant to this thesis. More comprehensive reviews can be found in Wells et al. (2019) and Hitchen (2017).

The full system of equations governing mushy layer growth cannot be solved analytically, so theoretical approaches often rely on stability analyses of varying complexity. In a stability analysis, a stable solution to the governing equations, known as a *base state*, is computed then the evolution of small perturbations to this state are considered for different parameters. For parameters where these perturbations grow the configuration is deemed to be unstable, otherwise it is considered to be stable. A convenient base state for analysing the stability of a growing mushy layer is most readily found in the case of directional solidification where, as described in § 1.3.2, growth proceeds at a fixed rate V. In this setting, Fowler (1985) found analytic solutions for solidification in the absence of flow. Assuming that $\mathscr{C} \gg 1$, Fowler (1985) then found an analytic expression for a critical Rayleigh number, above which small perturbations were convectively unstable.

By solving numerically, Worster (1992b) was able to consider the linear stability of a similar steady base state under a wider range of parameters. In particular, Worster (1992b) found that the critical Rayleigh number for convection increases as the concentration ratio is decreased. Worster (1992b) also identified two basic modes of instability; a boundary layer mode in a solutal boundary layer on the liquid side of the mush-liquid interface, and a mushy layer mode which penetrates further away from the mush-liquid boundary into the mushy layer. Channel formation requires substantial flow through the mushy layer to dissolve the solid matrix. The boundary layer mode predominantly drives flow in the liquid, having only a weak effect on the mushy layer. Instead, it is the mushy-layer mode which is believed to be primarily responsible for the development of channels (Worster, 1992b).

Channel formation is an inherently nonlinear process, motivating the use of more complicated weakly non-linear analyses. Amberg and Homsy (1993) found that, under certain conditions, the critical Rayleigh number may increase with increasing $\mathscr{C}$, in

contrast to the monotonic decrease found by Worster (1992b) using linear stability. Chung and Chen (2000) found that the development of channels is dependent on $\mathscr{C}$. For small $\mathscr{C}$, channels develop at the mush-liquid interface and grow into the mushy layer whilst for large $\mathscr{C}$ channels may also form inside the mushy layer and grow out towards the mush-liquid interface.

A sufficiently strong shear flow in the fluid adjacent to a mushy layer may enhance convective instability (Neufeld and Wettlaufer, 2008a; Feltham, 2002). In the case of sea ice, Neufeld and Wettlaufer (2008a) estimate that a flow of magnitude 1 m s^{-1} would be required. Whilst early studies (see review by Worster, 1997) considered the stability of a mushy layer with a rigid mush-liquid boundary, Roper et al. (2008) found that allowing deformations to this interface reduces the critical Rayleigh number for convection.

The nature of the convective instability has been most widely studied in the near-eutectic limit, where $\mathscr{C} \gg 1$. In this case, oscillatory modes of convection may occur (Anderson and Worster, 1996), with the exact nature of the instability depending on the magnitude of the permeability and the extent to which the permeability varies with porosity (Amberg and Homsy, 1993; Guba and Worster, 2006). Regarding pattern formation, the results of Amberg and Homsy (1993) suggest that 2-D rolls are most likely, whilst Anderson and Worster (1995) found that either hexagonal or 2-D rolls may be possible (see Worster, 1997, for a detailed review). Whilst Amberg and Homsy (1993) and Anderson and Worster (1995) considered a superposition of discrete 2-D rolls and hexagons, Keating et al. (2011) took a more general approach by considering a superposition of a continuum of planforms and found that many possible arrangements are possible including, but not limited to, hexagons and 2-D rolls.

1.3.4 Numerical simulations and nonlinear solutions

Numerical simulations offer the ability to explore states with fully developed convection through liquid channels. Transient simulations have shown promise, but ultimately struggled to explain or replicate all of the observed features of mushy layer convection. Oertling and Watts (2004) simulated sea ice growth from a fixed cold boundary and found salt drainage rates comparable to experiments, but their simulations did not reproduce the observation that a critical ice depth is required for convection to occur.

Meanwhile, Katz and Worster (2008) simulated directional solidification of NH_4Cl in a Hele-Shaw cell and observed the onset of convection after sufficient simulation time but were unable to fully resolve the narrow brine channels which formed. Both Katz and Worster (2008) and Oertling and Watts (2004) used a single domain *enthalpy method* to solve for the evolving mushy-liquid interface, whereby a single set of equations are solved in both the mushy layer and liquid regions. Felicelli et al. (1992) and Kaempfer and Rappaz (2003) have also simulated solidification of metallic alloys, which typically have a much higher porosity than sea ice.

Other authors considered steady state flow through a periodic array of convection cells during directional solidification. Schulze and Worster (1998) used a scaling analysis to deduce appropriate boundary conditions for numerical calculations, and predicted the existence of a thermal boundary layer adjacent to the narrow channels. Schulze and Worster (1998) then solved numerically for flow and solidification solely within the mushy layer using a lubrication approximation to asymptotically approximate flow in the narrow channels. They found that at low Rayleigh numbers there are two possible solutions for flow with channels, and suggested that these may belong to stable and unstable branches of a subcritical bifurcation. Using the same numerical method, Schulze and Worster (1999) found that channels may emerge from liquid inclusions within the mushy layer. Extending this numerical approach, Chung and Worster (2002) solved separately for flow in the mushy layer and adjacent liquid, coupling the two regions via appropriate boundary conditions whilst retaining the lubrication approximation in the channel. Chung and Worster (2002) found that the critical Rayleigh number for flow was less than the prediction from linear stability. As Rm is increased, Chung and Worster (2002) also found that the channel width and mush depth decrease whilst the spacing between channels also possibly decreases.

When solving for an imposed periodic array of channels, it is necessary to specify the spacing between adjacent channels. Observations of natural sea ice suggest that during the early stages of growth the channel spacing decreases as the ice growth rate increases, whilst for thicker ice the channel spacing is roughly constant (Wakatsuchi and Saito, 1985). Meanwhile, the experiments of Middleton et al. (2016) and simulations performed by Katz and Worster (2008) suggest that the channel spacing is proportional

to the depth of the mushy layer. Wells et al. (2010) hypothesised that the system selects the channel spacing which maximises the dissipation of potential energy, which also results in convection cells with a width proportional to their height.

Using the optimal hypothesis, Wells et al. (2011, 2013) found that in the limit $Rm \gg 1$ and $Rm/\mathscr{C} = O(1)$ convection occurs throughout the full depth of the mushy layer whilst the flux of solute through the channels scales linearly with the Rayleigh number. In the same limit, Rees Jones and Worster (2013) constructed a semi-analytical model which reproduces the same leading order behaviour at a reduced computational cost. In their Chimney-Active-Passive (CAP) model, Rees Jones and Worster (2013) consider a narrow active boundary layer adjacent to a channel, with variable vertical flow and curved isotherms, along with a passive region away from the channel with uniform vertical flow. Both approaches seem consistent with experimental results for solute fluxes and flow from a growing layer of sea ice (Wells et al., 2011; Rees Jones and Worster, 2013, 2014) despite the fact that $\mathscr{C} \ll 1$ in the experiment whilst $\mathscr{C} \gg 1$ is assumed in the models. For $Rm \gg \mathscr{C}$, the numerical results of Wells et al. (2013) hint that the flux increases sublinearly with Rm although they did not explore this behaviour in detail. This may have important implications for sea ice growth, where often $\mathscr{C} \approx 0.15$ and $Rm = O(10)$.

1.3.5 Parametrising convection in sea ice

The importance of accurately describing the multiphase physics of brine transport in sea ice within large scale climate models has been demonstrated by a number of authors (see Hunke et al., 2011, for a review). However, these dynamics occur on scales far smaller than those which can be explicitly resolved in such models. Hence, it is necessary to develop simplified approximations for brine transport which depend solely on quantities which can be resolved along with a series of parameters - a process known as *parametrisation*. Guided by simulations, observations, and experiments, a range of different treatments have been proposed for brine rejection in climate models. Until recently, the standard approach enforced a fixed salinity profile $S(z)$ whilst solving for the nonlinear diffusion of heat through the ice (e.g. Bitz and Lipscomb, 1999). Modern developments mean that salt transport is now typically described

in 1D column models with some combination of parameterised turbulent diffusion, parameterised advection, local salt sinks and sources, or relaxation to an equilibrium profile (see Worster and Rees Jones, 2015, for a review). Vancoppenolle et al. (2010) include enhanced solute diffusion once the local Rayleigh number is above a critical value. Other authors have developed schemes which are physically more appropriate, parametrizing advection in terms of a Rayleigh number which is either calculated at each grid cell (Turner et al., 2013; Griewank and Notz, 2013) or over an entire column of ice (Rees Jones and Worster, 2014). The latter is arguably more effective at accurately depicting the nonlocal features of convection. Rees Jones and Worster (2014) suggest that the models of both Turner et al. (2013) and Griewank and Notz (2013) can produce desalination rates lower than those actually observed. However, a lack of observational evidence makes it difficult to constrain these various proposals for capturing gravity drainage (Hunke et al., 2011). All three models constitute a new generation of parametrisations which are crucial improvements on previous purely thermodynamic models of sea ice (Cox and Weeks, 1988). Determining which should be implemented in climate models, and how to tune their parameters, is still an open question (Hunke et al., 2011; Worster and Rees Jones, 2015).

1.3.6 Wider implications of brine transport in sea ice

Convection in sea ice plays a significant role within the global earth system, motivating much of the study of this process. Brine rejection increases the density of the ocean beneath the ice, which tends to sink downwards. Along with wind forcing, such buoyancy transformation contributes to the global thermohaline circulation (e.g. Abernathey et al., 2016). Downwelling in the polar regions is matched by upwelling at lower latitudes and a horizontal flow between the two which transports heat and salt around the global oceans (Schmitz Jr., 1995). Other mechanisms also contribute to the densification of polar waters, including evaporation, precipitation, and surface run off (e.g. rivers), however Abernathey et al. (2016) found that brine rejection was the dominant mechanism in the formation of deep water in the Antarctic. The dense waters formed in the Antarctic, known as Antarctic Bottom Water (AABW) are the coldest in the ocean (Gordon, 2001). Production of AABW is particularly intense within polynyas (Ohshima et al.,

2016), where sea ice is transported by prevailing winds or ocean currents maintaining a region of open ocean within which ice can grow rapidly (Morales Maqueda et al., 2004).

The importance of understanding brine rejection is further highlighted by studies which find that the salinity structure in global climate models is sensitive to the representation of ice-ocean salt fluxes (Duffy et al., 1999; Vancoppenolle et al., 2009). The full significance of the thermohaline circulation, to which brine rejection contributes, is still an active area of research. The deep oceans contain $\sim 30\times$ more CO_2 than the atmosphere, and therefore small changes to their circulation could have large consequences for the global distribution of CO_2 (Skinner et al., 2010). Meanwhile, the strength of the global overturning circulation is affected by the rate of bottom water production. Sévellec et al. (2017) found that sea ice decline may reduce the strength of the Meridional Overturning Circulation in the Atlantic ocean.

Brine rejection plays a key role in determining the ocean structure within the polar regions (e.g. in the Arctic, Coachman and Aagaard (1974), and Antarctic, Foldvik and Gammelsrød (1988)). In the Arctic, the top ~ 50 m of the ocean is typically colder than $-1.5°$C whilst below ~ 200 m the intrusion of warmer Atlantic water can raise the temperature above 1°C (Rudels et al., 2004). If these two layers had an equal salinity, the lower layer would be relatively buoyant and mix upwards warming the surface of the polar oceans with sufficient heat content to melt all of the sea ice (e.g. Wells and Wettlaufer, 2007). However, there is a sharp change in salinity between the two layers, with the lower layer being saltier, which prevents mixing between the two (Rudels et al., 2004). Brine rejection is believed to play a key role in the formation of the Arctic Halocline by driving convection in the upper ocean (Aagaard and Woodgate, 2001). Indeed, Nguyen et al. (2009) found that an improved representation of brine rejection from rapid ice growth in leads helps to improve modelling of the Arctic halocline in a general circulation model.

The role of fluid transport within sea ice in the global biogeochemical cycle is an increasingly active area of study (see Vancoppenolle et al., 2013, for a recent review). Sea ice forms a permeable barrier between the ocean and the atmosphere, with a significant flux of biogenic gases being observed through the ice such as CO_2 (see Loose et al., 2011), methane (Damm et al., 2015), and dimethyl sulfide (Gourdal et al.,

2019). Under the ice, a key control of phytoplankton growth is the availability of iron (Lancelot et al., 2009). During ice growth, iron accumulates in sea ice in far higher concentrations than usually found in the ocean (Lannuzel et al., 2007) which may then be released, either by ice melt or warming-triggered brine rejection (e.g. Widell et al., 2006), promoting biological activity.

1.4 Summary

Salinity gradients within porous sea ice are generally unstable and, if sufficiently large relative to the ice permeability, can lead to nonlinear convection. The downwelling salty brine provides an important buoyancy forcing for the global oceans, whilst fluid flow through sea ice can transport dissolved nutrients with consequences for the local biogeochemistry.

Whilst numerical simulations are a useful tool for studying convection in mushy layers, previous studies have tended to focus on systems in the near eutectic limit which may behave differently to sea ice. It is not clear whether the results obtained in this limit will still apply in the far-from eutectic case, where feedbacks between porosity and flow may be more pronounced. Any differences between the two limits could have important consequences for the representation of sea ice in global circulation models, and for interpretation of observations made in the field. This motivates the study of mushy-layer convection in systems with $\mathscr{C} \ll 1$. Furthermore, sea ice formation is a transient process which results in complex behaviour not present in the steady-state growth which has often been studied to date. Understanding these transient dynamics will be important for faithfully representing sea ice in climate models.

To direct the rest of this thesis, it is helpful to consider some outstanding questions which, if answered, would improve our understanding of convection within sea ice.

1. Do the same scaling laws apply to steady-state convection with $\mathscr{C} \ll 1$ as in the case $\mathscr{C} \sim O(Rm)$?

2. Do any of the properties of transient mushy-layer growth, particularly the mush-liquid solute flux, obey simple scaling laws?

3. If they do, are the scaling laws consistent with the results from steady-state growth?

4. How might flow dynamics in sea ice, which is inherently 3-D, differ from models and theories developed in 1-D and 2-D?

2

Sea ice model

This chapter describes the mushy-layer model for sea ice which will be used throughout the remainder of this thesis. In § 2.1 we introduce the governing conservation equations, including the approximations required to derive them. Section 2.2 explains the choices I made for the boundary conditions when solving these equations numerically. I then nondimensionalise the equations in § 2.3. Finally, in § 2.4, I summarise the key points from this chapter.

2.1 Governing equations for thermodynamics and flow in sea ice

The equations governing a mushy layer are based on the fundamental principles of conservation of energy, mass, momentum, and solute (salt). Equations describing these laws are reviewed in Worster (1997), derived in Worster (1983), and will be described below.

On the pore scale, mushy layers consist of a complex mixture of solid crystals and interstitial fluid. When interested in dynamics on scales much larger than the pore scale, as is the case here, continuous conservation equations may be derived by averaging over a suitable control volume $\mathcal{V}$ which is simultaneously much larger than dendritic spacing and smaller than the finest resolution of the model. Within a control volume, there will be a mixture of liquid brine $\mathcal{V}_l$ and solid ice $\mathcal{V}_s$, with the liquid fraction or porosity given by $\chi = \mathcal{V}_l/(\mathcal{V}_l + \mathcal{V}_s)$ (see fig. 2.1 for an illustration). Conversely, the solid fraction is given by $\phi = 1 - \chi$. I assume that within a control volume the system is in local thermodynamic equilibrium - that the solid and liquid phases have equal temperature T and the salinity in the liquid phase S_l is uniform. This assumption

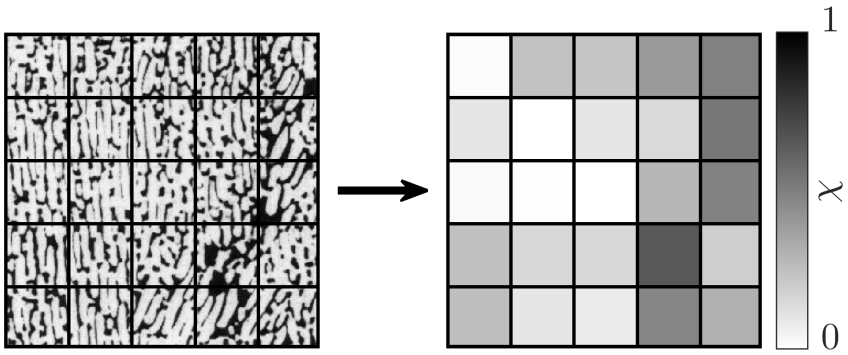


Figure 2.1: Example of the volume averaging procedure. The image on the left is an MRI scan of a sample of sea ice taken from Eicken et al. (2000). On the pore scale, there is a complex mixture of liquid regions (dark) and solid regions (white). Averaging over a volume larger than the pore scale (indicated by the grid boxes), we obtain the porosity field χ on the right.

relies on either solidification or dissolution, with the accompanying release or uptake of latent heat and fresh water, restoring equilibrium at the pore scale on a faster timescale than the macroscale transport processes we are interested in.

In general, the material properties of a mushy layer are determined by the microstructure and the material properties of the solid and liquid phases (Petrich and Eicken, 2010). Some quantities, such as the conductivity and diffusivity, are tensors whose values can vary significantly between spatial directions due to the structure of the porous ice matrix. Others, such as the heat capacity, are scalars which depend solely on the relative fractions of liquid and solid and the properties within each phase. For simplicity, I will assume that sea ice is an isotropic medium (Worster, 1997) and therefore compute the material properties as the volume weighted average of the solid and liquid properties (with subscript s and l, respectively),

$$\bar{c}_p = \chi c_{p,l} + (1-\chi)c_{p,s}, \quad \text{(specific heat capacity)}. \tag{2.1}$$

$$\bar{k} = \chi k_l + (1-\chi)k_s, \quad \text{(heat conductivity)}. \tag{2.2}$$

$$\bar{D} = \chi D_l + (1-\chi)D_s, \quad \text{(salt diffusivity)}. \tag{2.3}$$

The values of these and other material properties are given in table 2.1. In some cases the ice crystals tend to align in a specific direction, such as the vertical direction in fig. 2.1a. Here, volume averaging will be less appropriate for tensors (such as

the thermal conductivity) if the material properties between the two phases differs significantly. For example, the solute diffusivity is far greater in the liquid than the solid so on the scale of the grid in fig. 2.1a the solute diffusivity will in reality not be isotropic but will be greater in the vertical direction than the horizontal. Such effects will not be considered in this thesis.

For the sake of simplicity I will ignore the temperature and salinity dependence of these properties and treat them as constant, with the exception of buoyancy forcing in the momentum equation as discussed below. This significantly reduces the nonlinearity of the coupled equations, and is reasonable given the modest variations over the temperature and salinity ranges of interest (roughly $-40°\mathrm{C} < T < 0°\mathrm{C}$ and $0\,\mathrm{g/kg} < S < 200\,\mathrm{g/kg}$).

2.1.1 Mass conservation

When considering flow in porous media, it is often most convenient to work with the Darcy flux $\mathbf{U} = \chi\mathbf{u}_l$, where $\mathbf{u}_l$ is the velocity of the interstitial fluid. Note that whilst $\mathbf{U}$ represents the phase-weighted volume flux of fluid per unit volume of mixture, it is often referred to as the *Darcy velocity*. In principle the solid phase may have some velocity $\mathbf{u}_s$, however we will assume that $\mathbf{u}_s = 0$ here. Conservation of total mass within a control volume $\tilde{V}$ is then given by

$$\frac{\partial}{\partial t}\int_{\tilde{V}} \left[\rho_l\chi + \rho_s(1-\chi)\right]\, d\tilde{V} = -\oint_{\tilde{A}} \rho_l\chi\mathbf{u}_l\cdot\mathbf{n}\, d(\tilde{A}), \tag{2.4}$$

where $\tilde{A}$ is the surface which encloses the control volume $\tilde{V}$, t is the time and $\mathbf{n}$ is a unit vector normal to the surface $\tilde{A}$. The density in the solid phase ρ_s is constant to a very good approximation. With the Boussinesq approximation I neglect the variation of the liquid density ρ_l with the solute concentration and temperature, and assume that ρ_l is also a constant here. Hence, using the divergence theorem I find

$$\nabla\cdot\mathbf{U} = \frac{\rho_s - \rho_l}{\rho_l}\frac{\partial\chi}{\partial t}. \tag{2.5}$$

When $\rho_s \neq \rho_l$, as is the case for sea ice where $\rho_s/\rho_l \approx 0.9$, expansion or contraction of the fluid during phase change can drive flow (Chiareli and Worster, 1992; Chiareli et al., 1994). Notz and Worster (2009) found that in sea ice this mechanism does not contribute to a measurable flux of salt out of the ice, and therefore we choose to simplify the dynamics by neglecting the difference in density between the two phases. Setting $\rho_s = \rho_l$, we obtain an incompressible Darcy flow

$$\nabla \cdot \mathbf{U} = 0. \tag{2.6}$$

2.1.2 Energy conservation

As we are interested in phase change, we must consider both sensible heat and latent heat. This can be done by writing the enthalpy,

$$H = \rho_0 \bar{c}_p(\chi) T + \rho_0 \chi L, \tag{2.7}$$

where L is the latent heat of fusion and we use a constant reference density $\rho_s = \rho_l = \rho_0$ equal to that of salt water at 0°C. In writing (2.7) we have assumed that the heat capacity in each phase $(c_{p,s}, c_{p,l})$ is independent of temperature. The enthalpy within a control volume $\tilde{V}$ evolves due to advective fluxes in the liquid and phase and conduction through both the solid and liquid,

$$\frac{\partial}{\partial t} \int_{\tilde{V}} H d\tilde{V} = \oint_{\tilde{A}} \left[\bar{k}(\chi) \nabla T - \mathbf{U} \rho_0 c_{p,l} T \right] \cdot \mathbf{n} \, d\tilde{A}. \tag{2.8}$$

Using the divergence theorem, and recalling that ρ_0 and $c_{p,l}$ are constant, we find the differential form

$$\frac{\partial H}{\partial t} + \nabla \cdot (\mathbf{U} \rho_0 c_{p,l} T) = \nabla \cdot \left[\bar{k}(\chi) \nabla T \right]. \tag{2.9}$$

2.1.3 Salt conservation

Salt can also be advected through the liquid or diffused through the liquid and solid. However diffusion through the solid is significantly slower than the other two processes

and therefore we only consider liquid diffusion and advection. Hence the change in total (bulk) salinity $S = \chi S_l + (1-\chi)S_S$ within a control volume $\tilde{V}$ is given by

$$\frac{\partial}{\partial t}\int_{\tilde{V}} \rho_0 \, S \, d\tilde{V} = \oint_{\tilde{A}} \rho_0 \left[D_l \chi \nabla S_l - \mathbf{U} \, S_l \right] \cdot \mathbf{n} \, d\tilde{A}. \tag{2.10}$$

Or, in differential form,

$$\frac{\partial S}{\partial t} + \nabla \cdot (\mathbf{U} \, S_l) = \nabla \cdot \left[D_l \chi \nabla S_l \right]. \tag{2.11}$$

The salinity in the solid phase S_S is usually small and therefore the partition coefficient $p_c = S_S/S_l \approx 0$ is usually very small. Some authors have simply used $S = \chi S_l$ (Wettlaufer et al., 2000) whilst Katz and Worster (2008) used a non-zero value ($p_c = 10^{-5}$) which they found improved the stability of their numerical method. For $p_c \ll 1$, the choice of p_c does not affect the dynamics (Lu and Chen, 1994) and therefore the choice of p_c is somewhat arbitrary. As I will be using a similar method to Katz and Worster (2008), I choose to follow their approach and retain a small finite p_c.

2.1.4 Momentum conservation

On the pore scale, fluid flow in the interstices of a porous medium is governed by the Navier-Stokes equations. On larger scales, the appropriate momentum equation is found by averaging the Navier-Stokes equation over the control volume $\mathcal{V}$. There is some disagreement in the literature as to the correct way to do this, with subtly different equations resulting from the assumptions made (e.g. see Shyy et al., 1997; Beckermann et al., 1999; Kaempfer and Rappaz, 2003). We follow Le Bars and Worster (2006a) who derive the Darcy-Brinkman equation

$$\rho_0 \frac{\partial \mathbf{U}}{\partial t} + \rho_0 \mathbf{U} \cdot \nabla \left(\frac{\mathbf{U}}{\chi} \right) = \chi \left(-\nabla p - \rho g \mathbf{e}_z - \frac{\eta}{K(\chi)} \mathbf{U} \right) + \eta \nabla^2 \mathbf{U}, \tag{2.12}$$

where η is dynamic viscosity of the fluid, g is the acceleration due to gravity, $\mathbf{e}_z$ is a unit vector in the vertical direction and the permeability function $K(\chi)$ is a material property, the details of which are described in § 2.1.5. The first term on the left hand

side describes the rate of the change of the Darcy velocity, whilst the second describes the advection of momentum by the flow, noting that only the liquid velocity $\mathbf{u} = \mathbf{U}/\chi$ is advected. On the right hand side, the first term describes pressure gradient forces, the second buoyancy forces, and the fourth describes viscous forces in the liquid. The third term on the right hand side describes the dissipative forces acting on a flow passing through a material of porosity χ and permeability $K(\chi)$, and comes from averaging over microscopic viscous stresses on the pore scale (Bear, 1972).

As $\chi \to 1$, (2.12) becomes the Navier-Stokes equation for flow in a pure fluid as long as the permeability satisfies $K \to \infty$ as $\chi \to 1$. In this way, (2.12) can model fluid flow during the transition between porous and pure fluid regions. When the permeability is small, as is generally the case in sea ice (Petrich and Eicken, 2010), the momentum balance is dominated by microscopic viscous stresses on the porous matrix and (2.12) is well approximated by Darcy's law (Bear, 1972)

$$\mathbf{U} = \frac{K(\chi)}{\eta}\left(-\nabla p - \rho g \mathbf{e}_z\right). \tag{2.13}$$

In this thesis I will consider both Darcy's law (2.13) and the Darcy-Brinkman formulation (2.12).

2.1.5 Permeability

The permeability of a porous material depends on its porosity as well as microscopic properties such as the geometry and connectedness of pores. In a continuum model, such as this one, the microscopic details are unknown so we require an expression for the permeability K in terms of the macroscopic porosity χ. Kozeny (1927) and Carman (1937) independently derived such a relationship by approximating a porous medium as an array of parallel tubes surrounded by impermeable material. Considering Poiseuille flow through these tubes, they found the commonly used Kozeny-Carman equation

$$K(\chi) = K_0 \frac{\chi^3}{(1-\chi)^2}. \tag{2.14}$$

Observations of sea ice often reveal low porosities $\chi < 0.1$ over most of the depth, except for high porosity regions near the mush-liquid boundaries (Eicken et al., 2000). For low porosity, the Kozeny-Carman relation reduces to a cubic $K \approx K_0\chi^3$. This agrees well with the experiments of Freitag (1999), who used a bail test to measure the permeability of laboratory grown sea ice. In this method, a hollow cylindrical tube of radius ~ 5 cm is inserted into the ice and water is added to apply a hydraulic head. As the fluid flows through the ice, the temporal evolution of the water level is measured and from this the permeability is deduced. Freitag (1999) found that a good fit for their observations of young sea ice was

$$K(\chi) = K_0\chi^{3.1}. \tag{2.15}$$

A polynomial expression for the permeability does not have the desired property of $K(\chi \to 1) \to \infty$ in the liquid region so we will make use of the Kozeny-Carman relation, noting that it recovers the desired limit for low porosities.

The magnitude of the permeability of sea ice (i.e. the value of K_0) is poorly constrained. The experiments conducted by Freitag (1999) found $K_0 = 10^{-8}$. Meanwhile, Saeki et al. (1986) measured sea ice permeabilities in the range $10^{-13} < K < 10^{-10}\,\mathrm{m}^{-2}$ in the laboratory for ice with porosities in the range $0.01 - 0.15$. The variation of K with χ measured by Saeki et al. (1986) is consistent with a power law relationship $K \sim \chi^a$ where $2 \lesssim a \lesssim 3$. Freitag and Eicken (2003) took in situ measurements in the Laptev Sea during the Arctic summer and found $10^{-11} < K < 10^{-7}\,\mathrm{m}^{-2}$ for ice of an estimated porosity $\chi \approx 0.2$. Kawamura et al. (2006) made in situ measurements in a brackish coastal lagoon (Lake Saroma, Japan) towards the end of the winter and found $10^{-11} < K < 10^{-10}\,\mathrm{m}^{-2}$. In this thesis, I will typically use permeabilities at the lower end of this range ($K_0 \sim 10^{-10} - 10^{-9}\,\mathrm{m}^2$).

Experiments on mushy layers are often conducted in a Hele-Shaw cell, which consists of two plates separated by a small gap width d yielding a quasi-two-dimensional environment (Peppin et al., 2007; Katz and Worster, 2008; Middleton et al., 2016). The narrow gap width enforces a constraint on the maximum permeability of the system which can be determined to be $K_c = d^2/12$ by considering Poisseuille flow

in a slot (Bear, 1972). In this thesis I will often consider settings where flow and solidification occur within a Hele-Shaw cell, and in this case I will usually follow Katz and Worster (2008) and combine the mushy layer permeability $K_m(\chi)$ and the Hele-Shaw cell permeability K_c to obtain the overall permeability,

$$K^{-1} = K_m(\chi)^{-1} + K_c^{-1}, \tag{2.16}$$

with K_m given by (2.14). When the Hele-Shaw gap width is sufficiently narrow, flow in the liquid phase is well described by Darcy's law (2.13) which can therefore be used to describe flow throughout the domain in both porous and pure liquid regions. In chapter 4 I will also considered a geometry where the Hele-Shaw permeability $K_c = K_0$, whilst $K_m(\chi) = K_0\chi^3$. In this case, I will take the total permeability to be $K = \min(K_m, K_c)$.

2.1.6 Equation of state

Using the Boussinesq approximation (Kundu et al., 2012), we consider the liquid density to be constant in the momentum equation except where it contributes to density differences in the buoyancy term. In general the liquid density is a nonlinear function of temperature, salinity, and pressure, but for simplicity we use the linearised form

$$\rho = \rho_0 \left[1 + \beta(S - S_0) - \alpha(T - T_0)\right], \tag{2.17}$$

where the reference density ρ_0 is given at $(S_0, T_0) = (35\ \text{g/kg}, 0°\text{C})$. The thermal and haline expansivities for sea water, α and β are given in table 2.1.

2.1.7 Phase diagram

Depending on the enthalpy H and bulk salinity S, the system may be in one of four distinct composite phases; solid, liquid, eutectic solid, or mushy layer. We here determine which phase the system is in via an idealised phase diagram, as illustrated in fig. 2.2b. Following previous authors (e.g. Worster, 1997) the liquidus $T_L(S)$ and

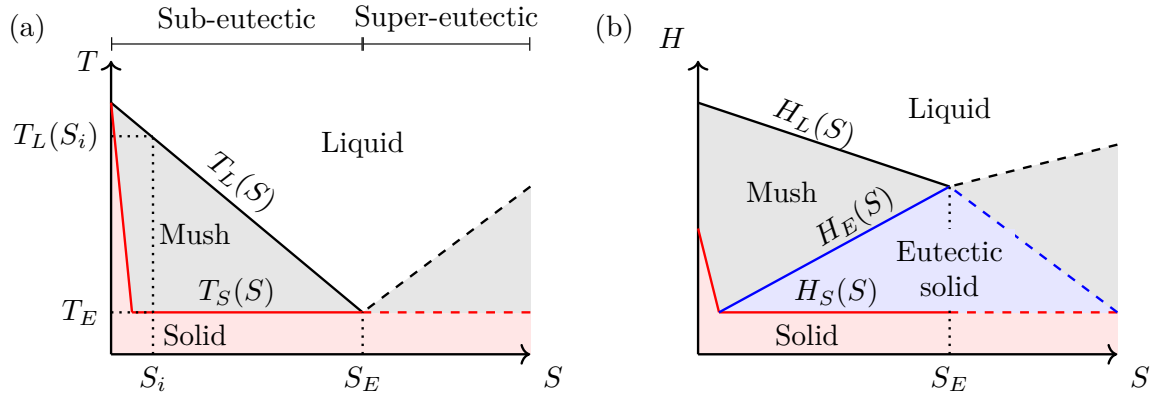


Figure 2.2: Simplified phase diagram for a binary alloy in (a) T–S space and (b) H–S space. We have assumed that the liquidus $T_L(S)$ is a linear function of S. Below the eutectic composition C_E (region where phase boundaries are marked by solid lines), the solid phase of the mushy-layer is composed of the solvent. For example, for an NaCl-H_2O system with concentration below 230 g/kg the mushy-layer consists of water ice crystals and salty brine. Other alloys, such as NH_4Cl-water, are typically considered to the right of the eutectic composition (shown with dashed lines). For temperature and composition above the liquidus $T_L(S)$ the alloy is purely liquid, and below the solidus $T_S(S)$ there is only solid. In between a mushy region forms, comprising a mixture of pure solid crystals on the solidus curve and solute enriched liquid on the liquidus curve, with liquid fraction χ and phase-weighted bulk concentration S. Considering H–S space, with liquidus $H_L(S)$ and solidus $H_S(S)$, highlights that there is an additional region of eutectic solid in addition to the mush. On the mush-eutectic phase boundary ($H_E(S)$ in (b)) $T = T_E$ and the porosity depends on the bulk concentration via $\chi = \chi_E(S)$. The eutectic solid is a phase the system often passes through during the transition from the mushy layer phase to the solid phase; the enthalpy difference $H_E(S) - H_S(S)$ represents the energy which must be extracted for this transition to occur, with $T = T_E$.

solidus $T_S(S)$ have been linearised according to

$$T_L(S) = T_E - \Gamma(S_l - S_E), \tag{2.18}$$

$$T_S(S) = \max\left[T_E, T_E - \frac{\Gamma}{p_c}(S_S - p_c S_E)\right]. \tag{2.19}$$

The slope of the liquidus, Γ, is chosen such that $T_L(S_E) = T_E$ and $T_L(0) = 0$. In practice, the liquidus is not linear and the slope varies with S. Qualitatively this does not affect the dynamics, however it can result in notable quantitative differences (Notz and Worster, 2006). For a given salinity S, we see from fig. 2.2b that the phase is uniquely determined by the enthalpy H. For temperatures above the liquidus,

the system is entirely liquid,

$$\chi = 1, \quad T = \frac{H - \rho_0 L}{\rho_0 c_{p,l}}, \quad S_l = S, \quad S_S = 0. \tag{2.20}$$

As the solution is cooled, ice starts to form. The salt is mostly not included in the ice ($p_c \ll 1$) so increases the salinity of the local liquid and depresses the freezing point as described by the liquidus (2.18). We assume that melting and freezing occurs sufficiently quickly to ensure that the ice-brine mixture is always in local thermodynamic equilibrium. This assumption relies on solute transport on the pore scale being sufficiently rapid relative to thermal heating (Feltham et al., 2006). Solute transport, and therefore the validity of the thermal equilibrium assumption, is highly dependent on the internal microstructure. In the case of sea ice, thermal equilibrium is a reasonable assumption for timescales $>$ 10s (Feltham et al., 2006). With this assumption the temperature and liquid salinity of the mushy layer must follow $T = T_L(S_l)$ whilst, from the definition of the bulk salinity S and partition coefficient $p_c = S_S/S_l$,

$$S_l = \frac{S}{\chi + p_c(1-\chi)}, \quad S_S = \frac{S}{p_c^{-1}\chi + (1-\chi)}. \tag{2.21}$$

The porosity χ is determined by a quadratic equation, obtained by combining eqs. (2.7), (2.18) and (2.21); the relevant coefficients can be found in § 2.3.1.

Upon further cooling, the residual liquid reaches the eutectic point $(T, S_l) = (T_E, S_E)$ where the salt starts to precipitate out of the solution. As the eutectic point is at the end of the liquidus, the porosity can be found from (2.21) with $S_l = S_E$ and the solid salinity then follows from the bulk salinity,

$$\chi_E = \frac{S - p_c S_E}{S_E(1-p_c)}, \quad S_S = \frac{S - \chi_E S_E}{1 - \chi_E}. \tag{2.22}$$

When the system transitions from the mushy layer phase to the solid phase, it usually passes through the eutectic solid phase (see fig. 2.2b). This is not a physical phase in which the system is usually found, hence it is not apparent in the $T - S$ phase diagram fig. 2.2a, but rather it is a region of $H - S$ space which is crossed during solidification. The enthalpy difference $H_E(S) - H_S(S)$ represents the energy which

must be extracted to transition from the mush side of the eutectic (with $\chi = \chi_E(S)$) to the solid side (with $\chi = 0$) at a fixed temperature $T = T_E$.

Below the eutectic, we make the simplifying assumption that all the salt has precipitated out leaving a solid mixture of ice and salt crystals. In reality, this process occurs over a range of temperatures with about half the salt precipitating out immediately and a few percent still remaining down to $-52°$C (Richardson, 1976). For a solid we can write

$$\chi = 0, \quad T = \frac{H}{\rho_0 c_{p,s}}, \quad S_l = 0, \quad S_S = S. \tag{2.23}$$

With these equations, we can determine the temperature, porosity and liquid salinity at every point in the domain from the enthalpy H and bulk salinity S. Thus, given the conservation equations for heat, solute, mass, and momentum, we have a closed system of equations which describe the evolution of the system in time.

This approach, where a single set of equations are considered which apply throughout the domain, is known as the *enthalpy method* (Alexiades and Solomon, 1993). One common alternative is to solve different equations in each phase, whilst additionally solving for the evolution of the interface between the phases (Worster, 1986). At the mush-liquid interface there must be continuity of heat and solute, effectively yielding a Stefan condition. Due to the presence of a porosity field, problems involving mushy-layer solidification require one further boundary condition at this interface. Worster (1983) proposed a condition of marginal equilibrium,

$$\mathbf{n} \cdot \nabla T = -\Gamma \mathbf{n} \cdot \nabla S, \tag{2.24}$$

which serves to eliminate supercooling on the liquid side of the interface and has since been widely adopted in the literature. These conditions are naturally encapsulated within the enthalpy method. The Stefan conditions for the continuity of heat and solute fluxes across the boundary can be found by integrating (2.9) and (2.11), whilst the condition of marginal equilibrium is automatically satisfied; any grid cells where the enthalpy is below the liquidus (due to supercooling or otherwise) will be treated as a mushy layer.

Property		**Value**	**Units**	**Reference**
Specific heat capacity (liquid)	$c_{p,l}$	$4185 + 0.1T - 5.367S$	J kg^{-1} °C^{-1}	Fit to data from Jamieson et al. (1969) and Nayar et al. (2016)
Specific heat capacity (solid)	$c_{p,s}$	$2112.2 + 7.7T$	J kg^{-1} °C^{-1}	Notz (2005)
Heat conductivity (liquid)	k_l	$0.523 + 0.01T$	W m^{-1} °C^{-1}	Petrich and Eicken (2010)
Heat conductivity (solid)	k_s	$2.22 - 0.01T$	W m^{-1} °C^{-1}	Petrich and Eicken (2010)
Reference liquid density	ρ_0	1028	kg m^{-3}	Sharqawy et al. (2011)
Solid density	ρ_s	$917 - 0.14T$	kg m^{-3}	Petrich and Eicken (2010)
Latent heat of freezing	L	333.4	kJ kg^{-1}	Petrich and Eicken (2010)
Thermal expansivity	α	3.87×10^{-5}	°C^{-1}	Jenkins (2011)
Solutal expansivity	β	7.86×10^{-4}	(g/kg) $^{-1}$	Jenkins (2011)
Dynamic viscosity	η	1.77×10^{-3} $-4.99 \times 10^{-5}T$ $+3.08 \times 10^{-6}S$	kg m^{-1} s^{-1}	Fit to data from Sharqawy et al. (2011)

Eutectic temperature	T_E	-23	°C	Richardson (1976)
Eutectic salt concentration	S_E	230	g/kg	Richardson (1976)
Liquidus slope	Γ	-0.10	°C $(\mathrm{g/kg})^{-1}$	$\Gamma = T_E/S_E$
Water distribution coefficient	p_c	10^{-5}		Katz and Worster (2008)
Reference permeability	K_0	2×10^{-8}		Freitag (1999)
Salt diffusivity (liquid)	D_l	6.8×10^{-10}	$\mathrm{m^2\ s^{-1}}$	Mellor (1989)
Salt diffusivity (solid)	D_s	negligible	$\mathrm{m^2\ s^{-1}}$	Worster (1991)
Frame advection velocity	V	–	$\mathrm{m\ s^{-1}}$	

Table 2.1: Measured material properties and constants for sea ice, which form the basis for the values used in this thesis. The liquid phase is salt water, and the solid phase is ice. In general, these properties vary with temperature and salt concentration as illustrated in the table but these variations are sufficiently small that we neglect them as a first approximation whilst studying the fundamental mechanisms. A notable exception is the liquid density in the momentum equation. All temperatures are in °C, and all salinities are in g/kg. The water distribution coefficient p_c is the fraction of salt incorporated in the solid relative to the liquid, and is chosen to be a small non-zero constant for numerical convenience. The reference permeability K_0 gives a typical permeability scale for sea ice; the spatially variable permeability can still vary by orders of magnitude depending on the liquid fraction. A constant frame advection velocity V is required to describe experiments conducted in a frame of reference moving with the freezing front. The liquidus slope Γ is a linear approximation between $(T, S) = (0°\mathrm{C}, 0\,\mathrm{g/kg})$ and (T_E, S_E), which is slightly larger than the local gradient of the nonlinear liquidus near $T \approx 0°\mathrm{C}$.

2.1.8 Directional solidification

The equations presented above are valid for mushy layer growth from a fixed boundary. It can also be useful to consider growth between hot and cold heat exchangers translated at a fixed speed V, so called *directional solidification*. For example, in the laboratory various authors have studied mushy layer dynamics using a Hele-Shaw cell which is translated between two fixed heat exchangers. In this thesis, I will also consider mushy layer dynamics in this setting, in which case the governing equations in the reference frame where the heat exchangers are fixed are given by the transformation

$$\frac{\partial}{\partial t} \to \frac{\partial}{\partial t} + \mathbf{V} \cdot \mathbf{e}_z \frac{\partial}{\partial z}. \tag{2.25}$$

Note that V is the velocity of the sample relative to the heat exchangers. V is negative in the case of ammonium chloride solidification, where the mushy layer forms at the bottom boundary, and positive for sea ice formation where the mushy layer forms at the top of the domain. Therefore the process of directional solidification acts to remove the mushy layer from the domain, replacing it with liquid at the opposite boundary.

2.2 Initial and boundary conditions

The dynamics of flow and phase change in sea ice are strongly influenced by, and often driven by, the atmosphere or ocean. In our model, these interactions will be described by the initial and boundary conditions used which are illustrated in fig. 2.3 and described below.

When simulating ice growth, as in chapter 4 and chapter 5, the initial state of the system will be entirely liquid with a uniform temperature and salinity, and no flow;

$$\chi = 1, \quad T = T_i, \quad S = S_l = S_i, \quad \mathbf{U} = 0. \tag{2.26}$$

When simulating the response of a layer of sea ice to warming, as in chapter 6, we will first grow a layer of ice using the initial conditions described in (2.26) then use this as the initial state.

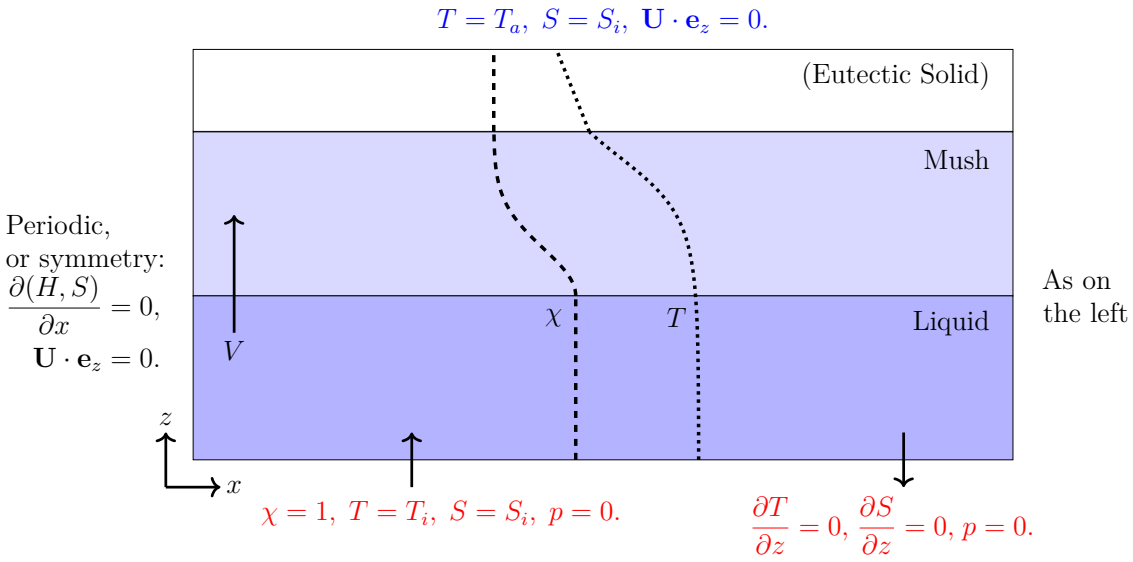


Figure 2.3: Illustration of the domain and boundary conditions we will consider. In some cases the temperature at the top of the domain is below the eutectic and a layer of eutectic solid (white) will form.

2.2.1 Atmospheric boundary conditions

In general, the radiative balance at the ice-atmosphere interface contains contributions from sensible heat fluxes $\mathbf{F}_s$, long wave radiation in and out of the ice surface ($\mathbf{F}_{LW}^{in}$, $\mathbf{F}_{LW}^{out}$), and thermal conduction into the ice $\mathbf{F}_c$ (Maykut and Untersteiner, 1971),

$$\mathbf{e}_z \cdot \left(\mathbf{F}_s - \mathbf{F}_{LW}^{out} + \mathbf{F}_{LW}^{in} + \mathbf{F}_{\text{latent}} - \mathbf{F}_c\right) = 0. \tag{2.27}$$

In general this flux balance results in a boundary condition which can depend nonlinearly on the temperature and its derivatives (Maykut and Untersteiner, 1971). Motivated by common experimental configurations, I will consider an isothermal atmospheric boundary $T = T_a$ to build dynamical understanding. This approximation will break down at early times, and when the loss of heat away from the ice into the atmosphere is weak relative to thermal diffusion within the mushy ice (see Hitchen and Wells, 2016, for more details). There may be relatively weak heat loss to the atmosphere if an insulating layer of snow exists above the ice, in which case this approximation would be less valid. This choice of boundary condition also neglects temporal variability in fluxes between the ice and the atmosphere.

I assume that the atmospheric boundary is impermeable to fluid flow,

$$\mathbf{U} \cdot \mathbf{e}_z = 0, \tag{2.28}$$

neglecting fluid mass loss via evaporation or input via surface melt through any open pores. Therefore the salt flux across the top boundary is purely diffusive,

$$F_s = -D_l \chi \frac{\partial S_l}{\partial z}. \tag{2.29}$$

When the temperature at the top boundary is below the eutectic, $T < T_E$, the porosity $\chi = 0$ and there is no salt flux across the boundary. When $T \geq T_E$, there could be a small diffusive salt flux as follows. Atmospheric cooling (or warming) introduces a temperature gradient $\partial T/\partial z$. Due to the liquidus constraint $T = T_L(S_l)$ this corresponds to a liquid salinity gradient $\partial S_l/\partial z = -(1/\Gamma)\partial T/\partial z$. In this case, I assume there exists a thin layer *above* the domain with a fixed bulk salinity S which may diffusively exchange solute with the domain. Physically, this layer may be composed of either porous sea ice or snow. Whilst this assumption may not be entirely accurate, due to the weak nature of solute diffusion any discrepancies should be small. If we instead imposed $\partial S/\partial z = 0$ at the top boundary, the solute would slowly diffuse downwards leaving a narrow fresh layer at the top of the sea ice which would freeze solid to form a thin impermeable crust (c.f. Worster, 1986, §6).

2.2.2 Ocean boundary conditions

Our model describes flow in both porous sea ice and the underlying liquid. The bottom of the computational domain is treated as an open boundary, permitting the transfer of salt, heat, and momentum in and out of the domain. The temperature and salinity are given by the initial conditions, which ensure that the boundary remains entirely liquid,

$$\chi = 1, \quad T = T_i, \quad S = S_i. \tag{2.30}$$

To allow fluid flow in and out of the domain, we impose a constant pressure on the bottom boundary. In the case of Darcy flow (2.13), a consequence of this choice is that there will be no horizontal pressure gradients at the bottom of the domain, and hence no horizontal flow. In the case of Darcy-Brinkman flow (2.12), horizontal flow is in principle still possible at a constant pressure boundary, but we require a second boundary condition as (2.12) is a second order equation. We impose a condition of no horizontal flow as as the second condition for consistency with our approach to the Darcy equation. The governing PDEs (2.12, 2.13) are invariant under the transformation $p \to p + p'$, where p' is a global constant, so we can choose to enforce any constant value of p that we wish at the bottom boundary. We opt for $p = 0$.

2.2.3 Side boundaries

In the horizontal direction I consider either periodic conditions, or symmetry conditions given by

$$\mathbf{U} \cdot \mathbf{x} = 0, \quad \frac{\partial(H, S, T, S_l, \chi)}{\partial x} = 0. \tag{2.31}$$

Symmetry conditions are used when we wish to model a horizontal array of identical channels with a fixed separation.

2.3 Nondimensionalisation

It is convenient to nondimensionalise the equations using characteristic physical scales. Given the initial salinity S_i, I choose characteristic scales for salinity $\Delta S = S_E - S_i$, temperature, $\Delta T = T_L(S_i) - T_E$, and enthalpy $\Delta H = c_{p,l}\Delta T$, where T_E and S_E are the eutectic temperature and salinity, and $T_L(S_i)$ is the liquidus temperature at the initial composition (see the phase diagram in fig. 2.2). I scale lengths by the domain height $\mathcal{H}$, use the diffusive timescale $\mathcal{H}^2/\kappa_l$, and scale velocities by $\kappa_l/\mathcal{H}$, where $\kappa_l = k_l/\rho_l c_{p,l}$ is the thermal diffusivity. Finally pressure is scaled with $\rho_l\kappa_l^2/\mathcal{H}^2$, and permeability with a reference value K_0. The dimensionless temperature and salinity are defined

with respect to a reference point (T_r, S_E),

$$\theta = \frac{T - T_r}{\Delta T}, \quad \Theta = \frac{S - S_r}{\Delta S}, \quad \Theta_l = \frac{S_l - S_r}{\Delta S}, \tag{2.32}$$

where the choice of (T_r, S_r) will be discussed in § 2.3.1. The dimensionless enthalpy is given by

$$\mathscr{H} = \mathscr{S}\chi + [\chi + (1-\chi)c_p]\,\theta, \tag{2.33}$$

where the specific heat ratio $c_p = c_{p,s}/c_{p,l}$ is a constant, whilst the Stefan number $\mathscr{S} = L/(c_{p,l}\Delta T)$ gives the ratio between the latent heat release per unit mass of liquid upon freezing, and typical variations in the sensible heat. The governing equations become

$$\frac{\partial \mathscr{H}}{\partial t} + \mathbf{U}\cdot\nabla\theta = \nabla\cdot[\chi + (1-\chi)k]\,\nabla\theta, \tag{2.34}$$

$$\frac{\partial \Theta}{\partial t} + \mathbf{U}\cdot\nabla\Theta_l = \frac{1}{Le}\nabla\cdot\chi\nabla\Theta_l, \tag{2.35}$$

$$\nabla\cdot\mathbf{U} = 0, \tag{2.36}$$

$$\frac{\partial \mathbf{U}}{\partial t} + \mathbf{U}\cdot\nabla\left(\frac{\mathbf{U}}{\chi}\right) = -\chi\nabla p + Pr\nabla^2\mathbf{U} + \chi Pr\,(Ra_T\theta - Ra_S\Theta_l)\,\mathbf{e}_z - \frac{Pr\,\chi\mathbf{U}}{Da\,\Pi}, \tag{2.37}$$

where the dimensionless permeability is given by

$$\Pi^{-1} = \Pi_m(\chi)^{-1} + \Pi_H^{-1}, \quad \text{where } \Pi_m(\chi) = \frac{K(\chi)}{K_0},\ \Pi_c = \frac{K_c}{K_0} = \frac{d^2}{12\,K_0}. \tag{2.38}$$

The dimensionless phase diagram equations are given in § 2.3.1. The additional dimensionless parameters that emerge are:

- The Lewis number $Le = \kappa_l/D_l$, which is the ratio of heat to salt diffusivity and is usually large.
- $k = k_s/k_l$ the ratio of solid to liquid thermal conductivity, which is $O(1)$.
- Ra_T, Ra_S, thermal and haline Rayleigh numbers which control the strength of

the buoyancy driven flow, compared to dissipative mechanisms.

$$Ra_T = \frac{\rho_l g \alpha \Delta T \mathcal{H}^3}{\kappa_l \eta}, \quad Ra_S = \frac{\rho_l g \beta \Delta S \mathcal{H}^3}{\kappa_l \eta}. \tag{2.39}$$

I use the thermal diffusivity, κ_l, for both the thermal and haline Rayleigh numbers as thermal diffusivity is far greater than haline diffusivity, and is therefore the dominant dissipative method.

- The Darcy number $Da = K_0/\mathcal{H}^2$, which describes the relative importance of viscous drag on macroscopic scales compared to the permeability dependent viscous drag in the pore space, and is generally small.

- The Prandtl number, $\mathrm{Pr} = \eta/(\rho_l \kappa_l)$, which is the ratio of fluid viscosity to heat diffusion.

- The Stefan number $\mathscr{S} = L/(c_{p,l}\Delta T)$, which is the ratio of latent heat to sensible heat.

- The concentration ratio,

$$\mathscr{C} = \frac{S_r - S_S}{\Delta S}, \tag{2.40}$$

which gives the difference in salinity between the liquid and solid phases relative to the salinity variations in the liquid. Hence, the dimensionless bulk salinity is given by

$$\Theta = \chi \Theta_l - (1-\chi)\mathscr{C}. \tag{2.41}$$

- The dimensionless Hele-Shaw permeability $\Pi_c = d^2/(12\,K_0)$ which controls the permeability of flow in the liquid phase for a Hele-Shaw cell.

We note that in the limit $\Pi_c Da \ll 1$ the Darcy term in (2.37) becomes large and can only be balanced by buoyancy and pressure forces, leading to the dimensionless

form of Darcy's law,

$$\frac{Pr}{Da}\frac{\mathbf{U}}{\Pi(\chi)} = -\nabla p + (Ra_S\Theta_l - Ra_T\theta)\,\mathbf{e}_z. \tag{2.42}$$

2.3.1 Phase diagram

There is some variation between previous studies over the choice of reference point in (T, S) space about which to nondimensionalise, which has consequences for the dimensionless form of the phase diagram. To ease comparison, so far I have considered a general reference point (T_r, S_r) such that

$$\theta = \frac{T - T_r}{\Delta T}, \quad \Theta = \frac{S - S_r}{\Delta S}, \quad \mathscr{C} = \frac{S_r - S_S}{\Delta S}. \tag{2.43}$$

In this case, the dimensionless solidus, eutectic, and liquidus are given by

$$\mathscr{H}_S(\Theta) = c_p\theta_S(\Theta) = c_p\left\{\theta_E + \max\left[0, \frac{1}{p_c}(\Theta + \mathscr{C})\right]\right\}, \tag{2.44}$$

$$\mathscr{H}_E(\Theta) = \chi_E\mathscr{S} = \left(\frac{\mathscr{C} + \Theta}{\mathscr{C} + 1}\right)[\mathscr{S} + \theta_E(1 - c_p)] + c_p\theta_E, \tag{2.45}$$

$$\mathscr{H}_L(\Theta) = \mathscr{S} + \theta_L(\Theta) = \mathscr{S} - \Theta + \theta_E + \Theta_E, \tag{2.46}$$

where θ_E and Θ_E are the dimensionless eutectic temperature and salinity. The porosity, temperature, liquid salinity, and salinity in the solid phase are then given by

$$\chi = \begin{cases} 0 & \mathscr{H} \le \mathscr{H}_S \\ (\mathscr{H} - \theta_E c_p)/(\mathscr{S} + \theta_E(1 - c_p)) & \mathscr{H}_S < \mathscr{H} \le \mathscr{H}_E \\ \left[-B - \sqrt{B^2 - 4AC}\right]/(2A) & \mathscr{H}_E < \mathscr{H} < \mathscr{H}_L \\ 1 & \mathscr{H} \ge \mathscr{H}_L \end{cases} \tag{2.47}$$

where $A = \mathscr{C}(c_p - 1) + \mathscr{S}(p_c - 1)$ (2.48)

$B = \mathscr{H}(1 - p_c) - \mathscr{S}p_c + \mathscr{C}(1 - 2c_p) - \Theta(c_p - 1)$ (2.49)

$C = \mathscr{H}p_c + c_p(\mathscr{C} + \Theta)$ (2.50)

$$\theta = \begin{cases} \frac{\mathscr{H}}{c_p} & \mathscr{H} \leq \mathscr{H}_S \\ \theta_E & \mathscr{H}_S < \mathscr{H} \leq \mathscr{H}_E \\ -\Theta_l & \mathscr{H}_E < \mathscr{H} < \mathscr{H}_L \\ \mathscr{H} - \mathscr{S} & \mathscr{H} \geq \mathscr{H}_L \end{cases} \tag{2.51}$$

$$\Theta_l = \begin{cases} N/A & \mathscr{H} \leq \mathscr{H}_S \\ \Theta_E & \mathscr{H}_S < \mathscr{H} \leq \mathscr{H}_E \\ \frac{\Theta + \mathscr{C}(1-\chi)}{\chi + (1-\chi)p_c} & \mathscr{H}_E < \mathscr{H} < \mathscr{H}_L \\ \Theta & \mathscr{H} \geq \mathscr{H}_L \end{cases} \tag{2.52}$$

$$\Theta_S = \begin{cases} \Theta & \mathscr{H} \leq \mathscr{H}_S \\ \frac{\Theta}{1-\chi} & \mathscr{H}_S < \mathscr{H} \leq \mathscr{H}_E \\ \frac{p_c\Theta - \mathscr{C}\chi}{\chi + (1-\chi)p_c} & \mathscr{H}_E < \mathscr{H} < \mathscr{H}_L \\ N/A & \mathscr{H} \geq \mathscr{H}_L \end{cases} \tag{2.53}$$

For most of this thesis, I take $(T_r, S_r) = (T_L(S_i), S_i)$, in which case $\theta_E = -1, \Theta_E = 1$ and the concentration ratio takes values $0 \leq \mathscr{C} < \infty$ with the far-from eutectic limit corresponding to $\mathscr{C} \ll 1$. A common alternative choice is to nondimensionalise relative to the eutectic point, $(T_r, S_r) = (T_E, S_E)$, in which case $\theta_E = \Theta_E = 0$ whilst the concentration ratio takes values $1 \leq \mathscr{C} < \infty$ with the far-from eutectic limit corresponding to $\mathscr{C} - 1 \ll 1$.

2.3.2 Other comparisons with previous studies

In § 2.3.1 I mentioned how different choices of nondimensionalisation can lead to subetley different equations. In this section, I highlight some of the other differences between the dimensionless equations and parameters used in this thesis and those used by other authors. To compare parameters between studies, I will use a superscript JP to indicate parameters in this study, and an asterix (*) for study, or studies, being compared to.

Katz and Worster (2008) only considered flow in a Hele-Shaw cell, so the relevant Darcy number in their study is equivalent to our dimensionless Hele-Shaw permeability: $Da^* = \Pi_c^{JP}$.

Many authors have considered directional solidification with an imposed frame advection velocity V, which they used as their characteristic velocity scale (e.g. Worster, 1991; Schulze and Worster, 1998; Chung and Worster, 2002; Wells et al., 2013). Hence, their characteristic length scale, κ_l/V, differs from ours with consequences for the Darcy number $Da^* = (V\mathcal{H}/\kappa_l)^2 Da^{JP}$. The same set of studies also restricted themselves to flow governed by Darcy's law, so they grouped the Pr/Da term in (2.13) with the fluid Rayleigh number to construct the mushy Rayleigh number $Rm = (Da/\mathrm{Pr})Ra_S$.

Most previous studies have focussed on the solidification of ammonium chloride solutions, which is typically studied in the so-called *super-eutectic* limit where the initial solute concentration C_i is greater than the eutectic, $C_i > C_E$. Hence, these systems exist on the opposite side of the phase diagram (to the right of the eutectic concentration in fig. 2.2) from the sea ice we will be considering. In the super-eutectic limit the solute precipitates out of the solution to form the solid component of the porous matrix, and hence the solute concentration in the liquid phase decreases during cooling. Therefore the liquidus has the opposite sign to systems below the eutectic concentration, but otherwise the governing equations and dynamics are analogous.

2.4 Summary

In this chapter I have presented a model for solidification and fluid flow in sea ice using mushy layer theory. Using the enthalpy method, it is possible to solve problems with solid, porous, and liquid regions using a single set of equations. I have also described how this model can be applied to different settings, including ice growth in a Hele-Shaw cell and convection during directional solidification.

In the following chapter, I will describe how we numerically solve this system of nonlinear partial differential equations. Then, I will solve the model in a vareity of different settings. In chapter 4 I find steady state solutions in the context of directional solidification. Chapter 5 considers transient growth from a fixed boundary.

Finally, in chapter 6 I return to a fixed upper boundary but explore the effects of imposed warming on a layer of sea ice.

3

Method

In this chapter, I will describe the numerical method I have developed to solve the sea ice model introduced in chapter 2. To begin, I will use some simple scaling arguments to predict the width of the narrow brine channels I wish to resolve (§ 3.1.1). These predictions motivate the development of a numerical algorithm which includes Adaptive Mesh Refinement (AMR). In § 3.1.2 I introduce the principles behind AMR, then in § 3.1.3 I discuss approaches used by previous authors to solve this problem numerically. I then describe my algorithm (§ 3.2) and demonstrate its accuracy (§ 3.3) and some expansions (§ 3.4) before summarising in § 3.5.

A manuscript based on selected parts of this chapter has been submitted for review in J. Comp. Phys. (Parkinson et al., 2019).

3.1 Introduction

We wish to model mushy layer convection by solving the model presented in chapter 2. For convenience, we repeat the dimensionless governing equations for conservation of heat, solute, momentum, and mass below.

$$\frac{\partial \mathscr{H}}{\partial t} + \mathbf{V}_{frame} \cdot \nabla \mathscr{H} + \mathbf{U} \cdot \nabla \theta(\mathscr{H}, \Theta) = \nabla \cdot \left[\chi + k(1-\chi)\right] \nabla \theta(\mathscr{H}, \Theta), \tag{3.1}$$

$$\frac{\partial \Theta}{\partial t} + \mathbf{V}_{frame} \cdot \nabla \Theta + \mathbf{U} \cdot \nabla \Theta_l(\mathscr{H}, \Theta) = \frac{1}{Le} \nabla \cdot \chi \nabla \Theta_l(\mathscr{H}, \Theta), \tag{3.2}$$

$$\frac{\partial \mathbf{U}}{\partial t} + \mathbf{U} \cdot \nabla \left(\frac{\mathbf{U}}{\chi}\right) = -\chi \nabla p + Pr \nabla^2 \mathbf{U} + \chi Pr \left(Ra_T \theta - Ra_S \Theta_l\right) \mathbf{e_z} - \frac{Pr\, \chi \mathbf{U}}{Da\, \Pi}, \tag{3.3}$$

$$\nabla \cdot \mathbf{U} = 0. \tag{3.4}$$

We consider a modified Carman-Kozeny permeability function appropriate to solidification in a thin Hele-Shaw cell,

$$\Pi(\chi) = \left\{ \Pi_c^{-1} + \left[\frac{\chi^3}{(1-\chi)^2} \right]^{-1} \right\}^{-1}. \tag{3.5}$$

In the pure liquid region $\chi \to 1$ and the permeability takes the value $\Pi_c = d^2/(12K_0)$, which is the dimensionless permeability for a thin Hele-Shaw cell with narrow gap-width d and sets a limit on the total permeability of the system. We will also consider the case where the Darcy-Brinkman equation (3.3) is replaced with the simpler Darcy flow law,

$$\mathbf{U} = \Pi \left[-\nabla \tilde{p} + Da \left(Ra_T \theta - Ra_S \Theta_l \right) \mathbf{e}_z \right]. \tag{3.6}$$

where we have rescaled the pressure $\tilde{p} = (Da/Pr)p$.

3.1.1 Initial scaling analysis

Previous authors simulating mushy layer growth have struggled to fully resolve brine channels due to their narrow width. Sparse observations provide some idea of their size (e.g. Wakatsuchi and Saito, 1985), and I wish to complement this with a scaling analysis to determine how the width depends on the physical properties of sea ice. I below contrast scalings for a channel in open liquid (c.f. Wells et al., 2013; Rees Jones and Worster, 2013) versus flow in a narrow Hele-Shaw cell.

Brine channels are entirely liquid ($\chi = 1$) so the momentum balance (3.3) reduces to the Navier-Stokes equation,

$$\frac{\partial \mathbf{U}}{\partial t} + \mathbf{U} \cdot \nabla \mathbf{U} = -\nabla p + Pr \nabla^2 \mathbf{U} + Pr \left(Ra_T \theta - Ra_S \Theta_l \right) \mathbf{e}_z. \tag{3.7}$$

The channel height h_c is large relative to their radius a, so I invoke a lubrication approximation to ignore the inertial terms (c.f. Schulze and Worster, 1998; Chung and Worster, 2002). Considering the steady state and taking the curl of (3.7) results

in the vorticity equation

$$0 = \nabla \times (Ra_T \theta - Ra_S \Theta)\, \mathbf{e}_z + \nabla^2 \boldsymbol{\omega}, \tag{3.8}$$

where $\boldsymbol{\omega} = \nabla \times \mathbf{U}$ is the vorticity. Restricting ourselves to two dimensions initially, I write the fluid velocity in terms of a streamfunction $\mathbf{U} = (-\partial\psi/\partial z,\, \partial\psi/\partial x)$, such that the vorticity is given by $\boldsymbol{\omega} = \nabla \times \mathbf{U} = (\nabla^2 \psi)\, \mathbf{e}_y$. To constrain the magnitude of the streamfunction ψ I consider a steady state energy balance in a convection cell where horizontal and vertical length scales are roughly equal,

$$\left(-\frac{\partial \psi}{\partial z}, \frac{\partial \psi}{\partial x}\right) \cdot \nabla \theta = \nabla^2 \theta \implies \psi = O(1), \tag{3.9}$$

where I have used the fact that both sides of the heat equation are equidimensional in θ and $\mathbf{x}$ so that length and temperature scales cancel. Now returning to the narrow brine channels, where the horizontal length scale a is much less than the vertical scale h_c, (3.8) becomes

$$0 = \underbrace{Ra_T \frac{\partial \theta}{\partial x}}_{O(Ra_T/a)} - \underbrace{Ra_S \frac{\partial \Theta}{\partial x}}_{O(Ra_S/a)} + \underbrace{\nabla^2 \nabla^2 \psi}_{O(1/a^4)}, \tag{3.10}$$

where we have used the fact that, by construction, θ and Θ are $O(1)$. The buoyancy forcing is dominated by saline effects, so $Ra_S \gg Ra_T$ and the vorticity balance (3.10) implies a channel width

$$a \sim \left(\frac{1}{Ra_S}\right)^{1/3}. \tag{3.11}$$

The same result has been obtained through different considerations by other authors for 2D geometries; Wells et al. (2013) considered thermal balances across the channel wall, whilst Rees Jones and Worster (2013) consider mass conservation between the channel and the mushy layer, both within the framework of coupled self-consistent scaling arguments for the full mushy layer.

A different scaling emerges for channels produced in a Hele-Shaw cell, where the momentum balance is given by Darcy's law (3.6) due to the finite maximum permeability Π_c enforced by viscous drag at the cell walls. Therefore (3.10) is replaced by

$$0 = \underbrace{Da\Pi_c \left(Ra_T \frac{\partial \theta}{\partial x} - Ra_S \frac{\partial \Theta}{\partial x} \right)}_{O(Da\Pi_c Ra_S/a)} + \underbrace{\nabla^2 \psi}_{O(1/a^2)}, \tag{3.12}$$

where the cell permeability Π_c is constant. This gives a channel width

$$a \sim \frac{1}{Da\ Ra_S\ \Pi_c}. \tag{3.13}$$

I will mostly be considering 2-D simulations in a Hele-Shaw cell, where typical values are $DaRa_S = \mathrm{O}(10)$, $\Pi_c = 10$ with a length scale $l = 1$ m, resulting in channel widths $a \sim 10^{-2}$m, comparable to the observed scales (Eide and Martin, 1975). This may explain why Maksym and Jeffries (2001), whose computational mesh had a grid spacing of 5 mm, struggled to fully resolve brine channels, and suggests that a resolution of O(1 mm) is required in the vicinity of channels, to resolve them with of order 10 grid points.

Experimental observations show that the spacing between channels R can vary considerably with time, but is generally in the range $1 < R < 10$ cm (Eide and Martin (1975), Wettlaufer et al. (1997a)). To allow for multiple channels to form, migrate, and interact we need a computational domain width L large enough to contain multiple channels. If, for example, we take $L = 1$ m then the constraint on the maximum size of a grid cell due to the brine channels would require around 10^3 horizontal points in each direction on a uniform mesh. First year sea ice can grow to depths of a few metres so a similar number of grid points are required in the vertical directional, requiring around 10^9 grid cells in total for simulations in three dimensions. For comparison, this is about the same as a 5km resolution global atmospheric model, or 0.05° resolution ocean model, with 100 vertical layers. Such configurations would be considered state-of-the-art by current standards. The typical resolution of global models for climate prediction is currently 100km (Palmer, 2014). Clearly such a

computational task requires substantial high performance computing resources, so we appeal to the advantages of Adaptive Mesh Refinement (AMR).

3.1.2 Introduction to adaptive mesh refinement

Many physical systems have features which exist on a range of scales. In order to resolve fine scale features in a numerical simulation, a high resolution computational mesh is required which can require considerable (and unpractical) computing power. If these fine features are localized in space, it can be possible to use a *variable mesh* whose resolution varies throughout the domain such that high resolution is placed only where it is needed. This can reduce the computational burden of running such simulations. If the problem is time dependent, and fine scale features evolve in time, then the *variable mesh* must also evolve in time to track these features; this is an *adaptive mesh*.

Sea ice is an example of a multiscale physical system. As discussed above, brine channels are narrow and therefore require a higher resolution mesh than the surrounding ice (Lake and Lewis, 1970). As they are separated by much larger distances, typically > 10 cm, they only occupy a few percent of the total ice volume (Wettlaufer et al., 1997a), and an even smaller fraction of a domain containing both ice and ocean. Additionally, the position and size of brine channels evolves in time as liquid regions form, migrate through the ice and then freeze again. Therefore, we intend to develop an adaptive mesh scheme for our simulations.

The computational savings provided by AMR come at the cost of increased algorithmic complexity. There are a variety of approaches to generating refined grids in an AMR scheme (Diachin et al., 2006). Most generally, you can use an *unstructured grid* which is simply a collection of points in space, each connected to a fixed number of other points, whose positions adapt to the solution. Such schemes are useful for problems with complex geometries, but difficult to implement numerically. If you enforce the constraint that each grid cell must be a rectangle, but allow the length of each side to vary arbitrarily, the method becomes known as *mesh distortion*. A second class of schemes is based on *structured refinement*, where every cell is constrained to be square/cuboidal and refinement is achieved by subdividing cells into smaller equally sized squares/cuboids. This can either be *point-wise*, where any single cell

can be refined, or *block-structured*, where rectangular collections of cells are refined together. Structured refinement schemes, particularly block-structured refinement, can be implemented with greater accuracy and efficiency as the boundaries between refined regions are simpler (Diachin et al., 2006).

To speed up the development of the model, we will use an existing set of AMR tools provided by the software library Chombo (Adams et al., 2016) which have already been used to solve a variety of problems, including the Navier-Stokes equations (Martin et al., 2008) and marine ice sheet dynamics (Cornford et al., 2013). Chombo uses finite volume methods on rectangular grids, with block-structurd refinement. A coarse grid covers the entire domain at a uniform resolution, and refined regions are generated at each timestep by dividing a grid cell into $2^D, (2^D)^2, ..., (2^D)^n$ equally sized small cells, where D is the number of spatial dimensions and $n \in \mathbb{N}$ is the *level* of refinement.

If using explicit advection schemes, fluid flow within sea ice places a restriction on the maximum simulation timestep Δt according to the Courant-Friedrichs-Lewy (CFL) criterion

$$\left| \frac{\mathbf{U}\Delta t}{\Delta x} \right| \leq 1, \tag{3.14}$$

where Δx is the grid spacing and $\mathbf{U}$ is the fluid velocity (Courant et al., 1928). Clearly, refined grid cells must be advanced with a smaller timestep than unrefined cells. Chombo provides a framework for respecting this requirement without having to advance the coarse grid cells at a smaller timestep than necessary, which would be computationally inefficient. Known as subcycling in time, the algorithm first advances the coarsest level, then interpolates boundary conditions in space and time in order to advance the first refined level with a reduced timestep. The process continues recursively until all levels of refinement have reached the same time as the coarsest level, at which point synchronisation steps are applied to ensure consistency across the domain. The simulation then moves on to the next time step. This approach will be exploited in some of the simulations considered here.

3.1.3 Previous numerical approaches

With the broad concept of AMR in mind, I now review previous work to provide the relevant context for the new developments in this thesis. Channel formation is strongly nonlinear; to accurately model the feedbacks involved, the governing equations must be integrated numerically. Previous authors have approached this problem in a variety of ways.

A split domain approach involves solving separately for liquid, solid, and 'mushy' regions along with the free boundaries which separate them. Various authors have used this method to find steady-state solutions (Schulze and Worster, 1998; Chung and Worster, 2002; Wells et al., 2013) for a periodic array of channels, given a prescribed channel spacing. An alternative is the single domain 'enthalpy method' (Alexiades and Solomon, 1993; Beckermann et al., 1999) in which a single set of equations are solved throughout the entire domain. This approach removes the need to explicitly solve for the free boundaries, which are often convoluted. Instead, mush-liquid boundaries are implicitly captured via variations of the porosity field. It is therefore a good choice for computing transient solutions where the channels and mush-liquid boundaries evolve over time, and is the approach we employ here. The enthalpy method formulation has been used extensively to simulate binary alloy solidification in a variety of physical settings, using both finite volume methods (Katz and Worster, 2008; Oertling and Watts, 2004) and finite element methods (Felicelli et al., 1998; Le Bars and Worster, 2006b).

Fully coupled nonlinear simulations are computationally expensive as they feature multiple scales. Narrow channels and diffusive boundary layers develop over time and require high resolution, but are restricted to a small portion of the domain. AMR can be a useful approach for efficiently solving problems with multiple spatial scales. Various approaches to AMR exist, which can be broadly divided into either finite element methods on unstructured meshes (e.g. Löhner, 1987), or finite volume methods on structured meshes (following Berger and Oliger (1984); Berger and Colella (1989)). Adaptive mesh refinement has been used to study binary alloy solidification without fluid flow in the context of microstructural dendritic growth (Provatas et al., 1998), and directional solidification of mushy layers (Provatas et al., 2003). Recently, various authors have studied channel formation and mushy layer convection using a similar

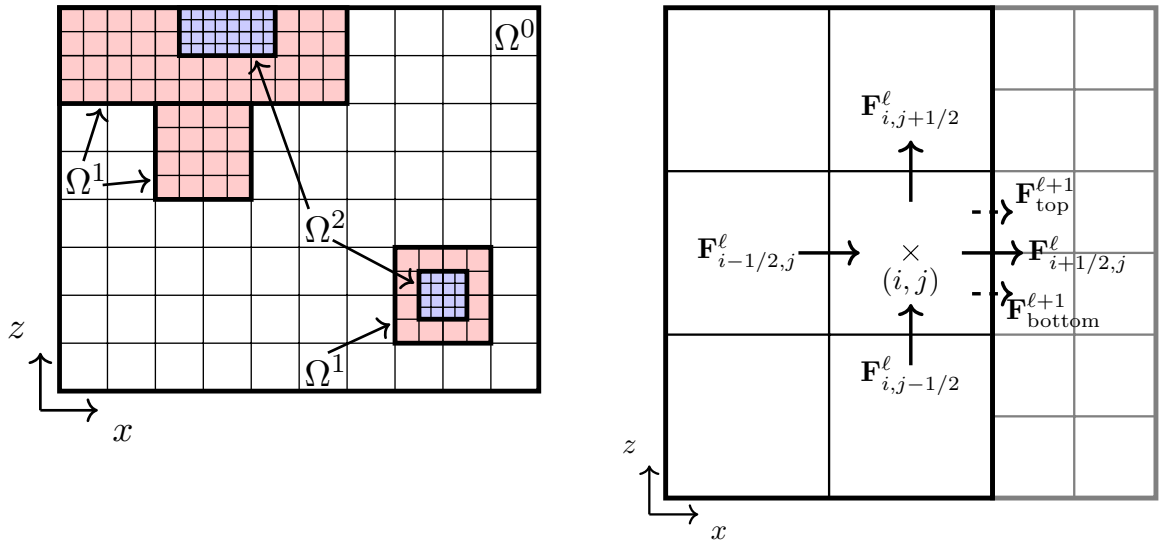
model to the one considered here but using finite elements (Kaempfer and Rappaz, 2003; Liu et al., 2009; Sajja and Felicelli, 2011).

In this chapter I will describe the development of an AMR code to simulate the solidification of binary alloys. In contrast to previous studies, which used finite elements, we implement a finite volume method based on block-structured meshes. Supported by the Chombo framework (Adams et al., 2016), which scales efficiently on thousands of processors (Van Straalen et al., 2009), we implement adaptivity in time (so called 'subcycling') as well as space: coarser levels can be advanced by fewer, larger, timesteps as each refinement level is advanced at roughly the same Courant-Friedrichs-Lewy (CFL) number

Respecting conservation laws with subcycling is not trivial. The solution on regions covered by a fine grid is calculated after the coarse grid, meaning that the more accurate fine fluxes cannot directly influence the coarse solution. Previous authors have accounted for this via 'reflux' corrections for hyperbolic problems (Berger and Colella, 1989) and elliptic problems with linear operators (Almgren et al., 1998). For nonlinear elliptic equations, such as those encountered here, Pretorius and Choptuik (2006) applied Berger-Oliger timestepping to the hyperbolic parts of the equations, with the elliptic parts found by extrapolation, before performing an implicit solve for the elliptic parts over the entire hierarchy of grids. We use a different approach; by linearising the elliptic operators, we follow Almgren et. al. Almgren et al. (1998) and solve implicitly for the small diffusive flux corrections which emerge at coarse-fine boundaries as detailed in § 3.2.4.

3.2 Numerical method

I solve the governing equations (3.1-3.4) on a hierarchy of block-structured, non-uniform meshes using a finite volume discretisation, facilitated by the Chombo framework (Adams et al., 2016). I extend the AMR algorithm for solving the Navier-Stokes equations presented in Martin et al. (2008) to include the Darcy-Brinkman correction, for describing porous media flow, and the effects of buoyancy. Additionally, I extended the Chombo toolbox to solve the nonlinear evolution equations for the enthalpy and



(a) **(b)**

Figure 3.1: (a) An example AMR hierarchy consisting of three levels $\ell = 0, 1, 2$ whose meshes consist of between 1 and 3 rectangular subsets of the full domain. (b) Cells and fluxes at a coarse-fine boundary. Differences between the coarse and fine fluxes, $\delta\mathbf{F}^{\ell} = \mathbf{F}^{\ell}_{i+1/2,j} - \left(\mathbf{F}^{\ell+1}_{\text{top}} + \mathbf{F}^{\ell+1}_{\text{bottom}}\right)$, require a 'reflux' correction to maintain conservation by ensuring that the fluxes used to update both coarse- and fine-level solutions are consistent.

bulk composition implicitly using the Full Approximation Scheme (FAS) (see § A.2 for more details). Advective terms in the momentum equation and advection-diffusion equations are computed using a conservative unsplit Godunov method (see § A.3 for more details). The scheme is second-order in space and first-order in time. We introduce our choice of AMR notation in § 3.2.1. We then introduce our algorithm (§ 3.2.2), which consists of recursive updates on individual levels of refinement (§ 3.2.3) followed by synchronisation operations once a timestep has been completed (§ 3.2.4) in order to maintain conservation and stability as needed.

3.2.1 AMR structure and notation

Our notation follows several previous works on AMR algorithms with Berger-Oliger timestepping (Berger and Colella, 1989; Martin et al., 2008; Martin and Colella, 2000), which we summarise here for a self contained presentation. A rectangular domain is discretized on a hierarchy of cell-centred grids Γ^{ℓ} with grid spacing Δx^{ℓ}, where the level of refinement has index $\ell = 0, 1, 2, ..., \ell_{max}$. On each level ℓ we define the *level domain* Ω^{ℓ}, which consists of one or more rectangular subsets of Γ^{ℓ} (see fig. 3.1a); it is

on the level domains that we solve our equations. The coarsest level domain covers the entire problem domain $\Omega^0 = \Gamma^0$. Each level domain is *properly nested* (Berger and Colella, 1989): no interfaces exist between Ω^ℓ and $\Omega^{\ell\pm2}$, only between Ω^ℓ and $\Omega^{\ell\pm1}$ and possibly Ω^ℓ and the domain boundary $\delta\Omega$.

The grid spacing is chosen such that the refinement ratio $n^\ell_{\text{ref}} = \Delta x^\ell / \Delta x^{\ell+1}$ satisfies $n^\ell_{\text{ref}} = 2^m,\ m = 1, 2, 3...$. We write the refinement ratios for an entire AMR hierarchy as $n_{\text{ref}} = (n^0_{\text{ref}}, n^1_{\text{ref}}, ..., n^{\ell_{\max}-1}_{\text{ref}})$. The timestep on each level Δt^ℓ scales with the grid spacing, $n^\ell_{\text{ref}} = \Delta t^\ell / \Delta t^{\ell+1}$, and satisfies a Courant-Friedrichs-Lewy (CFL) condition which ensures that $\Delta t^\ell < \sigma\ \Delta x^\ell / \text{Max}|\mathbf{U}^\ell|$ where the velocity $\mathbf{U}^\ell$ is taken from the previous timestep and $0 < \sigma < 1$. When solving problems where the fluid acceleration $a \sim Pr\ \text{Max}\left(|\mathbf{U}^\ell|/Da,\ Ra_T,\ Ra_S\right)$ is large, but flow has not yet fully developed, we also ensure that $\Delta t^\ell < \sigma\sqrt{\Delta x^\ell / a^\ell}$ for stability. The level ℓ on which a variable is computed is denoted by a superscript ℓ, whilst the timestep t^{n_l} is indicated by a second superscript, e.g. $\psi^{\ell,n_l+1/2} = \psi(t^{n_l} + \Delta t^{n_l}/2)$. Unless otherwise stated, time-centred fields are found by linear interpolation e.g. $\theta^{\ell,n+1/2} = (\theta^{\ell,n} + \theta^{\ell,n+1})/2$. Variables are cell-centred unless otherwise indicated; a subscript f denotes face-centred values (see § A.1 for more details of our discretisation). Where required, conversion from cell-centred to face-centred values, or vice versa, is achieved by linear interpolation and denoted by $\text{Av}^{C\to F}$, e.g. $\theta_f = \text{Av}^{C\to F}\theta$.

The *level domain* Ω^ℓ can be divided into *valid* and *invalid* regions, where $\Omega^\ell_{\text{valid}}$ is the part of Ω^ℓ not covered by $\Omega^{\ell+1}$. I assume that the solution on the finer level $\Omega^{\ell+1}$ is more accurate than the solution on $\Omega^\ell_{\text{invalid}}$, the part of Ω^ℓ covered by the finer level mesh $\Omega^{\ell+1}$. We define single level operators as those which are applied to both *valid* and *invalid* regions of ℓ using a superscript, e.g. ∇^ℓ. In contrast, *composite* operators are applied to the solution on a union of *valid* regions and do not have a superscript.

3.2.2 AMR update

Following (Martin et al., 2008), we implement adaptivity in time via Berger-Oliger timestepping (Berger and Oliger, 1984; Berger and Colella, 1989) as illustrated in fig. 3.2. To advance the AMR solution from time t to $t + \Delta t$, we employ a recursive timestepping scheme. Starting with the coarsest level $\ell = 0$, we advance the solution

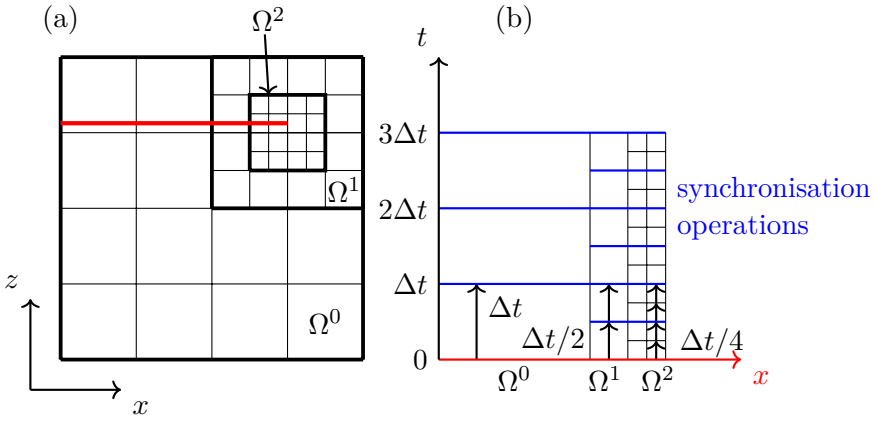


Figure 3.2: Berger-Oliger timestepping. A cross section (red) through an example AMR hierarchy traverses three levels of refinement, which are advanced from coarsest (Ω^0) to finest (Ω^2) as shown on the right. Finer levels have a smaller timestep for stability, and hence require more updates for each coarse grid timestep. Once two or more levels have reached the same time (in this example, $t = n\,\Delta t/2$, where $n = 1, 2, 3, ...$), synchronisation operations (blue) are applied to ensure conservation.

on level ℓ from time t^ℓ to $t^\ell + \Delta t^\ell$. The next finer level is then advanced n^ℓ_{ref} times with a timestep $\Delta t^{\ell+1} = \Delta t^\ell / n^\ell_{\text{ref}}$, and so on recursively, where the algorithm used on each level is identical and described in § 3.2.3. Once all levels finer than ℓ have reached $t^\ell + \Delta t^\ell$, we perform a series of synchronisation steps.

The solution on a fine level $\ell + 1$ will have been updated using more accurate fluxes than were used to update ℓ, which can lead to a discrepancy between the fluxes across a coarse-fine boundary as shown in fig. 3.1b, with a resulting loss of conservation. We compute any difference between the coarse fluxes $\mathbf{F}^\ell$ and the sum of the fine fluxes $\mathbf{F}^{\ell+1}$, $\delta\mathbf{F}^\ell = \mathbf{F}^\ell - \sum \mathbf{F}^{\ell+1}$, and correct our solution on the coarse level grid Ω^ℓ, to account for this as described in § 3.2.4. This step is called *refluxing*.

It is also desirable for a numerical scheme to be *freestream preserving*; an initially constant scalar field λ should remain constant when advected by a divergence-free velocity field. However this is not the case in our scheme following refluxing: whilst we have ensured conservative fluxes by refluxing, the advection velocities are not discretely divergence-free across coarse-fine interfaces. Therefore we use the strategy suggested by Martin and Colella (2000) and evolve a scalar field λ according to

$$\frac{\partial \lambda}{\partial t} + \mathbf{U} \cdot \nabla \lambda = 0, \tag{3.15}$$

where $\lambda(\mathbf{x}, t = 0) = 1$. Deviations in λ from its initial value are then used to compute a lagged correction to the velocity field, $\mathbf{U}_p$, as part of the synchronisation step (see § 3.2.4 for more details).

The pressure is computed using a projection method, as in Martin and Colella (2000) section 1.1 but modified to account for the porosity factor in the pressure gradient term. In general, below we solve problems of the form

$$\nabla \cdot (\chi \nabla p) = \nabla \cdot \mathbf{U} \tag{3.16}$$

for a pressure p given the initial estimate of the velocity field $\mathbf{U}$ which does not, in general, satisfy the divergence constraint (3.4).

3.2.3 Single level update

On a single level of refinement ℓ, we begin a timestep at time t and wish to evolve the primary cell-centred variables, namely $\mathscr{H}^\ell(t), \Theta^\ell(t)$, and the two velocity components $\mathbf{U}^\ell(t) = \left[U^\ell(t), V^\ell(t)\right]$, by a time interval Δt^ℓ. In addition to the primary variables we have a scalar $\lambda^\ell(t)$ and a vector $\mathbf{U}_p^{\ell,n}(t)$ which we use to correct for errors in freestream preservation at coarse-fine boundaries, as discussed later (§ 3.2.4). The pressure is cell-centred, computed at the half time step $\left(t^\ell \pm \frac{1}{2}\Delta t^\ell\right)$, and decomposed into two parts, $p^\ell = \pi^\ell + e$, where π^ℓ is the pressure computed during a single level update and e is a small correction, computed when synchronizing multiple levels of refinement to ensure that the velocity is divergence-free across coarse-fine boundaries. A separate cell-centred pressure field, ϕ^l, is computed to correct the face-centred advection velocities, as described in step 1 below.

Boundary conditions at the interface between a fine level $\ell + 1$ and coarse level ℓ are computed via interpolation in space and time, as described in Appendix A of Martin et al. (2008). To maintain $O(\Delta x^2)$ global accuracy, we require at least $O(\Delta x)$ accuracy along the coarse-fine boundaries and domain boundaries (which have one dimension less than the domain itself). Diffusive operators involve division by Δx^2 and therefore interpolation must be $O(\Delta x^3)$, whilst for the advection operator we require interpolation of $O(\Delta x^2)$. To satisfy this requirement, we use quadratic spatial

interpolation for diffusive operators and bilinear interpolation for advection operators. In both cases, we use linear interpolation in time. Domain boundary conditions are first order in space and implemented via ghost cells.

The update has 5 main steps. Step 1 follows the work of Martin and Colella (2000), whilst steps 3 and 4 are based on Martin et al. (2008).

1. *Compute advection velocities.* We require a face-centred velocity $\mathbf{U}_{AD}^{\ell,n+1/2}$, in order to compute the advective terms $(\mathbf{U}\cdot\nabla)$ in (3.1-3.3). This is complicated by the χ terms in the Darcy-Brinkman equation. Rewriting the advection operator as $\mathbf{U}\cdot\nabla\left(\mathbf{U}/\chi\right) = \left(\mathbf{U}/\chi\right)\cdot\nabla\mathbf{U} - \left(\mathbf{U}/\chi^2\right)\mathbf{U}\cdot\nabla\chi$ and omitting the pressure term initially, to be added later, the momentum equation (3.3) becomes

$$\left(\frac{\partial}{\partial t} + \frac{\mathbf{U}}{\chi}\cdot\nabla\right)\mathbf{U} = \underbrace{\begin{array}{l} Pr\nabla^2\mathbf{U} + \chi Pr(Ra_T\theta - Ra_S\Theta)\mathbf{e}_z \\ \quad - Pr\ \chi\mathbf{U}/\left(Da\ \Pi\right) + \left(\mathbf{U}/\chi^2\right)\mathbf{U}\cdot\nabla\chi \end{array}}_{S}. \tag{3.17}$$

Following Appendix A.1 of Martin et al. (2008), we treat the right hand side of (3.17) as a source term S evaluated at time t^n and predict a face-centred velocity $\mathbf{U}_f^{\ell,n+1/2}$ using a hyperbolic tracing scheme (see also chapter A). Note that advection on the LHS of (3.17) used in the hyperbolic tracing scheme is transporting with an effective velocity $\mathbf{U}/\chi$. This 'advection' velocity is found by averaging from cell-centres to faces; $(\mathbf{U}/\chi)_f^{\ell,n} = \mathrm{Av}^{C\to F}(\mathbf{U}/\chi)^{\ell,n}$. In principle, if $\mathbf{U}/\chi$ is large enough it may be necessary to use a CFL condition based on $(\mathbf{U}/\chi)\Delta t/\Delta x < 1$. However this situation was not encountered here, because $\mathbf{U}$ typically becomes small in regions with small χ.

To ensure the advection velocities are divergence free, we solve for the pressure field ϕ^ℓ,

$$\nabla^\ell\cdot\left(\chi_f^{\ell,n}\nabla^\ell\phi^\ell\right) = \nabla^\ell\cdot\mathbf{U}_f^{\ell,n+1/2}, \tag{3.18}$$

which is used along with the freestream preservation correction $\mathbf{U}_p^\ell$ from the

previous timestep (see below) to construct the final advection velocity:

$$\mathbf{U}_{AD}^{\ell} = \mathbf{U}_{f}^{\ell,n+1/2} - \chi_{f}^{\ell,n}\nabla^{\ell}\phi^{\ell} + \mathbf{U}_{p}^{\ell}. \tag{3.19}$$

2. *Update scalar fields* $\mathscr{H}, \Theta, \lambda$. For each scalar field $s \in \{\mathscr{H}, \Theta, \lambda\}$, upwinded face-centred scalar values $s^{\ell,n+1/2}$ are predicted using the hyperbolic tracing scheme described in Martin and Colella (2000), from which we find the source term $S_{s}^{\ell,n+1/2}(\mathbf{u}) = \nabla^{\ell}\cdot\left(\mathbf{u}\, s^{\ell,n+1/2}\right)$ due to the divergence of advected fluxes. The scalar λ is updated by solving (3.15) explicitly,

$$\lambda^{\ell,n+1} = \lambda^{\ell,n} + \Delta t^{\ell}\, S_{\lambda}^{\ell,n+1/2}\,(\mathbf{U}_{AD}^{\ell,n+1/2}), \tag{3.20}$$

where we have noted that $\nabla\cdot\mathbf{U}_{AD} = 0$ to write $\mathbf{U}_{AD}\cdot\nabla\lambda = \nabla\cdot(\mathbf{U}_{AD}\lambda)$. We treat the diffusion terms in the enthalpy and bulk composition evolution equations implicitly,

$$\begin{aligned}
\mathscr{H}^{\ell,n+1} - \Delta t^{\ell}\, N_{\mathscr{H}}\left(\mathscr{H}^{\ell,n+1}, \Theta^{\ell,n+1}\right) = \\
\mathscr{H}^{\ell,n} - \Delta t^{\ell}\left[S_{\mathscr{H}}^{\ell,n+1/2}(\mathbf{V}_{frame}) + S_{\theta}^{\ell,n+1/2}(\mathbf{U}_{AD}^{\ell,n+1/2})\right], \qquad (3.21)\\
\Theta^{\ell,n+1} - \Delta t^{\ell}\, N_{\Theta}\left(\mathscr{H}^{\ell,n+1}, \Theta^{\ell,n+1}\right) = \\
\Theta^{\ell,n} - \Delta t^{\ell}\left[S_{\Theta}^{\ell,n+1/2}(\mathbf{V}_{frame}) + S_{\Theta_l}^{\ell,n+1/2}(\mathbf{U}_{AD}^{\ell,n+1/2})\right], \qquad (3.22)
\end{aligned}$$

where $N_{\mathscr{H}}$ and N_{Θ} are nonlinear operators for the diffusive terms.

$$N_{\mathscr{H}}(\mathscr{H}, \Theta) = \nabla^{\ell}\cdot\left\{\left[(1-k)\chi(\mathscr{H}, \Theta) + k\right]\nabla^{\ell}\theta(\mathscr{H}, \Theta)\right\}, \tag{3.23}$$

$$N_{\Theta}(\mathscr{H}, \Theta) = \frac{1}{Le}\nabla^{\ell}\cdot\left[\chi(\mathscr{H}, \Theta)\nabla^{\ell}\Theta_{l}(\mathscr{H}, \Theta)\right]. \tag{3.24}$$

The coupled set of eqs. (3.21) and (3.22) are solved by the nonlinear FAS multigrid algorithm (Briggs et al., 2000), using a Gauss-Seidel routine for both the smoothing steps and for solving on the coarsest level. When evaluating the nonlinear operators (3.23 and 3.24), and following the solve, we compute $\theta, \Theta_l, \Theta_s$ and χ using the phase diagram described by eqs. (2.44) to (2.46). In implementing

this step, it was necessary to code a new nonlinear multigrid scheme which has been added to the Chombo code trunk (Adams et al., 2016).

3. *Compute new velocity* $\mathbf{U}^{\ell,n+1}$. We first compute an unprojected velocity $\mathbf{U}_*^{\ell,n+1}$, treating the viscous and Darcy terms implicitly;

$$\left\{1 - \Delta t^\ell \, Pr \left[\left(\nabla^\ell\right)^2 - \frac{1}{Da}\frac{\chi^{\ell,n+1}}{\Pi^{\ell,n+1}}\right]\right\}\mathbf{U}_*^{\ell,n+1} = \mathbf{U}^{\ell,n} + \Delta t^\ell \left\{-\chi^{\ell,n+1/2}\,\nabla^\ell \pi^{\ell,n-1/2} + \chi^{\ell,n+1/2}\left[Pr\left(Ra_T\theta^{\ell,n+1/2} - Ra_S\Theta^{\ell,n+1/2}\right)\right]\mathbf{e}_z - \mathbf{U}_{AD,CC}^{\ell,n+1/2}\cdot\nabla^\ell\left(\frac{\mathbf{U}}{\chi}\right)^{\ell,n+1/2}\right\}, \tag{3.25}$$

where $\mathbf{U}_{AD,CC}^{\ell,n+1/2} = \mathrm{Av}^{F\to C}\mathbf{U}_{AD}^{\ell,n+1/2}$ and $(\mathbf{U}/\chi)^{\ell,n+1/2}$ is found using the same hyperbolic tracing scheme used in step 2 for scalar fields.

Following the procedure detailed in step 6 (section 2.2) of Martin et al. (2008), we then apply a cell-centred projection operator to $\mathbf{U}_*^{\ell,n+1}$ in order to obtain the approximately divergence-free $\mathbf{U}^{\ell,n+1}$ (Martin and Colella, 2000);

$$\nabla^\ell\cdot\chi^{\ell,n+1/2}\nabla^\ell\pi^{\ell,n+1/2} = \frac{1}{\Delta t^\ell}\nabla^\ell\cdot\left(\mathbf{U}_*^{\ell,n+1} + \Delta t^\ell\,\chi^{\ell,n+1/2}\,\nabla^\ell\pi^{\ell,n-1/2}\right), \tag{3.26}$$

$$\mathbf{U}^{\ell,n+1} = \mathbf{U}_*^{\ell,n+1} + \Delta t^\ell\,\chi^{\ell,n+1/2}\left(\nabla^\ell\pi^{\ell,n-1/2} - \nabla^\ell\pi^{\ell,n+1/2}\right). \tag{3.27}$$

where (3.26) is solved first for the pressure correction $\pi^{\ell,n+1/2}$ for use in (3.27). Due to the approximate nature of this projection, we find that it is necessary to manually enforce the physical condition that cells with zero liquid fraction cannot have any fluid flow; $\mathbf{U}^{\ell,n+1} = 0$ if $\chi^{\ell,n+1} = 0$ in the update (3.27).

4. *Recursively update finer levels.* If a finer level $\ell+1$ exists, it is updated with a fractional timestep $\Delta t^{\ell+1} = \Delta t^\ell / n_{\mathrm{ref}}^\ell$ until it reaches the time of the current level, $t_l + \Delta t^\ell$. Where required, boundary conditions for the solve on $\ell+1$ are computed by interpolation in space and time using the solution just found on level ℓ.

5. *Synchronize with finer levels.* If a finer level $\ell + 1$ exists, the current level ℓ is synchronized with all finer levels as described in § 3.2.4

3.2.4 Synchronisation

Because coarse- and fine-level solutions have been evolved independently, the solution will be continuous but will not preserve properties like conservation, freestream preservation, and the divergence constraint (3.4) on the composite multilevel mesh. To ensure that the scheme is conservative, and that the velocity field is divergence free at coarse–fine interfaces, we must perform a series of synchronisation steps once all levels finer than some base level ℓ_{base}, have reached the same time, t^{sync}.

1. *Refluxing.* To ensure conservation, we correct for the flux mismatch $\delta\mathbf{F}^{\ell}$ at the interface between a coarse level ℓ and the fine level, $\ell + 1$. Following (Martin and Colella, 2000; Martin et al., 2008), we introduce this mismatch via a source term in the original evolution equations and decompose the flux-corrected solution into the portion already computed and a small correction, e.g $\mathbf{U}^{\ell,n+1}_{\text{Corr}} = \mathbf{U}^{\ell,n+1} + \delta\mathbf{U}^{\ell,n+1}$. The discretized equation for $\mathbf{U}$, (3.25), becomes

$$\left\{1 - \Delta t^{\ell}\, Pr\, \left[\left(\nabla^{\ell}\right)^2 - \frac{\chi^{\ell,n+1}}{Da\ \Pi^{\ell,n+1}}\right]\right\}\left(\mathbf{U}^{\ell,n+1} + \delta\mathbf{U}^{\ell,n+1}\right) = \mathbf{U}^{\ell,n} + \Delta t^{\ell}\nabla\cdot\left(\mathbf{F}_O - \delta\mathbf{F}^{\ell}_{\mathbf{U}}\right), \tag{3.28}$$

where $\mathbf{F}_O$ is the original source term and we have used (3.27) to eliminate $\mathbf{U}_*$. Using (3.25) we simplify (3.28) to

$$\left\{1 - \Delta t^{\ell}\, Pr\, \left[\left(\nabla^{\ell}\right)^2 - \frac{\chi^{\ell,n+1}}{Da\ \Pi^{\ell,n+1}}\right]\right\}\delta\mathbf{U}^{\ell,n+1} = -\Delta t^{\ell} D_R \delta\mathbf{F}^{\ell}_{\mathbf{U}} \quad \text{for } \ell \geq \ell_{\text{base}}, \tag{3.29}$$

which is solved implicitly for $\delta\mathbf{U}^{l,n+1}$ where D_R, the "reflux divergence", is the part of the coarse-level divergence operator operating on the flux mismatch on the coarse-fine interface (Martin and Colella, 2000). For enthalpy and bulk composition, we must also solve implicitly for the correction to ensure that the

scheme is stable. In contrast to the settings considered by Martin and Colella (2000) our diffusion operators are nonlinear, and depend on χ, which requires a modified approach. In order to diffuse the correction in a physically appropriate manner whilst reducing computational cost, we note that the flux mismatches $(\delta\mathscr{H}, \delta\Theta)$ are small and make the approximation $\chi(\mathscr{H}+\delta\mathscr{H}, \Theta+\delta\Theta) \approx \chi(\mathscr{H}, \Theta)$. Hence, we make the approximation $\chi(\mathscr{H} + \delta\mathscr{H}, \Theta + \delta\Theta) \approx \chi(\mathscr{H}, \Theta)$ and use the linearised forms of the nonlinear diffusion operators defined in (3.24),

$$N_{\mathscr{H}}(\mathscr{H} + \delta\mathscr{H}, \Theta + \delta\Theta) \approx N_{\mathscr{H}}(\mathscr{H}, \Theta) + \nabla \cdot [(1-k)\chi + k]\, \nabla\delta\theta, \tag{3.30}$$

$$N_{\Theta}(\mathscr{H} + \delta\mathscr{H}, \Theta + \delta\Theta) \approx N_{\Theta}(\mathscr{H}, \Theta) + \frac{1}{Le}\nabla \cdot \chi \nabla\delta\Theta_l, \tag{3.31}$$

in order to compute the composite corrections

$$\delta\mathscr{H}^{\ell,n+1} - \Delta t \nabla^{\ell} \cdot \left[(1-k)\chi^{\ell,n+1} + k\right] \nabla^{\ell}\delta\theta(\delta\mathscr{H}^{\ell,n+1}, \delta\Theta^{\ell,n+1}) = -\Delta t^{\ell} D_R \delta\mathbf{F}^{\ell}_{\mathscr{H}} \quad \text{for } \ell \geq \ell_{\text{base}}, \tag{3.32}$$

$$\delta\Theta^{\ell,n+1} - \Delta t \frac{1}{Le}\nabla^{\ell} \cdot \chi^{\ell,n+1} \nabla^{\ell}\delta\Theta_l(\delta\mathscr{H}^{\ell,n+1}, \delta\Theta^{\ell,n+1}) = -\Delta t^{\ell} D_R \delta\mathbf{F}^{\ell}_{\Theta} \quad \text{for } \ell \geq \ell_{\text{base}}. \tag{3.33}$$

Finally, the reflux correction for λ can simply be applied explicitly:

$$\lambda^{\ell,n+1} = \lambda^{\ell,n+1} - \Delta t^{\ell} D_R\, \delta\mathbf{F}^{\ell}_{\lambda} \quad \text{for } \ell \geq \ell_{\text{base}}. \tag{3.34}$$

2. *Apply multilevel projection.* To ensure the velocity is divergence free at coarse-fine boundaries, we apply a composite projection as in Martin and Colella (2000). A further correction to the pressure e_s is found by solving across the entire AMR hierarchy,

$$\nabla^{\ell} \cdot \chi^{\ell} \nabla^{\ell} e_s = \nabla^{\ell} \cdot \mathbf{U}^{\ell} \quad \text{for } \ell \geq \ell_{\text{base}}, \tag{3.35}$$

where boundary conditions are as in Martin et al. (2008). The velocity is then

corrected:

$$\mathbf{U}^\ell = \mathbf{U}^\ell - \chi^\ell \nabla^\ell e_s \quad \text{for } \ell \geq \ell_{\text{base}}. \tag{3.36}$$

3. *Compute freestream preservation correction.* The freestream preservation correction is computed in a composite sense for use in the next timestep. As in Martin and Colella (2000), we solve for the correction e_λ,

$$\nabla^\ell \cdot \left(\chi^\ell \nabla^\ell e_\lambda^\ell\right) = \zeta \frac{\lambda^\ell - 1}{\Delta t^{\ell_{\text{base}}}} \quad \text{for } \ell \geq \ell_{\text{base}}. \tag{3.37}$$

For stability, the constant satisfies $\zeta < 1$ such that the correction velocity,

$$\mathbf{U}_p^\ell = \chi^\ell \nabla^\ell e_\lambda^\ell \quad \text{for } \ell \geq \ell_{\text{base}}, \tag{3.38}$$

only partially corrects the solution in a given timestep. Additionally, we find from a linear stability analysis (§ 3.2.5) that the condition $\zeta < 2(1-\sigma)$ must also be met, in contrast to Martin et al. (2008) who instead found semi-empirically that $\zeta\sigma < 0.5$ was a sufficient condition for stability. We typically choose $\zeta = 0.95, \sigma = 0.4$.

4. *Replace coarse grid solution with average of fine grid solution.* For consistency, the solution on covered regions is replaced by the average of the solution on the overlying fine region, in a process applied recursively from ℓ_{max} down to ℓ_{base}.

3.2.5 Stability of the freestream preservation correction

As described in § 3.2.4, the freestream preservation correction $\mathbf{U}_p$ is calculated according to the method in Martin and Colella (2000) where, given an initial divergence-free estimate $\tilde{\mathbf{U}}$, the revised advection velocity is $\mathbf{U}_{AD} = \tilde{\mathbf{U}} + \mathbf{U}_p$. The discrete update for λ (3.20) can be written in continuous form as

$$\frac{\partial \lambda}{\partial t} + \nabla \cdot (\mathbf{U}_{AD} \lambda) = 0. \tag{3.39}$$

Substituting for $\mathbf{U}_{AD} = \tilde{\mathbf{U}} + \mathbf{U}_p$ whilst noting that $\nabla \cdot \tilde{\mathbf{U}} = 0$ yields

$$\frac{\partial \lambda}{\partial t} + \mathbf{U}_{AD} \cdot \nabla \lambda + \lambda \nabla \cdot \mathbf{U}_p = 0. \tag{3.40}$$

Substituting for $\nabla \cdot \mathbf{U}_p$ from (3.37), we then find

$$\frac{\partial \lambda}{\partial t} = -\mathbf{U}_{AD} \cdot \nabla \lambda - \lambda \, \zeta \frac{\lambda - 1}{\Delta t}. \tag{3.41}$$

To analyse the stability of the correction, we consider an upwind advection scheme and replace $\mathbf{U}_{AD}$ with a typical velocity scale U,

$$\lambda_j^{n+1} = \lambda_j^n - \Delta t \frac{U}{\Delta x} \left(\lambda_j^n - \lambda_{j-1}^n \right) - \zeta \lambda_j^n \left(\lambda_j^n - 1 \right). \tag{3.42}$$

We now consider the evolution of small deviations $\lambda_j^n = 1 + \epsilon A^n e^{ikx_j}$, yielding

$$1 + \epsilon A^{n+1} e^{ikx_j} = 1 + \epsilon A^n e^{ikx_j} - \sigma \epsilon A^n \left(e^{ikx_j} - e^{ikx_{j-1}} \right) - \zeta \left(1 + \epsilon A^n e^{ikx_j} \right) \epsilon A^n e^{ikx_j}, \tag{3.43}$$

where we have defined the CFL number $\sigma = (U \Delta t)/\Delta x$. Dropping terms of order ϵ^2 and dividing through by $A^n e^{ikx_j}$ leads to

$$A = 1 - \sigma \left(1 - e^{-ik\Delta x} \right) - \zeta, \tag{3.44}$$

where $x_j - x_{j-1} = \Delta x$. Taking the absolute value, after some algebra we find

$$|A|^2 = 1 + \zeta(\zeta - 2) + 2\sigma(1 - \sigma - \zeta) \left[\cos(k\Delta x) - 1 \right]. \tag{3.45}$$

We require $|A|^2 < 1$ for the scheme to be stable. By definition, $\zeta > 0$ and $\sigma > 0$, whilst $-2 < \cos(k\Delta x) - 1 < 0$. Therefore $|A|^2$ will be largest when $\zeta + \sigma > 1$, such that the final term of (3.45) is positive. In this case, the most unstable wavelength

gives $\cos(k\Delta x) = -1$ and the criteria for stability becomes

$$\zeta(\zeta - 2) - 4\sigma(1 - \sigma - \zeta) < 0. \tag{3.46}$$

The stability boundary yields a quadratic equation for ζ. Solving this equation and taking the root which gives $\zeta > 0$, we find the stability condition:

$$\zeta < 2(1 - \sigma). \tag{3.47}$$

3.2.6 Initialisation

At the start of a computation, or after the meshes have changed due to regridding, we must initialise the solution. We follow the steps described in Martin and Colella (2000) (section 3.7) and Martin et al. (2008) (section 2.4), repeating the key details here for convenience.

1. At the start of a computation, the primary variables $\mathscr{H}, \Theta$ and $\mathbf{U}$ are given some initial value. An approximation to the lagged pressure π is then found by taking a single non-subcycled timestep across all levels.

2. If regridding during a computation, newly defined fine meshes are filled by linear interpolation from the solution on the underlying coarse mesh.

3. Following any change of the grids, including at the start of a computation, the velocity field is projected in a composite sense to ensure that it is divergence free, and the freestream preservation correction $\mathbf{U}_p$ is recalculated based on the newly-initialized λ field.

3.2.7 Refinement

Regridding occurs every n_r timesteps. During this process, the solution at each grid cell on each level, whether valid or currently covered, is tested against some specified criteria to determine if refinement is required, in which case the cell is *tagged* for refinement. A new set of grids is then found where these tagged cells are covered by a

finer level, whilst still satisfying the rules introduced in § 3.2.1 regarding proper nesting. This procedure enables the refinement or coarsening of the grids over time.

The appropriate refinement criteria will vary between different problems. Typical choices we make are to tag cells which lie on the mush-liquid phase boundary, where $\chi < 1$ and $\chi = 1$ in adjacent cells, or to tag cells where the undivided gradient of the enthalpy field is above some threshold value. The strategy employed for each problem we consider will be explained where appropriate.

3.2.8 Algorithm for Darcy flow

For flow in a Hele-Shaw cell with a narrow gap width, such that $\Pi_c Da \ll 1$, the momentum equation (3.3) is well approximated by Darcy's law (3.6). In this case, the momentum $\mathbf{U}$ becomes a diagnostic rather than prognostic variable, and is entirely determined by the instantaneous enthalpy and bulk concentration. Solving (3.6) instead of (3.3) can be achieved via the changes to the algorithm described below. The resulting method requires less computational effort, making it advantageous in settings where (3.6) is a good description of the physics such as flow in a narrow Hele-Shaw cell.

In the single level update (§ 3.2.3) steps 2, 4, and 5 are unchanged, whilst step 3 is no longer required. During step 1, where we compute advection velocities, the predicted face-centred velocity is now computed at time t^n by averaging the appropriate combination of the known permeability, temperature, and liquid concentration from cell centres to faces;

$$\mathbf{U}_f^{\ell,n} = \mathrm{Av}^{C\to F}\left[\Pi^{\ell,n} Da\left(Ra_T\theta^{\ell,n} - Ra_S\Theta_l^{\ell,n}\right)\mathbf{e}_z\right], \tag{3.48}$$

whilst the pressure correction is found by solving

$$\nabla\cdot\left(\Pi_f^{\ell,n}\nabla\phi^l\right) = \nabla\cdot\mathbf{U}_f^{\ell,n}. \tag{3.49}$$

The final advection velocity is given by $\mathbf{U}_{AD}^{\ell} = \mathbf{U}_f^{\ell,n} - \Pi_f^{\ell,n}\nabla^\ell\phi^\ell + \mathbf{U}_p^{\ell}$.

During synchronisation (§ 3.2.4) we no longer need to compute a reflux correction for the momentum and the multilevel projection (step 2) is redundant. During initialisation

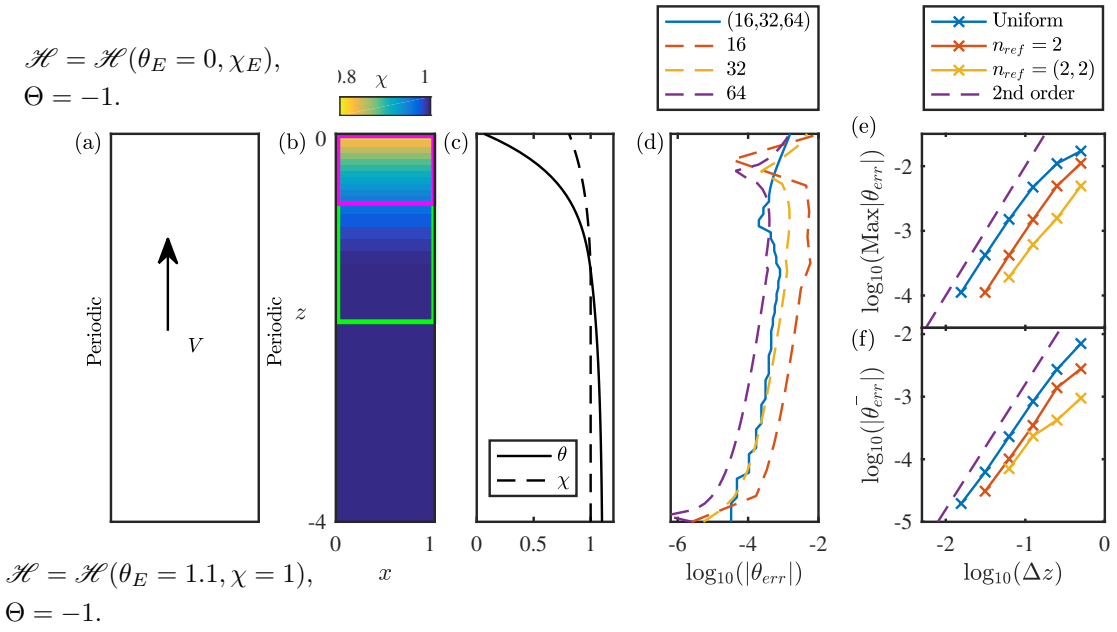


Figure 3.3: Diffusive solidification benchmark (§ 3.3.1). (a) Boundary conditions, (b) typical steady porosity field for an AMR simulation with $\mathscr{C} = 5, \mathscr{S} = 5$, and (c) 1D exact porosity and temperature profiles. Refinement in (b) is added where undivided temperature gradients are large ($\Delta x^\ell |\nabla^\ell \theta^\ell| > 1/2$); the borders of the refined regions $\ell = 1$ (green) and $\ell = 2$ (magenta) are highlighted. Defining $\theta_{err} = \theta - \theta_{\text{analytic}}$ and $\bar{\theta}_{err}$ as the volume average of θ_{err}, we plot 1D error profiles for three uniform mesh solutions with N_z =16 (red), 32 (gold), and 64 (purple) alongside an AMR solution (blue) with a coarse grid $N_z = 16$ and two refined levels. Convergence plots (e, f) confirm that our scheme is second order accurate in space, and that AMR enhances the accuracy of the solution relative to the uniform mesh case. The refinement ratio between successive levels n_{ref} is either a single value for the case with one refined level (red) or two values for the case of two refined levels (yellow).

we no longer need to compute an approximation to the lagged pressure in step 1. Following a change of grids (step 3) we do not need to project the velocity field.

3.3 Code validation

We next demonstrate the accuracy and efficiency of our method. First, we will consider two benchmark problems which separately test the two key components of the algorithm: solving for the nonlinear coupling of enthalpy and bulk composition (§ 3.3.1), and the solution of the Darcy-Brinkman momentum equation (§ 3.3.2). Then we consider a series of transient solutions to the fully coupled problem on both uniform and adaptive meshes, which reveal the computational savings provided by the implementation of AMR.

3.3.1 Diffusive solidification

An analytic solution exists for purely diffusive solidification in a semi-infinite domain (Worster, 1992b), which we use to validate our solution to the thermodynamic aspect of the problem. Specifically, we solve our governing equations with no salt diffusion ($Le = \infty$), equal solid and fluid properties ($k = c_p = 1$), no fluid motion ($Ra_T = Ra_S = 0$), and constant vertical frame advection $\mathbf{V}_{frame} = V_{frame}\mathbf{e}_z$ on the domain illustrated in fig. 3.3a. The bottom boundary is held at a fixed temperature above the liquidus $\theta = 1.1$; we then numerically invert the analytic solution to determine the far-field temperature $\theta(z = -\infty)$ and the corresponding solution within the domain. The top boundary is held at the eutectic temperature and porosity, $\mathscr{H}_{\text{top}} = \mathscr{H}(\theta_E = 0, \chi_E)$, and the $x-$direction is periodic. Initially, the domain is entirely liquid $\chi = 1$ and at temperature $\theta = \theta_{\text{analytic}}$. Simulations are stopped once a steady state is reached, defined by

$$\max \left| \theta^{\ell,n+1} - \theta^{\ell,n} \right| < 10^{-4}\Delta t, \quad \text{for } \ell_{min} \leq \ell \leq \ell_{max}. \tag{3.50}$$

We make use of the adaptive mesh to refine around regions where we expect the error to be largest: the mush-liquid interface and wherever the undivided temperature gradient is large ($\Delta x^\ell |\nabla^\ell \theta^\ell| > 1/2$). A typical steady state porosity field is shown in fig. 3.3b for a simulation with three levels of refinement ($\ell_{\text{max}} = 2$) and refinement ratio of 2 between each level, which we denote by $n_{\text{ref}} = (2, 2)$. A one-dimensional temperature profile is plotted in fig. 3.3c, along with the error $\epsilon = \theta - \theta_{\text{analytic}}$ in fig. 3.3d for a selection of AMR and uniform mesh simulations which reveal that the refined regions greatly reduce the local error compared to the coarser grid. Low error spikes in the uniform mesh solutions near the $z = 0$ boundary are due to θ_{err} changing sign rather than a change to the order of the error. We perform a convergence test using a uniform mesh, an adaptive mesh with one level of refinement ($n_{\text{ref}} = 2$) and an adaptive mesh with two levels of refinement ($n_{\text{ref}} = (2, 2)$), which confirms that the scheme has second order spatial accuracy (fig. 3.3e).

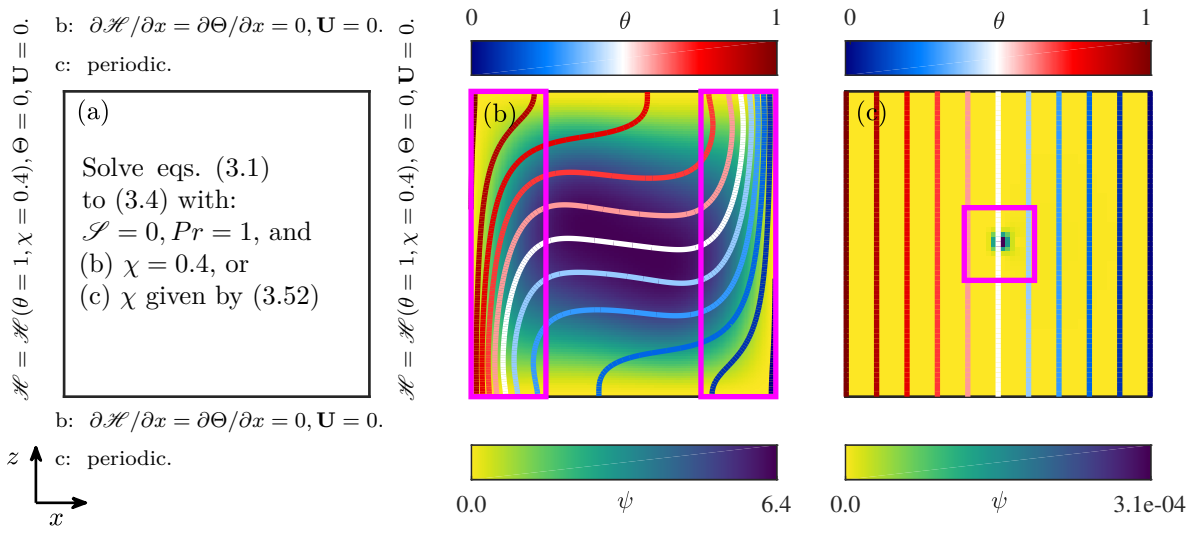


Figure 3.4: (a) Boundary conditions for the problem of thermal convection in a fixed porous medium with isothermal sidewalls of differing temperature. (b) Steady state solution with a uniform porosity $\chi = 0.4$ and $Ra_T = 10^5$, $\bar{Da} = 10^{-2}$. We implement a fixed variable mesh with coarse resolution in the interior and higher resolution along the left/right boundaries, as indicated by the magenta rectangles. Coloured lines show isotherms (top scale) whilst background yellow-green-blue colour shading shows the streamfunction (lower scale). (c) Solution at time $t = 10^{-3}$ with a variable porosity field given by (3.52), other parameters as in (a), and an adaptive mesh which has refined around the region of stronger flow at the centre.

Table 3.1: Comparison of the averaged Nusselt number Nu (given by (3.51)) with previous studies for $\chi = 0.4, k = 1, c_p = 1, Pr = 1$ and $\bar{Da} \equiv Da\ \chi^3/(1-\chi)^2$. Simulations were run on a variable mesh with a coarse resolution Δx^{coarse} and a fine resolution $\Delta x^{\text{coarse}}/2$ occupying the left and right quarters of the domain. Simulations are pursued at increasing resolution until Nu has converged to 3 significant figures.

$\bar{Da}$	Ra_T	Δx^{coarse}					Le Bars and Worster (2006b)	Yedder and Erchiqui (2009)
		1/32	1/64	1/128	1/256	1/512		
10^{-2}	10^3	1.01	1.01	1.01			1.01	1.01
	10^4	1.41	1.41	1.41			1.41	1.41
	10^5	3.18	3.17	3.17			3.17	3.17
	5×10^5	5.28	5.26	5.25	5.24	5.24	5.24	5.24
10^{-6}	10^7	1.06	1.07	1.08	1.08		1.08	1.08
	10^8	2.93	3.01	3.07	3.07		3.06	3.07
	10^9	13.0	13.3	13.2	13.0	13.0	12.9	12.85

3.3.2 Convection in a porous medium

To test the coupled evolution of the momentum and heat transfer, we consider convective flow in a porous medium with isothermal heated and cooled sidewalls, and without phase change ($\mathscr{S} = 0$). Following previous studies (Le Bars and Worster, 2006b; Nithiarasu

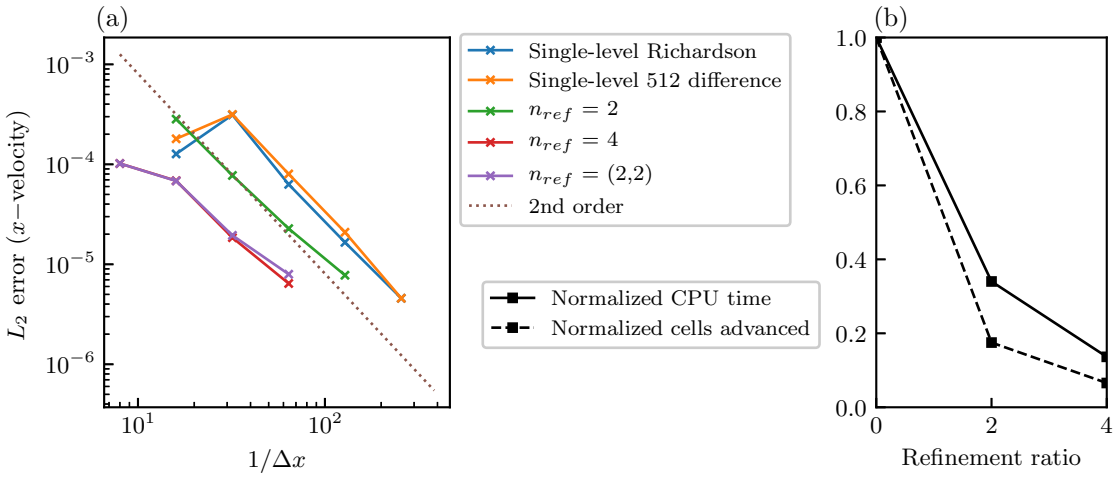


Figure 3.5: (a) L_2 convergence of $x-$velocity and (b) AMR performance for the problem of convection in a porous medium with spatially varying porosity (§ 3.3.2). "Single-level Richardson" errors are calculated as the difference between computations where the grid resolution differs by a factor of 2. The "Single-level 512" error is the difference between each computation and an equivalent calculation performed on a uniform 512×512 mesh. Note that $n_{ref} = 4$ differs only slightly from $n_{ref} = (2, 2)$. In (b), we compare three simulations with the same finest resolution ($\Delta x = 1/256$) and a refinement ratio of 0 (no refinement), 2, or 4. Normalized values are relative to the single-level case, where the number of cells advanced was 2.10×10^7 and the CPU time was 450 seconds. Simulations were performed on a single 2.6 G Hz processor, with GNU compilers and Ubuntu 14.04 operating system.

et al., 1997; Yedder and Erchiqui, 2009) we use the Darcy-Brinkman equation to simulate a fluid with equal solid and liquid properties ($k = c_p = 1$), a Prandtl number $Pr = 1$, and consider a variety of values for the thermal Rayleigh number Ra_T and modified Darcy number $\bar{Da} = Da\,\chi^3/(1-\chi)^2$ whilst $Ra_S = 0$. For the first test case we use a square domain ($0 < x < 1$, $0 < z < 1$), with imposed porosity $\chi = 0.4$ and boundary conditions as illustrated by case b in fig. 3.4a.

Following Almgren et al. (1998), for this problem we use a fixed variable mesh rather than an adaptive mesh. This choice ensures that all simulations will have the same grid hierarchy at all timesteps, permitting an accurate test of the convergence properties. We choose a mesh with enhanced resolution on the left and right walls of the domain to better resolve the boundary layers (see fig. 3.4b). Once simulations have reached steady state, we compute the Nusselt number,

$$Nu = \frac{\partial \theta}{\partial x}, \tag{3.51}$$

averaged over the left and right boundaries of the domain. As seen in table 3.1, our

results agree well with Le Bars and Worster (2006b) and Yedder and Erchiqui (2009) over a wide range of parameters. For the cases with $\bar{Da} = 10^{-6}$, our solutions indicate the presence of a fine scale boundary layer; consequently the quadratic convergence regime is only achieved on the finest grids. For $Ra_T = 10^9$ we find similar Nu values to Le Bars and Worster (2006b) and Yedder and Erchiqui (2009) when using the $\Delta x^{\text{coarse}} = 1/32$ mesh, but as we refine our mesh small discrepancies arise. This may be due to the relatively coarse meshes employed by these previous studies, which may not have fully resolved the fine boundary layer; Yedder and Erchiqui (2009) used an 81x81 mesh, whilst Le Bars and Worster (2006b) used an 81x81 variable mesh which provided somewhat enhanced resolution at the left and right boundaries.

To test the capability of the code to handle regions which low porosity and to adaptively refine around regions of interest, we next impose a porosity which varies spatially from 1 at the centre of the domain $(x_c, y_c) = (0.5, 0.5)$ to almost 0 at the boundaries according to

$$\chi = \min\left\{\exp\left[-\frac{(x-x_c)^2 + (z-z_c)^2}{a}\right], 1.0\right\}; \qquad a = 1/500. \tag{3.52}$$

The porosity χ given by (3.52) reaches machine precision (10^{-15}) at a distance $r = \sqrt{(x-x_c)^2 + (z-z_c)^2} \approx 0.25$ away from the center of the domain, at which point χ is effectively 0. The resulting convection is confined to the interior of the domain, as illustrated in fig. 3.4c, and we choose to refine around regions where the dimensionless velocity satisfies $|\mathbf{U}| > 15$. The solution is advanced from an initial state given by $\theta = x$, $\mathbf{U} = 0$ until a dimensionless time $t = 2 \times 10^{-4}$, using a fixed timestep $\Delta t = 1.6 \times 10^{-4} \Delta x$.

Following (Martin et al., 2008) we first demonstrate that our scheme is second-order accurate via Richardson error estimation, where the error is estimated as the difference between grids with successive resolutions. Then, we compute the error for both uniform and AMR simulations by considering the difference between them and a uniform 512×512 mesh. These results are shown in fig. 3.5a, where the grid spacing on the $x-$axis indicates the coarsest resolution used in a particular simulation. We see that the error for the 64×64 single level case is similar in magnitude (of order 10^{-4})

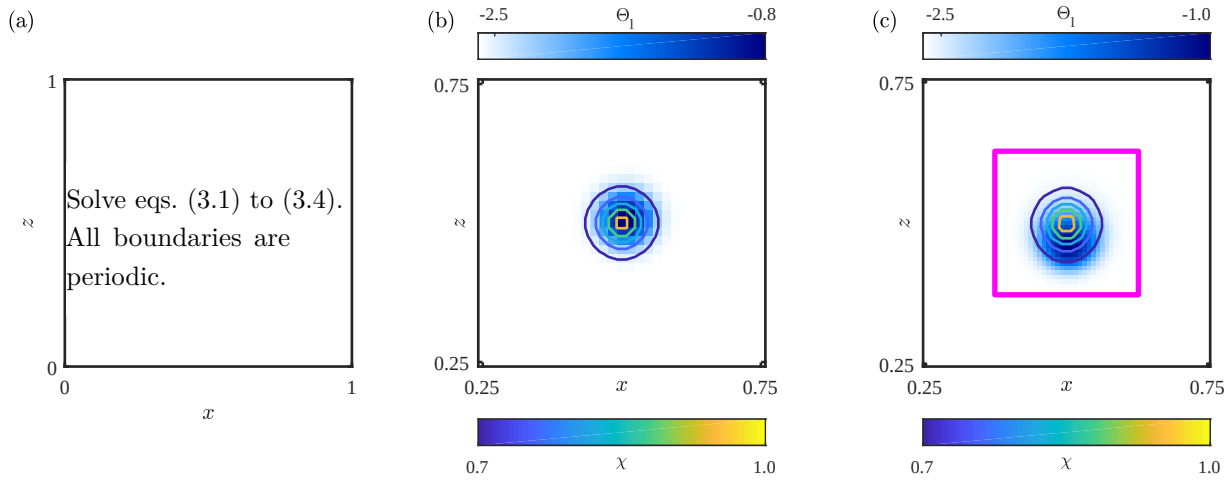


Figure 3.6: (a) Domain for simulations of a high porosity inclusion (§ 3.3.3.1). (b) Initial solution as described by eqs. (3.53) to (3.55), showing the liquid concentration Θ_l (colour, top scale) and porosity χ (contours, lower scale) for a uniform mesh with $\Delta x = 1/32$. (c) Solution at $t = 0.5$ for an AMR simulation with one level of refinement ($n_{\text{ref}} = 2$) and a coarse resolution $\Delta x = 1/32$. The refined region is outlined by the magenta box.

to the 32×32 case with $n_{\text{ref}} = 2$, and the 16×16 case with $n_{\text{ref}} = 4$ or $n_{\text{ref}} = (2, 2)$, demonstrating the accuracy of our mesh refinement.

We now illustrate the computational performance of our algorithm by measuring the runtime and total number of grid cells advanced during the 256×256 single-level simulation, and equivalent AMR calculations. As shown in fig. 3.5b, the use of AMR provides significant savings both in terms of memory (approximately indicated by the number of cells advanced) and run time.

3.3.3 Convection in a mushy layer

We next apply our method to the fully coupled problem (3.1 - 3.4) featuring flow and phase change using the Darcy-Brinkman equation. First we consider the evolution of a highly porous inclusion within a relatively impermeable material (§ 3.3.3.1), which confirms the accuracy and performance benefits of our scheme. Second, we simulate the solidification of an initially liquid solution from above ("fixed chill") (§ 3.3.3.2), which demonstrates the capability of our method to solve more complex problems.

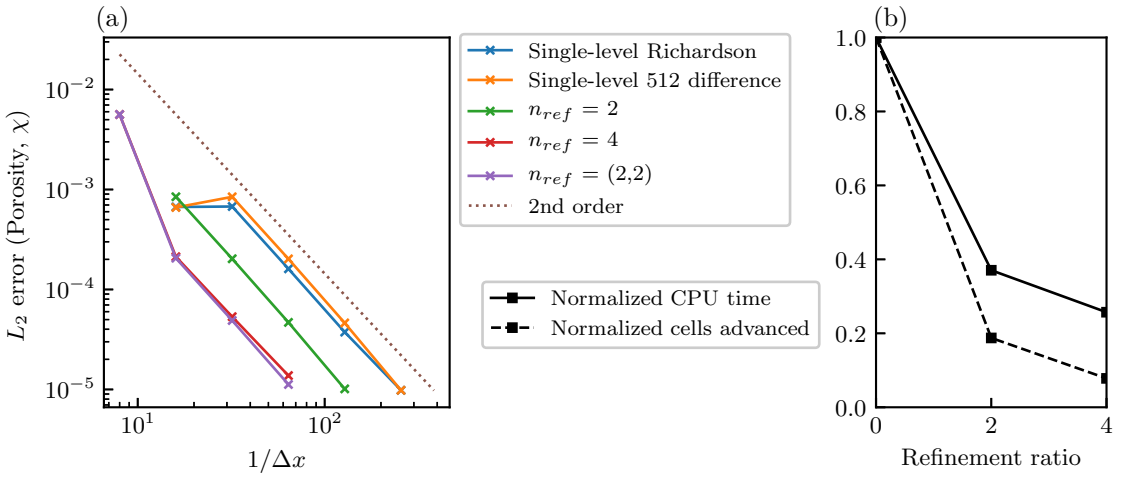


Figure 3.7: (a) L_2 convergence of porosity and (b) AMR performance for the problem of buoyancy-driven flow from an inclusion in a reactive porous medium (§ 3.3.3.1). "Single-level Richardson" errors are calculated as the difference between computations where the grid resolution differs by a factor of 2. The "Single-level 512" error is the difference between each computation and an equivalent calculation performed on a uniform 512×512 mesh. In (b), we compare three simulations with the same finest resolution ($\Delta x = 1/256$) and a refinement ratio of 0 (no refinement), 2, or 4. Normalized values are relative to the single-level case, where the number of cells advanced was 3.15×10^6 and the CPU time was 180 seconds. Simulations were performed on a single 2.6 G Hz processor, with GNU compilers and Ubuntu 14.04 operating system.

3.3.3.1 High porosity inclusion

Here, we simulate the evolution of a high porosity region within a relatively impermeable mushy layer on a periodic domain $0 < x < 1, 0 < y < 1$. Such inclusions can act as the precursor to fully developed channels (Schulze and Worster, 1999), and provide a simple test case for the full coupled system of equations eqs. (3.1) to (3.4).

We consider a material with differing solid and liquid properties ($k = 2, c_p = 0.5$) which is described by the dimensionless parameters $\mathscr{C} = 10$, $Pr = 10$, $Ra_T = 10$, $Ra_S = 10^6$, $Da = 10^{-3}$, $\mathscr{S} = 5$, $Le = 100$ on a doubly periodic domain in x and z. An initial state is given by

$$\mathscr{H} = \mathscr{S} + 0.5, \tag{3.53}$$

$$\Theta = -\mathscr{C}/2 + (\mathscr{C}/2 - 1.0) \exp\left[-\frac{(x-0.5)^2 + (z-0.6)^2}{0.04^2}\right], \tag{3.54}$$

$$\mathbf{U} = 10^{-3} \sin(\Pi x)\, \mathbf{e}_z, \tag{3.55}$$

which generates a small inclusion of higher porosity and higher fluid concentration, with a weak initial flow perturbation. This is evolved in time until $t = 1.5 \times 10^{-4}$ with a fixed timestep $\Delta t = 8 \times 10^{-4} \Delta x$. In order to replicate a hydrostatic pressure gradient on a periodic domain, we introduce the additional body force

$$\mathbf{F}_B = \chi_b \operatorname{Pr} \left(Ra_S \Theta_{l,b} - Ra_T \theta_b \right) \mathbf{e}_z, \tag{3.56}$$

where χ_b, θ_b, and $\Theta_{l,b}$ are computed from the background enthalpy and bulk concentration $(\mathscr{H}_b, \Theta_b) = (\mathscr{S} + 0.5, -\mathscr{C}/2)$. We plot the initial and final states in fig. 3.6. As the dense concentrated fluid sinks under gravity, it increases the local porosity by dissolution of the solid matrix.

As in § 3.3.2, we consider simulations on both a uniform mesh and a variety of adaptive meshes. The refinement criteria is chosen to focus on regions where undivided porosity gradients are large, i.e. $\Delta x \ |\nabla \chi| > 0.1$. As seen in fig. 3.7, we achieve second order spatial accuracy on a uniform mesh, whilst the AMR solution reduces the error to roughly the same magnitude as an equivalent uniform fine-level solution. The use of AMR with a refinement ratio $n_{\text{ref}} = 4$ reduces the memory requirement by a factor of ≈ 10, and the run time by up a factor of ≈ 3 (fig. 3.7b). We would expect the benefits of AMR to be larger for problems with greater spatial localisation in terms of domain volume, such as 3-D settings.

3.3.3.2 Fixed chill in a Hele-Shaw cell

To demonstrate the ability of our method to handle more complicated problems, we simulate the solidification of an initially liquid region from above. We consider a unit domain $0 \leq x \leq 1, 0 \leq z \leq 1$, with symmetry boundary conditions on the side walls (i.e. no lateral gradients). Fixed temperatures applied at the no slip top and bottom surfaces which are impermeable to salt according to:

$$\mathscr{H}(z = 0, t) = \mathscr{S} + 1.3, \quad \mathscr{H}(z = 1, t) = \mathscr{S}/2, \tag{3.57}$$

$$\frac{\partial \Theta}{\partial z}(z = 0, t) = \frac{\partial \Theta}{\partial z}(z = 1, t) = 0. \tag{3.58}$$

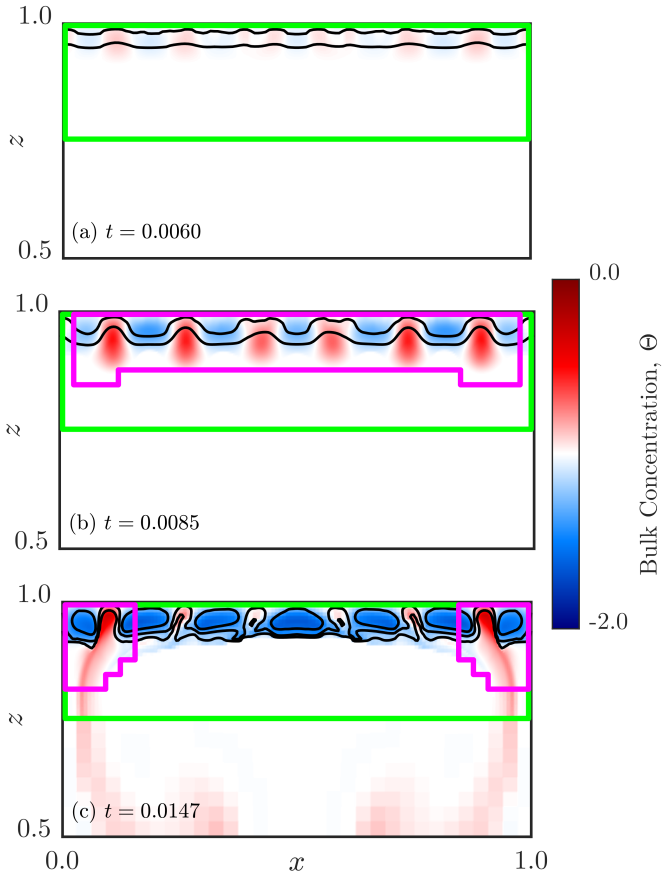


Figure 3.8: Bulk concentration (colour), porosity (contours, $\chi = 1 - 0.2\,n$, $n = 0, 1, 2, 3$) and AMR levels ($\ell = 1$: green, $\ell = 2$: magenta) for a simulation of convection during solidification of a binary alloy from a fixed cold upper boundary in a Hele-Shaw cell (parameters given in (3.59)). Panels (a)-(c) show 3 snapshots in the time development, where t is scaled by the timescale for thermal diffusion across the full box depth. Only the top half of the domain is shown, as this contains the most interesting dynamics.

The initial state is defined by $\mathscr{H}(t = 0) = \mathscr{S} + 1.3, \Theta(t = 0) = -1.0, \mathbf{U}(t = 0) = 0$, and we solve for the resulting flow and solidification given the parameters

$$\begin{aligned} &Ra_S = 10^6, \quad Ra_T = 0, \quad \mathscr{C} = 2, \quad Da = 10^{-4}, \quad \mathrm{Pr} = 10, \\ &\mathscr{S} = 5, \quad \Pi_c = 10^4, \quad k = 1, \quad c_p = 1. \end{aligned} \tag{3.59}$$

Simulations were run on a base mesh 32×32, with 2 unequal levels of refinement using $n_{\mathrm{ref}}^{\ell=0} = 4$, $n_{\mathrm{ref}}^{\ell=1} = 2$ so that the finest cells have $\Delta x = 1/256$. The first level of refinement is added wherever the porosity $\chi < 1$, in order to capture dynamics in the mushy layer. The second level of refinement is added wherever the domain

has already been refined to level 1 and

$$\Delta x|\nabla\chi|(\Theta+\mathscr{C})(\mathbf{U}\cdot\mathbf{e}_z)<-0.5, \tag{3.60}$$

which is chosen to ensure we add the second level of refinement around the narrow channels where porosity gradients and bulk concentration are high, and $\mathbf{U}\cdot\mathbf{e}_z$ is large and negative. As we are primarily interested in the mushy-layer dynamics we choose not to refine around the plumes once they leave the mushy region, which are left to mix and diffuse as they are advected downward through the liquid. Further levels of refinement could be added using (3.60) to increase the resolution around the narrow channels.

The evolution of the bulk concentration and porosity, along with the AMR grids, is shown in fig. 3.8. The mushy-layer grows diffusively at early times, before the convective instability triggers the formation of channels through which solute is transported into the underlying fluid. The transport of solute out of the mushy layer reduces the local porosity, whilst the salty plumes sink into the liquid. As solidification continues neighbouring channels either merge or die out, causing the typical channel spacing to increase. The highest level of refinement tracks the channels across the domain, ensuring that they are well resolved with around 10 grid cells across each channel. This provides an efficient means to overcome the limitations on resolution for resolving flow in channels experienced in previous simulations in wide domains with many channels.

3.4 Additional model capabilities

The work reported in this thesis will use the numerical method described so far in this chapter. In addition to this, there are a number of other features implemented in the code which have not been applied in this thesis but are summarised below for reference.

3.4.1 Variable fluid viscosity

So far we have assumed that the fluid viscosity η is constant, however in some materials η can vary significantly. For example, Aussillous et al. (2006) conducted experiments on a sucrose solution whose viscosity varied with both the temperature and liquid

concentration. It is straightforward to modify the algorithm for pure Darcy flow to consider a viscosity function of the form

$$\eta = \eta_0 \, f_\eta(\mathscr{H}, \Theta), \tag{3.61}$$

where η_0 is a reference viscosity and $f_\eta(\mathscr{H}, \Theta)$ is a dimensionless function which describes the dependence of the viscosity on the thermodynamic variables of the system.

Firstly, we redefine the Prandtl number and compositional and thermal Rayleigh numbers in terms of the reference viscosity,

$$Ra_T = \frac{\rho_l g \alpha \Delta T h^3}{\kappa_l \eta_0}, \quad Ra_S = \frac{\rho_l g \beta \Delta S h^3}{\kappa_l \eta_0}, \quad \mathrm{Pr} = \frac{\eta_0}{\rho_l \kappa_l}. \tag{3.62}$$

We then modify the dimensionless coefficients of the viscous and Darcy terms to include $f_\eta(\mathscr{H}, \Theta)$ such that the Darcy equation becomes

$$\mathbf{U} = \frac{\Pi}{f_\eta} \left[-\nabla \tilde{p} + Da \left(Ra_T \theta - Ra_S \Theta_l \right) \right]. \tag{3.63}$$

The f_η terms are then evaluated at the same time as the permeability at each stage of the algorithm.

The Darcy-Brinkman equation is more complicated due to the inclusion of f_η within the divergence part of the viscous operator, and is left for future work.

3.4.2 Biogeochemical tracers

In this thesis we will focus on the transport of salt through sea ice. However there can be many other chemical species dissolved in the liquid phase, whose transport can have profound biogeochemical consequences as mentioned in § 1.3.6.

We consider a passive tracer with bulk concentration X which is not incorporated into the solid phase and can either be advected or diffused within the liquid phase according to the dimensional transport equation

$$\frac{\partial X}{\partial t} + \nabla \cdot (\mathbf{U} X_l) = \nabla \cdot (D_X \chi \nabla X_l) + S(H, S, \mathbf{U}), \tag{3.64}$$

where $X_l = X/\chi$ is the liquid concentration of the tracer, D_X the tracer diffusivity, and S is a source/sink term which in principle can depend on any of the other fields. Nondimensionalising the tracer concentration relative to some reference value X_i, we obtain the dimensionless tracer concentrations $\xi = X/X_i$ and $\xi_l = X_l/X_i$, and dimensionless source term $\sigma = ST/X_i$ where $T = \mathcal{H}^2/\kappa_l$ is the diffusive timescale used in our nondimensionalisation (§ 2.3). Hence, the dimensionless tracer transport equation is given by

$$\frac{\partial \xi}{\partial t} + \nabla \cdot (\mathbf{U}\xi_l) = \nabla \cdot (D_\xi \chi \nabla \xi_l) + \sigma, \tag{3.65}$$

where $D_\xi = D_X/\kappa_l$ is the dimensionless tracer diffusivity coefficient. When the tracer diffusivity is small ($D_\xi \ll 1$), we typically find that the modified CFL stability condition $D_\xi \chi \Delta t/\Delta x^2 < 1/2$ is satisfied and we may treat the right hand side of (3.65) explicitly. Hence, we solve for the evolution of ξ in the same manner as we do for λ (3.20) with the addition of a source term $\nabla \cdot (D_\xi \chi \nabla \xi_l) + \sigma$ which is evaluated at the start of each timestep t^n. For tracers with higher diffusivities, it would be necessary to solve implicitly for ξ using a scheme analogous to that which we use for the coupled enthalpy-bulk salinity fields.

3.4.3 Nonlinear boundary conditions

Using the enthalpy method, thermodynamic boundary conditions are most naturally enforced by specifying conditions on the enthalpy and bulk salinity. However, physically it is often most convenient to write boundary conditions in terms of the temperature. Within a mushy layer, the nonlinear coupling of the thermodynamic variables presents a challenge for enforcing boundary conditions based purely on a temperature condition. In this thesis, we will typically consider boundaries with a fixed temperature and bulk salinity, which can be enforced by fixing the enthalpy and bulk salinity at a boundary. However in other circumstances it may be desirable to enforce a flux at one boundary, or use a condition which depends on both the temperature and the temperature flux.

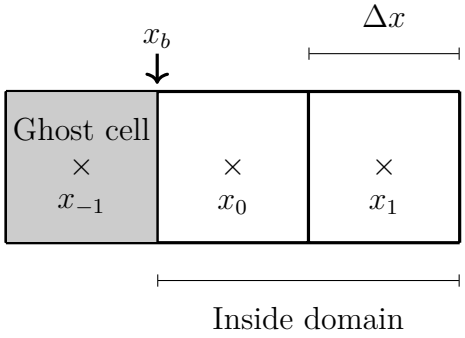


Figure 3.9: Grid cells around a domain boundary at $x = x_b$. With our numerical scheme, boundary conditions are enforced by specifying the enthalpy and bulk salinity at the ghost cell (grey) based on the solution at the interior points $(x_0, x_1, ...)$.

Here, we describe a method for enforcing a general boundary condition of the form

$$f(\theta(x_b)) = 0, \tag{3.66}$$

where f is some functional of the dimensionless temperature and its derivatives, and x_b is the position of the domain boundary. For example we might have

$$f(\theta) = \alpha \mathbf{n} \cdot \nabla\theta + \beta\theta = 0, \tag{3.67}$$

where $\mathbf{n}$ is a unit vector normal to the boundary. We restrict ourselves to the case where there is no flux of solute across the boundary, $\mathbf{n} \cdot \nabla\Theta|_{x=x_b} = 0$, which is physically appropriate for the case of ice growth from a fixed boundary.

With our algorithm, boundary conditions are enforced via a ghost cell whose center is located $\Delta x/2$ away from the boundary, as illustrated in fig. 3.9. Hence we must solve (3.66) to determine an appropriate enthalpy and bulk salinity at x_{-1}, given the enthalpy and bulk salinity in the interior of the domain. Given the specific condition of no bulk solute flux across the boundary, the bulk salinity at x_{-1} is simply given by $\Theta_{-1} = \Theta_0$ to eliminate the gradient. Therefore we seek the ghost cell enthalpy $\mathscr{H}_{-1}$ such that (3.66) is satisfied on the boundary. Given a discretisation of (3.66) of the form

$$\theta_{-1}(\mathscr{H}_{-1}, \Theta_0) + g(\mathscr{H}_0, \Theta_0) = 0, \tag{3.68}$$

where $\theta_{-1}(\mathscr{H}_{-1}, \Theta_0)$ is determined by the phase diagram and $g(\mathscr{H}_0, \Theta_0)$ is a known

function, we perform a fixed point iteration at each point along the boundary to solve for $\mathscr{H}_{-1}$. Starting from an initial guess $\mathscr{H}_{-1}^0 = \mathscr{H}_0$, we compute the residual

$$r = \theta_{-1}(\mathscr{H}_{-1}^j, \Theta_0) + g(\mathscr{H}_0^j, \Theta_0), \tag{3.69}$$

for iterate $\mathscr{H}_{-1}^j$ before correcting the estimate of the ghost cell enthalpy

$$\mathscr{H}_{-1}^{j+1} = \mathscr{H}_{-1}^j + r. \tag{3.70}$$

This process is repeated iteratively until $|r|$ is less than some threshold value which we typically take to be 10^{-5}. This was found to typically converge within 10 iterations for a selection of nonlinear $g(\mathscr{H}_0, \Theta_0)$. With a linear $g(\mathscr{H}_0, \Theta_0)$, we converge in 1 iteration.

To obtain an appropriate discretisation of (3.66), we use the approximations

$$\mathbf{n} \cdot \nabla\theta|_{x=x_b} = \frac{\theta_0 - \theta_{-1}}{\Delta x}, \quad \theta(x_b) = \frac{\theta_0 + \theta_{-1}}{2}. \tag{3.71}$$

For example, the condition given by (3.67) would become

$$\left(\frac{1}{2} - \frac{1}{\Delta x}\right)\theta_{-1}(\mathscr{H}_{-1}, \Theta_0) + \underbrace{\left(\frac{1}{2} + \frac{1}{\Delta x}\right)\theta_0(\mathscr{H}_0, \Theta_0)}_{g(\mathscr{H}_0, \Theta_0)} = 0. \tag{3.72}$$

3.5 Summary

In this chapter we have developed a method for simulating the transport of heat, mass, and solute during binary alloy solidification, using a finite volume approach with adaptive mesh refinement. Our algorithm features local refinement in space and time on block structured Cartesian grids, implemented via the Chombo framework, along with a series of synchronisation steps to ensure flux conservation. The algorithm is built on a previous technique for solving the incompressible Navier-Stokes equations (Martin et al., 2008). I extended this previous method to include a Darcy term in the momentum equation and the nonlinear thermodynamics of mushy layer solidification. Prior to this work, Chombo included native solvers capable of solving sets of hyperbolic and linear elliptic equations on a hierarchy of adaptively refined meshes. The equations for heat and

solute transport in a mushy layer (eqs. (3.1) and (3.2)) include nonlinear diffusive terms, hence we have extended the Chombo framework to include a solver for nonlinear elliptic equations using the Full Approximation Storage multigrid scheme. Using a hierarchy of test cases, we have demonstrated the second-order convergence of our method and the performance benefits which AMR can provide. The ability of our scheme to handle transient problems, with features evolving in time, has also been demonstrated.

The implementation of Adaptive Mesh Refinement has come at the cost of considerable algorithmic complexity, with a commensurate investment of time. Indeed, the validation of our method for the most complex test problems with AMR is a relatively recent development. However the first step to developing our method was implementing the algorithm on a single uniform mesh, which was achieved at a far earlier date. As a result of this chronology, the majority of the simulations presented in the remainder of this thesis have been conducted with the model run in uniform mesh mode, and were completed in parallel with the development of the AMR algorithm.

In the remainder of this thesis we will present a wide variety of numerical simulations, along with physical interpretation and explanations. However the potential applications of the method described in this chapter extend far beyond the subset of problems that we will consider here. Whilst we will primarily consider the growth of sea ice on Earth, this code could also be used to model sea ice in other contexts such as the effects of flushing from melt ponds or snow melt (e.g. Maksym and Jeffries, 2001; Vancoppenolle et al., 2013). It may also have applications to ice formed from binary mixtures on other planets, such as the icy moons of Jupiter and Saturn (e.g Spencer and Nimmo, 2013). Many other types of mushy layers could also be studied using this method, such as those formed during metal casting (Copley et al., 1970) or within the Earth's interior (Fearn et al., 1981). To aid the application of this method to other problems, the code we have written is open source and can be found at
`https://github.com/jrgparkinson/mushy-layer/tree/v1.0`.

A

Numerical methods

This appendix provides some additional details on the numerical methods introduced in chapter 3.

A.1 Discretisation

In order to maintain appropriate conservation properties, we use a finite volume discretisation, which is illustrated schematically in fig. A.1. On each level of refinement ℓ the domain is split into square grid cells of size Δx^ℓ in each dimension. Conserved quantities exist at the center of each grid cell, whilst fluxes exist on the cell faces. As momentum is conserved, we compute the Darcy velocites $\mathbf{U}$ at cell centers for Darcy-Brinkman flow. Meanwhile, we compute a divergence-free advection velocity $\mathbf{U}_{AD}$ at the cell faces, which we use to compute advective fluxes of heat and solute.

We compute the updates to the values at the cell centers using a flux conservative discretisation, where the update is written in terms of the divergence of the fluxes across the cell boundaries i.e.

$$\nabla^2\theta(\mathscr{H},\Theta) = \nabla\cdot\left[\nabla\theta(\mathscr{H},\Theta)\right]. \tag{A.1}$$

For example, the 1-D discrete form of the thermal diffusion operator is then

$$N_{\mathscr{H}}(\mathscr{H},\Theta)_i = \frac{\left[(1-k)\chi_{i-1/2}+k\right](\nabla\theta)_{i-1/2} - \left[(1-k)\chi_{i+1/2}+k\right](\nabla\theta)_{i+1/2}}{\Delta x}, \tag{A.2}$$

$$\text{where } \chi_{i-1/2} = \frac{\chi_i+\chi_{i-1}}{2}, \text{ and } \quad (\nabla\theta)_{i-1/2} = \frac{\theta_i-\theta_{i-1}}{\Delta x}. \tag{A.3}$$

Note that χ and θ are functions of $\mathscr{H}$ and Θ determined by the phase diagram. The

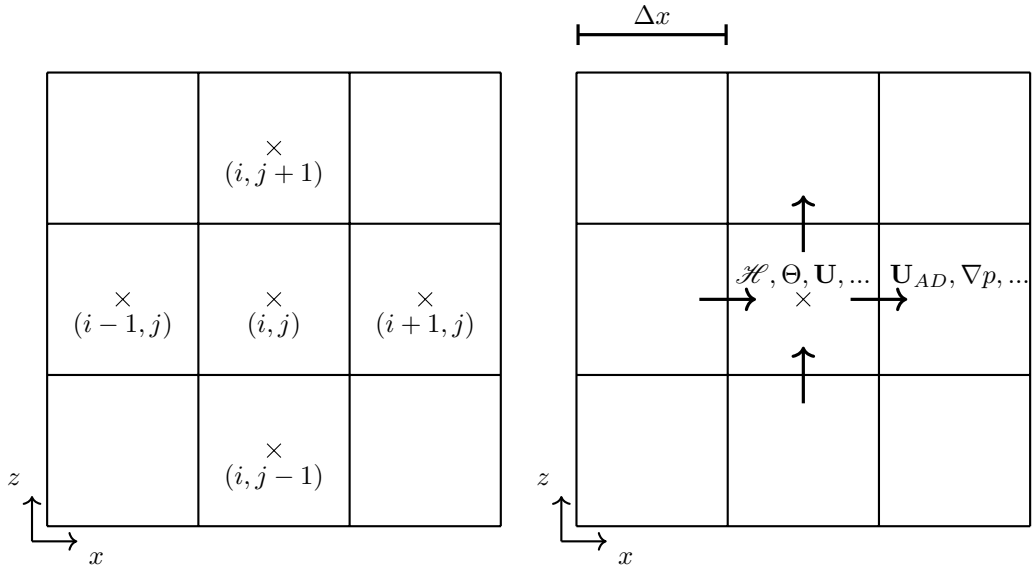


Figure A.1: Illustration of our finite volume discretisation. Conserved quantities (enthalpy $\mathscr{H}$, bulk salinity Θ, Darcy velocity $\mathbf{U}$ etc.) are located at the cell centers (i, j). Fluxes (advection velocity $\mathbf{U}_{AD}$, pressure gradients ∇p, etc.) are located on the cell faces (arrows).

solute diffusion operator $N_\Theta = (1/Le)\nabla \cdot \chi \nabla \Theta_l$ is found in a similar way, whilst the 2-D and 3-D forms generalise naturally from this example.

A.2 Multigrid

We make extensive use of multigrid methods to solve elliptic equations implicitly. A comprehensive introduction to multigrid methods can be found in Briggs et al. (2000), whilst a brief summary is given below. The principle behind multigrid is to apply an iterative solver on a hierarchy of coarser grids, solving the problem to a high accuracy on the coarsest grid before recovering the solution on the original fine mesh. Iterative methods are computationally inexpensive and are effective at removing high frequency noise, but they perform poorly with low frequency noise. With the multigrid approach, low frequency noise on the finer grids behaves like high frequency noise on the coarser grids, where it can be effectively removed.

For example, we consider the numerical solution of

$$\frac{\partial q}{\partial t} = N(q), \tag{A.4}$$

where $N(q)$ is some operator which may be linear or nonlinear. Using a simple 1st order discretisation in time, we obtain

$$q^{n+1} - \Delta t N(q^{n+1}) = q^n. \tag{A.5}$$

We wish to solve for the solution at the next time step q^{n+1}. Defining the residual at each grid point (i, j) via

$$R_{i,j}(q^{n+1}_{i,j}, q^n_{i,j}) = q^{n+1}_{i,j} - q^n_{i,j} - \Delta t N(q^{n+1})_{i,j}, \tag{A.6}$$

we could attempt to iteratively reduce the residual via a simple relaxation scheme where we continually update our best guess for the solution at the new time $q^{*+1}_{i,j}$ from our previous best guess $q^*_{i,j}$, e.g.

$$q^{*+1}_{i,j} = q^*_{i,j} - R_{i,j}(q^*_{i,j}, q^n_{i,j}). \tag{A.7}$$

However this method is not particularly efficient. Using a multigrid method, we use (A.7) to remove high frequency noise before computing the residual R and then transferring the solution to a coarser mesh. We then apply (A.7) to reduce the high frequency error on the new mesh before coarsening again, repeating this process until we arrive at a mesh which cannot be coarsened any further (e.g. a 1×1 mesh). At this point we use the iterative method (eq. A.7) to reduce the residual below some tolerance (usually 10^{-10}). The solution is then transferred back to the original grid via a series of *prolongation* operations (in this case, bilinear interpolation) combined with further iterative solves to remove the errors introduced by interpolation. This process, where the solution is reduced to the coarsest grid and then returned to the original grid is known as a single V-cycle. Multiple V-cycles are applied until the residual has been reduced satisfactorily.

The exact implementation of the multigrid method varies between linear and nonlinear operators. For linear problems we follow the approach described in chapter 3 of Briggs et al. (2000). For nonlinear problems we use the Full Approximation Storage (FAS) algorithm (Briggs et al., 2000, chapter 6).

A.3 Godunov's method

Chombo has a number of pre-existing methods for solving hyperbolic equations using a class of techniques known as Godunov methods (Colella, 1990; Saltzman, 1994; Colella et al., 2008). A detailed introduction to these methods can be found in LeVeque (2007). Using a Godunov method, we compute the update to the solution q at each grid cell by integrating the advective flux $\mathbf{F}$ over the cell faces. Below, we introduce this technique in the context of one dimensional advection with constant advection velocity.

Considering a one dimensional grid with values q_i at positions x_i, the one dimensional advection equation is given by

$$\frac{\partial q}{\partial t} + a\frac{\partial q}{\partial x} = 0, \tag{A.8}$$

where a is the constant advection velocity. Integrating (A.8) across the jth cell from $x_{i-1/2}$ to $x_{i+1/2}$ yields

$$\begin{aligned} \int_{x_{i-1/2}}^{x_{i+1/2}} \left[\frac{\partial q}{\partial t} + a\frac{\partial q}{\partial x}\right] dx &= \frac{\partial}{\partial t}\left[\int_{x_{i-1/2}}^{x_{i+1/2}} q\, dx\right] + [aq]_{x_{i-1/2}}^{x_{i+1/2}} = 0, \\ \implies \Delta x_i \frac{\partial q_i}{\partial t} + F_{i+1/2} - F_{i-1/2} &= 0, \end{aligned} \tag{A.9}$$

where we have defined

$$q_i = \frac{1}{\Delta x_i}\int_{x_{i-1/2}}^{x_{i+1/2}} q\, dx; \qquad F_i = aq_i. \tag{A.10}$$

Integrating (A.9) in time from t to $t + \Delta t$, we find

$$\begin{aligned} \Delta x_i \int_t^{t+\Delta t} \frac{\partial q_i}{\partial t}\, dt &= -\int_t^{t+\Delta t} F_{i+1/2} - F_{i-1/2}\, dt, \\ \implies q_i^{n+1} - q_i^n &= -\frac{1}{\Delta x_i}\int_t^{t+\Delta t} F_{i+1/2} - F_{i-1/2}\, dt. \end{aligned} \tag{A.11}$$

To evaluate (A.11), and hence advance q_i by one timestep, we need to calculate the integral of the flux difference across the cell boundaries. This is done by considering a so-called *Riemann problem*. At each cell boundary $x_{i\pm1/2}$ where we wish to integrate

the flux, we assume that q takes the form of a step function at time t:

$$q(x,t) = \begin{cases} q(x_i) & x \leq x_{i+1/2} \\ q(x_{i+1}) & x > x_{i+1/2} \end{cases} \tag{A.12}$$

Assuming the constant advection velocity a is positive, $q(x,t)$ will be translated in the positive x direction at speed a. Hence, $q(x_{i+1/2}, t+\Delta t) = q(x_i, t)$. For advection velocities $\mathbf{U}(\mathbf{x},t)$ which vary spatially and temporally, $q(x_{i+1/2}, t+\Delta t)$ is predicted numerically given $q(\mathbf{x},t)$ and $\mathbf{U}(\mathbf{x},t)$ in a process known as *hyperbolic tracing*. Recalling that $F_i = a\, q_i$ (A.10), we find

$$\int_t^{t+\Delta t} F_{i+1/2}\, dt = \int_t^{t+\Delta t} a q(x_{i+1/2}, t)\, dt, \tag{A.13}$$

$$= \int_t^{t+\Delta t} a q(x_i)\, dt = a\, q(x_i)\Delta t. \tag{A.14}$$

Similarly,

$$\int_t^{t+\Delta t} F_{i-1/2} = a\, q(x_{i-1})\Delta t, \tag{A.15}$$

and therefore the solution to the Riemann problem in this case is simply

$$\int_t^{t+\Delta t} F_{i+1/2} - F_{i-1/2}\, dt = a\, \left[q(x_i,t) - q(x_{i-1},t)\right] \Delta t. \tag{A.16}$$

Substituting into (A.11), we arrive at the discrete update for q_i

$$q_i^{n+1} = q_i^n - \frac{a\Delta t}{\Delta x_i} \left[q^n(x_i) - q^n(x_{i-1})\right]. \tag{A.17}$$

If instead $a < 0$, then $q(x_{i+1/2}, t+\Delta t) = q(x_{i+1}, t)$ and (A.17) becomes

$$q_i^{n+1} = q_i^n - \frac{a\Delta t}{\Delta x_i} \left[q^n(x_{i+1}) - q^n(x_i)\right]. \tag{A.18}$$

In general the advection velocity a is not a constant, and therefore the solution to the Riemann problem must be computed numerically.

4

Steady state growth

In this chapter we will consider mushy-layer growth during *directional solidification*, where a sample is translated at a fixed speed V relative to hot and cold heat exchangers (see fig. 4.1 for an illustration of the domain). Directional solidification is particularly relevant to industrial processes, such as metal casting. Due to the enforced fixed growth rate, a steady state may be achieved during directional solidification via removal of solid at the cold boundary which provides a convenient setting within which to study the dynamics of convection in mushy layers, and build understanding relative to more complex transient settings.

The solution for steady state growth in the absence of convection (Worster, 1991) provides a convenient base state for stability analyses. A common feature of these analyses (see Worster, 1997; Guba and Worster, 2010; Wells et al., 2019, for reviews) is that the system is stable unless the mushy Rayleigh number Rm exceeds a critical value, where Rm is here defined by

$$Rm = \frac{g\,\beta\,\Delta S\,K_0}{\nu V}, \tag{4.1}$$

where g is the acceleration due to gravity, β is the solutal expansion coefficient, $\Delta S = S_e - S_i$ is the difference between the eutectic salinity C_e and initial salinity of the fluid S_i, S_s is the concentration of the solute in the solid phase, K_0 is a reference permeability, ν is the kinematic viscosity of the fluid and V is the directional solidification rate. As noted previously, Rm describes the ratio of buoyancy to dissipative forces. The critical Rayleigh number Rm_{crit} can depend strongly on the other parameters of the system.

Channel formation is an inherently nonlinear process, motivating the use of numerical simulations to examine their origin and behaviour. I below recap key results from the literature review which are most relevant to this chapter. The enthalpy method, where

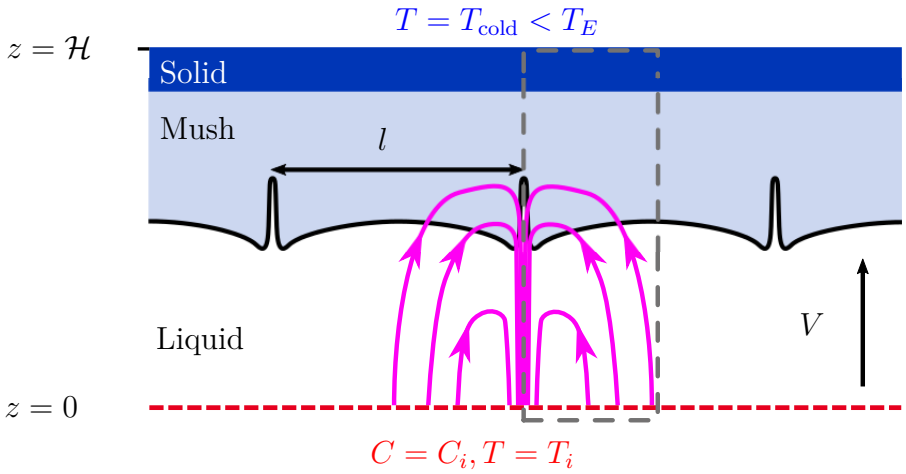


Figure 4.1: Illustration of the model considered in this chapter. Fluid of concentration S_i and temperature T_i is translated vertically upwards at speed V between fixed heat exchangers at $z = 0$ and $z = \mathcal{H}$, maintained at temperatures T_i and T_{cold} respectively. Solidification from the upper boundary, which is held below the eutectic point, results in the formation of a solid region at the top of the domain. Between the solid and liquid phases there is a porous mushy region, within which solidification releases dense concentrated fluid driving convective flow (magenta streamlines). Entirely liquid channels form in regions of downwelling. We consider a periodic array of channels with spacing l where, taking advantage of symmetry, our simulations will consider just the region outlined by the dashed grey box.

a single set of equations are solved in the mushy layer and the liquid, has been used to study the time-dependent evolution of channels in two dimensional systems (Katz and Worster, 2008; Oertling and Watts, 2004). Other authors have computed steady state solutions for a periodic array of channels during directional solidification, using a lubrication approximation to simplify the numerics in the narrow channels (Schulze and Worster, 1998; Chung and Worster, 2002; Wells et al., 2010). In doing so, it is necessary to specify the spacing between adjacent channels. Wakatsuchi and Saito (1985) studied samples of natural sea ice and found that during the early stages of transient growth the channel spacing decreases as the ice growth rate increases, whilst for thicker ice the channel spacing is roughly constant. The experiments of transient growth by Middleton et al. (2016) and simulations of steady growth performed by Katz and Worster (2008) suggest that the channel spacing is proportional to the depth of the mushy layer. Meanwhile, the transient experiments of Tait and Jaupart (1992) found that the channel spacing was proportional to the mushy layer depth in some parameter regimes (in particular, when convection penetrated through the full depth of the mush), but could be independent of the mushy layer depth when channels were

confined to a fraction of the mushy layer near the mush-liquid boundary.

Wells et al. (2010) hypothesised that the system selects the channel spacing which maximises the dissipation of potential energy, which also results in convection cells with a width proportional to their height. Using the optimal hypothesis, Wells et al. (2013) studied convection for directional solidification of a mushy layer with a periodic array of channels, for a wide range of parameters. In particular they considered the mushy Rayleigh number, Rm, and the concentration ratio, $\mathscr{C}$, which characterises the size of typical solutal variations and is here defined by

$$\mathscr{C} = \frac{S_i - S_s}{\Delta S}. \tag{4.2}$$

Hence, $\mathscr{C} \geq 0$. In the limit $Rm \gg 1$ with $Rm/\mathscr{C} = O(1)$ and hence $\mathscr{C} \gg 1$, the flux of solute through the channels has been shown to scale linearly with the Rayleigh number in studies which considered either direct numerical simulations (Wells et al., 2013) or a semi-analytical model (Rees Jones and Worster, 2013). Both approaches seem consistent with experimental results for solute fluxes and flow from a growing layer of sea ice (Wells et al., 2011; Rees Jones and Worster, 2013, 2014) despite the fact that $\mathscr{C} \ll 1$ in the experiment. For $Rm \gg \mathscr{C}$, the numerical results of Wells et al. (2013) hint that the flux increases sublinearly with Rm which may have important implications for sea ice growth (Wettlaufer et al., 1997a), where often $\mathscr{C} \approx 0.15$ and $Rm = O(10)$.

As sea ice forms in the winter months, salty brine drains into the ocean through buoyancy driven convection with important consequences for the climate system (see Wells et al., 2019, for a review). Whilst a variety of 1-D parametrisations of this process have been developed for use in global circulation models (Turner et al., 2013; Rees Jones and Worster, 2014; Griewank and Notz, 2013), questions remain over the 2-D structure of convection in mushy layers with $Rm \gg \mathscr{C}$. In particular, linear stability analyses suggest that convection should be confined to a narrow permeable region at the interface between the mushy layer and the liquid (Worster, 1992b; Hwang, 2013; Hitchen, 2017), in contrast to the full depth convection seen by Wells et al. (2013) for $Rm/\mathscr{C} = O(1)$.

In this chapter, we will simulate a mushy layer undergoing directional solidification. Following Wells et al. (2013), we will consider steady state flow with a periodic array

of channels, where the channel spacing is determined by an optimal flux hypothesis (Wells et al., 2010). We will consider a wide range of $\mathscr{C}$ but focus on systems with $\mathscr{C} \ll 1$, complementing the parameter range explored by Wells et al. (2013). Within § 4.1 we will consider flow in a narrow Hele-Shaw cell, such that it is appropriate to model the flow using Darcy's law in both the mushy layer and pure liquid. We will then derive scaling laws for flow with $\mathscr{C} \ll 1$ which are consistent with both our numerical results and previous experimental results for transient ice growth. Meanwhile, in § 4.2 we will consider some of the differences that emerge when modelling flow using a Darcy-Brinkman equation. The key results from the chapter are summarised in § 4.3.

4.1 Mushy layer growth with Darcy flow

In this section we will consider directional solidification of a mushy layer in a narrow Hele-Shaw cell of dimensional depth $\mathcal{H}$. Formally, we assume that the dimensionless Hele-Shaw permeability $\Pi_c = d^2/(12K_0)$ where d is the dimensional gap width and K_0 is the reference permeability for the mushy layer, satisfies $\Pi_c Da \ll 1$ where $Da = K_0/\mathcal{H}^2$ is the Darcy number. In this limit, fluid flow in both porous regions (with porosity $\chi < 1$) and liquid regions (where $\chi = 1$) is well described by Darcy's law (3.6). Such a geometry is commonly used in experiments to obtain a quasi-two-dimensional system (e.g. Katz and Worster, 2008; Peppin et al., 2008; Middleton et al., 2016).

We consider directional solidification at a fixed rate V, and wish to work with the nondimensional form of our governing equations (§ 2.3) where we scaled lengths with the box depth $\mathcal{H}$. For consistency with previous studies, where the governing equations are typically nondimensionalised using scales based on the solidification rate (e.g. Wells et al., 2013), we choose $V = \kappa_l/\mathcal{H}$. Hence, the dimensionless solidification rate $V_f = V\mathcal{H}/\kappa_l = 1$. We also choose the reference point for nondimensionalising the temperature and salinity (c.f. (2.43)) to be their initial values $(S_r, T_r) = (S_i, T_i)$.

Consequently, our governing equations are

$$\mathbf{U} = -\Pi\left(\nabla p + Rm\,\Theta_l\right), \tag{4.3}$$

$$\nabla \cdot \boldsymbol{u} = 0, \tag{4.4}$$

$$\left(\frac{\partial}{\partial t} + V_f\frac{\partial}{\partial z}\right)(\theta + \mathscr{S}\chi) + \mathbf{U}\cdot\nabla\theta = \nabla^2\theta, \tag{4.5}$$

$$\left(\frac{\partial}{\partial t} + V_f\frac{\partial}{\partial z}\right)\left[\chi\Theta_l - \mathscr{C}\left(1-\chi\right)\right] + \mathbf{U}\cdot\nabla\Theta_l = \frac{1}{Le}\nabla\cdot\left(\chi\nabla\Theta_l\right), \tag{4.6}$$

whilst we recall that the dimensionless parameters (2.39) -(2.40) are given by

$$Rm = \frac{g\beta\Delta S K_0}{\nu V}, \quad \mathscr{C} = \frac{S_i - S_s}{S_e - S_i}, \quad \mathscr{S} = \frac{L}{c_p\Delta T}, \quad Le = \frac{\kappa_l}{D_s}. \tag{4.7}$$

Derivatives of the form $\partial/\partial t + V_f\partial/\partial z$ correspond to a material derivative following material moving at the unit dimensionless frame advection speed. We assume that the dimensionless permeability in the mushy layer is given by $\Pi_m = \chi^3$, which is consistent with observations of sea ice (Petrich and Eicken, 2010) and previous studies (Schulze and Worster, 1998; Chung and Worster, 2002; Wells et al., 2013). Drag on the front and rear faces of the narrow Hele-Shaw cell imposes a finite minimum permeability on the entire system, given by $\Pi_c = d^2/(12K_0)$ (c.f. Katz and Worster, 2008). In the simulations we present here, we assume that $\Pi = \min\left(\Pi_m, \Pi_c\right)$.

Given the condition of incompressibility (4.4), it is also useful to define a stream-function ψ by $\mathbf{U} = (-\partial\psi/\partial z, \partial\psi/\partial x)$ which obeys the vorticity equation,

$$\nabla^2\psi = -Rm\Pi\frac{\partial\Theta_l}{\partial x} - \left(\frac{\nabla\psi\cdot\nabla\Pi}{\Pi}\right), \tag{4.8}$$

which was obtained by dividing (4.3) by Π and taking the curl. We will use this alternative when considering scaling arguments.

4.1.0.1 Numerical method

Our domain is the rectangular box with boundary conditions illustrated in fig. 4.2a, with dimensionless width $\lambda = V\mathcal{L}/(2\kappa_l)$ and height $\eta = \mathcal{H}V/\kappa_l$. For all simulations, $\eta = 0.4$

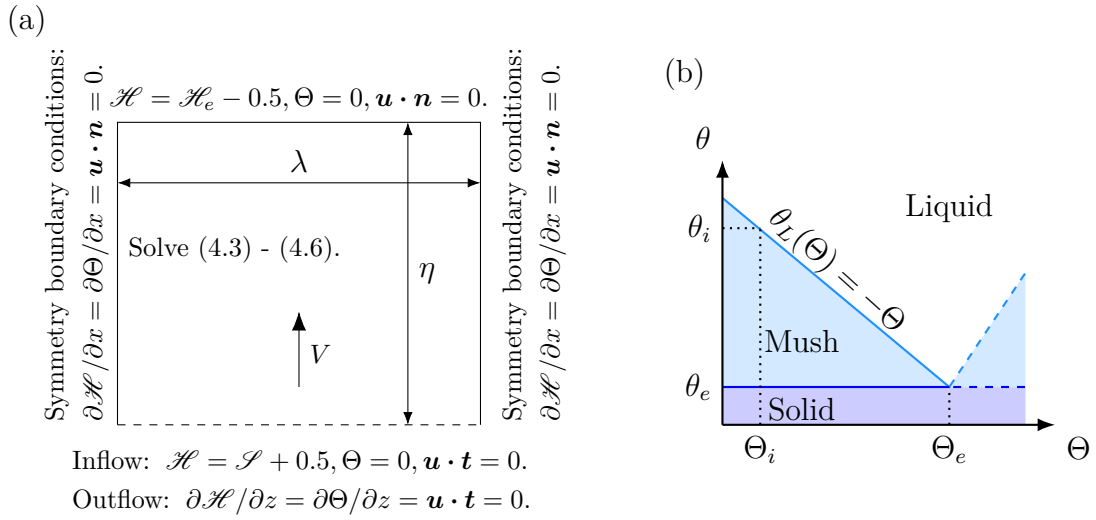


Figure 4.2: *(a)* Simulations are conducted in a rectangular box, with boundary conditions enforced through the dimensionless enthalpy $\mathscr{H} = \mathscr{S}\chi + \theta$ and bulk concentration $\Theta = \chi\Theta_l - \mathscr{C}(1-\chi)$ for liquid fraction χ. The Stefan number $\mathscr{S}$ and concentration ratio $\mathscr{C}$ are defined in the text. Symmetry conditions at the left and right boundaries enforce no horizontal flux of heat or solute, and no horizontal flow. The open bottom boundary permits flow in and out of the domain. *(b)* Idealised phase diagram for dimensionless temperature θ and concentration Θ. We consider systems below the eutectic concentration Θ_e, where the solid phase of the mushy-layer is composed of the solvent.

whilst λ is determined by an optimal flux criteria (see § 4.1.1 for more details). The solid upper boundary is held at $\theta = \theta_e - 0.5$, which is below the eutectic point θ_e ensuring the formation of a eutectic solid (with $\chi = 0$) at the top of the domain. An open bottom boundary allows for either inflow or outflow, where material entering the domain has a dimensionless temperature $\theta_i = 0.5$ and salinity $\Theta_i = 0$. Symmetry conditions on the left and right boundaries are consistent with the assumed periodic array of channels.

We use the enthalpy method described in chapter 3 for numerical computations. (4.3)-(4.6) are solved on a single domain including solid regions ($\chi = 0$), liquid regions ($\chi = 1$) and mushy regions ($0 < \chi < 1$), using the finite volume numerical scheme described in detail in chapter 3. Whilst the numerical method can be implemented on a hierarchy of adaptively refined grids, we found that for this problem a uniform mesh was sufficient and hence used here.

Simulations are initialised either from the analytic solution for solidification in the absence of flow (Worster, 1991), or continued from previous simulations with nearby parameters, and integrated in time until the temperature, solute concentration and

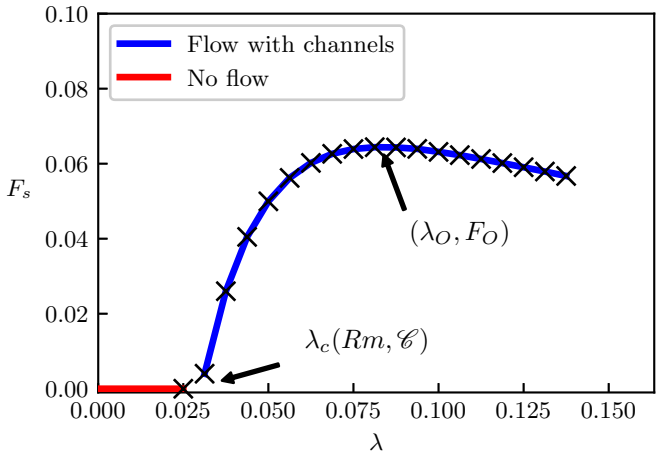


Figure 4.3: Variation of the numerically calculated vertical solute flux per unit width, F_s, with λ for $\mathscr{C} = 0.25, Rm = 250, Le = 200, \mathscr{S} = 5$ and $\Pi_c = 1$. For $\lambda > \lambda_c$, we find steady state solutions (black crosses) with convection through channel. For $\lambda < \lambda_c$, there is no flow for this set of parameters $(Rm, \mathscr{C})$. The optimal state (λ_O, F_O) is that which maximises the solute flux F_s.

Darcy velocity have reached a steady state according to the condition

$$\max \left| \left(\frac{\partial \theta}{\partial t}, \frac{\partial \Theta_l}{\partial t}, \frac{\partial \mathbf{U}}{\partial t} \right) \right| < 10^{-3}. \tag{4.9}$$

The timestep for integration Δt was chosen to obey a CFL condition; $\max|\mathbf{U}|\Delta t/\Delta x < 1$ where Δx is the grid spacing. All simulations use a uniform mesh with $\Delta x = \eta/256$. The accuracy of this resolution was checked by comparing against simulations conducted with $\Delta x = \eta/512$ for selected parameters. In all cases the deviation in the volume averaged enthalpy and bulk salinity fields is less than 1%.

4.1.1 Stability and bifurcation structure

We compute steady state solutions for $0.01 < \mathscr{C} < 20$ and a wide range of Rayleigh numbers Rm, whilst all other parameters ($\mathscr{S} = 5, Le = 200, \Pi_c = 1$) are fixed. For each set of parameters $(\mathscr{C}, Rm)$, we identify the so-called *optimal state* by varying the domain width to find the geometry which maximises the width-averaged solute flux,

$$F_s = \frac{1}{\lambda} \left| \int_0^\lambda \left\{ \left[(\mathbf{U} + \boldsymbol{k})\, \Theta_l - \frac{1}{Le} \nabla \Theta_l \right] \cdot \boldsymbol{n} \right\}_{z=0} dx \right|. \tag{4.10}$$

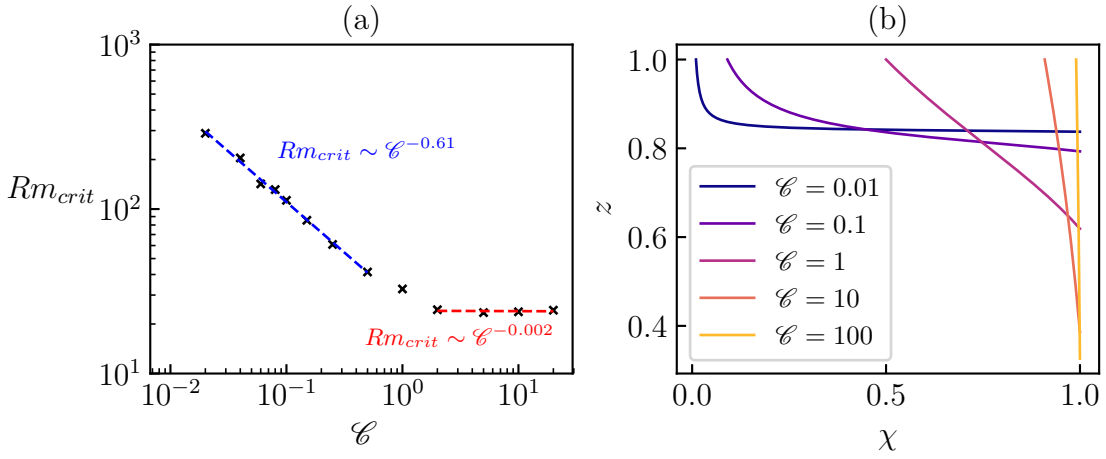


Figure 4.4: (a) variation of the critical Rayleigh number Rm_{crit} with the concentration ratio $\mathscr{C}$. To compute Rm_{crit}, I extrapolate from convecting states to find where the optimal solute flux $F_O(Rm)$ tends to zero for a given $\mathscr{C}$. For $\mathscr{C} \gtrsim 1$, the critical Rayleigh number is roughly independent of $\mathscr{C}$. A power law fit to the 4 data points with $\mathscr{C} > 1$ (red dashed line) reveals that $Rm_{crit} \sim \mathscr{C}^{-0.002 \pm 0.01}$ where the error is the 95% confidence interval. For $\mathscr{C} \lesssim 1$, the critical Rayleigh number increases with decreasing $\mathscr{C}$. A power law fit to the data points with $\mathscr{C} < 1$ (blue dashed line) finds $Rm_{crit} \sim \mathscr{C}^{-0.61 \pm 0.02}$. (b) Steady-state porosity $\chi(z)$ for directional solidification without flow from a eutectic boundary at $z = 0$, with a far field temperature $\theta(z = -\infty) = 0.5$, dimensionless parameters $\mathscr{S} = 5, V_f = 1, Le = \infty$ and various $\mathscr{C}$ (see legend). Profiles computed using the solution presented in Worster (1991).

In fig. 4.3 we plot the typical variation of F_s with the domain width λ for $\mathscr{C} = 0.25, Rm = 250$. The optimal flux at (λ_O, F_O) is computed by quadratic interpolation between the largest three computed states (black crosses), whilst the critical half-channel spacing λ_c where the flux $F_s \to 0$ is found by linear extrapolation from states with $F_s > 0$. We found a similar pattern of dependence of the flux F_s on λ for all the parameters considered in this study. In contrast to Wells et al. (2013), we do not observe an obvious saddle-node bifurcation during the transition from states without flow to those with flow. There are several differences between this model and the one considered by Wells et al. (2013) which may explain this difference. We solve for flow in the pure liquid, using Darcy's law, whilst Wells et al. (2013) used an asymptotically reduced description of flow in the pure fluid. We also consider the effects of solute diffusion, which was neglected by Wells et al. (2013).

States with convective flow only exist for Rayleigh numbers Rm above some critical value which varies with the concentration ratio, i.e. when $Rm > Rm_{crit}(\mathscr{C})$. Focussing on convective states carrying a non-trivial solute flux, I compute the critical Rayleigh

number $Rm_{crit}(\mathscr{C})$ by extrapolating backwards from states with flow (fluxes plotted in fig. 4.6) to find the point where the largest solute flux $F_O(Rm) \to 0$ for a given $\mathscr{C}$. This critical Rayleigh number is a nonlinear threshold, determined from finite amplitude calculations, in contrast to the critical thresholds found by linear or weakly nonlinear stability analyses. In fig. 4.4a I plot the variation of Rm_{crit} with $\mathscr{C}$. For $\mathscr{C} > 1$ the critical Rayleigh number is approximately independent of $\mathscr{C}$. This is confirmed by a power law fit (red dashed line) of the form $Rm_{crit} \sim \mathscr{C}^A$, which reveals that $A = -0.002 \pm 0.01$. For $\mathscr{C} < 1$ the critical Rayleigh number increases as $\mathscr{C}$ decreases. The trend is well described by a power law fit (blue line) where we find an exponent $A = 0.61 \pm 0.02$.

Previously, linear stability analyses have also found that the critical Rayleigh number increases as $\mathscr{C}$ decreases in a variety of settings (Worster, 1992b; Hwang, 2013; Hitchen, 2017). To understand this behaviour it can be helpful to consider a local Rayleigh number given by

$$Rm_l(z) = Rm \ |\Theta_l(z) - \Theta_l(z_{ml})| \, (z - z_{ml}) \bar{\chi}(z)^3, \tag{4.11}$$

(e.g. Aussillous et al., 2006; Notz and Worster, 2008) where z_{ml} is the vertical position of the mush-liquid interface. We have here scaled the global Rayleigh number Rm to account for the relevant local length scale $z - z_{ml}$ corresponding to distance above the mush-liquid interface, buoyancy scale $\Theta_l(z) - \Theta_l(z_{ml})$ and permeability, which varies with the porosity scale $\bar{\chi}(z)$. Convection can only occur within the mushy layer where this local Rayleigh number exceeds some critical value, $Rm_l(z) > Rm^*$. Hence, differences in the local structure of the mushy layer will affect the critical global Rayleigh number Rm_{crit} required for convection according to

$$Rm_{crit} \sim \frac{Rm^*}{|\Theta_l(z_{max}) - \Theta_l(z_{ml})| \, (z_{max} - z_{ml}) \bar{\chi}(z_{max})^3}, \tag{4.12}$$

where z_{max} is the maximum depth at which convection is possible. In fig. 4.4b I plot the steady-state porosity in a mushy layer undergoing directional solidification without flow (i.e. $Rm = 0$) for a range of $\mathscr{C}$ which span the values considered in our simulations.

When $\mathscr{C}$ is large ($\mathscr{C} \gg 1$), the porosity is high throughout the mushy layer $\chi \approx 1$ and convection can penetrate through the full depth of the mushy layer. Hence the buoyancy factor $|\Theta_l(z_{max}) - \Theta_l(z_{ml})|$ is simply the difference between the eutectic salinity and initial salinity $|\Theta_e - \Theta_i| = 1$. In this limit, from (4.12) we would expect to find that the critical global Rayleigh number varies like

$$Rm_{crit} \sim \frac{Rm^*}{h}, \tag{4.13}$$

where h is the dimensionless mushy layer depth. Worster (1991) demonstrated that h tends towards a constant value as $\mathscr{C} \to \infty$, which is consistent with the observed variation of Rm_{crit} with $\mathscr{C}$ in fig. 4.4a. Hitchen (2017) also found that Rm_{crit} tends towards a constant value as $\mathscr{C} \to \infty$ in a linear stability analysis for transient mushy layer growth. Where we find $Rm_{crit}(\mathscr{C} \to \infty) \approx 24$, Hitchen (2017) found $Rm_{crit}(\mathscr{C} \to \infty) \approx 49$ which is of the same order of magnitude. The differences between the two studies, which may explain the difference in quantitative results, will be discussed later.

When $\mathscr{C}$ is small ($\mathscr{C} \ll 1$), the porosity within the mushy layer becomes small except for a narrow porous layer near the mush-liquid interface. Further decreasing $\mathscr{C}$ reduces the depth of this high porosity region. For transient growth, Hitchen (2017) found using a linear stability analysis that convection would be confined to this narrow region, such that $z_{max} - z_{ml} \ll \hat{h}$. In this case, assuming a linear temperature and liquid salinity profile through the mushy layer, the difference in liquid salinity across the confined region is proportional to $z_{max} - z_{ml}$. Hence, noting that $\chi \approx 1$ within this narrow porous layer, the critical global Rayleigh number varies like

$$Rm_{crit} \sim \frac{Rm^*}{(z_{max} - z_{ml})^2}. \tag{4.14}$$

As $\mathscr{C}$ decreases, so too does $z_{max} - z_{ml}$ and consequently Rm_{crit} increases. For linear stability during transient growth Hitchen (2017) found that $z_{max} - z_{ml} \sim \mathscr{C}$, and therefore $Rm_{crit} \sim \mathscr{C}^{-2}$ for $\mathscr{C} \ll 1$. For linear stability during directional solidification, Worster (1992b) did not report a particular scaling for Rm_{crit}, but the data presented in their figure 9(c) is suggestive of a scaling $Rm_{crit} \sim \mathscr{C}^a$ where $a < -1$ for $\mathscr{C} \ll 1$. Here we

find a weaker exponent than these previous results: $Rm_{crit} \sim \mathscr{C}^{-0.61\pm0.02}$. The origin of our scaling is not clear, and would be an interesting question for future work to consider.

The weaker dependence of Rm_{crit} on $\mathscr{C}$ that we find may be due to our use of fully nonlinear simulations, whilst both Hitchen (2017) and Worster (1992b) used linear stability analyses. As channels form, they dissolve the solid matrix which increases the local porosity. This provides a positive feedback which aids the development of convection but is not captured by linear stability analyses (Worster, 1997). Hence we might expect to find a lower critical Rayleigh number here than in Hitchen (2017) and Worster (1992b). There are also notable differences between the geometry considered. Here we simulate flow in a box of fixed depth, with no constraints on the flow at the mush-liquid boundary. Meanwhile linear stability analyses consider a semi-infinite domain with a flat mush-liquid boundary where the flow is purely vertical (either enforced by a constant pressure condition, e.g. Hitchen (2017), or a no-slip condition, e.g. Worster (1992b)). With Darcy's law (eq. 4.3), the constant pressure condition is equivalent to enforcing no horizontal flow at the flat mush-liquid boundary. It may be that these differences also contribute to the different stability conditions found here in comparison to previous linear stability analyses.

4.1.2 Convection in the optimal state

For steady states with convective flow, the dynamics are strongly dependent on $\mathscr{C}$ and Rm as illustrated in fig. 4.5. In all cases (*a*-*d*), the cold upper boundary results in the formation of a layer of impermeable eutectic solid ($\chi = 0$) at the top of the domain. Below this, a mushy layer forms whose porosity increases with the concentration ratio $\mathscr{C}$. When $\mathscr{C} \gtrsim O(1)$ (panels *b*-*d*), the porosity is sufficiently high that significant convection may penetrate throughout the entire mushy layer. For smaller $\mathscr{C}$, the decrease in porosity with $\mathscr{C}$ reduces the flow strength and confines convection to the region of higher porosity near the mush-liquid interface. We can see this from the streamlines in fig. 4.5, which are logarithmically spaced whilst the arrowed contour, which corresponds to $\psi = 10^{-2}$, is closer to the mush-liquid interface in (a) illustrating the confinement of convection. The existence of a liquid channel depends on sufficiently strong downwelling, and therefore the channel depth is also confined to the high porosity region. Increasing

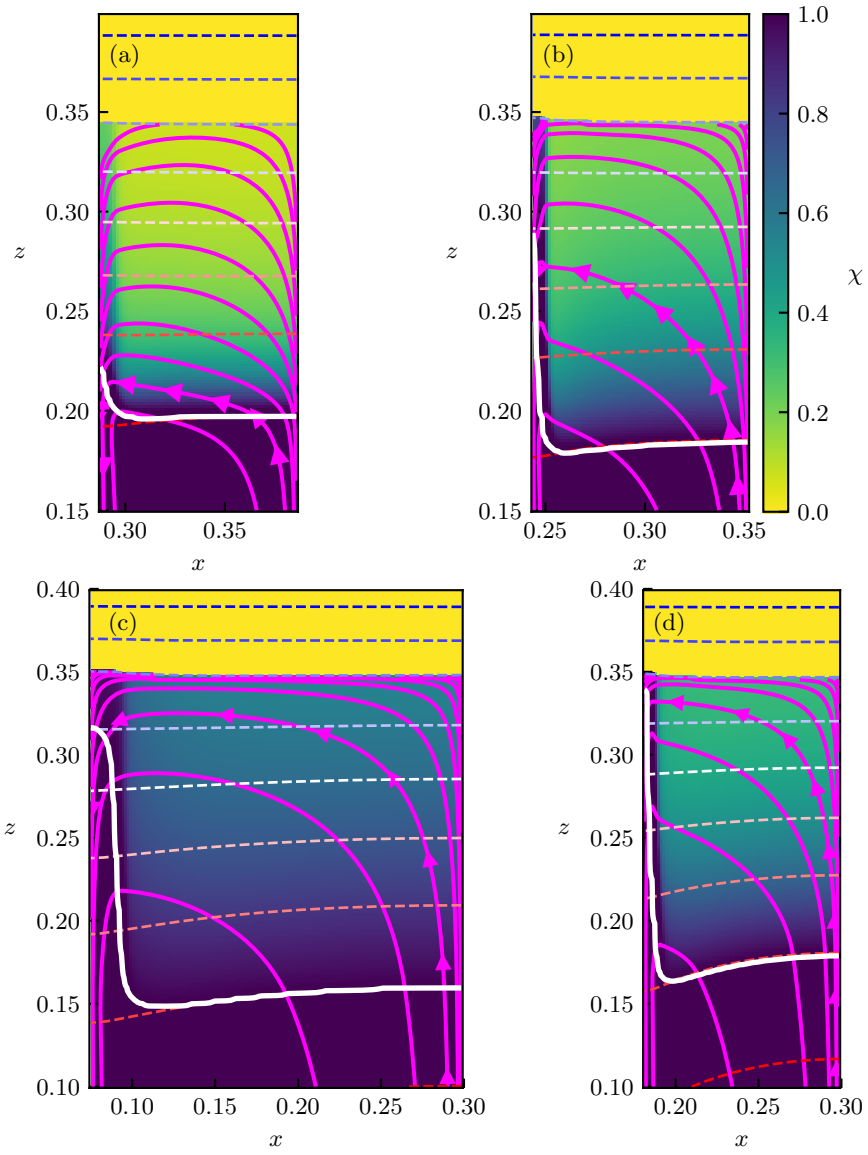


Figure 4.5: Porosity χ (color), streamlines of Darcy velocity $\mathbf{U}$ (magenta, logarithmically spaced according to $\psi = 10^m$, $m = -6, -5.5, -5, ..., 1$; the $m = -2$ contour includes arrows indicating the direction of flow), temperature (dashed contours, $\theta = -0.4 + 0.2n$, $n = 0, 1, 2...$) and mush-liquid interface (white) for the optimal states computed with (a) $\mathscr{C} = 0.1, Rm = 200$, (b) $\mathscr{C} = 0.5, Rm = 200$, (c) $\mathscr{C} = 2.0, Rm = 45$ and (d) $\mathscr{C} = 2.0, Rm = 200$. Only the top section of the domain (full depth $\eta = 0.4$) is shown in each panel; note that the $z-$axis is different between panels (a-b) and (c-d).

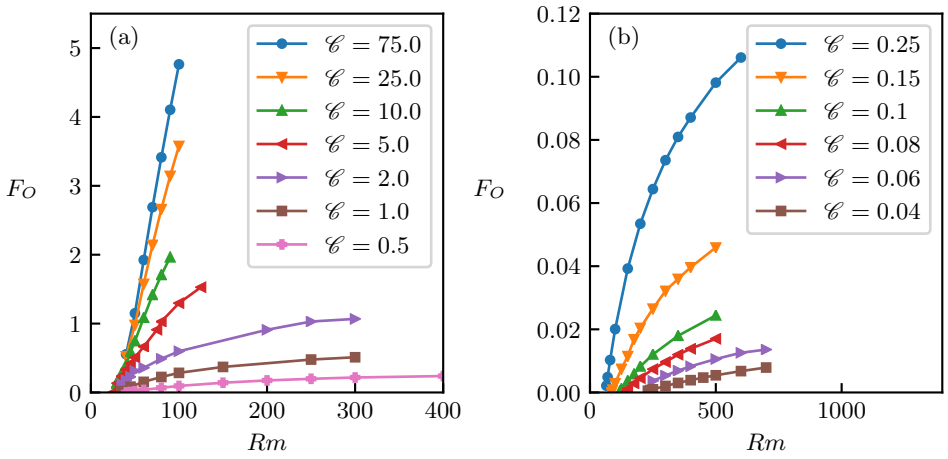


Figure 4.6: Variation of the optimal flux F_O with the mushy Rayleigh number Rm and concentration ratio $\mathscr{C}$. Due to the variation of F_O with $\mathscr{C}$, we split the data over two figures with different $y-$axes: in (a) we plot $\mathscr{C} \geq 0.5$, and in (b) we plot $\mathscr{C} < 0.5$

the Rayleigh number results in a stronger flow through channels, which have a closer optimal channel spacing, as illustrated in the difference between panels *(c)* and *(d)*. As the strength of convection increases, so too does the transport of solute out of the mushy layer which results in increased internal solidification and a reduction in the porosity.

The solute flux F_s between the mushy layer and the underlying liquid is dependent on both the strength of convection and the availability of solute. When the concentration ratio is large ($\mathscr{C} \gg 1$), the initial solute concentration is large and relatively close to the eutectic (c.f. (4.7)). Conversely, when $\mathscr{C} \ll 1$ the initial solute concentration is low and closer to the solid concentration. Consequently, increasing $\mathscr{C}$ results in an increased solute flux as illustrated in fig. 4.6. This behaviour is reinforced by the dependence of the porosity on $\mathscr{C}$: when $\mathscr{C} \gg 1$ the abundance of solute results in a highly porous mushy-layer, permitting a stronger flow. In contrast, when $\mathscr{C} \ll 1$ the porosity is low and the fluid flow is weak - reducing the solute flux. The flow strength is also strongly controlled by the mushy Rayleigh number Rm, which characterises the strength of buoyancy relative to dissipative forces. When $\mathscr{C}$ is sufficiently large relative to Rm – specifically, when $Rm/\mathscr{C} = O(1)$ – the solute flux increases linearly with Rm as described by Wells et al. (2013). When $Rm \gg \mathscr{C}$, the porosity of the mushy layer is significantly reduced by the removal of solute due to the fluid flow and consequently the solute flux increases sub-linearly, rather than linearly, with Rm. I develop scaling arguments below to characterise this dependence focussing on the limit $\mathscr{C} \ll 1$.

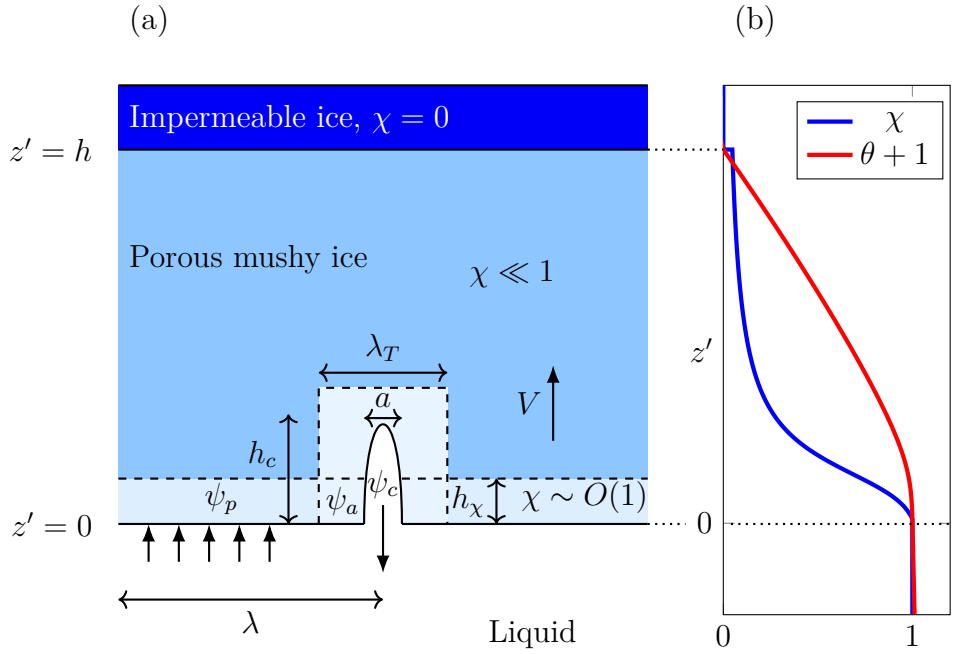


Figure 4.7: (a) Schematic illustrating the different dynamical regions during confined convection. Sinking fluid establishes a narrow liquid channel where the flow with streamfunction scale ψ_c is relatively large, whilst a weak return flow with scale ψ_p rises buoyantly through the mushy layer. The extraction of solute by this flow enhances the tendency for solidification leading to a narrower high porosity zone of depth h_χ. Horizontal flow is relatively strong adjacent to the channel (streamfunction scale ψ_a), removing solute from the mushy layer into the channel. (b) Diffusive solution (Worster, 1991) for $\mathscr{C} = 0.05, \mathscr{S} = 5, Le = \infty$. The temperature θ increases roughly linearly through the mushy layer except for very close to the mush-liquid interface, whilst the porosity decreases rapidly within a narrow region at base of the mushy layer.

4.1.3 Scalings for small concentration ratio

Having described qualitatively how the optimal states for convective flow depend on the concentration ratio and mushy Rayleigh number, we will now develop a set of self-consistent scaling arguments for convection with $\mathscr{C} \ll 1$. We will first explain our arguments qualitatively, then describe how the governing equations behave in distinct regions of the mushy layer before finally demonstrating that our theory agrees well with our numerical calculations. To aid our explanation below, we use an idealised illustration of our scalings (fig. 4.7) and transects through the numerically calculated optimal states (fig. 4.8).

We consider the limit $\mathscr{C} \ll 1, \mathscr{S} \gg 1, Le \gg 1$ and define the vertical co-ordinate $z' = z - z_{ml}$ where z_{ml} is the median height of the mush-liquid interface. In the absence of flow ($Rm = 0$) the solution to the mushy-layer equations (4.3) - (4.6) is given by

Worster (1991) and illustrated in fig. 4.7b. The porosity and permeability drop rapidly from 1 at the mush-liquid boundary to almost 0 in the interior of the mushy layer (see also fig. 4.8a). We assume that the region of high porosity near the mush-liquid interface is characterised by a depth h_χ except for the thermal boundary layer close to the channel, which depth of order h_c. Deeper into the mushy layer we assume that the flow is weak, so the temperature and porosity fields are well approximated by the diffusive solution illustrated in fig. 4.7b. Assuming that the high porosity region is small relative to the full depth of the mushy layer, $h_\chi, h_c \ll h$, the mushy layer depth h will be set by the diffusive solution. Within the narrow channel of width a and depth h_c and immediately adjacent mushy layer there is significant baroclinic torque which drives convection (fig. 4.8d). Flow within the rest of the mushy layer is controlled by the pressure drop across a thermal boundary layer of width λ_T, and is weak except in the narrow highly permeable region of height h_χ near the mush-liquid boundary. As solute is removed by the flow (c.f. the reduction in the bulk salinity with increasing Rm in fig. 4.8b), the mushy layer will become less porous and hence the depth h_χ of the high porosity layer will decrease. This reduction in h_χ can be inferred from fig. 4.8a, where we see that the permeability decreases with increasing in Rm (and decreasing $\mathscr{C}$), meaning that the region of mushy layer with high permeability (and hence high porosity) also decreases. The width of the convection cell shrinks as the flow strength increases. The picture of an active region around the channel within which baroclinic torque drives flow within the rest of the mushy layer is similar to the Chimney-Active-Passive model developed by Rees Jones and Worster (2013). Here we also consider the effect on the flow of a porosity field with significant vertical variation so that the passive region here has depth h_χ rather than the full depth of the mush as considered by Rees Jones and Worster (2013).

4.1.3.1 Scaling of the governing equations

We now scale the governing equations (4.3) - (4.6) within the different regions of the mushy layer. Variables will acquire different scales in different regions of the

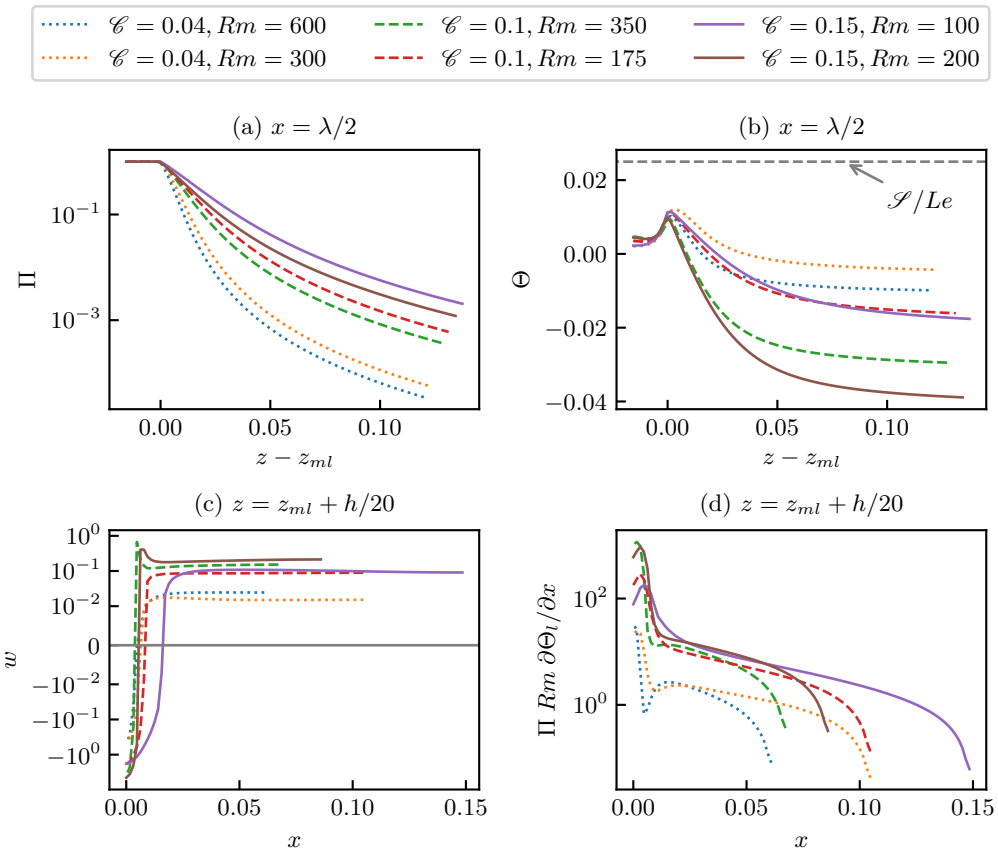


Figure 4.8: Transects through the numerically computed optimal states. (a-b): vertical transects at the mid-point of the convection cell of (a) permeability and (b) bulk solute concentration. In (b) we illustrate the order of magnitude of the bulk salinity at the mush–liquid interface $\bar{\Theta}_{ml} \sim \mathscr{S}/Le$ predicted by our scalings (grey line). (c-d): horizontal transects at a depth $z = h/20$ above the mush–liquid interface of (c) vertical velocity and (d) vorticity generation. Note that in (c-d) the states have been orientated such that the channel is at $x = 0$, and in (c) the w axis is linear between -10^{-2} and 10^{-2} but otherwise logarithmic whilst the grey line indicates where $w = 0$. For each $\mathscr{C}$ we plot two different values of Rm which differ by a factor of 2. The absolute values of Rm are different in each case to partially compensate the critical Rayleigh number decreasing with increasing $\mathscr{C}$.

domain, as summarised by

$$x = (\lambda, \lambda_T, a)\,\tilde{x}; \quad z = (h, h_c, h_\chi)\,\tilde{z}; \quad \psi \sim (\bar{\psi}_c, \bar{\psi}_a, \bar{\psi}_p)\tilde{\psi}; \quad \theta \sim \bar{\theta}\tilde{\theta}; \tag{4.15}$$

$$\Theta \sim (\bar{\Theta}, \bar{\Theta}_c, \bar{\Theta}_{ml})\tilde{\Theta}; \quad \Theta_l \sim \bar{\Theta}_l\tilde{\Theta}_l; u = (\bar{u}_c, \bar{u}_T, \bar{u}_p)\tilde{u}; w = (\bar{w}_c, \bar{w}_T, \bar{w}_p)\tilde{w}; \tag{4.16}$$

$$\chi \sim \begin{cases} 1 & \text{near the mush liquid boundary} \\ \bar{\chi}\tilde{\chi} & \text{in the interior of the mushy layer,} \end{cases} \quad \text{whilst } \Pi \sim \chi^3, \tag{4.17}$$

where quantities with a tilde ($\tilde{.}$) are $O(1)$, and the quantities in brackets are sets of scales to be determined which are valid in different regions. Where it is helpful, these

scales are denoted by an overbar ($\bar{.}$) to distinguish them from the $O(1)$ quantities.

4.1.3.2 Thermodynamics

We start by assuming that, in the limit $\mathscr{C} \ll 1$, the convection is weak and therefore the dynamical balances are approximately the same as in the case without flow (Worster, 1991). In particular, we assume that the temperature (and hence, by the liquidus constraint, the liquid concentration) are approximately linear functions of z:

$$\Theta_l = -\theta \approx z'/h, \tag{4.18}$$

(c.f. fig. 4.7b). Meanwhile, the vertical thermal balance (4.5) across the entire mushy layer is dominated by diffusive effects and the release of latent heat, which sets the total height h,

$$\frac{1}{h^2}\frac{\partial^2\tilde{\theta}}{\partial\tilde{z}^2} \sim \mathscr{S}\, V_f\, \frac{1}{h}\frac{\partial\tilde{\chi}}{\partial\tilde{z}} \implies h = O\left(\frac{1}{\mathscr{S}\, V_f}\right). \tag{4.19}$$

where we have noted that θ and χ vary by 1 across the depth of the mushy layer. In the mushy layer, the porosity is given by

$$\chi = \frac{\mathscr{C} + \Theta}{\mathscr{C} + \Theta_l} \approx \frac{\mathscr{C} + \Theta}{\mathscr{C} + z'/h}, \tag{4.20}$$

where we have used (4.18) to approximate the liquid concentration Θ_l and the bulk concentration Θ in principle varies spatially. The porosity varies from 1 at the mush-liquid boundary to some value $\bar{\chi}$ in the interior of the mushy layer. Assuming that the solute concentration in the interior is well approximated by the diffusive solution to the problem (Worster, 1991), $\Theta = 0$ and $\Theta_l \sim O(1)$ so the interior porosity is given by $\bar{\chi} \sim \mathscr{C}$ and the porosity drops to this value once $z' \gg \mathscr{C}h$. This neglects the change in the bulk concentration Θ due to the flow, but the assumption holds as long as $\Theta = O(\mathscr{C})$ following convective desalination. Assuming that the channel can penetrate through most of the depth of this high porosity region, we therefore

determine the depth of the high porosity region around the channel

$$h_c \sim \mathscr{C} h, \tag{4.21}$$

where $\chi = O(1)$.

4.1.3.3 Channel

Channels are entirely liquid, with $\chi = 1$. We assume that the channel height is constrained by the confinement depth h_c, and is much larger than the channel width a. Hence we can approximate $\nabla^2 \approx (\partial/\partial x)^2$ in and immediately adjacent to the channel. Flow in the channel is driven by baroclinic torque due to variations in salinity, whilst the salinity in the channel is set by the fluid entering the channel from the adjacent mushy layer. At the top of the channel $\Theta_l \sim \mathscr{C}$ from (4.18) and (4.21), which sets the salinity scale driving flow in the channel; $\Theta_c \sim \mathscr{C}$. The vorticity equation (4.8) then scales like

$$\frac{\bar{\psi}_c}{a^2}\frac{\partial^2\tilde{\psi}}{\partial\tilde{x}^2} \sim Rm\frac{\bar{\Theta}_c}{a}\frac{\partial\tilde{\Theta}}{\partial\tilde{x}} \implies \bar{\psi}_c \sim a\,Rm\,\bar{\Theta}_c. \tag{4.22}$$

Horizontal salinity gradients can be large in the narrow channels, leading to significant salt diffusion which will balance the advection of salt into the channel according to

$$\frac{\bar{\psi}_c\bar{\Theta}_c}{ah_c}\tilde{\mathbf{U}}\cdot\tilde{\nabla}\tilde{\Theta} \sim \frac{\bar{\Theta}_c}{a^2 Le}\frac{\partial^2\tilde{\Theta}}{\partial\tilde{x}^2} \implies a \sim \frac{h_c}{\bar{\psi}_c Le}. \tag{4.23}$$

From (4.19) and (4.21) - (4.23) we find scales for the channel width a and the streamfunction $\bar{\psi}$,

$$a \sim \frac{1}{\sqrt{Rm\,Le\,\mathscr{S}\,V_f}}; \quad \bar{\psi}_c \sim \mathscr{C}\sqrt{\frac{Rm}{Le\,\mathscr{S}\,V_f}}. \tag{4.24}$$

The flow in the channel $\mathbf{U}_c = (u_c, w_c)$ will have horizontal and vertical components which scale like

$$\bar{u}_c \sim \frac{\bar{\psi}_c}{h_c} \sim \sqrt{\frac{Rm\,\mathscr{S}\,V_f}{Le}}; \qquad \bar{w}_c \sim \frac{\bar{\psi}_c}{a} \sim \mathscr{C}\,Rm. \tag{4.25}$$

4.1.3.4 Thermal boundary layer

Whilst the dominant thermal balance in the interior of the mushy layer is vertical, as described by (4.19), the channel introduces notable heterogeneity in the horizontal direction. A thermal boundary layer with width λ_T surrounds the channel, due to a balance between horizontal diffusion of heat and fluid advection. The mass flux through this boundary layer must balance the outflow through the channel so that $\psi \sim \bar{\psi}_c$, and therefore

$$\frac{\bar{\theta}}{\lambda_T^2}\frac{\partial^2\tilde{\theta}}{\partial\tilde{x}^2} \sim \frac{\bar{\psi}_c\bar{\theta}}{\lambda_T\, h_c}\tilde{\mathbf{U}}\cdot\tilde{\nabla}\tilde{\theta} \implies \lambda_T \sim O\left(\frac{h_c}{\bar{\psi}_c}\right) \sim \left(\frac{Le}{Rm\mathscr{S}V_f}\right)^{1/2}. \tag{4.26}$$

The resulting thermal gradient and local thermodynamic equilibrium leads to compositional gradients which provide a baroclinic torque to drive flow in the active region (§ 4.1.3.6).

4.1.3.5 Passive region

Flow through the rest of the mushy layer is driven by the pressure drop established in the thermal boundary layer, where the horizontal velocity scales like $\bar{u}_T \sim \bar{\psi}_c/h_c$. Hence

$$\Delta p_T \sim \frac{\partial p}{\partial x}\Delta x \sim \bar{u}_T\lambda_T \sim O(1), \tag{4.27}$$

where the second step invokes Darcy's law (4.3) with $\Pi = O(1)$. Horizontal flow in the interior of the mushy layer is generally very weak as the permeability is small; $\Pi = O(\mathscr{C}^3) \ll 1$ in the interior of the mushy layer where $\chi = O(\mathscr{C})$. However there exists a high porosity region near the mush-liquid boundary of depth h_χ where $\Pi \sim O(1)$ and therefore

$$u_p = -\Pi\frac{\partial p}{\partial x} \implies \bar{u}_p \sim \frac{\Delta p_T}{\lambda} \sim \frac{1}{\lambda}, \tag{4.28}$$

where we assume the width of this region scales with the chimney half-spacing λ. Integrating $-\partial\psi/\partial z \sim u$, the mass flux through the passive region will then scale like

$$\bar{\psi_p} \sim \bar{u}_p h_\chi \sim \frac{h_\chi}{\lambda}. \tag{4.29}$$

where (4.28) is used in the latter step. Within this region solute transport due to the flow will either be balanced by diffusion or frame advection depending on the size of the dimensionless group $\mathscr{C}Le/\mathscr{S}$. We here consider the limit where $\mathscr{C}Le \gtrsim \mathscr{S}$, in which case advection by the flow balances frame advection. Then the solute equation scales like

$$\frac{\mathscr{C}}{h_\chi}\frac{\partial\tilde{\Theta}}{\partial\tilde{z}'} \sim \frac{\bar{\psi}_p}{\lambda\, h}\tilde{\mathbf{U}}\cdot\tilde{\nabla}\tilde{\Theta}_l \implies h_\chi \sim O\left(\frac{\mathscr{C}h\lambda}{\bar{\psi}_p}\right), \tag{4.30}$$

where we approximated $\mathbf{U}\cdot\nabla\Theta_l \approx w\frac{\partial\Theta_l}{\partial z}$, have used the liquidus constraint and background temperature gradient to note that $\partial\Theta_l/\partial z \sim 1/h$, and have assumed that the change in bulk salinity across this region scales like $\Delta\Theta \sim \mathscr{C}\Delta\chi$, with $\Delta\chi \sim O(1)$.

4.1.3.6 Active region

At the intersection of the high porosity layer near the mush-liquid interface and thermal boundary layer, there exists an active region with height h_χ and width λ_T where flow is driven by baroclinic torque (region with $\psi \sim \psi_a$ in fig. 4.7a). Assuming that $h_\chi \lesssim \lambda_T$ in this region, the vorticity equation scales like

$$\frac{\bar{\psi}_a}{h_\chi^2}\frac{\partial^2\tilde{\psi}}{\partial\tilde{z}^2} \sim \frac{Rm\, h_\chi/h}{\lambda_T}\frac{\partial\tilde{\Theta}_l}{\partial\tilde{x}}, \tag{4.31}$$

where we use (4.18) to set the scale for Θ_l. To close the model, we note that the mass flux through the channel is given by the sum of the flux entering the mushy layer through the active and passive regions, $\psi_c \sim \psi_a + \psi_p$. If the mass flux through the active region is much larger than that through the passive region, $\psi_a \gg \psi_p$, and $\psi_a \sim \psi_c$. Similarly, if $\psi_a = O(\psi_p)$ then $\psi_a \sim \psi_c$. Hence, from (4.31),

$$h_\chi \sim \left(\frac{\lambda_T\,\bar{\psi}_c\, h}{Rm}\right)^{1/3} \sim \left(\frac{\mathscr{C}}{Rm\,(\mathscr{S}\,V_f)^2}\right)^{1/3}, \tag{4.32}$$

where we use (4.21) and (4.26) in the latter scaling.

4.1.3.7 Summary

Combining (4.29) and (4.30) we find scalings for λ and ψ_p. In summary, using (4.19), (4.21), (4.24), (4.26), (4.29), (4.30), and (4.32), we find the following scales

$$
\begin{aligned}
&h \sim O\left(\frac{1}{\mathscr{S} V_f}\right), \quad h_c \sim O\left(\frac{\mathscr{C}}{\mathscr{S} V_f}\right), \quad h_\chi \sim \left(\frac{\mathscr{C}}{Rm\,(\mathscr{S} V_f)^2}\right)^{1/3}, \\
&\lambda \sim O\left(\frac{1}{(\mathscr{C}\,\mathscr{S} V_f)^{1/6} Rm^{1/3}}\right), \quad \lambda_T \sim \left(\frac{Le}{Rm\,\mathscr{S} V_f}\right)^{1/2}, \quad a \sim \frac{1}{\sqrt{Rm\,Le\,\mathscr{S} V_f}}; \\
&\bar{\psi}_c \sim \mathscr{C}\sqrt{\frac{Rm}{Le\,\mathscr{S} V_f}}, \quad \bar{\psi}_p \sim O\left(\sqrt{\frac{\mathscr{C}}{\mathscr{S} V_f}}\right).
\end{aligned} \tag{4.33}
$$

4.1.3.8 Self consistency

To derive the scalings in (4.33) we made a number of assumptions regarding the relative sizes of these scales. For these assumptions to be self-consistent, we require the following balances to hold:

$$\frac{a}{\lambda_T} \lesssim 1 \implies \frac{1}{Le} \lesssim 1, \tag{4.34}$$

$$\frac{\lambda_T}{\lambda} \lesssim O(1) \implies \left[\left(\frac{\mathscr{C}\,Le}{\mathscr{S} V_f}\right)^2 \frac{Le}{\mathscr{C}\,Rm}\right]^{1/6} \lesssim O(1), \tag{4.35}$$

$$\frac{h_\chi}{\lambda_T} \lesssim 1 \implies \left[\left(\frac{\mathscr{C}\,Le}{\mathscr{S} V_f}\right)\frac{\mathscr{C}\,Rm}{Le^4}\right]^{1/6} \lesssim 1, \tag{4.36}$$

$$\frac{h_c}{h} \lesssim 1 \implies \mathscr{C} \lesssim 1, \tag{4.37}$$

$$\frac{h_\chi}{h} \lesssim 1 \implies \left(\frac{\mathscr{C}^2\,\mathscr{S} V_f}{\mathscr{C}\,Rm}\right)^{1/3} \lesssim 1, \tag{4.38}$$

$$\frac{\psi_p}{\psi_a} \lesssim 1 \implies \left(\frac{Le}{\mathscr{C}\,Rm}\right)^{1/2} \lesssim 1, \text{ not satisfied unless } \mathscr{C}\,Rm \gtrsim Le. \tag{4.39}$$

Recalling that we are considering the limit $\mathscr{C} \ll 1$, $Rm, Le, \mathscr{S} \gg 1$ with $\mathscr{C}Le/\mathscr{S} \gtrsim 1$, whilst noting that we require $Rm \gtrsim 1/\mathscr{C}$ for the system to be unstable, we find that (4.34), (4.36), (4.37) and (4.38) are well satisfied for all parameters considered. The second balance (4.35) is well satisfied for states with strong flow (large Rm) but may

break down for states only just above the threshold for the onset of convection where the thermal boundary layer width λ_T becomes large relative to the predicted channel half-spacing λ. The final balance (4.39) is only satisfied if $Rm \gtrsim Le/\mathscr{C}$, so again may break down for states which are marginally stable where the mass flux through the passive region ψ_p may be larger than the mass flux through the active region ψ_a.

4.1.3.9 Solute flux

Solute exits the mushy layer through the channel into the underlying liquid, so we can calculate the horizontally averaged flux by integrating over the flow out of the base of the channel where $\partial/\partial x \sim 1/a$. The salinity of fluid leaving the channel is set by the salinity at the mush liquid interface, where we integrate (4.6) over a weak solutal boundary layer from $z = -\infty$ to the mush liquid boundary z_{ml},

$$\frac{1}{Le}\int_{-\infty}^{z_{ml}} \frac{\partial^2 \Theta_l}{\partial z^2} dz \sim V_f \int_{-\infty}^{z_{ml}} \frac{\partial \Theta}{\partial z} dz, \tag{4.40}$$

$$\frac{1}{Le}\left[\frac{\partial \Theta_l}{\partial z}\right]_{-\infty}^{z_{ml}} \sim V_f \left[\Theta\right]_{-\infty}^{z_{ml}}. \tag{4.41}$$

Assuming that $\partial\Theta_l/\partial z = \Theta = 0$ at $z = -\infty$ (c.f. fig. 4.7b) and $\partial\Theta_l/\partial z \sim 1/h \sim \mathscr{S} V_f$ at z_{ml} from (4.18) and (4.19), this yields

$$\bar{\Theta}_{ml} \sim O\left(\frac{\mathscr{S}}{V_f\, Le}\right), \tag{4.42}$$

In fig. 4.8b we demonstrate that the observed bulk salinity at the mush-liquid interface $\bar{\Theta}_{ml}$ is indeed $O(\mathscr{S}/Le)$ in order of magnitude (noting that $V_f = 1$). Hence, the width-averaged flux out of half a convective cell is

$$F_O = \frac{1}{\lambda}\int_0^a w_c\, \Theta\, dx \sim \frac{\bar{\psi_c}\bar{\Theta}_{ml}}{\lambda}, \tag{4.43}$$

$$\sim \frac{\mathscr{C}^{7/6}\, Rm^{5/6}\mathscr{S}^{2/3}}{Le^{3/2} V_f^{1/3}}. \tag{4.44}$$

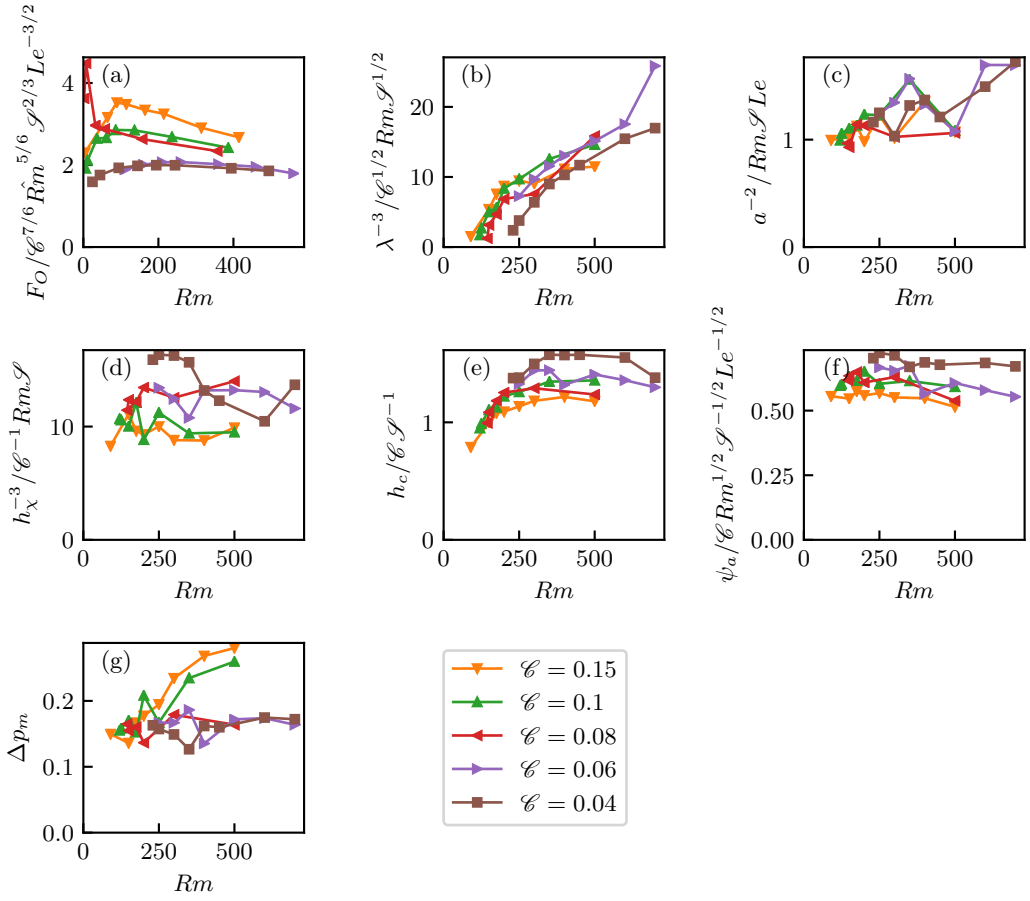


Figure 4.9: Comparison of predicted scalings with numerical results for $\mathscr{S} = 5, Le = 200, V_f = 1$ whilst Rm and $\mathscr{C}$ are varied. The scalings are derived for $\mathscr{C} \ll 1$, so we plot the states with small $\mathscr{C}$. The flux F_O (a) is scaled relative to $\hat{Rm} = Rm - Rm_{crit}$ where Rm_{crit} is the numerically determine critical Rayleigh number for a given $\mathscr{C}$, as this metric tends towards 0 as $Rm \to Rm_{crit}$. Note that $V_f = 1$ is omitted from the axis labels for clarity. See the text for details of how we calculate these metrics.

4.1.4 Comparison with numerical results

We compare these scalings with our numerical results in fig. 4.9, where the collapse of each scaled metric to a constant signifies that our scaling is capturing the key dynamics. We define h_χ to be the median height above the mush-liquid interface at which the porosity drops to 1/2, and h_c to be the greatest depth of the channel above the mush-liquid interface. The horizontal pressure drop Δp_m is found by computing the pressure drop across the mushy layer (from $|p(x = a) - p(z = \lambda)|$) for each z and then taking the vertical median over the region where $0 < z - z_{ml} < h_c$; from (4.27) we expect this to be $O(1)$ and independent of Rm and $\mathscr{C}$. There is a weak increase in Δp_m with Rm for larger $\mathscr{C}$, but otherwise the data is reasonably consistent with the

predicted scaling. In all our simulations we observe that the maximum streamfunction in the mushy layer is located near the channel, so we compute ψ_a as $\max|\psi(\chi < 1)|$. The channel width a is found by computing the channel width at each height $a(z)$ for $0 < z - z_{ml} < h_c$ then taking the median value.

There is some noise in the data for a variety of reasons, but particularly due to the sampling methods. Many of these diagnostics are sensitive to the position of the mush-liquid boundary, which has been discretised. Whilst we estimate the position of $h(x, z)$ by interpolating between the grid cells which straddle the boundary (one with $\chi = 1$, the other with $\chi < 1$), there is still some uncertainty in this value which feeds back on h_χ and h_c, particularly where these values are small. For $\mathscr{C} = 0.04$, the smallest values of h_χ are just a few grid cells and therefore only marginally resolved. The choice of averages also impacts the smoothness of the diagnostics, where we typically use the median. Whilst using a mean average would result in smoother curves, the mean is more susceptible to extreme values so we usually use the median (e.g. for h_χ and Δp_m).

In general, the scalings match the numerical results well in the limit $\mathscr{C} \ll 1$, $Rm \gg Rm_{crit}$. The significant deviations occur either as $\mathscr{C}$ increases towards 1, where our theory of convective confinement no longer applies, or as $Rm \to Rm_{crit}$, where the flow becomes weak and the self-consistency of the scalings (§ 4.1.3.8) breaks down. For example, as $\mathscr{C}$ increases the scaled solute flux (panel a) begins to diverge. Similarly, as $Rm \to Rm_{crit}$ the scaled channel depth (panel e) deviates from a constant. The scaled channel spacing (panel b) approximately collapses onto a single curve for a range of $\mathscr{C}$, but shows some variation with Rm for all parameters considered. It may be that the variation of λ with Rm is not fully captured by these scalings, or that the asymptotic regime has not yet been reached.

Notwithstanding the deviations discussed above, the numerical results are broadly consistent with the scaling laws developed in § 4.1.3. This suggests that the simplified theory illustrated here is a faithful approximation to much of the dynamics observed in the numerical simulations, and therefore provides a useful description of confined mushy layer convection in the limit $\mathscr{C} \ll 1, \mathscr{S} \gg 1, Le \gg \mathscr{S}/\mathscr{C}, Rm \gg 1/\mathscr{C}$.

4.1.5 Comparison with experimental observations of transient growth

Previous scaling laws for the limit $Rm/\mathscr{C} = O(1)$ found that the solute flux $F_O \propto Rm$, which is in reasonable correspondence with experimental data for transient sea ice growth (Wells et al., 2011). However, we have here obtained a different scaling result (4.44) where $F_O \sim \zeta \mathscr{C}^{7/6}(Rm - Rm_{crit})^{5/6}$ for $\mathscr{C} \ll 1$ which has a different scaling with Rm. We therefore wish to test the applicability of our scaling laws to the transient growth of a mushy layer following an analogous approach to Wells et al. (2011). Whilst we have also predicted that F_O varies with $\mathscr{S}$ and Le, we have not tested this dependence and therefore here we will only consider the variation of F_O with Rm and $\mathscr{C}$ in this section. Wettlaufer et al. (1997b) conducted a series of experiments where a sodium chloride solution was solidified from above in a container of depth $\mathcal{H}$, whilst measuring the change in salinity of the underlying liquid due to brine rejection. By varying the initial salinity of the solution, S_i, and the temperature of the top freezing surface, T_t, they explored a wide range of parameter space. In particular, the relevant definition of the concentration ratio for their experiments is given by

$$\mathscr{C} = \frac{S_i - S_S}{S_t(T_t) - S_i}, \tag{4.45}$$

where S_t, the salinity at the top plate, replaces the eutectic salinity in our previous definition (4.7) as the largest possible salinity in the system. We use a cubic liquidus (Vancoppenolle et al., 2019) to determine this salinity given the temperature at the top plate T_t,

$$S_t = -18.7T_t - 0.519T_t^2 - 0.00535T_t^3. \tag{4.46}$$

Accordingly, the experiments of Wettlaufer et al. (1997b) span a range of approximately $0.03 < \mathscr{C} < 0.72$.

Generalising the analysis of Wells et al. (2011), we first consider how the liquid

salinity measured by Wettlaufer et al. (1997b) should vary with time given a scaling law

$$F_O \sim \zeta \mathscr{C}^a (Rm - Rm_{crit})^b \tag{4.47}$$

for the dimensionless salt flux, where Rm_{crit} is the critical Rayleigh number, ζ is a constant prefactor of $O(1)$, and a and b may take any value. As the dimensional ice thickness $\hat{h}(t)$ increases, the salinity in the liquid $S_l(x, z, t)$ will change due to the salt flux $\mathbf{F}$. Integrating the solute budget over the volume of the underlying liquid we find

$$\int_{\mathcal{V}} \frac{\partial \tilde{S}_l(x, z, t)}{\partial t} \, d\mathcal{V} = \int_{\mathcal{V}} \nabla \cdot \mathbf{F} \, d\mathcal{V}, \tag{4.48}$$

$$= \int_{\mathcal{S}} \mathbf{F} \cdot d\mathcal{S}, \tag{4.49}$$

where we have used the divergence theorem in the second step. Assuming that the salinity in the liquid is well mixed, such that $\tilde{S}_l(x, z, t) \approx \tilde{S}_l(t)$, and that there is no solute flux from the side walls or base of the tank, and dividing by the box width we find

$$\left[\mathcal{H} - \hat{h}(t)\right] \frac{d}{dt} \left[S_l(t) - S_i\right] \approx \hat{F}_s, \tag{4.50}$$

where $S_l(t) - S_i$ is the change in salinity of the underlying liquid and $\hat{F}_s$ is the dimensional salt flux from the mush into the liquid. The relevant Rayleigh number and concentration ratio for transient growth will be dependent on the mushy layer depth, $\hat{h}(t)$, and the difference in salinity between the top of the mushy layer S_t and the liquid $S_l(t)$;

$$Rm(t) \sim \frac{\rho_0 g \beta \left[S_t - S_l(t)\right] K_0 \hat{h}(t)}{\mu \kappa_l}, \quad \mathscr{C}(t) \sim \frac{S_l(t) - S_S}{S_t - S_l(t)}. \tag{4.51}$$

The dimensional salt flux is given by $\hat{F}_s = F_O \Delta S \kappa_l / \hat{h}$, where $\Delta S = [S_t - S_l(t)]$ is the salinity scale. Substituting for F_O from (4.47) with Rm given by (4.51) yields

$$\hat{F}_s \sim \zeta \left(\frac{\rho_0 g \beta K_0}{\mu}\right)^b \kappa^{1-b} \left(S_t - S_l\right)^{1+b} \mathscr{C}^a \hat{h}^{b-1} \left(1 - \frac{\hat{h}_c}{\hat{h}}\right)^b, \quad \text{for} \quad \hat{h} > \hat{h}_c, \tag{4.52}$$

where the critical mush depth, h_c, is determined by the height at which the transient

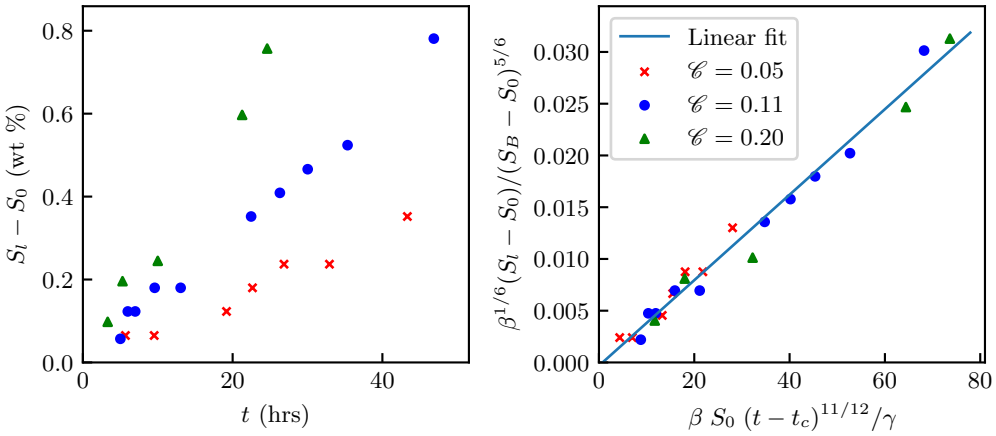


Figure 4.10: (a) Change in salinity $(S_l - S_0)$ of the liquid below a growing mushy layer over time t as measured by Wettlaufer et al. (1997b) during three different experiments. The concentration ratio $\mathscr{C}$ for each experiment is calculated using (4.45). (b) collapse of the data in (a) using (4.55) and our flux scaling $F_O \sim \mathscr{C}^{7/6} Rm^{5/6}$. The linear fit has a slope $\zeta = 0.018$ and $R^2 = 0.99$.

mushy Rayleigh number $Rm(t)$ is equal to the critical mushy Rayleigh number. We assume that the mushy layer grows diffusively, so $\hat{h} \sim \hat{h}_0\sqrt{\kappa t}$ for some constant $\hat{h}_0$. Wettlaufer et al. (1997b) actually found slightly slower growth, but a diffusive growth model approximately captures the observed behaviour (see also chapter 5). Once the mushy layer depth is well above the critical depth, but still far less than the depth of the experimental cell ($\mathcal{H} \gg \hat{h} \gg \hat{h}_c$) we can rewrite (4.50) as

$$\frac{d}{dt}\left[S_l(t) - S_i\right] \sim \zeta\ \ \gamma^{-1}\ \beta^b\ \left[S_t - S_l(t)\right]^{1+b} \mathscr{C}^a t^{(b-1)/2}, \tag{4.53}$$

$$\text{where} \quad \gamma^{-1} = \left(\frac{\rho_0 g K_0}{\mu}\right)^b \frac{\kappa^{(1-b)/2}}{\mathcal{H}} \hat{h}_0^{b-1}. \tag{4.54}$$

Making the further assumption that the change in liquid salinity is small relative to the changes in salinity through the system, $S_l(t) - S_i \ll S_t - S_i$, we can approximate $S_l(t) \approx S_i$ at leading order on the right hand side of (4.53) and integrate to find

$$\beta^{1-b} \frac{S_l(t) - S_i}{(S_t - S_i)^b} \sim \zeta\ \beta\ (S_t - S_i)^{1-a}\ \ (S_i - S_S)^a\ \frac{t^{(b+1)/2}}{\gamma} \frac{2}{b+1}. \tag{4.55}$$

Our flux scaling $F_O \sim \mathscr{C}^{7/6} Rm^{5/6}$ should apply in the limit $\mathscr{C} \ll 1$. Therefore, in fig. 4.10, we consider the three datasets from Wettlaufer et al. (1997b) with the

smallest concentration ratios. In fig. 4.10a we plot the changes in salinity observed by Wettlaufer et al. (1997b), whilst in fig. 4.10b we demonstrate that this data collapses to a single line, with $R^2 = 0.99$, given (4.55) with the assumption of a scaling law $F_O \sim \mathscr{C}^{7/6} Rm^{5/6}$ (i.e. $a = 7/6$ and $b = 5/6$). Therefore, we conclude that our flux scaling is consistent with the experimental observations of sea ice growth. With a scaling law $F_O \sim \mathscr{C} Rm$ we also find a good linear fit with $R^2 = 0.99$, suggesting that both scalings are consistent with the observational data.

Whilst the parametric dependence of the scalings on $\mathscr{S}$ and Le has not been tested, the slope of the linear fit, $\zeta = 4 \times 10^{-4}$, is of a similar magnitude to the prefactor predicted by (4.44): $\mathscr{S}^{2/3} Le^{-3/2} \approx 10^{-3}$. A further test of the collapse of the experimental data under different potential scalings is to compute a power law fit for $y = Ax^B$ where y and x are the left and right hand sides of (4.55). An exponent $B = 1$ would indicate a linear fit, supporting the validity of a particular scaling. We find $B = 1.00 \pm 0.05$ for our scaling ($a = 7/6$ and $b = 5/6$) and $B = 0.98 \pm 0.05$ for the scaling $F_0 \sim \mathscr{C}\, Rm$ ($a = 1, b = 1$) obtained by Wells et al. (2011). Both cannot be distuingished from 1 within the error bounds, reinforcing the conclusion that both possible scalings are consistent with the experiments conducted by Wettlaufer et al. (1997b).

4.1.6 Discussion

In this section we will discuss some of the implications of the scalings identified in § 4.1.3. We find that, in the limit $\mathscr{C} \ll 1$, strong flow will be confined to the high porosity region at the mush-liquid interface. In the context of sea ice, this high porosity region may be related to the *skeletal layer* identified by Reeburgh (1984) as a region of active convection. Our scalings predict that the channels themselves will also be confined to a fraction of the mushy layer depth, a feature seen in some experiments of mushy layer solidification (e.g. Aussillous et al., 2006). However Lake and Lewis (1970) found evidence for brine channels penetrating well past the skeletal layer in sea ice samples. It may be that brine channels of the type observed by Lake and Lewis (1970) are the result of transient growth, whilst our scalings are derived in the context of growth at a fixed rate. We explore this in chapters 5 and 6.

Our scalings and numerics reveal the existence of a large passive region, whilst flow is driven by baroclinic torque in the relatively narrow channel. It might be expected that the optimal state would eliminate this passive region as a denser array of channels would lead to a greater horizontally averaged solute flux. We propose that the passive region helps to balance downwelling within the channel. Flow between the two passes through the active region where it is either transported directly into the channel, or up into the thermal boundary layer before entering the channel deeper into the mushy layer. This mechanism requires the mass flux in all three regions to be of equal magnitude, $\bar{\psi}_c \sim \bar{\psi}_a \sim \bar{\psi}_p$. The scalings found here (4.33) reveal that $\bar{\psi}_c \sim \bar{\psi}_a$ whilst ψ_c and $\bar{\psi}_p$ are asymptotically different as $Rm \to \infty$, but are numerically similar in magnitude for the regions of parameters space explored.

We find that the ratio λ/h_χ is independent of Rm, and therefore also independent of the length scale κ_l/V. Hence, we predict that the dimensional channel spacing $L = \lambda\kappa_l/V$ is proportional to the dimensional depth of the high porosity region $\hat{h}_\chi \sim h_\chi\kappa_l/V$. Tait and Jaupart (1992) considered a system with $\mathscr{C} \gg 1$, where we might not expect the scalings found here to be relevant, but nonetheless found that the channel spacing was independent of the mush depth for a sufficiently thick mushy layer, with channels confined to a narrow porous layer near the mush-liquid boundary. It is not clear whether this behaviour is related to the dynamics we have identified or not. Previous authors have found that in systems without convective confinement (e.g. Katz and Worster (2008) considered a system with $\mathscr{C} \gg 1$) the channel spacing is proportional to the dimensional depth of the mushy layer, $\hat{h}$, which could be interpreted as the limit of our predicted scaling ($L \sim \hat{h}_\chi$) as $\hat{h}_\chi \to \hat{h}$. We will explore the spacing of brine channels in more depth with the aid of transient simulations in chapter 5.

We have made several significant departures from previous studies of flow in periodic arrays of channels during directional solidification (Schulze and Worster, 1998; Chung and Worster, 2002; Wells et al., 2013; Rees Jones and Worster, 2013). In particular, we considered flow in a narrow Hele-Shaw cell so that flow in both the liquid regions and the mushy layer is well described by Darcy's law, and we included the effects of salt diffusion within our model. Indeed, we found that salt diffusion plays a significant role in our scalings - particularly within the liquid channels where solute diffusion

balances fluid advection to set the channel width. Previous authors have typically modelled flow in the narrow channels using the Navier-Stokes equations via a lubrication approximation, which should result in a stronger flow through narrower channels. Our scalings, particularly the predicted solute flux, are heavily dependent on the dynamics in the channel and therefore we expect that flow through purely liquid channels might lead to a modified scaling. However we find that the solute flux follows the same broad trends with Rm and $\mathscr{C}$ as Wells et al. (2013). In particular, we recover the same linear scaling of the solute flux with Rm in the limit $\mathscr{C} \sim O(Rm)$ that Wells et al. (2013) found using a purely liquid channel and without solute diffusion. Wells et al. (2013) also found that the solute flux for smaller $\mathscr{C}$ varied sublinearly with Rm, behaviour which we have explored in detail. However there are also some differences between this study and those conducted by previous authors, most notably the bifurcation structure where we do not find the saddle-note bifurcation which others have (e.g. Schulze and Worster, 1998; Chung and Worster, 2002; Wells et al., 2013).

The physics described by our scalings closely resembles some of the features of the semi-analytical Chimney-Active-Passive (CAP) model proposed by Rees Jones and Worster (2013). Considering the near-eutectic limit with $\mathscr{C} \gg 1$, where the porosity is high throughout the mushy layer, they suggested that flow was driven by baroclinic torque in an active region near the channel, whilst away from the channel the mushy-layer was passive with upwelling that is independent of the horizontal position x. The two regions were patched together by considering the continuity of temperature, heat flux, velocity, and pressure, whilst the channel was a passive conduit which extends through the full depth of the mushy-layer. Here, we also find that away from the channel there is a passive region with flow driven by baroclinic torque generated within and adjacent to the channel. In contrast to the CAP model, we have considered the far-from-eutectic limit where the porosity within the mushy layer is typically low except for a narrow layer adjacent to the mush-liquid interface. Consequently we identify depth scales h_c for the channel (with $h_c \ll h$) and h_χ for flow (with $h_\chi \ll h_c$) which are controlled by both the thermodynamics of solidification and the dynamics of the flow. In particular, the depth of the porous layer shrinks as solute is rejected from the mushy layer due to the decrease in porosity.

4.2 Mushy layer growth with Darcy-Brinkman flow

Thus far, we have considered simulations where the fluid phase is governed by Darcy's law. Whilst this is justifiable when flow is constrained by a narrow Hele-Shaw cell, the extent to which such results are applicable to sea ice growth is unclear. We now consider a fluid phase governed by the Navier-Stokes equations, with the transition to flow in porous media handled by the addition of a Darcy term yielding a Darcy-Brinkman equation (2.12). The permeability is given by the Kozeny-Carman law (2.38), with $\Pi_c = 10^{10}$ acting as a numerical regularisation term. For convenience, we repeat the governing equations below.

$$\frac{\partial \mathbf{U}}{\partial t} + \mathbf{U}\cdot\nabla\left(\frac{\mathbf{U}}{\chi}\right) = -\chi\nabla p + Pr\nabla^2\mathbf{U} + \chi Pr\left(Ra_T\theta - Ra_S\Theta_l\right)\mathbf{e_z} - \frac{Pr\,\chi\mathbf{U}}{Da\,\Pi}, \tag{4.56}$$

$$\nabla\cdot\mathbf{U} = 0, \tag{4.57}$$

$$\left(\frac{\partial}{\partial t} + V_f\frac{\partial}{\partial z}\right)(\theta + \mathscr{S}\chi) + \mathbf{U}\cdot\nabla\theta = \nabla^2\theta, \tag{4.58}$$

$$\left(\frac{\partial}{\partial t} + V_f\frac{\partial}{\partial z}\right)\left[\chi\Theta_l - \mathscr{C}\left(1-\chi\right)\right] + \mathbf{U}\cdot\nabla\Theta_l = \frac{1}{Le}\nabla\cdot\left(\chi\nabla\Theta_l\right), \tag{4.59}$$

where the permeability is given by

$$\Pi(\chi) = \left(\Pi_c^{-1} + \frac{(1-\chi)^2}{\chi^3}\right)^{-1}. \tag{4.60}$$

In this section all simulations will use $Pr = 10$, and $Da = 5\times10^{-3}$ for consistency with previous studies (Chung and Worster, 2002; Wells et al., 2013). We use a computational domain similar to that in fig. 4.2a with a dimensionless depth $\eta = 1$. As in § 4.1 we select the domain width which maximises the horizontally averaged solute vertical solute flux given by (4.10).

In contrast to § 4.1, where we performed a systematic study of mushy layer convection over a wide range of Rm and $\mathscr{C}$, here we will conduct a more restricted

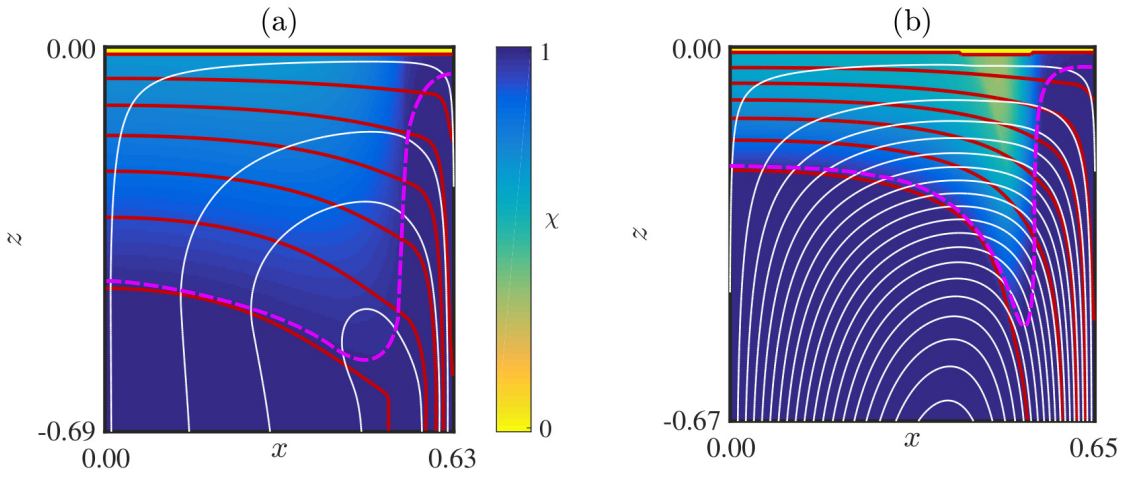


Figure 4.11: Simulations of a single convection cell using (a) Darcy's law and (b) the Darcy-Brinkman equation showing porosity (color), liquid salinity (red contours, spaced for visual convenience at $\Theta_l = 0, -1/7, -2/7, ..., -1$), streamlines (white contours, clockwise, $\psi = 0.25, 0.5, 0.75, ...$), and the mush-liquid interface (magenta, dashed). Both simulations use the same parameters; $\mathscr{C} = 5, \mathscr{S} = 5, V_f = 1, Le = 200$, and a mushy Rayleigh number $Rm = 35$, which arises in (b) from choosing $Ra_S = 7000$ and $Da = 5 \times 10^{-3}$. The two domains have an equal height ($\eta = 1$) and identical boundary conditions. Using Darcy-Brinkman results in a stronger flow (in both plots the weakest streamline is $\psi = 0.25$); the enhanced upwelling of warm fresh liquid reduces the mushy layer height whilst increasing solidification within the mush.

study. Motivated by the observation that, in the limit $\mathscr{C} \gg 1$, we recovered the same scalings for the solute flux as Wells et al. (2013) despite contrasting physics, we will consider the effects of solute diffusion on the dynamics within brine channels by varying the Lewis number Le (§ 4.2.2). First, we briefly compare solutions computed using Darcy's law with those computed using a Darcy-Brinkman equation in § 4.2.1.

4.2.1 Comparison between Darcy and Darcy-Brinkman flow

In fig. 4.11 we compare typical steady state solutions obtained using Darcy-Brinkman simulations with those calculated using Darcy's law. Whilst the general structures of the two solutions are the same, there are also some significant differences. Within the mushy layer, the Darcy-Brinkman equation is well approximated by Darcy's law so we expect the differences between (a) and (b) to be primarily dependent on the dynamics in the liquid region. For example, a stronger flow in (b) increases the upward transport of warm fresh liquid which both reduces the typical mushy layer height and increases internal solidification. The brine channels carry a significantly stronger

flow in (b), but are of a roughly similar size. The ice-ocean salt flux predicted in § 4.1 was dependent on the dynamics in the channel, and therefore we might expect a different result to apply here. In the remainder of this section we will explore the factors which control the width of brine channels in this model.

4.2.2 Channel dynamics with solute diffusion

Previous authors have used numerical simulations and scaling considerations to argue that the channel width depends primarily on the mushy Rayleigh number Rm and the Darcy number Da (Schulze and Worster, 1998; Chung and Worster, 2002; Rees Jones and Worster, 2013; Wells et al., 2013), which we note can be combined to give the fluid Rayleigh number $Ra_S = Rm/Da$. All these studies neglected salt diffusion. Hence, we investigate the hypothesis that in potentially narrow channels, with a salinity which varies rapidly in the horizontal direction, the diffusive transport of salt may be non-negligible. Local salinity, along with temperature, determines whether a region is liquid or partially frozen. Therefore the transport of salt may play a significant role in controlling the width of brine channels.

For comparison with previous studies, we consider the limit $\mathscr{C} \gg 1$ such that convection penetrates the full depth of the mushy layer h, and the permeability is generally high (see fig. 4.11b for example). As in § 4.1 we take $V_{\text{frame}} = 1$, and use the scales

$$x = a\tilde{x}, \quad z = h\tilde{z}, \quad \psi = \bar{\psi}\tilde{\psi}, \tag{4.61}$$

where quantities with a tilde are $O(1)$, and $\bar{\psi}$ represents a characteristic streamfunction scale. The salinity Θ and temperature θ, are both $O(1)$ as convection is not confined significantly by porosity variations.

In the liquid channels ($\chi = 1$) I consider the balance between inertial and viscous terms for the simulation in fig. 4.11b,

$$\frac{\mathbf{U}\cdot\nabla\mathbf{U}}{Pr\nabla^2\mathbf{U}} \approx \frac{Ua}{Pr} \approx \frac{10\times 0.1}{10} \ll 1. \tag{4.62}$$

Hence the flow is well approximated by the Stokes equation

$$0 = -\nabla p + Pr\nabla^2\mathbf{U} + Pr\left(Ra_T\theta - Ra_S\Theta_l\right)\mathbf{e_z}. \tag{4.63}$$

Introducing the stream function ψ, where $\mathbf{U} = (-\partial\psi/\partial z, \partial\psi/\partial x)$, and noting that $Ra_S \gg Ra_T$, we obtain the vorticity equation by taking the curl of (4.63)

$$\nabla^4\psi \approx Ra_S\frac{\partial\Theta_l}{\partial x}. \tag{4.64}$$

Assuming that the brine channel width a is much less than the height h, the governing equations (4.58,4.59) and (4.64) scale like

$$\frac{V_f}{h}\frac{\partial\tilde{\Theta}}{\partial\tilde{z}} + \frac{\bar{\psi}}{ah}\tilde{\mathbf{U}}\cdot\tilde{\nabla}\tilde{\Theta} \approx \frac{1}{Le}\frac{1}{a^2}\frac{\partial^2\tilde{\Theta}}{\partial\tilde{x}^2}, \tag{4.65}$$

$$\frac{V_f}{h}\frac{\partial(\tilde{\theta}+\mathscr{S}\chi)}{\partial\tilde{z}} + \frac{\bar{\psi}}{ah}\tilde{\mathbf{U}}\cdot\tilde{\nabla}\tilde{\theta} \approx \frac{1}{a^2}\frac{\partial^2\tilde{\theta}}{\partial\tilde{x}^2}, \tag{4.66}$$

$$\frac{\bar{\psi}}{a^4}\frac{\partial^4}{\partial\tilde{x}^4}\tilde{\psi} \approx Ra_S\frac{1}{a}\frac{\partial\tilde{\Theta}}{\partial\tilde{x}}. \tag{4.67}$$

From the momentum balance (4.67) we obtain $\bar{\psi} \sim a^3 Ra_S$. Substituting for $\bar{\psi}$ into (4.66) and rearranging yields

$$a^2V_f\frac{\partial(\tilde{\theta}+\mathscr{S}\chi)}{\partial\tilde{z}} + a^4Ra_S\,\tilde{\mathbf{U}}\cdot\tilde{\nabla}\tilde{\theta} \sim h\frac{\partial^2\tilde{\theta}}{\partial\tilde{x}^2}. \tag{4.68}$$

Assuming that $a^2Ra_S \gg V_f\mathscr{S}$, so that frame advection is negligible, we find a balance between advection and diffusion yielding

$$a \sim \left(\frac{h}{Ra_S}\right)^{1/4}. \tag{4.69}$$

This is self-consistent with our assumption that frame advection is negligible (which required $a^2Ra_S \gg \mathscr{S}V_f$) provided $Ra_S^{1/2} \gg \mathscr{S}V_f/h^{1/2}$. The latter is well satisfied given that we consider a parameter regimes with $Ra_S > 1000$, $V_f = 1$, $\mathscr{S} \sim 5$ and $h = O(1/\mathscr{S})$.

Turning to the salt equation, we note that the frame advection and fluid advection

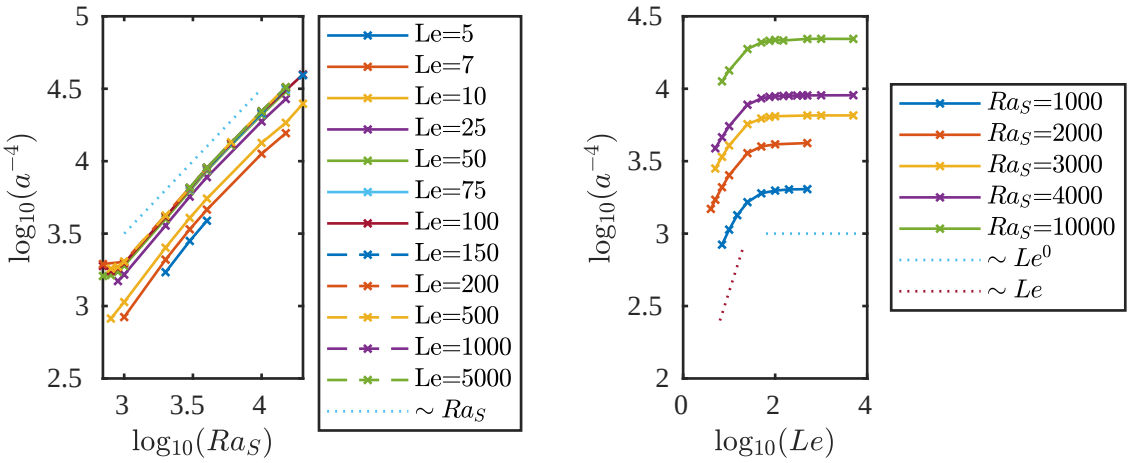


Figure 4.12: Observed scaling of a^{-4} with the Lewis number Le and haline Rayleigh number Ra_S for Darcy-Brinkman flow with $\mathscr{C} = 5.0$ and all other parameters as in fig. 4.11.

scale in the same way as in the heat equation. Hence frame advection can be neglected, yielding

$$\tilde{\mathbf{U}} \cdot \tilde{\nabla}\tilde{\Theta} = \frac{h}{a^4 Ra_S Le} \frac{\partial^2 \tilde{\Theta}}{\partial \tilde{x}^2}. \tag{4.70}$$

In the limit $Le \gg Ra_S\ a^4/h$, the salt equation is dominated by advection and the channel width is determined by thermal considerations via (4.69). Using (4.69) we can rewrite this limit as $Le \gg 1$. When Le approaches 1, a balance emerges between salt advection and diffusion in (4.65) leading to an alternative channel scaling

$$a \sim \left(\frac{h}{Ra_S\, Le} \right)^{1/4}, \qquad (Le \lesssim O(1)\,). \tag{4.71}$$

In our numerical simulations, we find that the mush depth $h \sim 1/\mathscr{S}$ is approximately independent of Rm and therefore we expect to find a channel width given by

$$a \sim \begin{cases} \left(\frac{1}{Ra_S\, \mathscr{S}\, Le}\right)^{1/4} & (Le \lesssim O(1)\,), \\ \left(\frac{1}{Ra_S\, \mathscr{S}}\right)^{1/4} & (Le \gg 1\,). \end{cases} \tag{4.72}$$

A comparison of these scalings with the numerical results is presented in fig. 4.12. For $Le \gg 1$, we see in the left hand figure that $1/a^4$ varies approximately linearly with Rm consistent with the proposed scale. For small Le, we see in the right hand plot

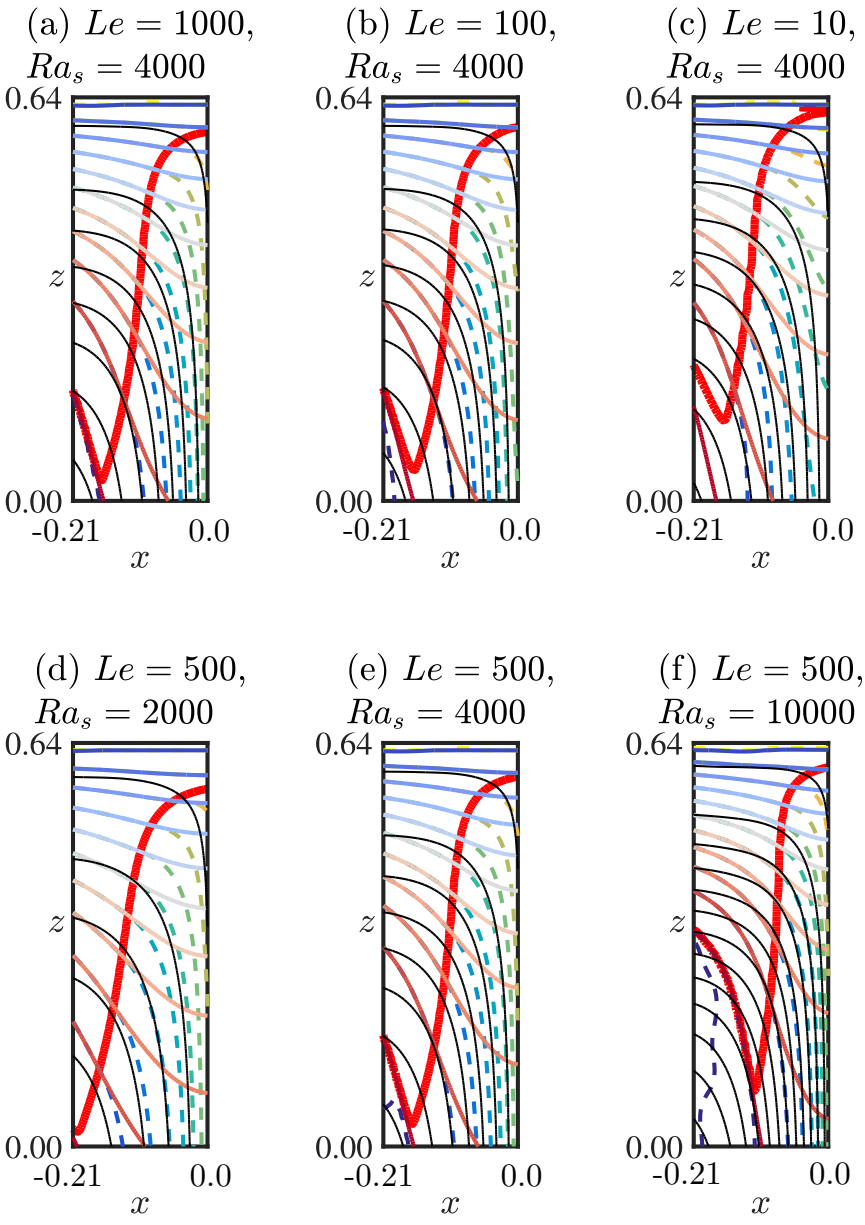


Figure 4.13: Numerically calculated temperature (solid, coloured), liquid salinity (dashed) and stream function (solid, black) fields inside a channel. The mush-liquid interface (red) divides the mushy layer (above and to the left) from the channel (right). Only a small portion of the domain has been shown - see fig. 4.11 (b) for context, noting that the position of the origin has changed so that the channel centre is at $x = 0$. Contour intervals are the same in all plots ($\theta = 0, 0.1, 0.2...$ and $\psi = 0.1, 0.2, ...$) and the flow is clockwise. Parameters are as in fig. 4.11 except where specified.

that the channel width has some dependence on Le, though it is not clear whether this matches the predicted $a \sim Le^{-1/4}$ scaling, which is indicated by the red dotted line. It is difficult to compare the scaling with $Le < 1$ due to the narrow range of Le over which the scaling applies; when the Lewis number is reduced further, we find that diffusion of salt out of the mushy layer reduces the salinity stratification and convection stops. Small deviations from our predictions at small Rm are the result of channels shrinking as convection shuts down.

Inspection of the dynamics within a brine channel (fig. 4.13) lends further support to the origin of these scalings. Stronger solutal diffusion increases the transport of salt from the highly saline channel centre to the edge - as Le decreases from panel (a) through to (c) the liquid salinity contours in the channel become more spread out. This process enhances dissolution, widening the channel. Meanwhile stronger flow can cool the channel wall more efficiently, promoting solidification until the horizontal temperature gradient is strong enough for diffusion to provide sufficient heat to maintain a steady state. As Ra_S increases from (d) to (f), the streamlines become closer packed and the gradient of the isotherms increases.

The Lewis number is typically large in physical systems of interest; for salt water, $Le \sim 200$. In this case, the appropriate scaling of the channel width is independent of Le. Consequently, the streamfunction scale $\bar{\psi} \sim a^3 Ra_S$ is also independent of Le. This suggests that it is reasonable for previous studies to neglect the effect of salt diffusion on the channel spacing when comparing to either 3-D systems, or in quasi-2-D systems where the channel width is narrower than the Hele-Shaw width so that the Hele-Shaw permeability is negligible. Experimental confirmation of the scaling (4.71) would require a binary alloy with small Le - one possible candidate is a mixture of water and isopropanol, as previously used by Worster (1997).

4.3 Summary

In this chapter I have investigated buoyancy driven convection in mushy layers formed during directional solidification of a binary alloy. In § 4.1 I considered flow in a narrow Hele-Shaw cell, rationalising the use of Darcy's law to model flow in both

the liquid and mushy regions. Motivated by the phenomena of brine rejection in sea ice, I focussed on systems with small concentration ratios, $\mathscr{C} \ll 1$, and find that convection is mostly confined to a narrow porous layer near the boundary between the mushy layer and adjacent liquid phase.

Using the optimal flux criterion hypothesised by Wells et al. (2010) to determine the spacing of a periodic array of convection cells, I systematically studied the behaviour of state steady convection over a wide range of mushy Rayleigh numbers Rm and concentration ratios $\mathscr{C}$. In the limit $\mathscr{C} \ll 1$, I find new scaling laws (4.33, 4.44) which are broadly consistent with numerical simulations. The scalings capture the confinement of convection in response to decreasing $\mathscr{C}$, which leads to a narrow high porosity boundary layer near the mush-liquid interface. Increasing Rm further reduces the depth of this boundary layer by removing solute and hence reducing the porosity of the mushy-layer.

Considering flow at the base of the narrow channels, I predict a solute flux scaling $F_O \sim \mathscr{C}^{7/6} Rm^{5/6}$ in the limit $\mathscr{C} \ll 1$, which is consistent with experimental observations of transient ice growth (Wettlaufer et al., 1997b). Whilst this builds confidence in the validity of our analysis and potential applicability to real sea ice growth, it is important to note that Wells et al. (2011) found a scaling $F_O \sim \mathscr{C} Rm$ was also consistent with the same experimental results, despite the linear scaling with Rm only being formally justified in the limit $Rm/\mathscr{C} = O(1)$ (Wells et al., 2013). Future experimental or observational work to discriminate between the two scalings would be a valuable but challenging endeavour. The predicted variation with Rm deviates only by a power of 1/6 between the two scalings. To separate these would require measurements over many orders of magnitude.

It is interesting that the salt flux computed in § 4.1 reproduces the same broad trends seen by Wells et al. (2013) despite the notable differences between these two models. For example, we considered a system trapped in a narrow Hele-Shaw, and then solved directly for the resulting porous flow in the pure liquid, whilst Wells et al. (2013) parametrised the effect of flow in a liquid using asymptotic reductions of the Navier-Stokes equations. We also included the effect of solute diffusion, which Wells et al. (2013) neglected. Other than the inclusion, or not, of solute diffusion, both models consider the same physical processes within the mushy layer (where

$\chi < 1$). The similarities between the solute fluxes between the two models suggests that these fluxes are more strongly controlled by the dynamics in mushy layer, rather than the dynamics in the adjacent pure liquid.

In § 4.2 I then relaxed the assumption of flow in a narrow Hele-Shaw cell, modelling flow via a Darcy-Brinkman equation which reduces to the Navier-Stokes equations in purely liquid regions. Focussing on the dynamics within the channels, I found when $Le < O(1)$ solutal diffusion can increase the width of the channels by balancing the advection of solute from the mushy layer into the channel. However in most physical scenarios, including sea ice, $Le \gg 1$ and we find a channel width determined purely by the solutal Rayleigh number in the fluid Ra_S.

Previous studies have considered flow through a periodic array of channels by solving for Darcy flow in the mushy layer and parametrising flow in the liquid channels via a lubrication approximation. We have demonstrated in § 4.2 here that it is possible to solve for flow in both regions using a single set of equations, without having to parametrise flow in the liquid channels. Future studies may be able to exploit this method to test the accuracy of previous approaches.

A key question that this chapter raises is whether the Darcy-Brinkman model would recover the same solute flux scaling that we found in the model with Darcy flow in a Hele-Shaw cell. This is because the Darcy-Brinkman model bears a closer resemblance than the Darcy model to sea ice growth, where flow in the liquid is not trapped within a Hele-Shaw cell but rather is fully 3-D. It is also important to remember that both the models considered in this chapter relate to directional solidification. In reality, sea ice growth is a transient process where the growth rate varies continuously. It is not immediately clear whether one can apply the steady scalings found here. Motivated by this key difference, in the next chapter we will move on to consider transient sea ice growth from a fixed boundary.

Despite the approximations involved in the Darcy model, which most notably involved solving for flow in the pure fluid phase using Darcy's law, the consistency between the scalings derived in § 4.1 and the experimental results of Wettlaufer et al. (1997b), which were conducted in a 3-D tank, suggests that the scaling $F_O \sim \mathscr{C}^{7/6} Rm^{5/6}$ found here may be a useful tool for predicting salt fluxes from growing sea ice. One

possible conclusion to draw from this favourable comparison, along with the similarities between these results and those found by Wells et al. (2013) using a different model, is that solute fluxes are primarily controlled by the dynamics within the mushy layer. The mushy layer dynamics are the aspects of both models which involve the fewest approximations and therefore most faithfully describe the physics of sea ice growth.

5

Growth from a fixed boundary

In this chapter I will investigate mushy layer growth from a fixed cold boundary. This setting is particularly applicable to sea ice growth, where growth proceeds from the cold atmosphere-ocean interface, whilst many laboratory experiments also grow mushy layers from a stationary cold boundary.

Mushy layer growth from a fixed boundary is initially transient, with the depth of the mushy layer evolving over time before eventually being eliminated on very long timescales due to solutal diffusion (Gewecke and Schulze, 2011). This is in contrast to the steady state growth found in the case of directional solidification. As a result, theoretical approaches such as stability analyses are less common here and the majority of previous studies have been conducted in the laboratory or the field. Many such studies exist, but here I will focus on work involving solidification of NaCl-H_2O solutions due to their relevance to sea ice formation. It is challenging to make non-invasive measurements of ice growth in the laboratory or the field. Wettlaufer et al. (1997b) measured the salinity and volume of the underlying fluid during ice growth, and hence inferred the ice-liquid salt flux between mushy ice and the liquid and the volume of ice formed. Cottier and Wadhams (1999) dissected a layer of artificially grown sea ice to determine the distribution of salinity, whilst Notz and Worster (2008) made in-situ measurements of the salinity within a layer of growing ice. Other authors have grown ice in a narrow Hele-Shaw cell, which enables the visualisation of porosity variations within the ice (Eide and Martin, 1975; Chen, 1995; Middleton et al., 2016).

With numerical simulations it is possible to measure all modelled properties of the system. The difficulty instead lies in solving the governing equations. Maksym and Jeffries (2001) modelled flow and solidification in a system composed of a flooded slush layer above mushy sea ice, and observed the spontaneous development of narrow

saline channels. Oertling and Watts (2004) describe numerical simulations of sea ice growth which agree quantitatively with the ice-liquid salt flux measured by Wettlaufer et al. (1997b), and also with the salinity profiles measured by Cox and Weeks (1975). Petrich et al. (2004) also numerically simulated ice growth and found salinity profiles which reproduced the classical C-shape, despite being underresolved. Since this, no other numerical studies have been reported in the literature, and therefore there are a range of open questions which this chapter will start to address.

In § 5.1 I will describe the results from three simulations of sea ice growth conducted with different atmospheric temperatures. In § 5.2 I will consider a suite of simulations with the same boundary conditions which span a wide range of values of the concentration ratio. Both these sections will consider growth in a narrow quasi-two-dimensional Hele-Shaw cell, whilst in § 5.3 I will simulate growth in three spatial dimensions and describe some of the similarities and differences between the two cases. Finally, I will summarise the key results in § 5.4.

5.1 Sea ice growth

In this section I will present the results from three simulations of sea ice growth in a narrow, horizontally-periodic, 2-D Hele-Shaw cell as illustrated in fig. 5.1. In each simulation the atmospheric temperature at the top of the cell will be fixed to a different value $T_a = -10, -15$ or $-20°\mathrm{C}$, whilst all other parameters will be kept the same. As discussed in chapter 2, it is appropriate to model flow in a narrow Hele-Shaw cell using Darcy's law where the permeability in the open liquid is controlled by drag on the front and back cell faces. In this section I present results in dimensional form for ease of comparison to experiments. For convenience, the

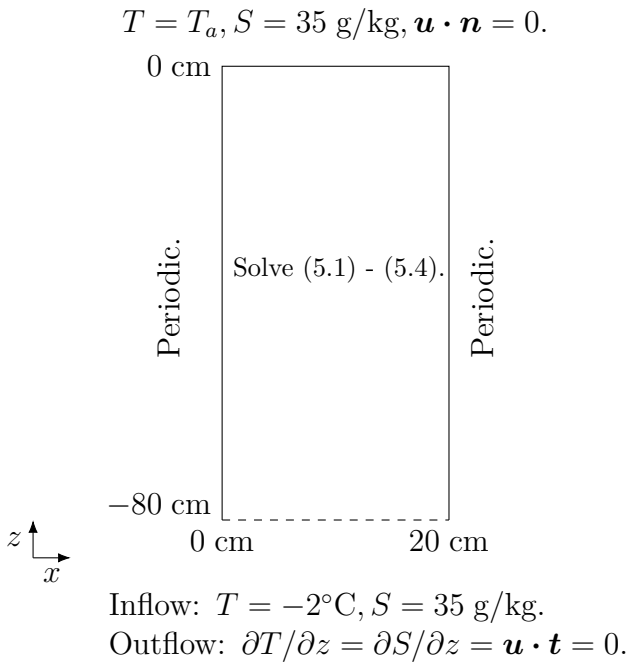


Figure 5.1: Simulations of sea ice growth are conducted in a narrow Hele-Shaw cell, with a fixed temperature at the top boundary and an open bottom boundary. The domain is periodic in the horizontal (x) direction, with a resolution of 1024 grid cells in the vertical direction and 256 cells in the horizontal direction. Tests demonstrate that the salt rejection from the modelled sea ice has converged at this resolution.

governing equations are repeated below,

$$\frac{\partial H}{\partial t} + \nabla \cdot (\mathbf{U}\rho_0 c_{p,l} T) = \nabla \cdot \left[\bar{k}(\chi)\nabla T\right], \tag{5.1}$$

$$\frac{\partial S}{\partial t} + \nabla \cdot (\mathbf{U} S_l) = \nabla \cdot \left[D_l \chi \nabla S_l\right], \tag{5.2}$$

$$\mathbf{U} = \frac{K(\chi)}{\eta}\left(-\nabla p + \rho g \mathbf{k}\right), \tag{5.3}$$

$$\nabla \cdot \mathbf{U} = 0. \tag{5.4}$$

For simplicity, for these simulations I assume that the liquid and solid phases have equal thermal properties so $c_{p,l} = c_{p,s}$ and $k_l = k_s$. The other physical parameters are as listed in table 2.1 with the exception of the reference permeability which we take to be somewhat smaller, $K_0 = 10^{-10}\text{m}^{-2}$, to restrict the strength of convection in the mushy layer, which reduces the flow timescales allowing integration over longer growth timescales. Similarly, to control the strength of convection in the liquid I use a narrow Hele-Shaw gap width, $d = 0.1$ mm, such that cell permeability K_c is ≈ 8

Dimensionless parameter		Value
Compositional Rayleigh number	Rm	800
Thermal Rayleigh number	Rm_T	40
Concentration ratio	$\mathscr{C}$	0.18
Stefan number	$\mathscr{S}$	5.0
Hele-Shaw cell permeability	Π_c	8.0
Heat capacity ratio	c_p	1.0
Heat conductivity ratio	k	1.0

Table 5.1: Dimensionless parameters for sea ice simulations in § 5.1.

times larger than K_0. The resulting dimensionless parameters are listed in table 5.1. Simulations are initialised from a state of rest ($\mathbf{U} = 0$) with the domain filled with salty water at a uniform temperature ($T = T_h = -2°\text{C}$) and salinity ($S = S_i = 35$ g/kg). Growth is then simulated over a period of approximately 4 days.

5.1.1 Phenomenology of transient growth

In fig. 5.2 I plot snapshots of each simulation illustrating the porosity of the ice (χ) and the liquid salinity S_l in the open liquid region. Once the ice has reached a critical depth, in this case after around 4 hrs, convection begins and channels form at the mush-liquid interface through which salty fluid (yellow) is rejected into the underlying liquid. As growth progresses, convection continues in a region of ice close to the mush-liquid interface. Active brine channels, which are entirely liquid and carry salty fluid, are identifiable as yellow regions in fig. 5.2. Meanwhile remnant brine channels, which are no longer entirely liquid, are visible as the high porosity (medium-to-dark blue) regions in the upper layers of the ice. Occasionally, remnant brine channels may be reactivated as seen at $t = 51$hrs for $T_a = -10°\text{C}$, where three active brine channels penetrate through the full depth of the mushy layers. The brine channel density typically decreases over time, as discussed further in § 5.1.5.

Channels, and the salty plumes below them, are initially strongly aligned with the vertical direction. For all three atmospheric temperatures, some degree of horizontal variation is apparent by the end of each simulation. For the warmest atmospheric temperature, $T_a = -10°\text{C}$, this is most apparent in the plumes which begin to leave the mush at an angle to the vertical after around 50hrs.

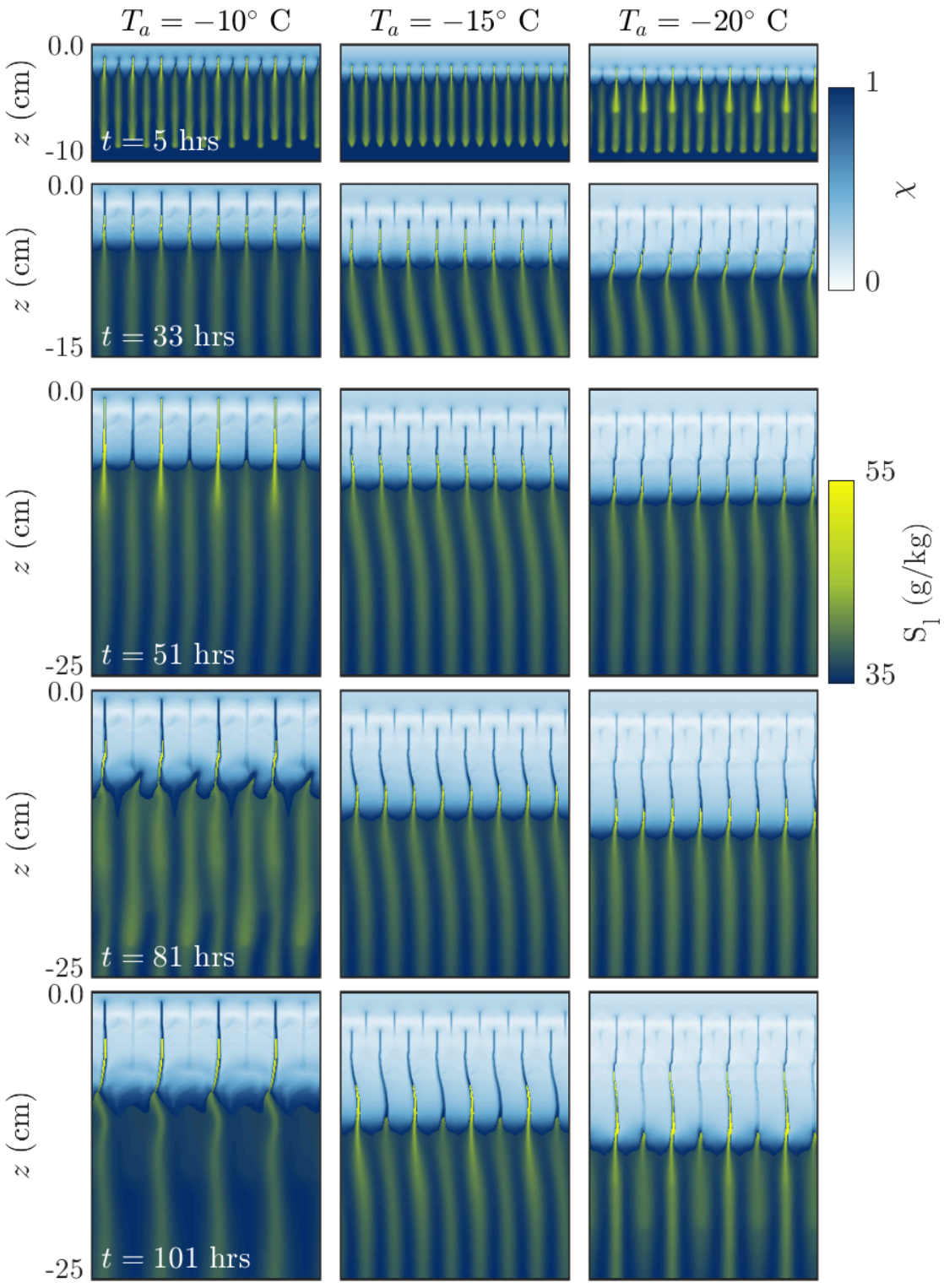


Figure 5.2: Timeseries of sea ice growth from a cold boundary held at $T_a = -10, -15$, or $-20°$C as labelled. Within the ice the colour scale gives the porosity χ. In the liquid, where $\chi = 1$, the colour scale instead gives the salinity S_l. Only the top section of the full domain, which extends down to $z = -80$ cm, is shown.

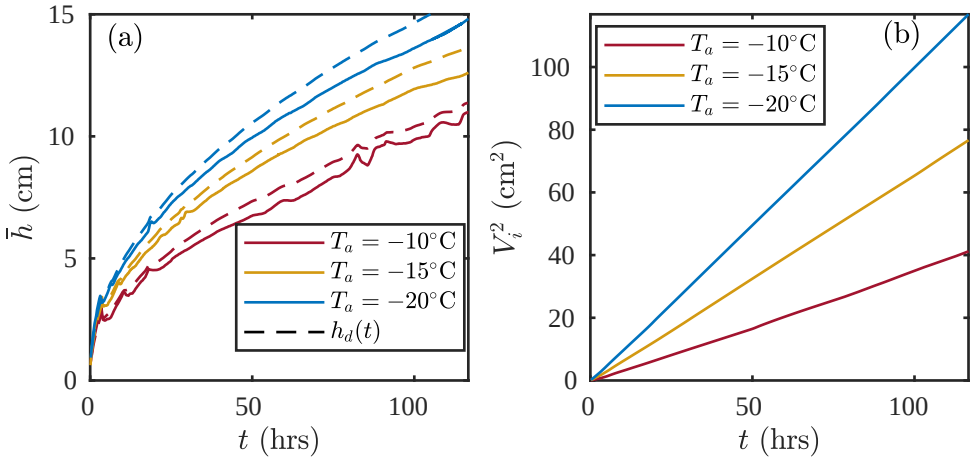


Figure 5.3: (a) The ice depth h (solid lines) is in reasonable agreement with the depth predicted for diffusive growth (5.5) where $h_d(t) \sim \sqrt{t}$ (dashed lines), suggesting that it is primarily controlled by thermal diffusion. (b) The volume of solid ice produced per cross sectional area, V_i, increases smoothly and also like $\sqrt{t}$. Dashed lines like in (a) are indistinguishable from the data plotted.

5.1.2 Rate of ice growth

There are various ways to measure the depth of the sea ice in these simulations. The height of the mush-liquid interface, where $\chi = 1$, varies significantly in the horizontal direction due to the presence of brine channels, and therefore I compute an effective ice-depth as the median: $\bar{h}(t) = \text{median}\,[h(t, x)]$. I plot the evolution of $\bar{h}(t)$ in fig. 5.3a (solid lines), alongside dashed lines h_d that are given by

$$h_d(t) = \sqrt{\frac{2k_s(T_f(S_i) - T_a)}{\bar{\phi}\,\rho_s\,L}t}, \tag{5.5}$$

where $\bar{\phi}$ is the average solid fraction in the mushy layer. This is the mush depth predicted by the Stefan condition (Worster and Rees Jones, 2015). Equation (5.5) slightly overestimates the mush depth relative to the observed growth, but is otherwise in reasonable agreement with our simulations suggesting that the modelled ice growth is controlled by thermal diffusion.

Ice growth can also be measured by computing the total volume of solid ice formed per unit width, given by

$$V_i = \frac{1}{\mathcal{L}}\int_{\mathcal{A}} \phi \, d\mathcal{A}, \tag{5.6}$$

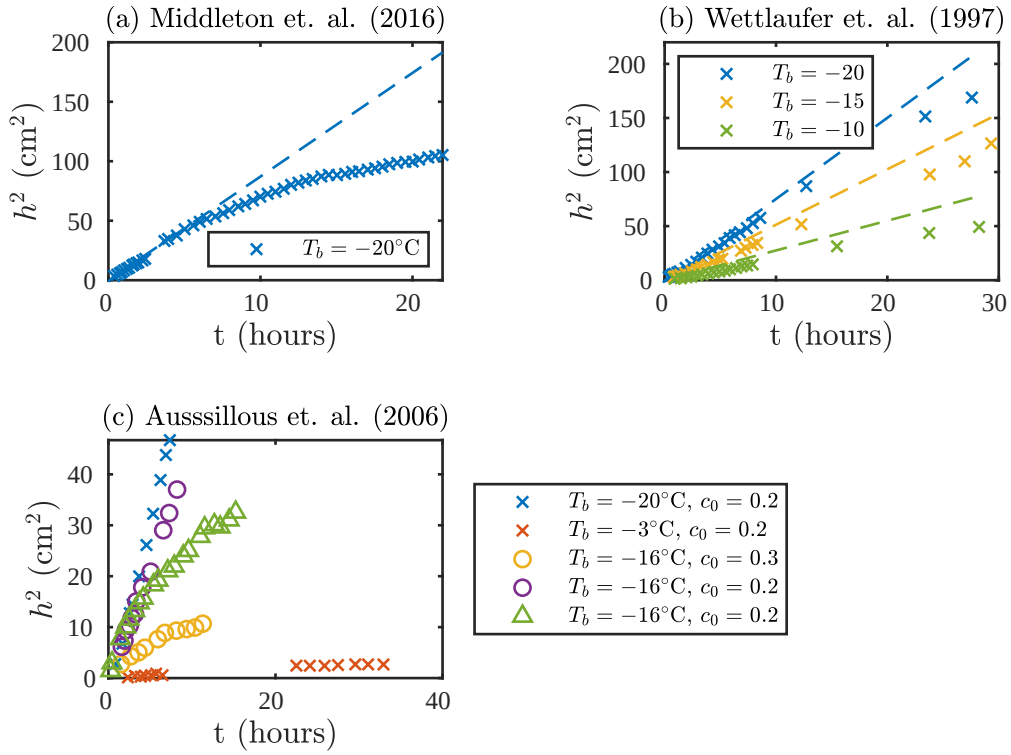


Figure 5.4: Mushy layer thickness measured during various experiments usually follows $h^2 \sim t$ at sufficiently early times. Dashed lines indicate the predicted depth (5.5) due to diffusive growth. (a) Middleton et al. (2016) grew ice from NaCl salt water (30 g/kg) in Hele-Shaw cell (height × width × depth = 64cm × 34cm × 3 mm). (b) Wettlaufer et al. (1997a) froze NaCl salt water (70 g/kg) in a cuboidal tank (height × width × depth = 37.6cm × 20cm × 20cm). (c) Aussillous et al. (2006) froze a sucrose-water solution in three different settings: a cubic tank in the laboratory (20cm in each direction, symbol: ×), and a cylindrical tank (diameter 3.7cm, height 18cm) in either the laboratory (○) or inside an MRI scanner (△). In all cases T_b is the temperature of the cold upper surface of the apparatus. In case (c) the initial liquid concentration c_0 was also varied, whilst the thermal conductivity of the sucrose solution was not reported so the mush depth predicted by (5.5) cannot be computed.

where $\mathcal{L}$ is the domain width and the integral is over the region of the domain $\mathcal{A}$ covered by the mushy layer (with $\phi > 0$). I plot $V_i^2(t)$ in fig. 5.3b, which reveals a remarkably smooth evolution over time. The linearity of $V_i^2(t)$ suggests that $V_i(t)$ also closely follows a $\sqrt{t}$ power law.

The mushy layer growth seen in these simulations, which closely follows the growth predicted by (5.5), is consistent with the classical solution to the Stefan problem (Stefan, 1891). The growth of mushy layers in the laboratory can be affected by a variety of factors which are not present in my simulations, leading to variation in the observed ice thickness. In fig. 5.4 I compile results from a variety of authors. Note

that the $y-$axis in fig. 5.4 is $h^2(t)$ so a linear relationship is consistent with growth that follows $h \sim \sqrt{t}$, as in my simulations. The experiments conducted by Wettlaufer et al. (1997b) all follow this trend closely at early times, as do those of Aussillous et al. (2006) which were performed in a cubic tank (fig. 5.4c, crosses $\times$). Aussillous et al. (2006) found that mushy layer growth in a smaller, cylindrical, container initially followed $h \sim \sqrt{t}$ before then slowing, which they attributed to heat transfer through the sides of the container which was not perfectly insulating. Middleton et al. (2016) studied solidification in a Hele-Shaw cell and also observed growth which initially follows $h \sim \sqrt{t}$ before slowing. Whilst Middleton et al. (2016) do not comment on this, it is plausible that the explanation is the same as that proposed by Aussillous et al. (2006). Indeed, when Katz and Worster (2008) modelled directional solidification in a Hele-Shaw cell they included an additional term in the heat equation to account for cooling through the plates of the cell.

The data from Middleton et al. (2016) shows good quantitative agreement with the mush depth predicted by the Stefan condition (5.5) over the range of times where $h^2 \sim t$. However the mush growth from Wettlaufer et al. (1997a) is notably slower despite being consistent with $h \propto \sqrt{t}$. Wettlaufer et al. (1997a) suggested that a growth model based on Kerr et al. (1990a,b) was a more appropriate fit to their data. Kerr et al. (1990a) showed that convection in the underlying liquid can affect the heat flux at the mush-liquid interface, resulting in growth rates which deviate from the typical Stefan solution. At very early times ($t \ll \tau$ where $\tau = h^2/\kappa$ is the diffusive timescale) convection in the liquid reduces the solidification rate by removing the supercooling which otherwise drives solidification. At later times ($t \sim \tau$) the growth rate is enhanced by convection removing the latent heat released during solidification. Meanwhile Kerr et al. (1990b) demonstrated that undercooling, where the interfacial temperature T_i is less than salinity dependent freezing point $T_f(S)$, can affect the rate of ice growth.

In our simulations, convection in the underlying liquid is weak due to the narrow Hele-Shaw cell plate separation and we have assumed that the system is in local thermodynamic equilibrium. In principle it is possible that brine plumes may carry a significant heat flux, though the agreement between the growth rates observed and those predicted by (5.5) suggests that the effect is relatively minor. It may be

that the Hele-Shaw cell used by Middleton et al. (2016) also restricts convection in the underlying liquid, hence the agreement between their mush depth and the prediction from diffusive growth theory.

5.1.3 Salt rejection

As discussed in § 5.1.2 the rate of ice production is relatively unaffected by fluid flow in these simulations, instead being primarily explained by thermodynamics. However, the flux of salt between the ice and the underlying liquid is controlled by nonlinear convection through brine channels. It is challenging to directly measure the flux between the ice and ocean numerically as the interface evolves transiently. Instead, I measure the change in bulk salinity of the mushy layer relative to the initial salinity S_i, and hence infer the horizontally averaged quantity of salt rejected into the underlying liquid

$$\check{S}(t) = \rho_0 \frac{1}{\mathcal{L}} \int_{\mathcal{A}} \left[S_i - S(x,z,t) \right] \, d\mathcal{A}, \tag{5.7}$$

where $\mathcal{L}$ is the domain width and the integral is computed over the region of the domain $\mathcal{A}$ where $\chi < 1$. In fig. 5.5, I plot $\check{S}$ and the average solid fraction of the ice $\bar{\phi}$. Initially, there is no convection and therefore no significant transport of salt between the ice and the underlying liquid ($\check{S} \approx 0$). During this period ($t < 2$ hrs), the average solid fraction $\bar{\phi}$ is roughly constant and increases as the temperature at the top of the domain, T_a, decreases. This behaviour is consistent with the analytical predictions for solidification of a mushy layer without flow (Worster, 1991). Once the ice has reached a critical depth, h_c, convection begins and $\check{S}$ increases. The removal of solute from the mushy layer promotes further internal solidification, as seen by the rapid increase in $\bar{\phi}$ in fig. 5.5b.

We can compare the solid fraction measured here with the predictions of our steady state scalings. In chapter 4 we found that during steady state growth convection was confined to a region of dimensionless depth $\tilde{h}_\chi$ where the porosity $\chi_p \sim O(1)$, whilst throughout the rest of the mushy layer (of dimensionless total depth $\tilde{h}$) the porosity was determined by the diffusive solution to the problem $\chi_{\text{interior}} = S_{\text{interior}}/S_l$. Assuming that the temperature profile within the ice is linear, the liquid salinity is given by $S_{l,\text{interior}} = S_i + \Delta S(z-h)/h$ according to the liquidus constraint (2.18). Motivated

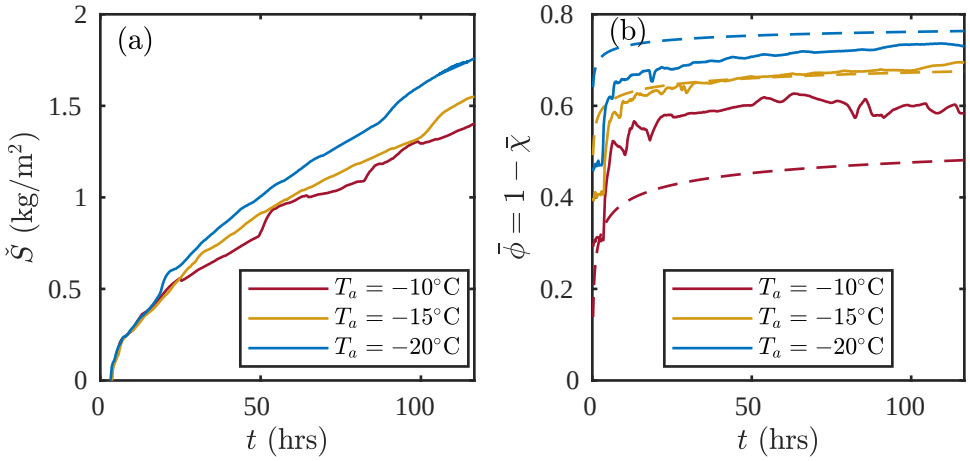


Figure 5.5: (a) Total quantity of salt $\check{S}$ rejected from the simulated sea ice increases over time following a short initial period of no salt rejection. (b) Average solid fraction within the ice $\bar{\phi}$ (solid lines) increases dramatically when salt rejections begins at around $t = 4$ hrs. The mean solid fraction also increases as the temperature at the cold boundary T_a is reduced. Dashed lines indicate the solid fraction predicted by our steady state scalings.

by the simulations (e.g. see fig. 5.8), I assume that due to the brine rejection the bulk salinity in the interior of the ice is $S_{\text{interior}} \approx 20$ g/kg in all simulations. Hence, averaging $S_{l,\text{interior}}$ over the depth of the mushy layer, the porosity within the interior is given by $\chi_{\text{interior}} \approx S_{\text{interior}}/(S_i + \Delta S/2)$. Taking the depth weighted average of χ_p and χ_{interior}, the average porosity for the whole mushy layer scales like

$$\bar{\chi} \sim \frac{1}{\tilde{h}}\left[\chi_p \tilde{h}_\chi + \frac{S_{\text{interior}}}{S_i + \Delta S/2}(\tilde{h} - \tilde{h}_\chi)\right] \sim \chi_p \frac{\tilde{h}_\chi}{\tilde{h}} + \frac{S_{\text{interior}}}{S_i + \Delta S/2}. \tag{5.8}$$

Substituting in the scalings for $\tilde{h}_\chi$ and $\tilde{h}$ (4.33), whilst recalling the definitions of the dimensionless parameters,

$$Rm = \frac{g\beta K_0 \Delta S h(t, T_a)}{\eta \kappa_l}; \quad \mathscr{C} = \frac{S_i}{\Delta S}; \quad \mathscr{S} = \frac{L}{c_p \Delta T}, \tag{5.9}$$

where we have chosen the mush depth $h(t, T_a)$ as the length scale in Rm and $\Delta T = T_f(S_i) - T_a$ whilst $\Delta S = \Delta T/\Gamma$ from the liquidus constraint (2.18), we find

$$\bar{\chi} \sim \chi_p \mathscr{S} V_f \left(\frac{\mathscr{C}}{Rm \mathscr{S}^2 V_f^2}\right)^{1/3} + \frac{S_{\text{interior}}}{S_i + \Delta S/2}, \tag{5.10}$$

$$\sim \chi_p \frac{L}{c_p\, \Delta T}\left[\frac{S_i c_p^2 (\Delta T)^2 \kappa_l \eta}{(\Delta S)^2 L^2 g \beta K_0 h(t, T_a)}\right]^{1/3} + \frac{S_{\text{interior}}}{S_i + \Delta S/2}, \tag{5.11}$$

where we have noted that $V_f = 1$. I assume that the mushy layer grows diffusively according to (5.5), and that in the high porosity boundary layer the average value of $\chi_p \approx 0.5$. Substituting for $\Delta S = \Delta T/\Gamma$, I obtain a prediction for the average mushy layer porosity as a function of the temperature difference across the mushy layer $\Delta T = T_f(S_i) - T_a$,

$$\bar{\chi} \sim \frac{L}{c_p\,\Delta T}\left[\frac{\Gamma^2 S_i c_p^2 \kappa_l \eta}{L^2 g\beta K_0\, h(t,T_a)}\right]^{1/3} + \frac{S_{\text{interior}}}{S_i + \Delta T/(2\Gamma)}, \tag{5.12}$$

which will vary as the atmospheric temperature T_a is changed. In fig. 5.5b I plot this prediction (dashed lines). The theoretical prediction captures the variation of $\bar{\phi}$ with time t reasonably accurately, whilst the exact quantitative agreement is better for some T_a than others. The variation with t is dictated by the first term in (5.12), which is the result of the $\tilde{h}_\chi$ scaling from chapter 4 suggesting that this scaling may have some utility in predicting the properties of transient growth. The quantitative disagreement is partly influenced by the approximations made in deriving (5.12). In particular, I assumed that the bulk salinity within the interior of the mushy layer was constant and independent of T_a, and that in the high porosity boundary layer $\chi_p \approx 0.5$. In the numerical simulations, there are modest deviations from these two assumptions. Additionally, the scale for the depth $\tilde{h}_\chi$, which determines the first term on the right hand side in (5.12), could in principle have a dimensionless prefactor which would alter the predicted $\bar{\chi}$.

Following the onset of convection (see § 5.1.4 for further discussion), the flux of salt out of the ice is initially very similar for each cold boundary temperature T_a. After about a day the three simulations begin to diverge. As the temperature of the top boundary is decreased, the ice growth rate increases (fig. 5.3a) and the density gradient increases, which tends to increase the rate of salt rejection, whilst the porosity of the ice decreases (fig. 5.5b), which tends to inhibit convection within the ice and reduce the quantity of salt rejected. We find that the first effect is more dominant, and therefore $\check{S}$ increases as T_a decreases. If instead we consider salt rejection as a function of ice depth, as in fig. 5.6a, we do indeed find that warmer ice rejects more salt for each centimetre of growth. The higher porosity of warmer ice also reduces the critical depth for the onset of convection.

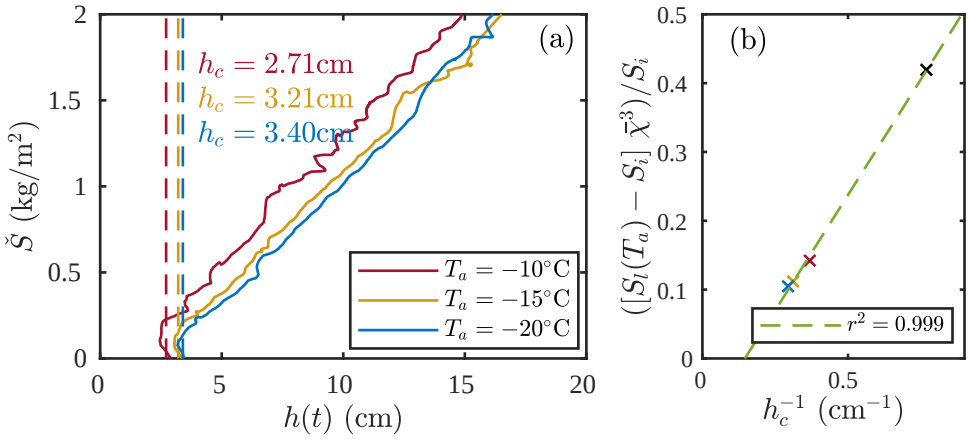


Figure 5.6: (a) Convection, and hence salt rejection, begins once the ice has reached a critical depth h_c. After the onset of convection, the ice depth initially decreases slightly as warm upwelling liquid causes melting at the mush-liquid interface. (b) It has been suggested that a local Rayleigh number proportional to $h_c\,[S_l(T_a) - S_i]\,\bar{\chi}^3$ controls the onset of convection (Wettlaufer et al., 1997a). The linear trend seen here supports this hypothesis. The black cross is the additional simulation run with a higher reference permeability $K_0 = 4 \times 10^{-10}\,\mathrm{m}^2$ (the other simulations use $K_0 = 10^{-10}\,\mathrm{m}^2$.

These results are broadly consistent with the experimental study of Wettlaufer et al. (1997b), who grew ice from salt water in a rectangular tank. Wettlaufer et al. (1997b) also found that salt rejection only begins once the ice has reached a critical depth, and that thereafter the rate of salt rejection and its variation with time, ice depth, and the cold boundary temperature is qualitatively similar to our observations.

In chapter 4 we saw that the salt rejection measured by Wettlaufer et al. (1997b) was consistent with the scaling law we identified for salt fluxes during steady state growth. In an analogous manner, I will now compare the numerically calculated salt fluxes with a dimensionless salt flux $F_s \sim \zeta \mathscr{C}^a (Rm - Rm_{crit})^b$, where $a = 7/6$ and $b = 5/6$ are the exponents which were found in chapter 4. Integrating the solute equation (5.2) across the area of the domain covered by ice $\mathcal{A}$ and using the divergence theorem yields

$$\rho_0 \int_{\mathcal{A}} \frac{\partial (S_i - S)}{\partial t} d\mathcal{A} = \rho_0 \int_{\mathcal{S}} \hat{\mathbf{F}}_s \cdot \mathbf{e}_z d\mathcal{S}. \tag{5.13}$$

Scaling by the constant domain width $\mathcal{L}$, and noting that the solute flux is 0 on all boundaries except the mush-liquid interface, I manipulate the integral on the

left hand side of (5.13) to obtain

$$\frac{\partial}{\partial t}\left(\check{S}\right) + \frac{\rho_0}{\mathcal{L}}\int_0^{\mathcal{L}} \left[S_i - S(h)\right] \frac{\partial h(t)}{\partial t} dx = \frac{\rho_0}{\mathcal{L}}\int_0^{\mathcal{L}} \hat{F}_s dx, \tag{5.14}$$

where $\check{S}$ was defined in (5.7). The horizontally averaged salt flux into the underlying liquid is given by $(\int_0^{\mathcal{L}} \hat{F}_s dx)/\mathcal{L} = F_s \Delta S \kappa_l / h$, where I have assumed that $\Delta S = S_t - S_i$ is the relevant salinity scale, κ_l/h is the velocity scale, and F_s is given by (4.44). In chapter 4 we found that the dimensionless bulk salinity at the mush-liquid interface is given by $\Theta(h) - \Theta_i \sim \mathscr{S}/Le$, and therefore $S(h) - S_i \sim (S_t - S_i)\mathscr{S}/Le$ which is independent of h, x and t. This estimate suggests that $S(h) - S_i \approx 5$ g/kg, which is consistent with the values seen in the numerical simulations. Integrating (5.14) in time from t_c to t yields

$$\check{S}(t) - \rho_0 \left[\frac{\mathscr{S}(S_t - S_i)}{Le} - S_i\right] \left[h(t) - h(t_c)\right] = \rho_0 \int_{t_c}^{t} \hat{F}_s(t')dt', \tag{5.15}$$

where I assume that there is no salt rejection before the onset of convection at t_c so $\check{S}(t_c) = 0$. Assuming that the mush depth $h(t)$ is given by (5.5), and that $h(t)$ is the relevant length scale in the mushy Rayleigh number Rm whilst $\Delta S = S_t - S_i$ is the relevant salinity scale in the concentration ratio $\mathscr{C}$ such that

$$Rm = \frac{\rho_0 g \beta K_0 h(t)}{\mu \kappa_l}, \quad \mathscr{C} = \frac{S_i}{S_t - S_i}. \tag{5.16}$$

Noting that the salinity in the underlying liquid does not change significantly due to the open bottom boundary, I follow the same procedure as in § 4.1.4 to integrate the right hand side of (5.15) yielding

$$\check{S} \sim \rho_0 \left(S_h - S_i\right) h_0 \sqrt{t} + \zeta\, \gamma (S_t - S_i)^{1+b-a} t^{(b+1)/2}, \tag{5.17}$$

$$\text{where} \quad \gamma = \rho_0 \frac{2}{b+1} \left(\frac{\rho_0 g \beta K_0}{\mu \kappa_l}\right)^b \kappa_l h_0^{b-1} S_i^a,$$

$$h_0 = \sqrt{\frac{2k_s(T_i - T_a)}{\rho_0 L}},$$

$$S_h = \frac{\mathscr{S}(S_t - S_i)}{Le}.$$

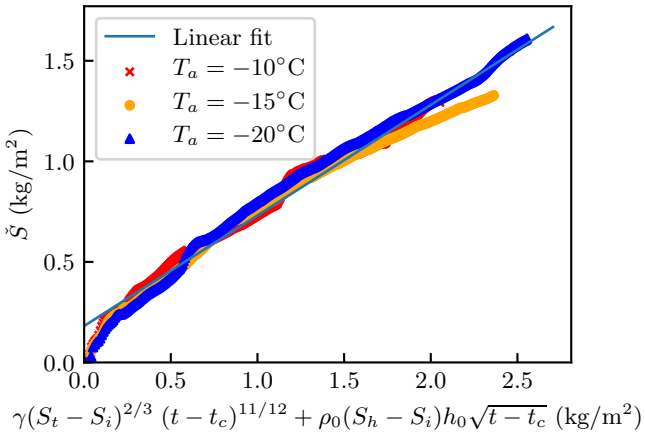


Figure 5.7: Comparison of the total quantity of salt rejected during transient simulations $\check{S}$ with the predictions from the steady state scalings found in chapter 4.

In fig. 5.7 I test the extent to which the numerical simulations obey this relationship. I find that the variation with T_a is well described by (5.17), as the three different curves approximately lie on top of each other. The variation with time is reasonably well described at late times, where there is a roughly linear relationship between $\check{S}$ and the right hand side of (5.17), but appears to break down at early times. This could be due to an initial transient adjustment following the onset of convection, during which time the steady state scalings are a less accurate representation of the dynamics. As well as the variation of $\check{S}$ with t and T_a being approximately consistent with the steady state scaling, it is encouraging to find that the magnitude of $\check{S}$ is well predicted without the use of tuning factors.

In fig. 5.8 I plot horizontally averaged profiles of the bulk salinity $\bar{S}$ within the ice. Panels (a-c) correspond to the simulations considered so far, whilst panel (d) is an additional simulation with a larger sea ice permeability. The profiles follow the commonly observed C-shaped form (Cox and Weeks, 1974; Galley et al., 2015); at the top and bottom of the ice the salinity remains at the initial value, $S_i = 35$ g/kg, whilst within the ice interior salt has been removed by convection. Some observations also find that the salinity is heavily depleted towards the top of the ice (e.g. Notz and Worster, 2008) which can result from a variety of processes not included in our idealised simulations such as flushing from melt water, turbulence during initial ice formation and accumulation of frazil ice, or upward salt transport from brine expulsion.

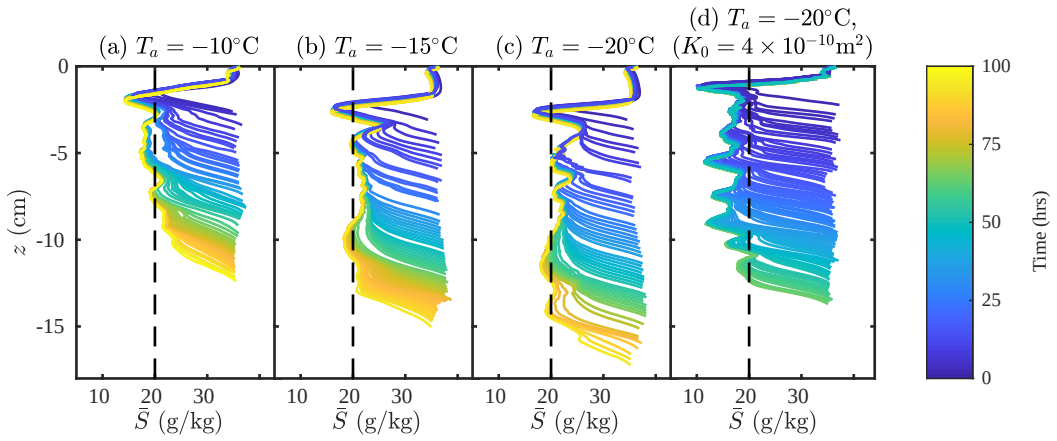


Figure 5.8: Horizontally averaged bulk salinity $\bar{S}$ within the sea ice for each simulation considered so far (a-c) and an additional simulation (d) where the sea ice permeability has been increased by a factor of 4. The dashed black line indicates highlights $\bar{S} = 20$ g/kg in each panel for ease of comparison. $\bar{S}$ remains at the initial value $S_i = 35$ g/kg at the top of the ice, where no salt rejection has occurred, and at mush-liquid interface at the bottom. Within the ice, the bulk salinity is depleted and relatively uniform through the region which has been desalinated. More desalination occurs in the simulation with higher permeability (d).

The bulk salinity within the interior of the ice shows small scale variability with depth about a roughly constant value, with a notable minimum near the top of the ice where convection first begins. This is consistent with the observations made by Nakawo and Sinha (1981). The bulk salinity is slightly lower for warmer atmospheric temperatures T_a, which is consistent with warmer ice being more porous and permitting stronger convection which desalinates the ice more efficiently.

The bulk salinity oscillates irregularly with depth, which is a feature also seen in some observations (e.g. Nakawo and Sinha, 1981; Cox and Weeks, 1974; Backstrom and Eicken, 2006) and 1-D models where brine convection has been parametrized (Griewank and Notz, 2013). The oscillations suggest that brine rejection is not a smooth process but rather that convection is, to some extent, episodic. More intense convection will drain more salt, whilst periods of weaker convection will leave more salt in the ice. Regions with lower bulk salinity will usually be less porous. Referring back to the timeseries of the porosity field during ice growth (fig. 5.2) we see some evidence for this variation. Most strikingly, in all three simulations there is a band of particularly low porosity ice near the depth where convection first begins ($z \approx -3$ cm). There is a hint that the regions of particularly low bulk salinity are related to channel coarsening

events (the variation of channel density will be discussed further in § 5.1.5). The shut down of flow in a channel is often accompanied by a brief period of strong flow which drains solute, allowing the channel to freeze up and hence preventing further flow. For example in fig. 5.2 we can see that the porosity of channels sometimes decreases visibly from one frame to the next, e.g. with $T_a = -10°\text{C}$ from $t = 33\text{hrs}$ to $t = 51\text{hrs}$ and with $T_a = -20°\text{C}$ from $t = 81\text{hrs}$ to $t = 101\text{hrs}$. It is interesting that these oscillations, which are seen in some observations (Nakawo and Sinha, 1981) are absent in others (e.g Notz and Worster, 2008) despite similar atmospheric conditions, vertical resolutions, and horizontal averaging regions in both cases. This is consistent with the suggestion that the oscillations are the result of convective dynamics, which are highly complex and may vary significantly due to small differences between sea ice growth conditions.

The average interior bulk salinity in fig. 5.8(a-c) is around 20 g/kg, whilst observed values are typically around $5 - 10$ g/kg (Notz and Worster, 2008). This is likely a consequence of using a relatively small ice permeability $K_0 = 10^{-10}\,\text{m}^2$ which restricts the strength of convection within the ice but is a practical necessity for performing these simulations over long timescales using the available computational resources. To test this hypothesis, a larger reference permeability $K_0 = 4 \times 10^{-10}\,\text{m}^2$ was considered in fig. 5.8d, which results in stronger convection and desalinates the ice more intensely. The oscillations in horizontally averaged bulk salinity are larger in the simulation with a larger permeability (fig. 5.8d), but otherwise the profiles are qualitatively similar.

5.1.4 Onset of convection

Wettlaufer et al. (1997b) hypothesised that the onset of convection is controlled by a Rayleigh number,

$$Rm_h(t) = \frac{g\,\beta\,\Delta S_l\,K(\chi)\,h(t)}{\kappa_l\,\nu}, \tag{5.18}$$

where $\Delta S_l = S_l(T_a) - S_i$ is the difference in liquid salinity between the top of the mushy layer and the liquid, and $K(\bar{\chi})$ is the characteristic permeability of the mushy layer.

Previous authors have considered the appropriate way to write the characteristic permeability for a series of vertical layers in 1-D models. Rees Jones and Worster

(2014) suggest using the harmonic mean of the permeability at each layer, whilst Vancoppenolle et al. (2010) and Notz and Worster (2008) take the least permeable layer. In multiple dimensions, the problem has received less attention. Rees Jones and Worster (2014) analysed the data from Wettlaufer et al. (1997b) and found that a permeability $K = K_0(1 - \bar{\phi})^2$ was consistent with the assumption that convection is controlled by a local Rayleigh number. Theoretically, this form of the permeability results from an array of cylinders aligned with the temperature gradient. In my numerical simulations, I have used the permeability law suggested by Freitag (1999) for sea ice: $K = K_0(1 - \phi)^3$. Inserting this relation into (5.18), I expect to find that

$$h_c^{-1} \propto [S_l(T_a) - S_i]\,\bar{\chi}^3 \tag{5.19}$$

if convection is indeed governed by a constant local Rayleigh number. In fig. 5.6b I test this hypothesis using the simulations illustrated in fig. 5.8, where the $y-$axis has been nondimensionalised by the constant initial salinity S_i. There is a good collapse to a straight line supporting the idea that the onset of convection is controlled by a suitably defined local Rayleigh number. From the gradient of the fit in fig. 5.6b we compute the value of the critical Rayleigh number $Ra_S = 0.7$. This is an order of magnitude smaller than suggested by observations of convection in sea ice (Notz and Worster, 2008) and linear stability analyses (Worster, 1992b). It is also around an order of magnitude smaller than the value we obtained in chapter 4 for steady-state growth in a narrow Hele-Shaw cell. This may be due to the effect of the underlying liquid, where the permeability $\Pi = \Pi_c = O(10)$ is relatively large. Whilst the onset of convection in our simulations is consistent with a Rayleigh number defined in terms of average properties of the mushy layer, there may also be a boundary layer mode of instability within the liquid (e.g. see Worster, 1992b) which could aid the onset of convection by a fixed constant factor which in all cases is $O(\Pi_c) = O(10)$.

5.1.5 Channel spacing

It is clear from fig. 5.2 that the number of active brine channels decreases over time or, equivalently, that the channel spacing increases with the mush depth. This picture

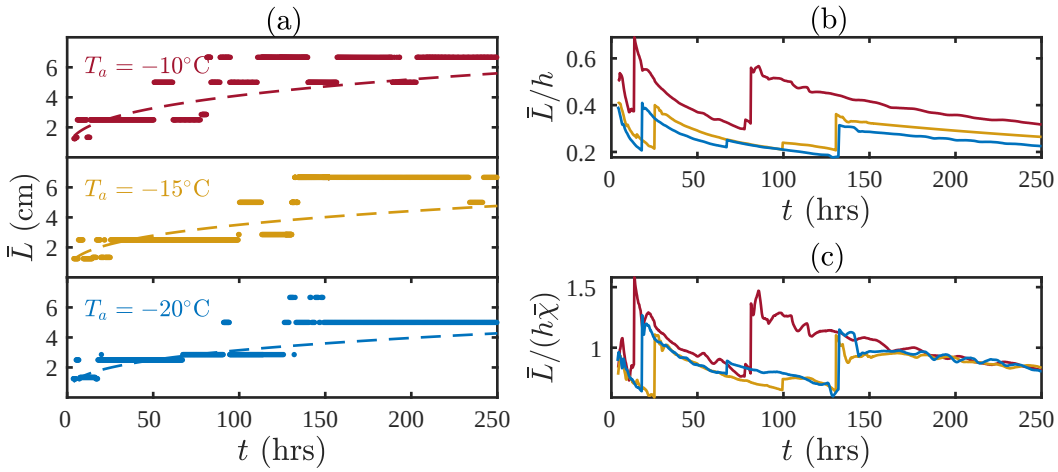


Figure 5.9: (a) Dots: average channel spacing $\bar{L}$ during simulated sea ice growth increases over time. Dashed lines: channel spacing predicted by our steady state scalings (eq. 5.23) with the assumption of diffusive growth. (b) Ratio of the channel spacing $\bar{L}$ to mush depth h. (c) Ratio of the channel spacing to the product of the mush depth and the porosity χ. For clarity, in (b) and (c) I have filtered the data to ensure that $\bar{L}$ increases monotonically over time by setting $\bar{L}(t)$ equal to maximum value of $\bar{L}(t')$ for times $t' \leq t$.

is qualitatively consistent with experiments (Middleton et al., 2016; Wakatsuchi and Saito, 1985; Tait and Jaupart, 1992) and simulations of directional solidification (Katz and Worster, 2008).

In fig. 5.9a I plot average channel spacing $\bar{L} = W/N$ for each simulation, where W is the domain width and N is the number of active brine channels found by identifying peaks in the liquid salinity field at the mush-liquid interface using the `findpeaks` function in MATLAB. Due to the finite domain width, the number of channels and hence the average spacing $\bar{L}$ is quantised. For all three values of T_a, the channel spacing fluctuates but typically increases with time. $\bar{L}$ does not vary monotonically, however, but can both increase and decrease. For $T_a = -10°C$, between 100 and 250 hours the channel spacing appears to oscillate between two different values as brine channels oscillate between being active and inactive. Solomon and Hartley (1998) saw similar behaviour during transient growth in an ammonium chloride solution, whilst Middleton et al. (2016) reported similar 'on-off' behaviour during solidification of NaCl-water in a Hele-Shaw cell.

Previous authors have identified a strong relationship between the channel spacing $\bar{L}$ and the thermodynamic growth of the mushy layer. Katz and Worster (2008) found

that the ratio of the channel spacing to the mushy layer depth satisfied

$$\frac{\bar{L}}{h} = O(1) \tag{5.20}$$

when simulating directional solidification of ammonium chloride. In the case of sea ice, observations and experiments suggest that the brine channel density N is proportional to the ice growth rate $\dot{h} = \partial h/\partial t$ (Wakatsuchi and Saito, 1985; Tison and Verbeke, 2001). In my simulations, I find that whilst the ratio $\bar{L}/h$ is roughly $O(1)$ (fig. 5.9b), a better collapse of the data is found when considering $\bar{L}/(h\,\bar{\chi})$ (fig. 5.9c). The temporal behaviour of $\bar{L}/(h\,\bar{\chi})$ is characterised by a steady decline due to the increasing mush depth, interrupted by instantaneous jumps due to a coarsening of the channel spacing. The timing of these jumps varies between simulations, which is likely a further consequence of the quantisation imposed by the finite domain width.

The steady state scalings (4.33) predict a dimensionless channel spacing λ given by

$$\lambda \sim \frac{1}{(\mathscr{C}\mathscr{S}V_f)^{1/6}Rm^{1/3}}, \tag{5.21}$$

where the governing equations have been nondimensionalised by a length scale l determined by the growth rate $\dot{h}$ according to $l = \kappa_l/\dot{h}$. Assuming that growth is diffusive, as we found to be a good approximation in § 5.1.2, we find

$$l = \frac{\kappa_l}{\dot{h}} = \kappa_l \frac{L\rho_s h}{k_s \Delta T} = \kappa_l \sqrt{\frac{2L\rho_s}{k_s}\frac{t}{\Delta T}}, \tag{5.22}$$

where $\dot{h}$ and h were given by Worster and Rees Jones (2015). Recalling the definitions of $\mathscr{C}, \mathscr{S},$ and Rm (§ 2.3), whilst noting that $\Delta S = \Delta T/\Gamma$ due to the linear liquidus, $k_s = k_l$, and $\kappa_s = \kappa_l$, we predict the dimensional channel spacing

$$\bar{L} = l\,\lambda = \left(\frac{c_p\Gamma}{S_i}\right)^{1/6}\left(\frac{\eta\kappa_l}{g\beta K_0}\right)^{1/3}\left(\kappa_l\sqrt{\frac{2L\rho_s}{k_s}}\right)^{2/3}\left(\frac{t}{\Delta T}\right)^{1/3}. \tag{5.23}$$

This prediction is plotted as a dashed line in fig. 5.9a, where we see that it agrees remarkably well with our numerical simulations, given the quantisation effects for a finite width domain.

Our steady state scalings also provide a possible explanation for the observation that in our simulations the channel spacing satisfies

$$\frac{\bar{L}}{h\,\bar{\chi}} = O(1) \tag{5.24}$$

whilst Katz and Worster (2008) found $\bar{L}/h = O(1)$. In § 5.1.3 we argued that the average mushy layer porosity could be written as the weighted sum of the porosity in the interior of the mushy layer and the porosity in the narrow boundary layer at the mush-liquid interface (eq. 5.8). Assuming further that the interior porosity satisfies $\chi_{\text{interior}} \ll \mathscr{C}$, (5.8) will be dominated by the contribution from the porous boundary layer where $\chi_p = O(1)$ and we can simply write

$$\bar{\chi} = O\left(\frac{\tilde{h}_\chi}{\tilde{h}}\right), \tag{5.25}$$

where $\tilde{h}_\chi$ is the dimensionless boundary layer depth, and $\tilde{h}$ is the dimensionless mush depth. Hence $\bar{\chi}$ is simply the fraction of the mushy layer where the porosity remains $O(1)$. This suggests that in systems with $\mathscr{C} \ll 1$, such as the sea ice modelled here, the channel spacing is affected by the confinement of convection. In contrast, Katz and Worster (2008) were modelling a system with $\mathscr{C} \gg 1$ where $\bar{\chi} \approx 1$ and flow penetrated the full depth of the mushy layer. This may explain why they found the relationship $L/h \sim O(1)$, which can be interpreted as the limit of (5.24) as $\bar{\chi} \to 1$.

In fig. 5.10 I also show that my simulations show a rough tendency for N to increase with $\dot{h}$. This can be compared with the suggestion that the channel density is proportional to the growth rate of the ice,

$$N \propto \dot{h} \tag{5.26}$$

as found by various authors (Wakatsuchi and Saito, 1985; Tison and Verbeke, 2001; Middleton et al., 2016). With a number of assumptions, it is possible to reconcile the two different scalings (5.26) and (5.24). For typical diffusive growth, the

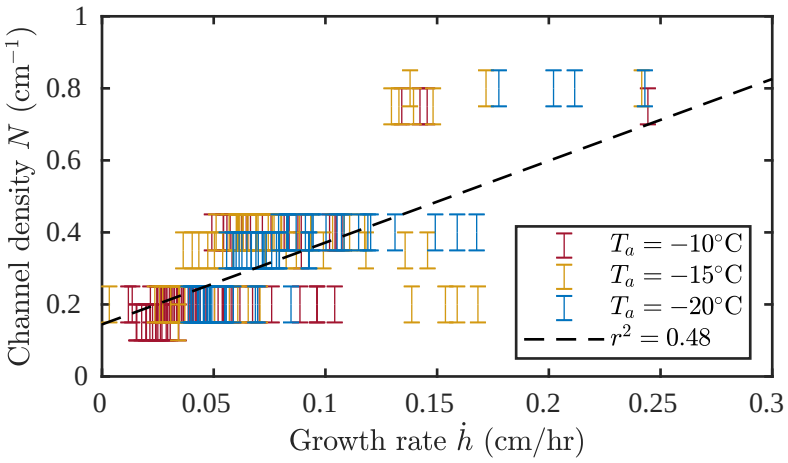


Figure 5.10: The channel density N increases with the ice growth rate $\dot{h}$, though the linear fit (dashed line) is poor ($r^2 = 0.48$) due to the noisy data. For clarity, data points are sampled from the simulation at an interval of approximately 1 per hour. Error bars indicate the possible range of channel densities due to the discretisation introduced by a finite-width domain. For each observed channel density N the error bar spans the range of densities that would be occupied if there were one less or one more channel, i.e. $[N - 1/W, N + 1/W]$ where W is the domain width.

growth rate scales like

$$\dot{h} \sim \frac{\Delta T}{\alpha\, h} \tag{5.27}$$

where ΔT is the temperature difference driving solidification, and $\alpha = k_s/(L\rho_s)$ is a dimensional constant (Worster and Rees Jones, 2015). Therefore, using the relationship we identified in (5.24), we can write the channel density as

$$N = \frac{W}{\bar{L}} \propto \frac{1}{h\,\bar{\chi}} \propto \alpha \frac{\dot{h}}{\Delta T\,\bar{\chi}}. \tag{5.28}$$

The temperature difference across the ice ΔT is constant once the top of the ice has reached the atmospheric temperature, at which point $\Delta T = T_i - T_a$. Meanwhile, in fig. 5.5b we saw that the mean porosity $\bar{\chi}$ was also approximately constant after the initial transient adjustment. Therefore the denominator in (5.28) is approximately constant so

$$N \propto \frac{\alpha}{S}\dot{h}, \tag{5.29}$$

which is equivalent to (5.26) but with a different constant prefactor α/S. Hence, (5.26) and (5.24) are consistent.

It is important to remember that the results presented here relate to a 2-D geometry. In 3-dimensions, the properties of interest are the typical channel drainage area, rather than the channel separation, and the density of channels per area. Observations suggest that (5.26) generalises to $N \sim \dot{h}^2$, and therefore I predict that in 3-D the channel drainage area will satisfy $A/(h\,\bar{\chi})^2 \sim O(1)$. This is the 3-D analogy of the 2-D result ($L/h\bar{\chi} = O(1)$) with $A \sim L^2$.

5.2 Variation with concentration ratio

In this section I will investigate the effect of the dimensionless concentration ratio on convection in mushy layers. All results, variables, and equations will, unless otherwise specified, now be in dimensionless form. Lengths have been nondimensionalised by the box depth $\hat{h}$, time by $\hat{h}^2/\kappa_l$, and velocity by $\kappa_l/\hat{h}$. As previously mentioned in § 1.2.3, the concentration ratio $\mathscr{C} = (S_i - S_s)/\Delta S$ has a strong influence on the dynamics of convection in mushy layers. In particular, when $\mathscr{C} \ll 1$ the mushy layer typically has a low porosity except at the mush-liquid interface, whilst when $\mathscr{C} \gg 1$ the porosity is very high throughout the mushy layer. Whilst for sea ice $\mathscr{C} \approx 0.15 \ll 1$, other systems can span a wide range of values (e.g. Wettlaufer et al. (1997b) considered $\mathscr{C}$ as small as 0.05, whilst Peppin et al. (2008) went as high as $\mathscr{C} \sim 16$). Whilst some features of mushy layer convection are observed for all $\mathscr{C}$, such as the presence of narrow liquid channels, there are also notable differences. For example, in systems with smaller $\mathscr{C}$ the critical mush thickness for convection is increased (Wettlaufer et al., 1997b; Aussillous et al., 2006) whilst the resulting convection is thereafter confined to a shallower region of the mush (Aussillous et al., 2006; Notz and Worster, 2008).

I will present dimensionless results from numerical simulations of mushy layer growth from a cold boundary which span $0.02 < \mathscr{C} < 100$. Simulations are conducted in a 2-D Hele-Shaw cell as illustrated in fig. 5.11, with the dimensionless parameters

$$\mathscr{S} = 5, \quad \Pi_c = 10, \quad Le = 100, \quad c_p = k = 1. \tag{5.30}$$

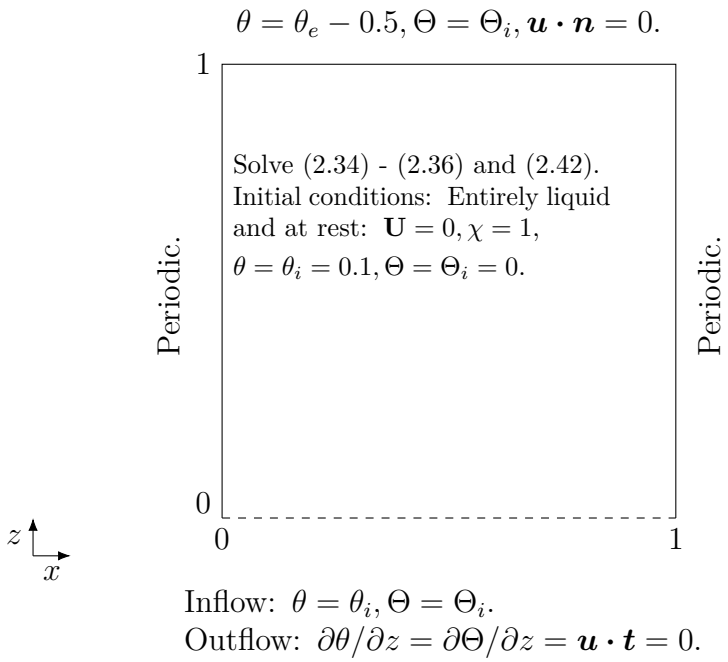


Figure 5.11: Simulations in § 5.2 are conducted in a narrow Hele-Shaw cell, with the top boundary held below the eutectic temperature and an open bottom boundary. The domain is periodic in the horizontal (x) direction, with a resolution of 256×256 grid points.

held fixed in most simulations. As in § 5.1, the fluid flow is well described by Darcy's law in both porous and purely liquid regions. I will consider a range of mushy Rayleigh numbers $50 \leq Rm \leq 200$, but will particularly focus on $Rm = 75$ to fix the strength of buoyancy forcing and consider the effect of varying $\mathscr{C}$. In § 5.2.1 I will investigate how the onset of convection is controlled by $\mathscr{C}$, then in § 5.2.2 I will describe qualitatively how the convective dynamics vary with $\mathscr{C}$. In § 5.2.3, I will present quantitative results for how the properties of the mushy layer vary with $\mathscr{C}$. Lastly, I will consider how the brine channels evolve in § 5.2.5.

5.2.1 Onset of convection

As in § 5.1, convection only begins once the mushy layer has reached a critical depth h_c which I plot in fig. 5.12 for a range of $\mathscr{C}$ and Rm. The critical depth was computed by first identifying the time where convection began (t_c) from the velocity field then deducing the mush depth at this time, as illustrated in fig. 5.13. Due to the approximations involved in this process, the data in fig. 5.12 shows some scatter.

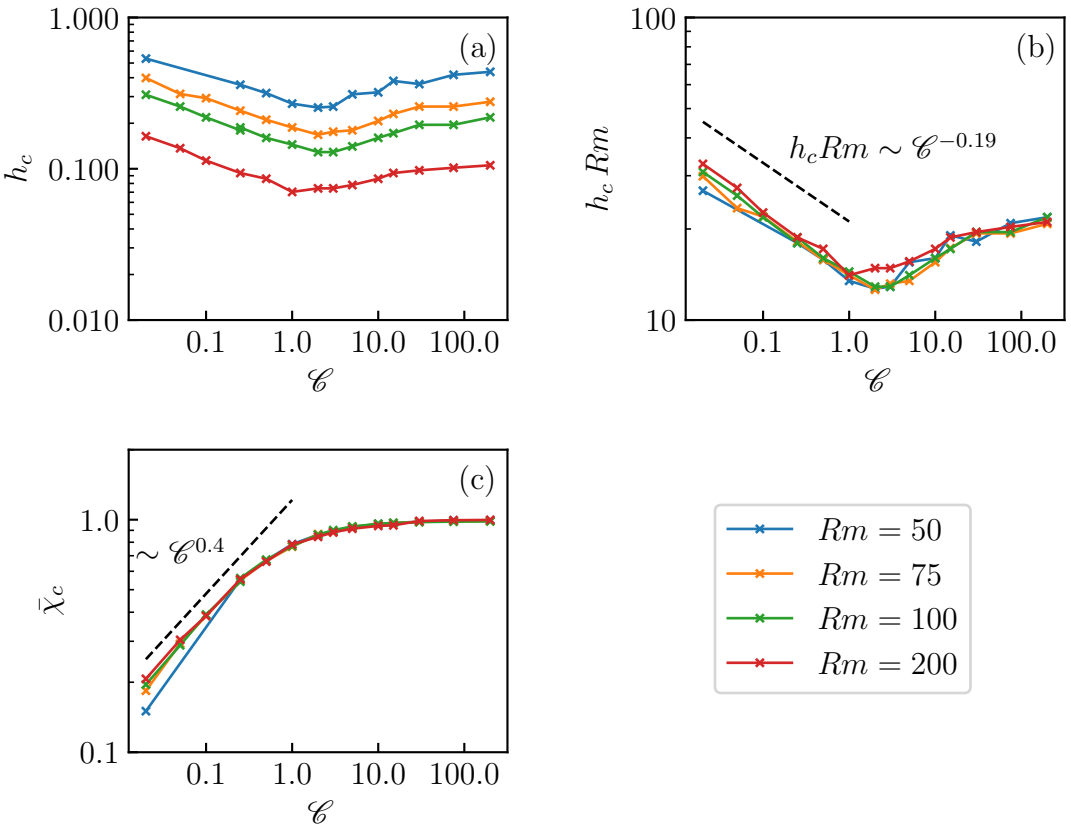


Figure 5.12: (a) The critical mushy layer depth h_c, after which convection begins, decreases as the concentration ratio $\mathscr{C}$ is increased for $\mathscr{C} \lesssim 1$, and then begins to increase as the $\mathscr{C}$ continues to increase for $\mathscr{C} \gtrsim 1$. The critical depth increases as the mushy Rayleigh number Rm is decreased. (b) Increasing Rm is equivalent to reducing the length scale, so $h_c\,Rm$ is approximately constant for fixed $\mathscr{C}$. (c) The average mushy–layer porosity at the onset of convection $\bar{\chi}$ is approximately independent of Rm and increases with increasing $\mathscr{C}$. For $\mathscr{C} < 1$, power law fits of the form $y \sim \mathscr{C}^a$ (dashed black lines, offset in the y direction) find exponents : $h_c Rm \sim \mathscr{C}^{-0.19}$ and $\bar{\chi}_c \sim \mathscr{C}^{0.40}$.

Increasing the mushy Rayleigh number,

$$Rm = \frac{g\,\beta\,\Delta S\,\mathcal{H}\,K_0}{\kappa_l\,\eta}, \tag{5.31}$$

is equivalent to increasing the box depth $\mathcal{H}$. Therefore the approximate collapse of the data in fig. 5.12b, where I plot $h_c\,Rm$, suggests that for a given value of $\mathscr{C}$ the onset of convection is controlled by a critical Rayleigh number

$$Rm_{crit} = Rm\,h_c = \frac{g\,\beta\,\Delta S\,\mathcal{H}\,K_0}{\kappa_l\,\eta}\frac{\hat{h}_c}{\mathcal{H}} = \frac{g\,\beta\,\Delta S\,\hat{h}_c\,K_0}{\kappa_l\,\eta}, \tag{5.32}$$

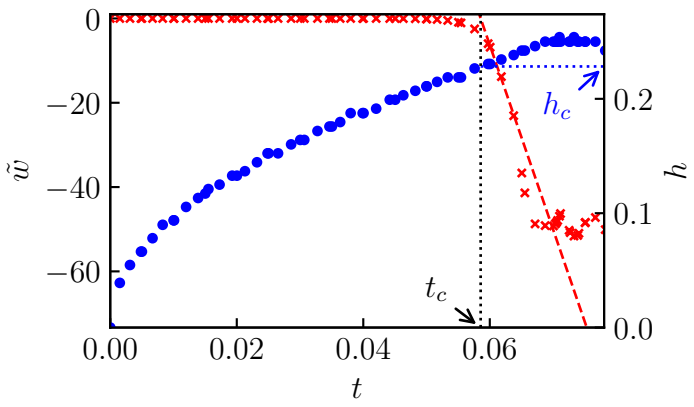


Figure 5.13: Example calculation of the critical mushy layer depth h_c. We first compute the critical time t_c by linear extrapolation from the first 3 values of the minimum vertical velocity $\tilde{w}$ (red, left axis) where $|\tilde{w}| > 0.1\ \max|\tilde{w}|$. $\max|\tilde{w}|$ is the maximum vertical speed found in the entire simulation. We then interpolate within the mushy layer depths h (blue, right axis) to find the critical depth h_c.

where $\hat{h}_c$ is the dimensional critical mushy layer depth.

The variation of the critical depth h_c with the global Rayleigh number Rm is analogous to experiments of growth during directional solidification where an imposed growth rate V controls the length scale. For example, Whiteoak et al. (2008) found that increasing V, and hence decreasing the thermal diffusion length scale κ_l/V, inhibited the onset of convection. In transient experiments changing the length scale is less achievable, however Tait and Jaupart (1992) found that the onset of convection was dependent on the fluid viscosity η with a relationship that was consistent with the onset being controlled by a critical Rayleigh number.

For $\mathscr{C} \lesssim 1$, we find that $h_c Rm$ increases with decreasing $\mathscr{C}$ in a manner roughly described by an empirical scaling $h_c Rm \sim \mathscr{C}^{-1/4}$ (fig. 5.12b). This is a somewhat weaker power than we found in § 4.1.1 (where $Rm_{crit} \sim \mathscr{C}^{-0.6}$) for steady state growth. In § 5.1.4 we saw that mushy layers grown from a colder boundary are less porous, which led to a larger critical thickness. Here the boundary conditions are identical in all simulations, but reducing $\mathscr{C}$ reduces the mushy–layer porosity (fig. 5.12c), and therefore the permeability which we see from (5.32) also controls the onset of convection. This is consistent with our observation that the critical thickness increases as $\mathscr{C}$ is decreased. The empirical scaling $h_c Rm \sim \mathscr{C}^{-1/4}$ is weaker than would be expected if the onset of convection is determined purely by the permeability of the mean porosity

within the mushy layer. We find that the critical porosity is well described by an empirical scaling $\bar{\chi}_c \sim \mathscr{C}^{0.4}$ for $\mathscr{C} \ll 1$ (fig. 5.12c), and therefore the permeability in the mushy layer will scale like $\Pi \sim \chi^3 \sim \mathscr{C}^{1.2}$ which is a significantly stronger dependence on $\mathscr{C}$. This suggests that in these simulations the onset of convection may be dependent on local variations within the mushy layer which are not captured by the mean values, or may be more dependent on the permeability of the Hele-Shaw cell than the permeability of the mushy layer. The latter behaviour could be indicative of the boundary layer mode of instability (Worster, 1992b), which develops at the mush-liquid interface rather than within the mushy layer itself.

For large $\mathscr{C}$ this trend is reversed, and h_c increases as $\mathscr{C}$ increases before appearing to tend towards a constant value as $\mathscr{C} \to \infty$. Using a linear stability analysis, Worster (1992b) found that the critical Rayleigh number for steady-state convection decreased with increasing $\mathscr{C}$ monotonically: base states with a higher porosity were less stable. The increase in h_c with large $\mathscr{C}$ in the fully nonlinear simulations here, which is equivalent to the critical Rayleigh number increasing with large $\mathscr{C}$, is contrary to this picture. To try and understand the origin of this behaviour, in fig. 5.14 I consider the variation of h_c with the other system parameters.

In fig. 5.14a I find that varying the Lewis number Le, which controls the strength of solute diffusion relative to thermal diffusion, has a relatively small effect on systems with large $\mathscr{C}$. $h_c\,Rm$ changes by at most a factor of 1.5 as Le varies by 2 orders of magnitude. When $\mathscr{C}$ is small, decreasing Le – and therefore increasing the strength of solute diffusion – slightly reduces h_c. This may be due to the diffusive transport of solute from the top of the mushy layer towards the mush-liquid interface, which would increase the porosity at the base of the mush layer and promote the development of flow within the boundary layer mode of instability.

In fig. 5.14b I find that varying the Stefan number $\mathscr{S}$ has a significant effect on the stability of the mushy layer for $\mathscr{C} \ll 1$. Decreasing $\mathscr{S}$ makes the system more stable. Worster (1992b) also found that decreasing $\mathscr{S}$ increases the stability, and suggested an explanation. Salty fluid sinking through the mushy layer becomes less dense as it dissolves the solid phase, slowing its descent and therefore inhibiting convection. Phase change is more readily achievable in systems with smaller $\mathscr{S}$, which effectively have a

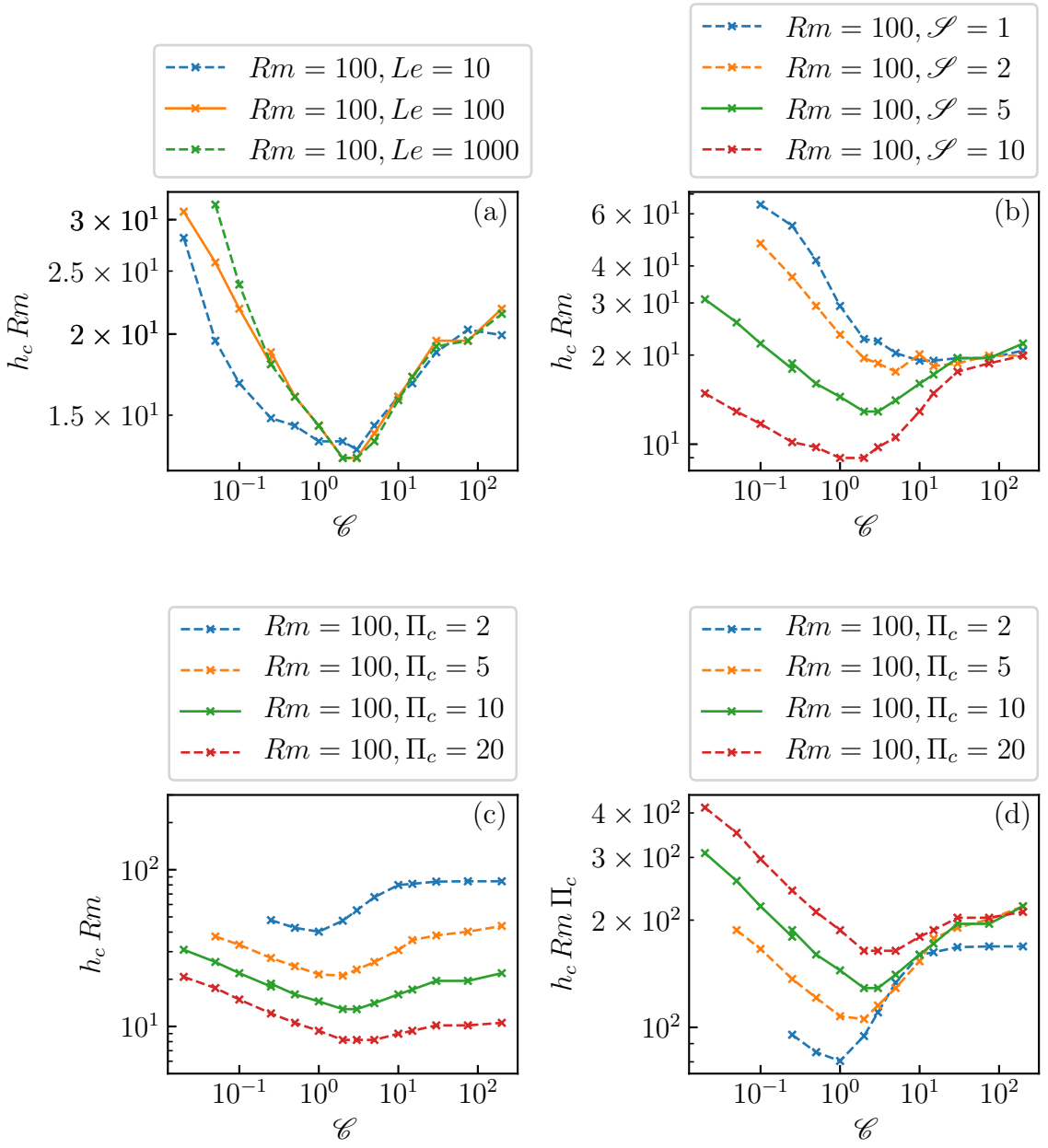


Figure 5.14: Variation of the critical depth with $\mathscr{C}$ and (a) the Lewis number Le, (b) the Stefan number $\mathscr{S}$ and (c, d) the Hele-Shaw cell permeability Π_c (note the different $y-$axes). In (d) we demonstrate that $h_c Rm \Pi_c$ is approximately constant for $\mathscr{C} \gtrsim 1$. In all panels the solid line is the simulation with $Rm = 100, \mathscr{S} = 5, \Pi_c = 10, Le = 200$. All plots use log-log axes.

lower latent heat and therefore are more stable. When $\mathscr{C} \gg 1$, the solid fraction is very small so this mechanism is no longer significant; there is only small variation in h_c with $\mathscr{S}$ and the curves in fig. 5.14b approach each other for large $\mathscr{C}$. It is particularly interesting that h_c varies monotonically for $\mathscr{C} > 0.1$ and $\mathscr{S} = 1$ as the results presented by Worster (1992b) were also calculated for these parameters. This may be why Worster (1992b) did not find the increase in critical Rayleigh number with $\mathscr{C}$ that we see here.

There is also significant variation in h_c with the permeability of the Hele-Shaw cell, Π_c, as seen in fig. 5.14c. In regions of high porosity ($\chi \approx 1$), Π_c controls the maximum permeability of the system, because

$$\Pi = \left[\Pi_c^{-1} + \Pi_m(\chi)^{-1}\right]^{-1} \sim \Pi_c \text{ as } \chi \to 1, \tag{5.33}$$

where $\Pi_m(\chi) = \chi^3/(1-\chi^2)$. Therefore increasing Π_c makes the system less stable. For large $\mathscr{C}$, the porosity $\chi \approx 1$ and therefore the total permeability is well approximated by $\Pi \approx \Pi_c$. The mushy Rayleigh number (5.31) scales linearly with permeability, which motivates fig. 5.14d where I scale $h_c Rm$ with the permeability of the Hele-Shaw cell. The collapse for $\mathscr{C} \gg 1$ is consistent with the earlier suggestion that in this limit $\chi \approx 1$ throughout the mushy layer, so $\Pi \approx \Pi_c$ is the relevant permeability scale. When $\mathscr{C} \ll 1$, the permeability is more strongly determined by the porosity of the mushy layer and hence the curves in fig. 5.14d show considerable variation for small $\mathscr{C}$. There is still significant variation of $h_c Rm$ with Π_c for all $\mathscr{C}$, which lends further support to the suggestion made earlier that the boundary layer mode of instability (Worster, 1992a) is at least partly responsible for the onset of convection.

The dependence of h_c on $\mathscr{C}, \mathscr{S}$, and Π_c is broadly consistent with the results of the weakly nonlinear stability analysis performed by Amberg and Homsy (1993) for steady state directional solidification in the limit $\mathscr{C} \gg 1$. By expanding the permeability as

$$\Pi(\phi) = 1 + \Pi_1 \phi + \Pi_2 \phi^2 + ..., \tag{5.34}$$

with $\phi = 1 - \chi$. Amberg and Homsy (1993) found a first order correction Rm_1 to the

critical Rayleigh number $Rm_{crit} = Rm_0 + Rm_1 + ...$ given by

$$Rm_1 = \frac{\pi(\Pi_1 - 2\mathscr{S})}{2\mathscr{C}}. \tag{5.35}$$

The correction (5.35) contains two terms which depend on $\mathscr{C}$ with opposite signs. The first term, $\pi\Pi_1/(2\mathscr{C})$, describes how decreasing the permeability (either by increasing the sensitivity Π_1 of the permeability to the solid fraction or decreasing the concentration ratio $\mathscr{C}$) will increase the critical Rayleigh number. This is because a less permeable mushy layer at lower $\mathscr{C}$ will offer more resistance to flow.

The second term, $-\pi\mathscr{S}/\mathscr{C}$, describes how increasing the effective heat capacity of the mushy layer (either by increasing $\mathscr{S}$ or decreasing $\mathscr{C}$) will decrease the critical Rayleigh number by inhibiting phase change with increasing $\mathscr{S}/\mathscr{C}$. We can gain some insight into the origin of this behaviour by considering the heat and solute equations in the limit $\mathscr{C} \gg 1$, where the heat equation decouples to become

$$\Omega\left(\frac{\partial\theta}{\partial t} + \mathbf{U}\cdot\nabla\theta\right) = \nabla^2\theta, \tag{5.36}$$

(Worster, 2000) where $\Omega = 1 + \mathscr{S}/\mathscr{C}$ is an effective scaled heat capacity. The effective heat capacity Ω describes both the specific heat and the energy required to change the solid fraction of the mushy layer due to the latent heat that must be extracted to solidify during cooling (or latent heat released to dissolve solid during warming). Systems with large $\mathscr{C}$ have a small solid fraction and hence a small effective heat capacity compared to systems with smaller $\mathscr{C}$. The dimensionless group Ω reveals that, in this context, increasing $\mathscr{C}$ has the same effect as decreasing $\mathscr{S}$. Systems with larger $\mathscr{C}$ have a greater abundance of solute, which makes it easier to dissolve the solid phase. This serves to increase the stability of the mushy layer, as dense fluid sinking through the mushy layer will become lighter through dissolution of the solid matrix which reduces its buoyancy. As $\mathscr{C} \to \infty$ there is a saturation effect so the effective heat capacity $\Omega \to 1$ and $Rm_1 \to 0$. This is reflected in our results, where we see that h_c tends towards a constant value as $\mathscr{C} \to \infty$.

When the variation of the permeability with the solid fraction $\phi = 1 - \chi$ is small, such that $\Pi_1 = \partial\Pi/\partial\phi \ll 2\mathscr{S}$, (5.35) is approximated by $Rm_1 \approx -\pi\mathscr{S}/\mathscr{C}$ and increasing $\mathscr{C}$ will have a stabilising effect, as I observe.

I next compare the consequences of (5.35) to the observed variation of stability. For the simulations here, the permeability is given by (2.38) and therefore

$$\Pi_1 = \frac{\partial\Pi}{\partial\phi} = -\frac{2\phi(1-\phi)+3\phi^2}{(1-\phi)^4\left(\Pi_c^{-1}+\phi^2/(1-\phi)^3\right)^2}. \tag{5.37}$$

Expanding for small $\phi \ll 1$ yields

$$\Pi_1 = \frac{\partial\Pi}{\partial\phi} \sim 2\phi\Pi_c^2. \tag{5.38}$$

In the limit $\mathscr{C} \gg 1$, the analytic solution for solidification without flow (Worster, 1991) reveals that the solid fraction varies approximately linearly through the mushy layer from 0 at the mush–liquid interface to $\phi_e = 1/\mathscr{C}$ at the eutectic boundary. Averaging $\phi \approx \phi_e z/h$ over the depth h, the typical solid fraction will scale like $\bar{\phi} \sim (0+\phi_e)/2 \sim 1/(2\mathscr{C})$. Hence,

$$\Pi_1 = \frac{\partial\Pi}{\partial\phi} \sim \frac{\Pi_c^2}{\mathscr{C}}, \tag{5.39}$$

$$\implies Rm_1 \sim \frac{\pi\left(\Pi_c^2/\mathscr{C} - 2\mathscr{S}\right)}{2\mathscr{C}}. \tag{5.40}$$

In fig. 5.15a I plot Rm_1 i for various values of Π_c and $\mathscr{C}$, whilst keeping $\mathscr{S} = 5$ fixed. Rm_1 has a minima at $\mathscr{C}^* = \Pi_c^2/\mathscr{S}$, which is highlighted by a black dashed line. For $\mathscr{C} < \mathscr{C}^*$, increasing $\mathscr{C}$ will decrease Rm_1 and therefore is destabilising. Conversely, for $\mathscr{C} > \mathscr{C}^*$, increasing $\mathscr{C}$ has a stabilising effect. In fig. 5.15b I compute the concentration ratio at which stability is minimised $\mathscr{C}^*$ for all of my numerical simulations (black crosses, see caption for details of the method) and compare these results with the value predicted by the weakly nonlinear stability analysis, $\mathscr{C}^* = \Pi_c^2/\mathscr{S}$ (dashed line). There is considerable scatter, but the data qualitatively captures the predicted increase in $\mathscr{C}^*$ with $\Pi_c^2/\mathscr{S}$. The quantitative comparison is less clear, particularly for smaller $\mathscr{C}$, though is potentially approaching the theoretically predicted slope for $\Pi_c^2/\mathscr{S} > 10$.

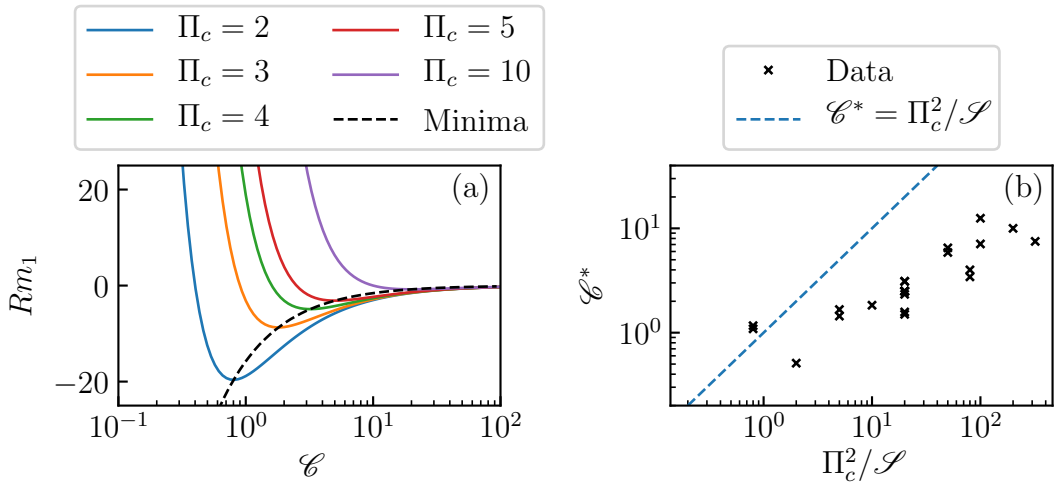


Figure 5.15: (a) Variation of the predicted 1st order correction to the critical Rayleigh number Rm_1 approximated via (5.40) with Π_c and $\mathscr{C}$ whilst $\mathscr{S} = 5$. Rm_1 has a minima at $\mathscr{C}^* \sim \Pi_c^2/\mathscr{S}$ (indicated by the black dashed line), above which increasing $\mathscr{C}$ increases Rm_1 and therefore has a stabilising influence. (b) The numerically determined $\mathscr{C}^*$ from our simulations (black crosses) roughly follows the predicted trend (blue dashed line). We compute the concentration ratio of minimum stability $\mathscr{C}^*$ by first identifying the minima of $h_c(\mathscr{C})$ using the `find_peaks` function in the `scipy.signal` python package, then fitting a quadratic to the three smallest values of $h_c(\mathscr{C})$ near the minima. There is considerable scatter due partly to both the uncertainty in computing h_c (discussed earlier in § 5.2.1) and the uncertainty in this fitting process.

Both the nonlinear stability analysis which yields (5.35) and the derivation of (5.38) assume that $\mathscr{C} \gg 1$, and therefore it is not surprising to see deviations from the linear trend for the smaller values of $\mathscr{C}$. The data may lie below the predicted trend due to the approximations made in computing Π_1. To evaluate (5.38) we assumed that the solid fraction ϕ was given by the average across the entire mushy layer, however previous results in this section have suggested that the instability may develop at the mush-liquid boundary. In this case, the appropriate ϕ should be calculated over some fraction of the mushy layer close to the mush-liquid boundary, which would make Π_1 smaller and shift the data towards the predicted scaling.

Experimental studies of mushy–layer convective instability have typically focused on the dependence of channel formation on the Rayleigh number, either by varying the fluid viscosity (Tait and Jaupart, 1992), the relevant length scales (Peppin et al., 2008) or the mushy layer porosity (Wettlaufer et al., 1997b). Peppin et al. (2008) also varied the concentration of the fluid they were solidifying, enabling them to consider

values of $\mathscr{C}$ up to ~ 16, but did not observe the increase in critical depth with $\mathscr{C}$ found here. This is not surprising as we found that this effect only occurs when $\mathscr{C} \gtrapprox \Pi_c^2/\mathscr{S}$. The Hele-Shaw cell used by Peppin et al. (2008) had a plate spacing $d = 0.5$ cm corresponding to a dimensionless permeability $\Pi_c = K_c/K_0 \approx 10^4$ (where we have estimated $K_0 \approx 10^{-9}$ for ammonium chloride following Tait and Jaupart (1992)). Hence $\mathscr{C} < \Pi_c^2/\mathscr{S}$ and we are not in the stabilising regime. It would be interesting for future experiments to explore the parameter regime $\mathscr{C} > \Pi_c^2/\mathscr{S}$ where, according to the numerical results here and previous nonlinear stability studies (Amberg and Homsy, 1993), increasing $\mathscr{C}$ may increase stability of a mushy–layer.

5.2.2 Phenomenology of convection

Once convection has begun, in all simulations the resulting behaviour is highly nonlinear. To illustrate the dynamics, the porosity field χ is presented for a range of simulations in fig. 5.16 at dimensionless time $t = 0.4$, and in fig. 5.17 at $t = 1.0$. These figures are representative of the flow and solidification seen across the range of times explored by our simulations.

The general patterns of convection are the same as those already seen in § 5.1. Narrow liquid channels form within the mushy layer where dense solute enriched fluid sinks into the underlying liquid. In simulations with small $\mathscr{C}$, the porosity is typically small which restricts flow (and hence channels) to the region of higher porosity at the mush–liquid interface (e.g. panels a–b). This is analogous to the confinement of convection predicted by the simulations and steady-state scalings in chapter 4 for small $\mathscr{C}$. As growth continues, the porosity in the upper layers of the mushy layer decreases, and the active layer within which convection can occur moves downwards with the mush–liquid interface. For example, in fig. 5.16a channels are visible in the range $0.55 \lesssim z \lesssim 0.65$ whilst in fig. 5.17a the mush has grown deeper and active channels exist for $0.35 \lesssim z \lesssim 0.45$. Where $\mathscr{C}$ is large, the porosity is higher and convection can penetrate through the full depth of the mushy layer.

For all values of $\mathscr{C}$, I find that channels can move horizontally through the mushy layer. In general the speed of horizontal motion is greater near the base of the mushy layer where the porosity is higher, leading to channels which are sloped relative to

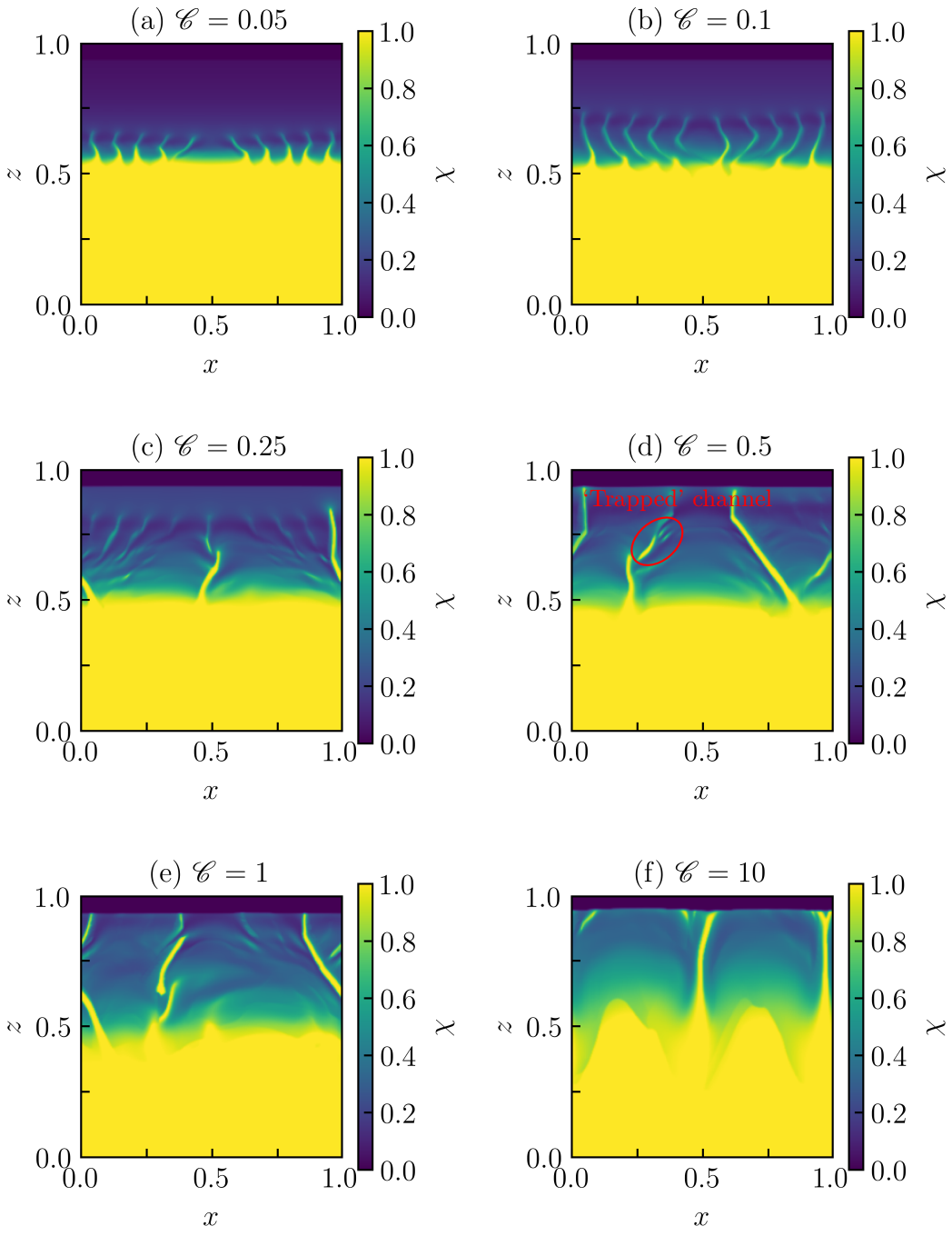


Figure 5.16: Porosity χ at dimensionless time $t = 0.4$ for a range of concentration ratios $\mathscr{C}$ with $Rm = 75$ (see sub panel titles). A 'trapped' channel – an entirely liquid region which has become detached from the underlying liquid – is circled in (d).

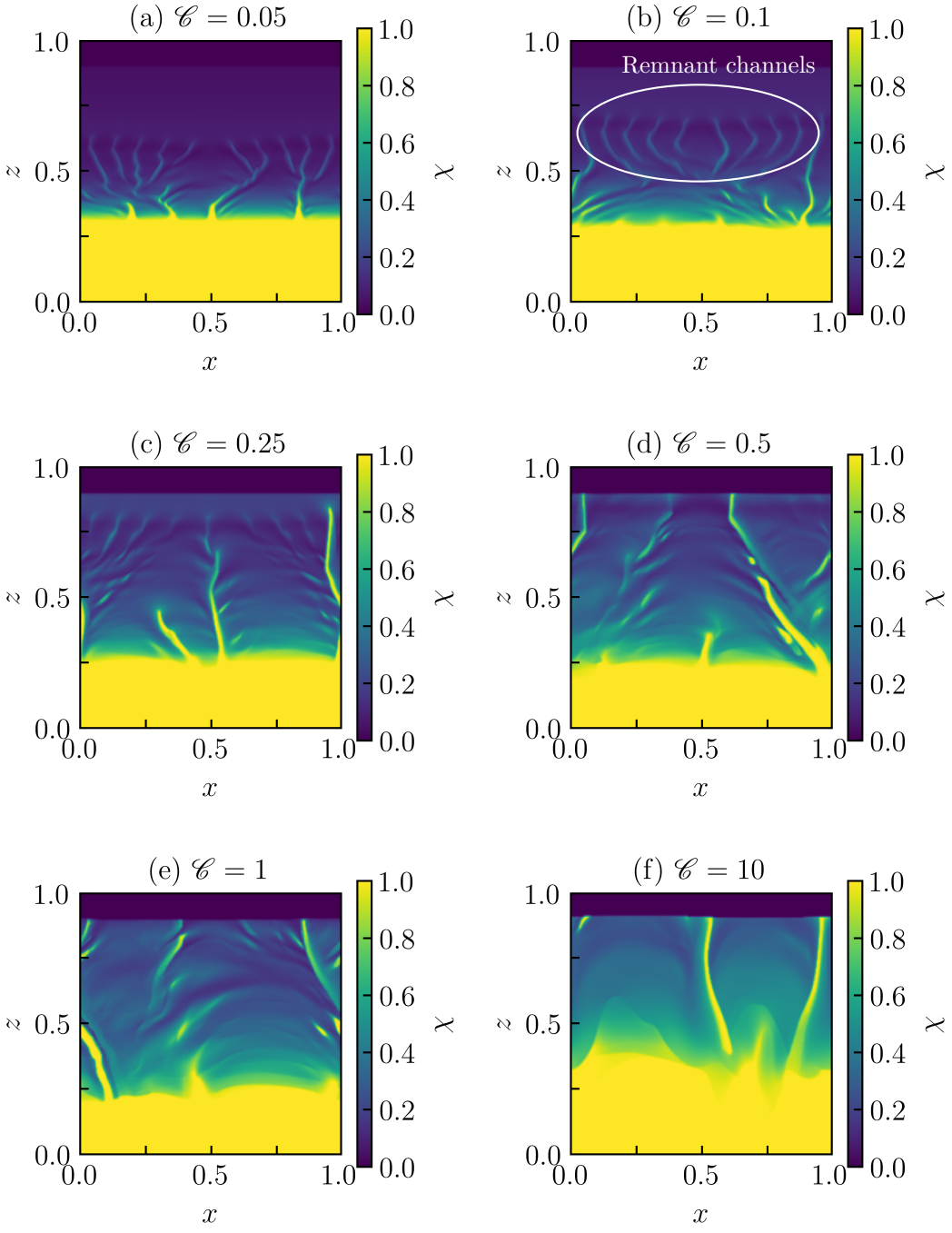


Figure 5.17: Porosity χ for a range of concentration ratios $\mathscr{C}$ with $Rm = 75$ as in fig. 5.16 but at a later time $t = 1.0$. Remnant brine channels – regions of higher porosity above the actively convecting layer – are circled in (b)

the vertical direction. When there are multiple channels, their horizontal movement allows them to collide and then merge.

Channels can also become 'extinct' (e.g. highlighted in fig. 5.17b). Channels only remain active because of the constant supply of solute enriched fluid. If this supply weakens then the solute concentration in the channel will decrease and it may begin to solidify, further reducing the flow through a runaway feedback. This can be thought of as the opposite of the positive feedback which drives channel formation in the first place (c.f. Worster, 1997). The initial weakening of the flow can be caused by the porosity in the adjacent mushy layer decreasing as solute is removed by the flow. Sometimes channels close up rapidly trapping a liquid inclusion within the mushy layer. These inclusions can be readily identified as regions of high porosity which are disconnected from the underlying liquid (e.g. see the circled inclusion in fig. 5.16d).

Through channel extinction and merging events, the spatial density of channels tends to decrease over time. For small $\mathscr{C}$ this is particularly evident because remnant channels are 'frozen in' to the mushy layer. For example, in fig. 5.17b around 10 remnant channels are circled, whilst there are just a few currently active channels. Similar behaviour is seen in fig. 5.17a. The initial channel spacing is larger in simulations with high $\mathscr{C}$, which is consistent with results from linear stability analyses which find that the most unstable wavelength increases with $\mathscr{C}$ (Worster, 1992b). Consequently, with the current domain width channel merging is a less common occurrence in these simulations and it is more typical to find a single large channel. This does not preclude the possibility for channel merging to occur regularly in wider domains with $\mathscr{C} \gg 1$.

5.2.3 Mushy layer properties

In this section I will consider how various mushy layer properties evolve over time during the simulations described qualitatively in § 5.2.2.

In fig. 5.18a I find that the mushy layer depth increases sublinearly with time in most simulations, and increases with $\mathscr{C}$. As seen in fig. 5.12c, the solid fraction $\phi = 1 - \chi$ within the mushy layer decreases as $\mathscr{C}$ is increased, so less heat must be extracted to grow a mushy layer of the same depth allowing growth to occur quicker. Worster and Rees

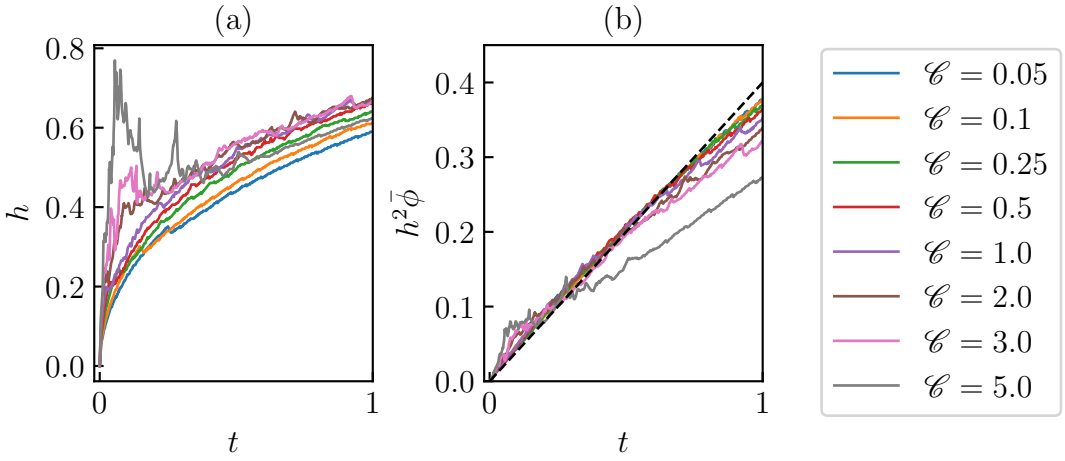


Figure 5.18: Variation of mushy layer depth with time for transient simulations with varying $\mathscr{C}$ and other parameters given by (5.30). As in § 5.1.2, the mushy layer depth $h(t)$ is calculated by taking the median depth of the mush-liquid interface. (a) Median mush depth $h(t)$ typically increases sublinearly with time, and also increases with $\mathscr{C}$. At early times, there is a spike in $h(t)$ for large $\mathscr{C}$. This is a consequence of solidification around the sinking plumes which are particularly solute-laden, and therefore cold, at the onset of convection. The solid formed near the base of the domain is quickly melted by the relatively warm fluid which enters through the open bottom boundary. (b) There is a good collapse of the data to a linear function of time when plotting the product of the mush depth squared with the average solid fraction, $h^2\bar{\phi}$. We also find very good agreement with the mush depth predicted by diffusive growth (black dashed line).

Jones (2015) showed that, under diffusive growth in a semi-infinite domain, the mushy layer depth should vary like $h \propto \sqrt{t/\phi}$. Nondimensionalising their eq. (2.3), we find

$$h^2\phi = \frac{2}{\mathscr{S}}t. \tag{5.41}$$

I find a good collapse of my data to this relationship in fig. 5.18b at early times ($t < 0.5$) for $\mathscr{C} < 5.0$. The growth begins to slow slightly at larger times, which is likely a consequence of the finite depth of the domain and fixed temperature applied to fluid entering the domain through the open bottom boundary. There are deviations from the predicted diffusive growth as $\mathscr{C}$ increases, and particularly for $\mathscr{C} = 5$. This is likely the result of the stronger convection in these cases (as discussed in the next paragraph). Following the initial onset of convection, a spike in the mushy layer thickness for larger $\mathscr{C}$ is caused by cold and solute rich fluid sinking rapidly and enabling solidification throughout the domain. At later times, stronger convection causes melting of the mushy layer due to the enhanced transport of relatively warm fluid from the bottom

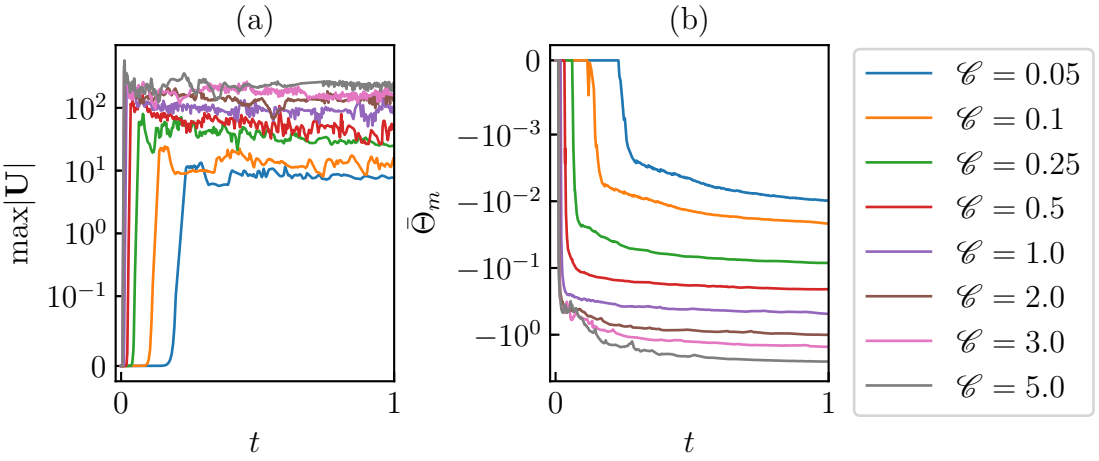


Figure 5.19: Variation of mushy layer diagnostics with time for transient simulations with varying $\mathscr{C}$ and other parameters as in (5.30). (a) Max fluid velocity max$|\mathbf{U}|$ increases rapidly signalling the onset of convection, and increases with $\mathscr{C}$. (b) Average bulk solute concentration in the mushy layer $\bar{\Theta}_m$ decreases rapidly following the onset of convection, and thereafter decreases slowly over time.

of the domain up to the mush-liquid interface.

In fig. 5.19a I plot the maximum fluid speed max$|\mathbf{U}|$. The onset of convection is clearly identifiable as the point where max$|\mathbf{U}|$ increases rapidly. Thereafter, the flow strength shows small fluctuations about a relatively constant mean value that increases with $\mathscr{C}$. There are multiple factors which may contribute towards this. The flow is driven by compositional differences, and moderated by the permeability of the mushy layer. As $\mathscr{C}$ is increased, the porosity of the mushy layer increases permitting a stronger flow. In our dimensionless units, the bulk solute concentration spans a range $\Theta \geq -\mathscr{C}$ whilst the initial and far field solute concentration is always fixed at 0. The fluid density is determined by the liquid solute concentration (which in the pure fluid equals the bulk concentration), so increasing $\mathscr{C}$ will lead to greater density contrasts in the underlying liquid, driving stronger convection.

The mean bulk solute concentration within the mushy layer $\bar{\Theta}_m$ provides an integrated measure of desalination caused by the solute fluxes. In fig. 5.19b, I show that $\bar{\Theta}_m$ remains at the initial concentration, $\Theta_i = 0$, until the onset of convection at which point it decreases rapidly. The sudden decrease in $\bar{\Theta}_m$ is associated with the build up of potential energy within the mushy layer during diffusive growth which is released during convection. The bulk solute concentration continues to decrease more slowly after this point as the flow continues to replace fluid within the mushy layer

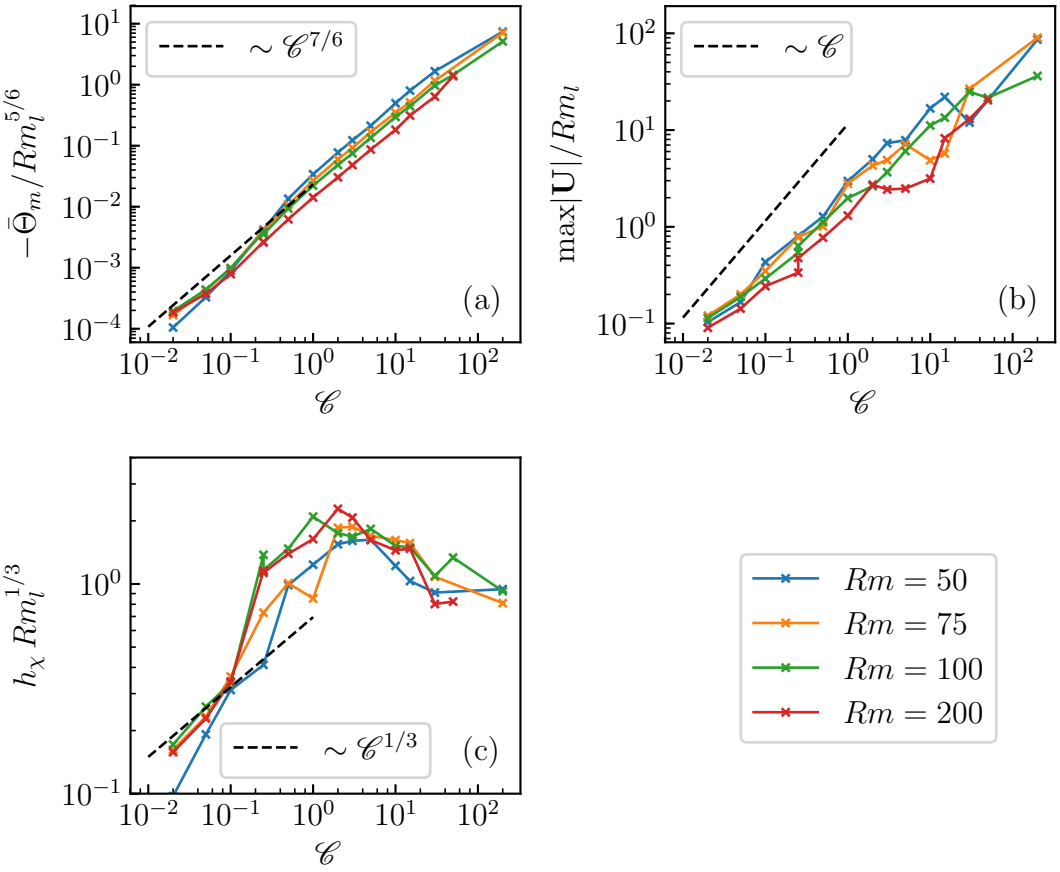


Figure 5.20: Variation of the diagnostics presented in fig. 5.19 and fig. 5.18, averaged over the time interval $0.9 < t < 1.0$, with $\mathscr{C}$ and Rm. The $y-$axis has been scaled with Rm in accordance with the predictions from the steady state scalings identified in chapter 4, whilst a dashed line indicates the predicted scaling with $\mathscr{C}$. Note the log–log axes. (a) The depletion of solute (note negative sign on y-axis). (b) Maximum fluid velocity in the mushy layer. (c) Confinement depth, defined by the height above the mush-liquid interface where the horizontally averaged porosity has dropped to 0.5.

with relatively fresh fluid from below. As $\mathscr{C}$ increases, so too does the decrease in $\bar{\Theta}_m$. The difference between the concentration of the initial fluid, Θ_i, and the concentration $\Theta = -\mathscr{C}$ of pure fluid entirely devoid of solute is given by $\Delta\Theta = 0 - (-\mathscr{C}) = \mathscr{C}$. Therefore, as $\mathscr{C}$ increases the quantity of solute which can be removed from the mushy layer also increases, and there is a greater change in $\bar{\Theta}_m$. The permeability of the mushy layer also increases with increasing $\mathscr{C}$, permitting a stronger flow and further promoting the removal of solute from the mushy layer.

5.2.4 Comparison with steady state scaling

Whilst some of the mushy-layer properties considered in this section evolve continuously in time, others approach an approximately constant value after a sufficiently long time. In fig. 5.20 I compute the average value of various properties for $0.9 < t < 1.0$, and consider how they vary with $\mathscr{C}$ and a local Rayleigh number $Rm_l = Rm/\dot{h}$ which is given by the global Rayleigh number Rm scaled with the local growth rate $\dot{h}$. Given the steady-state scalings found in chapter 4 for $\mathscr{C} \ll 1$, I predict (more details below) how each of these diagnostics should vary with Rm_l and $\mathscr{C}$. The $y-$axis has been scaled to reflect the predicted Rm_l dependence, whilst a dashed line has been added to indicate the predicted $\mathscr{C}$ dependence. Where the diagnostics for different Rm_l (different coloured lines) collapse to a single line, it indicates that the predicted Rm_l variation is consistent with the data. Where the solid lines are roughly parallel with the dashed line, it indicates that the predicted variation with $\mathscr{C}$ is consistent with the transient simulations.

The steady state confinement depth h_χ is given by (4.33);

$$h_\chi \sim \left(\frac{\mathscr{C}}{Rm_l(\mathscr{S}V_f)^2}\right)^{1/3}. \tag{5.42}$$

Assuming that the maximum fluid velocity in the mushy layer, $\max|\mathbf{U}|$, will scale like the maximum velocity near the channel, and thus like $\bar{w}_c$ (eq. 4.25), I predict that

$$\max|\mathbf{U}| \sim \mathscr{C}Rm_l. \tag{5.43}$$

To determine the predicted scale for the average mushy layer bulk solute concentration, $\bar{\Theta}_m$, I note that $\Theta \approx 0$ at the mush-liquid interface then decreases into the mushy layer with $|\bar{\Theta}_m|$ reaching a maximum value at the eutectic boundary. As there is no net solute flux through the side boundaries, Wells et al. (2013) demonstrated that in steady state the solute flux across the mush-liquid boundary must balance the flux across the mush-eutectic boundary, where the only transport is due to frame advection. Hence, the horizontally averaged solute flux can alternatively be written in terms of

the (dimensionless) bulk salinity Θ at the eutectic boundary ($z = z_{\text{eutectic}}$),

$$F_O \sim \frac{1}{\lambda}\int_0^{\lambda} [\Theta]_{z=z_{\text{eutectic}}}\, dx. \tag{5.44}$$

Hence, we expect that $\bar{\Theta}_m \sim O(F_O)$, where we have previously found that $F_O \propto \mathscr{C}^{7/6} Rm^{5/6}$ (eq. 4.44).

Overall, fig. 5.20 reveals that our steady state scalings are consistent with the qualitative trends observed in the transient simulations (i.e. quantities increase with $\mathscr{C}$ when the scalings predict so). On a quantitative level, some scalings agree reasonably well with our simulations in the limit $\mathscr{C} \ll 1$ (e.g. $\Delta\Theta_m$), whilst their are clear discrepancies between others (e.g. h_χ). In the remainder of this section I will compare the predicted scalings with the results from transient simulations in more detail.

In fig. 5.20a we see that the average mushy layer bulk solute concentration $\bar{\Theta}_m$ closely follows the predicted scaling for $\mathscr{C} \ll 1$. For larger $\mathscr{C}$ this scaling is slightly less convincing, as expected. In particular, the dependence on both $\mathscr{C}$ and Rm weakens. In the limit $\mathscr{C} = O(Rm)$, Wells et al. (2013) found that $F_O \sim Rm$, however our simulations do not extend to large enough $\mathscr{C}$ to test this prediction.

In fig. 5.20b I consider the maximum fluid velocity in the mushy layer. The variation with $\mathscr{C}$ is slightly weaker than the predicted linear scaling. The variation with Rm also appears to be slightly weaker than our predicted scaling, as there is a systematic tendency for the higher Rm lines to lie below the lower Rm lines. Interestingly, $\max|\mathbf{U}|$ appears to roughly follow the same scaling for all values of $\mathscr{C}$ considered by our transient simulations.

Finally, in fig. 5.20c we compute a measure of the confinement depth h_χ by finding the depth into the mushy layer h_χ where the horizontally averaged porosity has dropped to 0.5. As $\mathscr{C}$ becomes large, h_χ tends towards a constant value which is consistent with the prediction that flow is no longer confined in these cases. For $\mathscr{C} \ll 1$, the variation with $\mathscr{C}$ is approximately consistent with the prediction (dashed line). Meanwhile the collapse of the different lines is also consistent with the predicted Rm dependence.

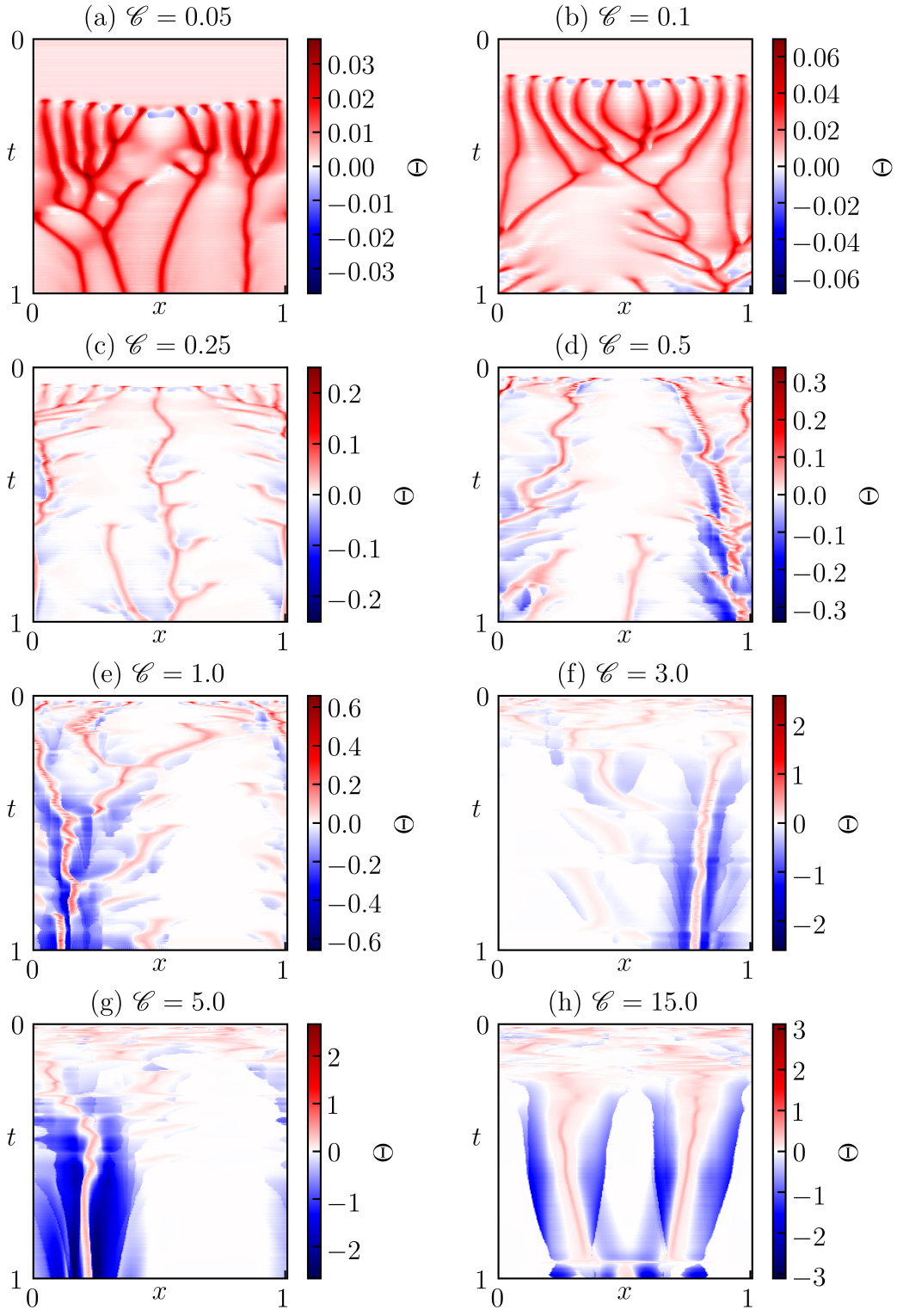


Figure 5.21: Variation of the bulk solute concentration Θ at the mush–liquid interface ($z = z_{ml}(t)$) over time, for $Rm = 75$ and a range of $\mathscr{C}$ (see panel titles). Channels are identifiable as regions of high solute concentration Θ (red). Note that the time $t = 0.0$ is at the top of the vertical axis, and time increases linearly downwards. The colour scale varies between panels. The initial bulk solute concentration is $\Theta = 0$. The number of channels generally decreases over time due to merging between adjacent channels.

5.2.5 Channel dynamics

In § 5.2.2 I described qualitatively some of the complex nonlinear behaviour exhibited by the channels during transient growth. In this section, I will identify the trajectories of individual channels and compute their statistics to complement the previous analysis.

Channels evolve continually in both spatial dimensions ($x - z$) and in time. To simplify the analysis, in this section I will track the channel positions at the effective mush-liquid interface $h(z,t)$ found by taking the median of $h(x,z,t)$ in the x direction . Whilst in general channels are identifiable as the entirely liquid regions within the mushy layer, along the mush-liquid interface the porosity $\chi = 1$ everywhere so I find that channels are most readily identified by spikes in the bulk solute concentration from the sinking brine plumes.

In fig. 5.21, I plot the bulk solute concentration Θ at the effective mush-liquid interface as a function of horizontal position along the interface, x, and time t (note that time increases downwards) for a range of $\mathscr{C}$. The bulk solute concentration varies as $\mathscr{C}$ changes between the panels, whilst the colour scale is centred on the initial concentration $\Theta_i = 0$ in all cases. Large values of Θ (dark red) correspond to highly saline plumes, whilst $\Theta < 0$ (blue) corresponds to regions of the mushy layer from which solute has been removed by the flow. Regions of solute depleted mushy layer (dark blue regions) are more evident in simulations with larger $\mathscr{C}$, as the mush-liquid interface features more deformation (e.g. see fig. 5.16f). This figure re-enforces some of the observations which have already been discussed in § 5.2.2. In simulations with smaller $\mathscr{C}$ there are more channels, and channel merging is more prevalent. In all simulations, the average spacing between channels tends to increase over time.

From the data in fig. 5.21 it is possible to identify the trajectory of individual channels in $x-t$ space. At each discrete time interval t_i, I use a peak finding algorithm (`find_peaks` from the `scipy.signal` python library) to identify the channel positions $\mathbf{x}_i$. Then, by recursively associating each channel position with the closest channel position from the previous timestep, $t_i - 1$, I construct the trajectories of individual channels. If no channel position from the previous timestep is sufficiently close (i.e. if the separation $d > 0.025$), or no previous timestep exists, then a new channel is

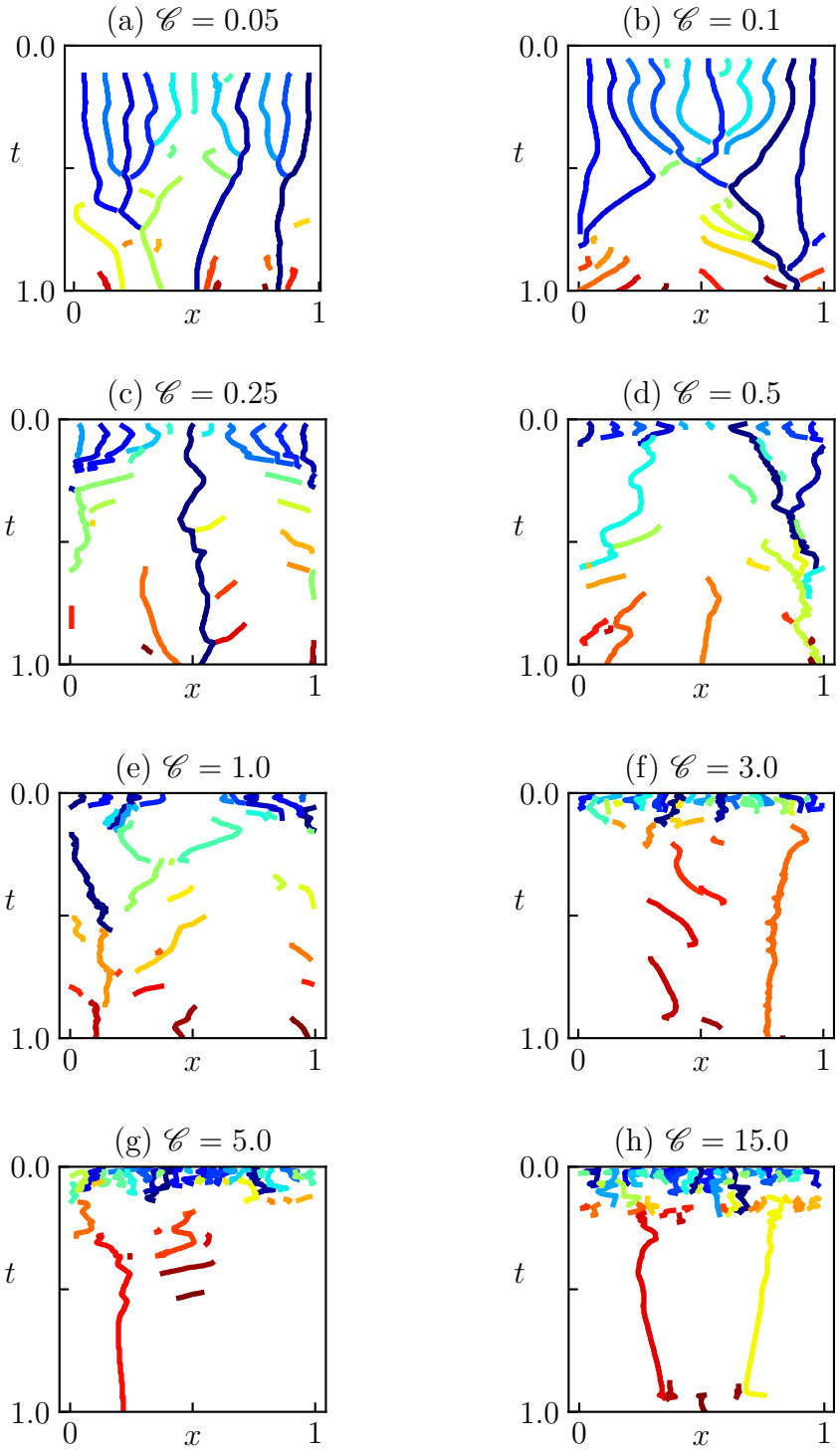


Figure 5.22: From fig. 5.21, I find the channel positions along the mush–liquid interface at each point in time and then identify individual channel trajectories (coloured lines) by combining nearby channel positions in $x - t$ space. Each channel is given a different colour indicating the order in which they form.

started. In fig. 5.22, I plot the channel locations identified at each time interval (black crosses $\times$) and the channel trajectories (coloured lines).

By performing this process automatically I eliminate human biases, but it is clear from comparing fig. 5.22 with fig. 5.21 that the process is not perfect. Channels are less distinct in simulations with larger $\mathscr{C}$ (see fig. 5.21), especially at early times, making it difficult to reliably identify channel trajectories. Additionally, when two channels merge to become one it is not clear which of the original trajectories should be continued. Nonetheless, I will now compute some of the properties of the deduced channel trajectories, and consider how these properties depend on the concentration ratio $\mathscr{C}$.

One simple metric which can be used to compare the trajectories is their duration, τ, given by the difference in time t between the start and end of a trajectory. The end of a trajectory is either defined by the point where one channel merges with another, or by the end of the simulation ($t = 1.0$). To build some insight into the horizontal movement of channels through the mushy layer, I will also compute the horizontal translation velocity of the channel, $u(t) = \partial x/\partial t$ at each time, and then consider the median average over time $\bar{u} = \text{median}(|u|)$. For each simulation, it is clear from fig. 5.22 that there will be a distribution of these metrics. To compare the distributions, I will compute the number of channels N for each simulation that fall into appropriately defined bins.

In fig. 5.23 I plot the distributions of the channel duration τ (a, c) and the mean horizontal channel speed $\bar{u}$ (b, d). In each case, I use $N_{\text{bin}} = 15$ equally sized bins to discretize the data, with the center of each bin indicated by a cross. Sensitivity studies confirm that the results are not dependent on the number of bins used for $N_{\text{bin}} \gtrapprox 10$. The colour of each line indicates the concentration ratio $\mathscr{C}$ (see colour bar). For clarity, I only plot the simulations with $Rm = 75$, but the same qualitative patterns persist across the range of Rayleigh numbers considered ($50 < Rm < 200$). Simulations with small $\mathscr{C}$ tend to feature more channels, so in panels (c-d) I normalise N by the total number of channels sum (N). I also use a log-log scale in (c-d) to highlight possible scaling behaviour, and include a comparison with power law scalings τ^{-1} and $\bar{u}^{-1}$ (dashed line).

Despite the complex nature of the simulations, the data plotted in fig. 5.23 shows some some clear trends. The distribution of τ (fig. 5.23c) is approximately independent of $\mathscr{C}$. Longer-lived channels are less likely – N decreases with τ – with the distribution

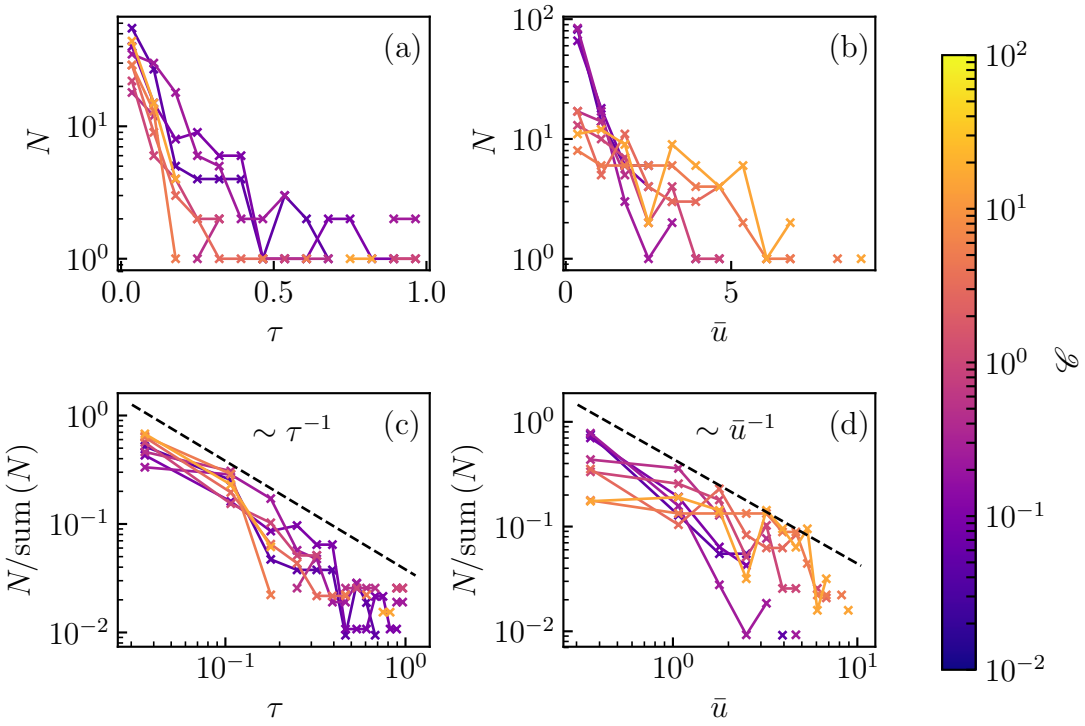


Figure 5.23: Distribution of the channel duration τ (a, c) and median horizontal velocity $\bar{u}$ (b, d) for a range of concentration ratios $\mathscr{C}$ (colour) with other parameters as in (5.30). In (c-d) the distribution has been normalised so that the area under each curve is the same for each $\mathscr{C}$. Note that in all panels the y-axis is on a log scale, whilst the $x-$axis is linear in (a-b) and logarithmic in (c-d).

possibly described by a power law $N \sim \tau^{-1}$ as highlighted in (c). A power law distribution seems plausible given the observation that smaller channels merge to form larger channels. A power law distribution also has the property that it is not particularly unlikely to find channels which exist for a long time. In contrast, distributions with an exponential tail would be less consistent with the observation that at least one channel appears to persist for the duration of a simulation. The largest largest τ will be limited by finite sample size effects due to the finite duration of the simulations.

The distribution of $\bar{u}$ does appear to show some variation with $\mathscr{C}$ (fig. 5.23d). For small $\mathscr{C}$, horizontal channel velocities are more likely to be smaller. As $\mathscr{C}$ increases, the distribution of horizontal channel velocities becomes more uniform as slower velocities become less likely, whilst larger velocities become more likely. The greater horizontal mobility of channels in simulations with larger $\mathscr{C}$ may be due to the smaller effective heat capacity $\Omega = 1 + \mathscr{S}/\mathscr{C}$. As Ω decreases, it becomes easier to dissolve the mushy layer, which may aid the horizontal movement of channels. Whilst there are fewer

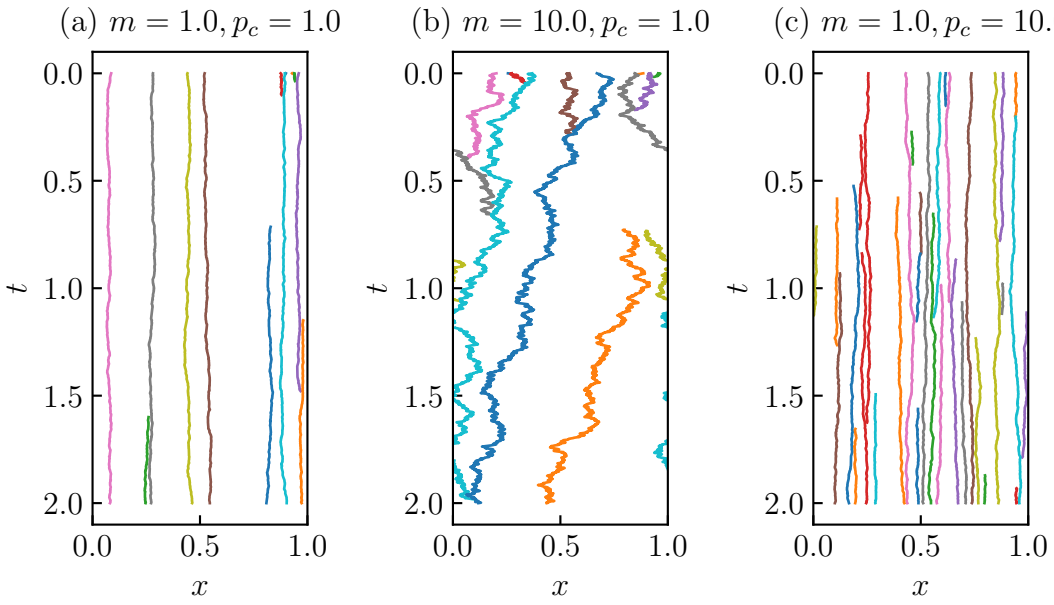


Figure 5.24: Example results from a simple statistical model of channel merging. In all cases, $n = 10$ and $d = 0.01$, whilst p_c and m are given in the panel titles. (b) increasing the horizontal channel velocity m leads to more merging, with fewer channels surviving by the end of the simulation. (c) increasing the probability of new channels forming, p_c, results in more channels at the end of the simulation.

channels with larger speeds $\bar{u}$, the distribution of $\bar{u}$ is a less convincing match to a $\bar{u}^{-1}$ scaling (fig. 5.23d) than the τ^{-1} distribution of channel durations (fig. 5.23c).

To further investigate the possibility of a power law distribution of channel durations, I will construct a simple stochastic model for channel merging. I begin at a timestep $t_j = 0$ with an initial set of n channels, distributed randomly on a periodic domain $0 < x < 1$. At subsequent timesteps, each channel moves a distance $\delta x = r\, m \Delta t$ where r is a uniformly distributed random number in the interval $[-1, 1]$ and m is a parameter which determines the maximum horizontal channel speed. If the separation D between two channels is less than some criteria d then I assume that they have merged. Finally, at each timestep (of size Δt) a new channel will be created with a probability $p_c \Delta t$ at a random point in space.

Example solutions of this simple model are presented in fig. 5.24, and bear some similarities to the trajectories observed in full numerical simulations (fig. 5.22). In particular, the rate of horizontal channel migration and frequency of merger events in fig. 5.24b are similar to those seen in our full numerical simulations.

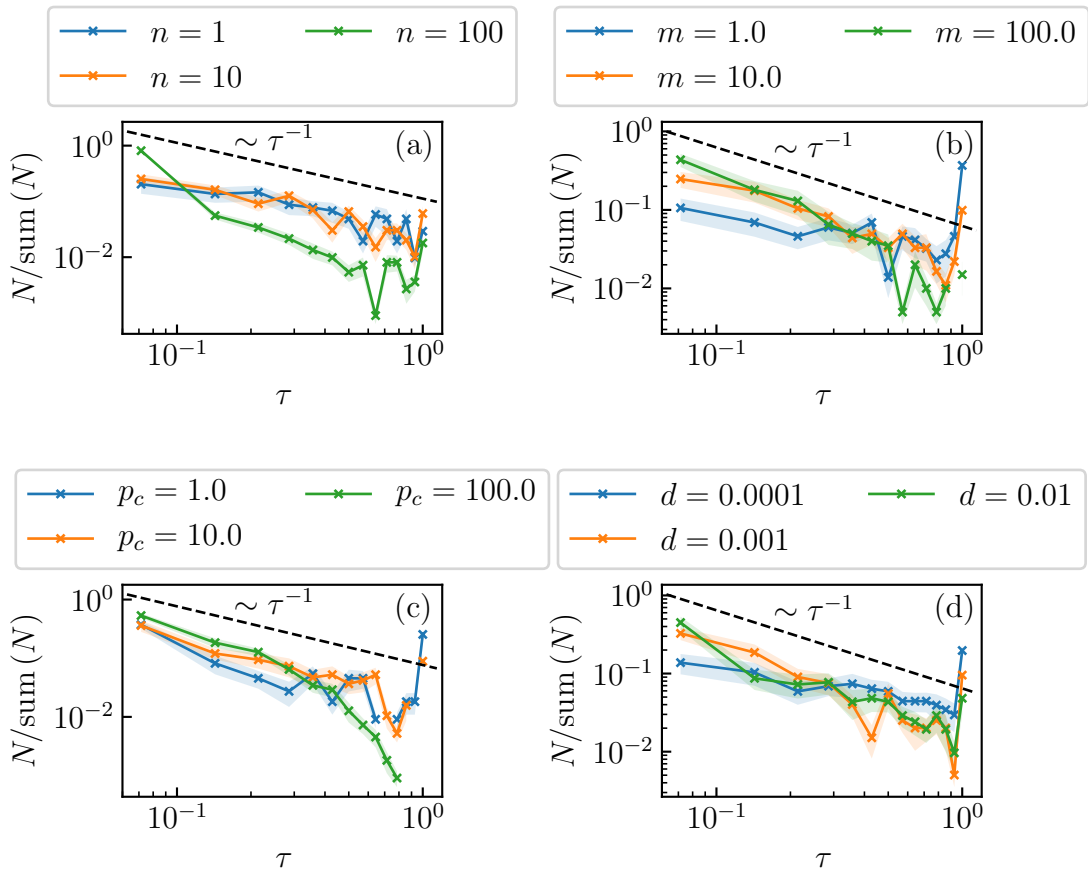


Figure 5.25: Distribution of channel durations in a simple model of channel merging, where each of the four parameters are varied in turn. Unless specified, $n = 10$, $m = 1$, $p_c = 1$, and $d = 0.01$. Coloured regions indicate the variation within an ensemble of 10 simulations.

In fig. 5.25 I consider the sensitivity of this model to its four parameters – the initial number of channels n, maximum channel displacement in a timestep $m\Delta t$, probability of a new channel $p_c\Delta t$, and the channel proximity for merging d. Simulations are conducted over a time interval $0 < t < 1$. We find that the model is sensitive to the timestep Δt when $\Delta t \gtrsim 0.01$, so we use $\Delta t = 0.001$. For each set of parameters I consider an ensemble of 10 simulations to find the mean distribution (solid lines) and standard deviation (shading). I typically find that the distribution of τ is relatively insensitive to these parameters, and that the simple model is mostly consistent with the power law scaling $N \sim \tau^{-1}$. Deviations from this scaling for large τ are partly explained by finite size effects. For example, decreasing the maximum channel translation speed m in fig. 5.25b is equivalent to decreasing the time over which simulations are conducted T. This artificially affects the channel dynamics, preventing channels from merging

and therefore permitting more channels with large durations τ to exist. In fig. 5.25c we see that for very large probabilities of new channel creation ($p_c = 100$) there is bias towards more short channels and fewer long lived channels. When p_c is large, there will be a high density of channels which will merge more often, preventing many channels from persisting for long times. Finally, in fig. 5.25d we see that as the required proximity for merging d decreases the frequency of long lasting channels (large τ) increases. This is as expected; as $d \to 0$ there would be no merging at all, and hence all channels should have $\tau = T$.

It is clear from fig. 5.22 that the channel dynamics are not as simple as in this simple model. Channels do not move randomly, but tend to move in a single direction for a prolonged period of time. This could be incorporated into the present statistical model by using a channel translation velocity which is correlated with the velocity at previous times (e.g. via a Langevin equation). Channel movement also appears to be somewhat influenced by neighbouring channels, with channels tending to move towards each other. That the simple model produces a similar distribution of channel durations despite neglecting these physical effects may be indicative of a fundamental property of these types of systems, or may be a complete coincidence. Similar pattern formation is seen in other systems such as river channel formation, where Cohen et al. (2015) find that a physically based model accurately predicts the channel structure. It may be that a similar approach is also appropriate here.

The observed power law behaviour, which is independent of the parameter regime, may be a manifestation of self-organized criticality (Jensen and Magnasco, 1999), a physical phenomenon which can occur in dynamical systems where there is a critical point which is also an attractor. Further investigation of this possibility will be left for future studies.

5.3 Comparing 3-D and 2-D simulations

Direct numerical simulations of convection in mushy layers in the literature have so far only considered two-dimensional geometries. However naturally occurring examples of this process, such as brine rejection in sea ice, are three-dimensional. In the

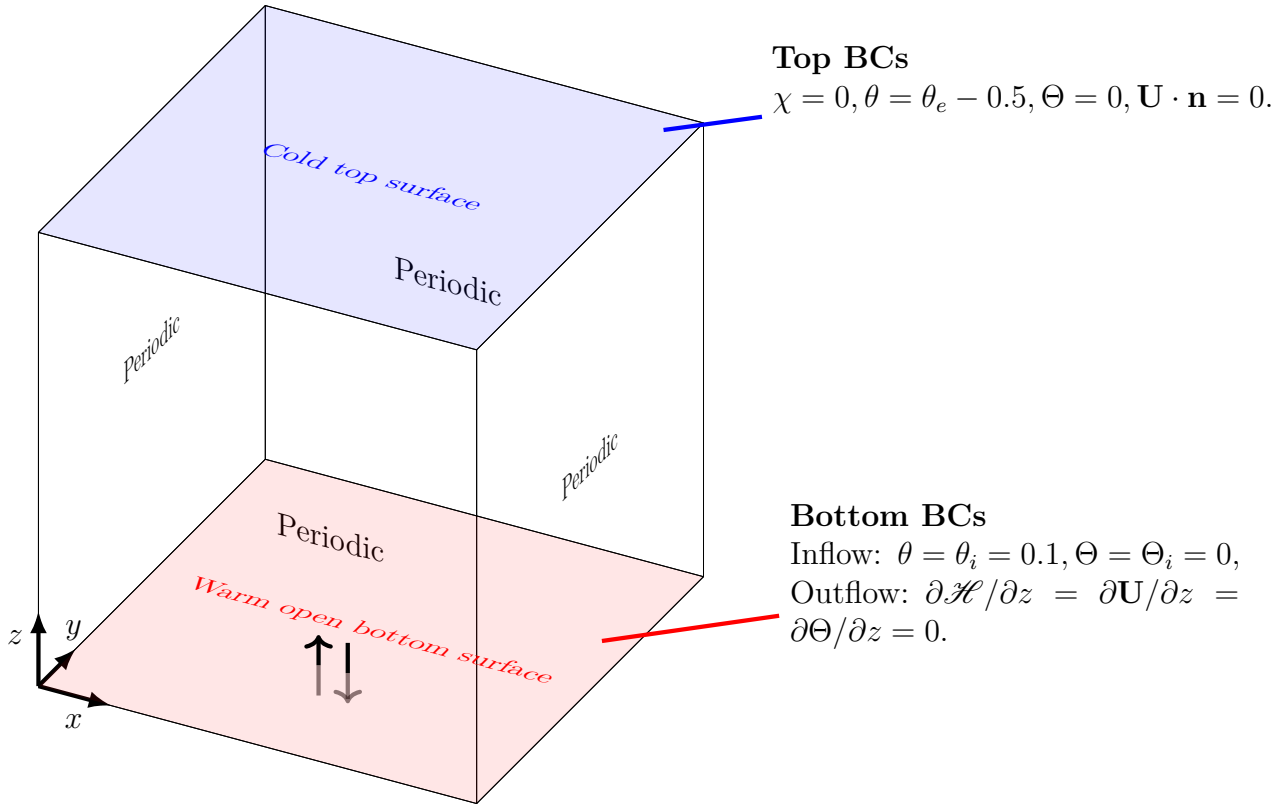


Figure 5.26: Boundary conditions for simulations in § 5.3 are the three-dimensional analogue of those used in § 5.2. In 2D, the domain is as used in § 5.2 – the top and bottom boundaries are the same whilst periodic conditions are retained in the horizontal $(x - y)$ direction. The box edges have length 1 in all directions.

case of non-reactive porous media, 3-D simulations have revealed both differences and similarities to results in 2-D. For example, Hewitt et al. (2014) found that for large porous medium Rayleigh numbers the heat transport (quantified by the Nusselt number) is well described by a similar functional form in 2-D and 3-D, but that in 3-D the transport is roughly 40% larger. In this section, I will compare simulated mushy layer convection in 3-D with the equivalent simulated conducted in 2-D. Due to the increased computational cost, I focus on a selected case study rather than a full exploration of the parameter space.

5.3.1 Experimental design

Simulations in this section will be conducted in a square box of dimensionless size 1 in all directions (x, y horizontal and z vertical) which is initially filled with stationary fluid with dimensionless bulk solute concentration $\Theta = \Theta_i = 0$ and temperature

$\theta = \theta_i = 0.1$. The top boundary ($z = 1$) is instantaneously decreased to a temperature below the eutectic, $\theta = \theta_e - 0.5$, whilst the bottom boundary is open and the side boundaries are periodic, as illustrated in fig. 5.26. I consider dimensionless parameters similar to those considered in § 5.2, with the concentration ratio chosen to ensure that the simulation is relevant to sea ice growth:

$$\mathscr{C} = 0.25, \quad Rm = 100, \quad \mathscr{S} = 5, \quad Le = 100, \quad \Pi_c = 10, \quad c_p = k = 1. \tag{5.45}$$

A complementary 2D simulation is considered with the same boundary conditions as in § 5.2. For consistency, in both simulations the same resolution $\Delta x = 1/128$ is used.

In two dimensions we considered flow in a Hele-Shaw cell, and hence used Darcy's law to model flow in both the mushy layer and the pure fluid. In three dimensions there is no longer a constraint on the permeability in the pure fluid. Whilst it would be more physically realistic in this case to use a Darcy-Brinkman equation to model the fluid flow, I continue to consider Darcy flow in 3-D, with the permeability in the free fluid given by Π_c, for a more faithful comparison with the two dimensional dynamics. This approach also allows us to achieve practical computational run times.

5.3.2 Results for flow in 2-D and 3-D

In fig. 5.27 I plot the porosity fields in 3-D (a) and 2-D (b) simulations at the same time $t = 0.3$. In the 3-D case, I also plot the vertical fluid velocity in the horizontal plane to give some indication of the convective patterns. In both cases the mushy layer has grown to approximately the same depth, whilst convection has led to the formation of narrow channels. At this particular time, convection in 2-D is dominated by two large channels, with two other smaller channels beginning to form between them. In contrast, convection in 3-D proceeds through a set of roughly equally sized channels which do not penetrate as far into the mushy layer as in the 2-D case. This behaviour is typical of the dynamics throughout each simulation, rather than being a transient phenomena specific to this particular time.

In 3-D, the flow is organised into square convective rolls; channels at the vertices are superimposed on a square grid of planar downwelling sheets with high porosity. This

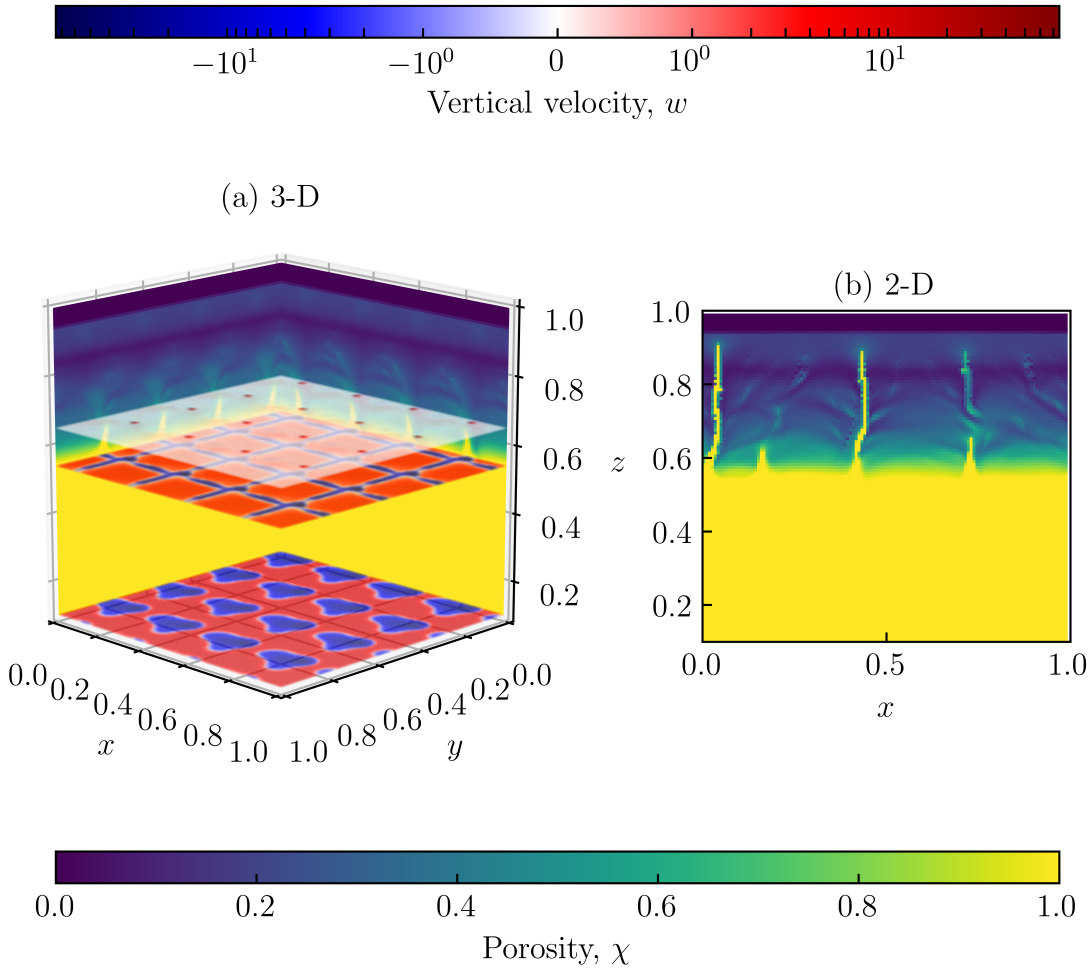


Figure 5.27: Porosity at $t = 0.3$ on vertical planes (lower colour scale) and vertical velocity on horizontal planes (top colour scale, double logarithmic for $|w| > 1$, linear for $|w| < 1$) during simulations in (a) 3-D geometry and (b) 2-D geometry with otherwise identical parameters and boundary conditions. In the top horizontal plane of (a), at $z = 0.65$ near the channel tips, the channel width is a single grid cell. The downflow in the channel (negative w, blue) is hard to distinguish from the upflow (positive w, red) which surrounds the channel.

arrangement can be seen in velocity fields in fig. 5.27a. At the mush-liquid interface (middle plane, $z \approx 0.55$) downwelling occurs at the edges of these squares. Above this plane, the velocity within the mushy layer is very weak except in the vicinity of the channels. Meanwhile, at the base of the domain the plumes which exit the channels can clearly be identified as the rounded patches of downwelling. Regions of downwelling within the mushy layer result in dissolution of the porous matrix, and the downwelling at the edge of the square convective cells are no exception. Consequently, the mush-liquid interface is corrugated by a regular array of ridges which, whilst not penetrating as

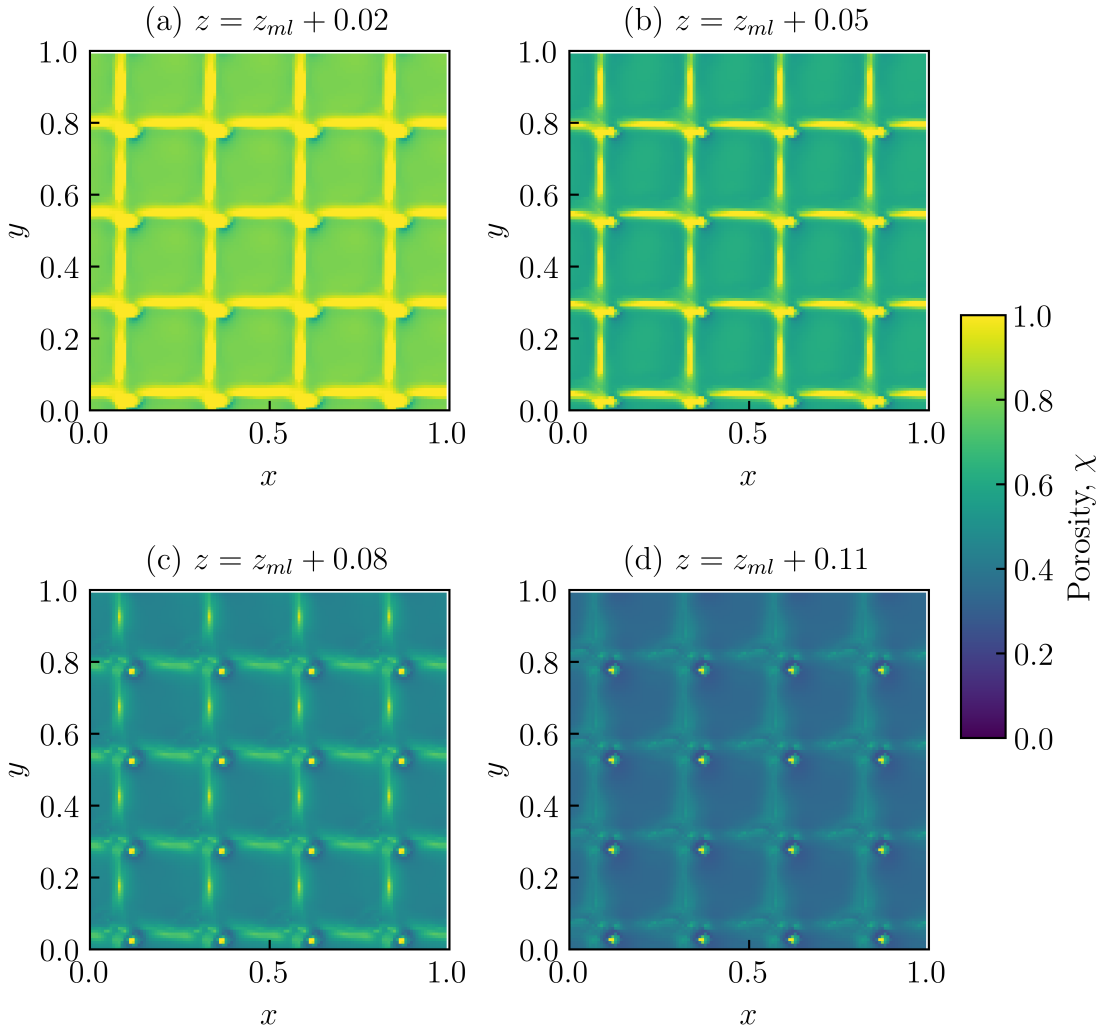


Figure 5.28: Porosity χ in the $x - y$ plane at $t = 0.3$ for several vertical positions z above the mush-liquid interface z_{ml} (see panel headings). Close to the mush-liquid interface (panels a, b) the square convective cells lead to a regular array of liquid ridges in the underside of the mushy layer. Further into the mushy layer (panels c-d) the only liquid regions with $\chi = 1$ are narrow channels which are slightly offset from the corners of the square convective cells.

far into the mushy-layer as the channels, are nonetheless noticeable. Tait et al. (1992) observed similar features during solidification of ammonium chloride, where convection was arranged into a hexagonal planform with ridges of dissolution along the edges of each hexagon and channels at the vertices. However, there is little evidence for these ridge features in experiments or observations of sea ice formation. The concentration ratio $\mathscr{C}$ varies significantly between these two cases – Tait et al. (1992) considered a solution with $\mathscr{C} \approx 20$, whilst for sea ice $\mathscr{C} \approx 0.15$ – and this might explain why ridges are visible in some experiments but not others. However this does not explain why ridges are seen in our simulations but not in sea ice, as the concentration in these simulations,

$\mathscr{C} = 0.25$, is similar to sea ice growth. Square-like convection cells are also seen in flow within non-reactive porous media at low-moderate Rayleigh numbers ($200 \lesssim Ra \lesssim 600$) (Hewitt et al., 2014), and therefore it is possible that the square array of porosity ridges we see are a consequence of using Darcy's law to model the flow in the liquid.

The square planform of convection may be a consequence of the decomposition of the domain into different boxes for parallel computations. As the initial formation of channels is triggered by numerical instability, any numerical noise generated at the boundaries between these boxes may seed the channel locations. In the 3-D simulation here, the domain was split into 64 boxes, each containing $32 \times 32 \times 32$ grid cells. Therefore in the $x - y$ plane there are 16 of these boxes, which may correspond to the 16 convection cells. To reduce the possibility of the domain decomposition influencing the results, an improved approach would have been to seed the initial state with a random perturbation of larger magnitude than the numerical noise. Another possible artificial influence on the pattern formation is the overall domain size and geometry, which enforces a quantisation on the number of convection cells. It may also be the case that the cuboidal domain encourages the formation of cuboidal convection cells as seen here. The influence of the domain geometry on the results could be tested by repeating this simulation in a range of settings, including both smaller and larger domains, and domains with different sizes in the x and y dimensions.

In fig. 5.28 I further investigate the dynamics within the mushy layer by plotting the porosity field in the $x - y$ plane at a range of heights above the mush-liquid interface z_{ml}. The square convective cells identified in the velocity field in fig. 5.27a are clearly evident in the porosity field just about the mush-liquid interface fig. 5.28(a-b), where downwelling solute rich fluid results in a regular array of high porosity ridges. Further into the mushy-layer (panels c-d) these ridges become less prominent and the only high porosity regions are the narrow channels which exist at single points in $x - y$ space. The location of channels in $x - y$ space varies with height z indicating that, as in 2-D, channels are not perfectly straight sided.

In fig. 5.29 I compare key diagnostics between the 3-D and 2-D geometries. The mushy-layer thickness h is almost identical in the two cases (fig. 5.29a) as is expected for growth controlled by thermal diffusion. The onset of convection occurs at the same

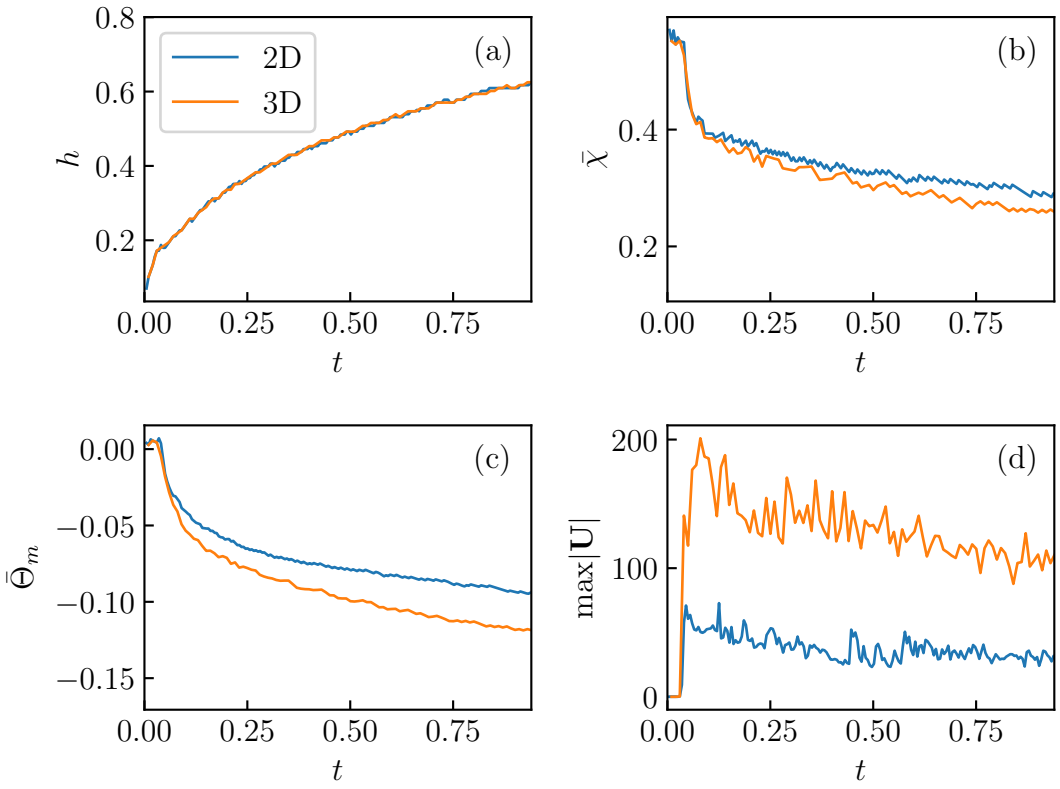


Figure 5.29: Comparison of diagnostics between 2D (blue line) and 3D (orange line) simulations with the same parameters. In panels (a-d) I plot the mushy layer thickness h, average mushy-layer porosity $\bar{\chi}$, average mushy-layer bulk concentration $\bar{\Theta}_m$, and maximum velocity max$|\mathbf{U}|$.

time t and mush thickness h in 2-D and 3-D, but following the onset of convection the dynamics are notably different. In 3-D the convection is stronger (fig. 5.29d) removing more solute from the mushy-layer than in 2-D (fig. 5.29c) and hence reducing its porosity (fig. 5.29b) and bulk concentration. This is a result which may have particularly significant geophysical implications. Some of the current attempts to parametrise salt rejection from sea ice are based on 2-D models (Worster and Rees Jones, 2015), which may be significantly underestimating the salt flux. The observation of enhanced heat or solute fluxes in 3-D relative to 2-D is also consistent with studies of flow in non-reactive porous media (e.g. Hewitt et al., 2014) and Rayleigh-Benard convection in a pure fluid (e.g. Van Der Poel et al., 2013).

In fig. 5.30 I consider the variation of the channel density and spacing in 2-D and 3-D. Channels are identified as peaks in $\Theta(\mathbf{U}\cdot\mathbf{e}_z)$ at the effective mush-liquid interface $z = h(t)$ using the Python libraries `scipy.signal.find_peaks` in 2-D and

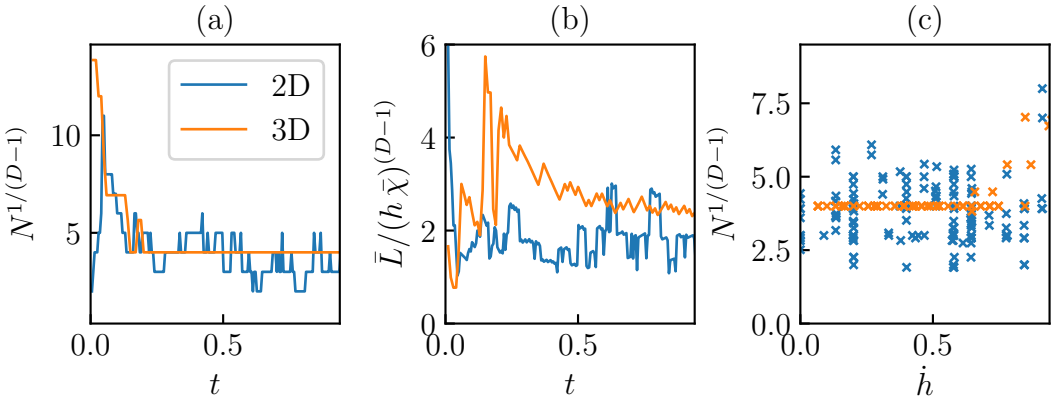


Figure 5.30: Channel density (N) and drainage area ($\bar{L} = 1/N$) in two dimensions ($D = 2$, blue lines/crosses) and three dimensions ($D = 3$, orange lines/crosses). (a) Channel density is similar in both cases when raised to an appropriate power (I plot N in 2-D and $N^{1/2}$ in 3-D). (b) Test of the scaling relation found in § 5.1.5. In 2-D, the channel drainage area $\bar{L}$ scales linearly with the product of the mushy layer thickness and average porosity $h\bar{\chi}$, corresponding to a horizontal line in (b). In 3-D, the data appear to be approaching an asymptote $\bar{L} \sim (h\bar{\chi})^2$. (c) Variation of the channel density N with the growth rate $\dot{h}$.

`skimage.feature.peak_local_max` in 3-D. The channel density N is related to the number of channels n_{chan} by $N = n_{\text{chan}}/L_x$ in 2-D, where L_x is the domain width, and $N = n_{\text{chan}}/A$ in 3-D, where A is the cross sectional area in the $x - y$ plane. In the simulations considered here $A = L_x = 1$, so $N = n_{\text{chan}}$ in both cases. The average channel drainage area is given by $\bar{L} = 1/N$, which in 2-D is equivalent to the average channel spacing.

I expect to find that the 3-D channel drainage area $\bar{L}_3$ is related to the 2-D drainage area $\bar{L}_2$ by $\bar{L}_3 = \alpha\,(\bar{L}_2)^2$, where α is a geometric factor which depends on the pattern formation in 3-D. Similarly, I expect that the channel density in 2-D, N_2, will be related to the density in 3-D, N_3, by $N_2 = \sqrt{\alpha\, N_3}$. Therefore, in fig. 5.30 I consider the channel density N_2 in 2-D alongside $\sqrt{N_3}$ in 3-D as indicated by the exponent $1/(D-1)$, where $D = 2$ or 3 is the number of spatial dimensions.

In fig. 5.30a I see that, when scaled in this way, the channel density is approximately the same in both 2-D and 3-D simulations. Given the observation in fig. 5.27 of square convective cells, I would expect to find a geometric factor $\alpha = 1$ and therefore that $N_2 = N_3^{1/2}$, which is consistent with the data in fig. 5.30a. The deviation in the channel density between 2-D and 3-D cases at very early times is due to the

peak finding algorithm erroneously identifying channels in 3-D simulations before the onset of convection, and should be ignored.

In § 5.1.5 I found that in 2-D the ratio $\bar{L}/(h\bar{\chi})$ was approximately $O(1)$ at all times, and hypothesised that in 3-D I would find $\bar{L}/(h\bar{\chi})^2 = O(1)$. In fig. 5.30b I test this scaling, and find that in these simulations the appropriate ratio $\bar{L}/(h\bar{\chi})^{(D-1)}$ is approximately $O(1)$ in both cases. In 2-D the ratio $\bar{L}/(h\bar{\chi})$ is fairly constant in time, whilst in 3-D $\bar{L}/(h\bar{\chi})^2$ appears to be asymptoting towards a constant value.

Other studies have found that in 3-D the channel density N_3 depends on the growth rate of the mushy layer, $\dot{h} = \partial h/\partial t$, according to $N_3 \sim \dot{h}^2$ (Tison and Verbeke, 2001; Wakatsuchi and Saito, 1985). As demonstrated in § 5.1.5, the 2-D analogue of this scaling is $N_2 \sim \dot{h}$. In fig. 5.30c I consider the variation of the channel density with the mushy-layer growth rate to test this scaling. Whilst there is significant variation in the data, I find that in both the 2-D and 3-D simulations the channel density tends to increase with the growth rate. The data is too noisy to confirm the scaling $N \sim \dot{h}^{(D-1)}$ found by previous authors. In 3-D, this scaling only holds for fast growth at early times, whilst for larger times (and smaller growth rates $\dot{h}$) the channel density N appears to approach a constant value. This may be an artificial consequence of the finite box depth.

5.4 Summary

This chapter has investigated convection during mushy layer growth from a fixed boundary. In § 5.1 I considered sea ice growth under different atmospheric conditions, then in § 5.2 I considered the effect of the concentration ratio $\mathscr{C}$ on the dynamics. In both these sections I modelled quasi-two-dimensional flow in a narrow Hele Shaw cell whilst in the final section (§ 5.3) I considered the difference between the dynamics in 2-D and 3-D.

In § 5.1 I found that the ice growth was controlled by thermal diffusion, and convection began once the mushy-layer had reached a critical thickness in line with previous observations (Wettlaufer et al., 1997b). This thickness varies as the atmospheric temperature is varied. Growth from a colder boundary results in a less porous mushy layer, which increases the critical thickness for convection. The data is consistent with the hypothesis that the onset is controlled by a mushy layer Rayleigh number

(Wettlaufer et al., 1997a) which has also been observed in experiments (e.g. Wettlaufer et al., 1997b). The atmospheric temperature also affects the density of brine channels, which appear to produce a spacing $\bar{L}$ that maintains $\bar{L}/(h\bar{\chi}) = O(1)$ where h is the mushy-layer thickness and $\bar{\chi}$ is the average porosity. I demonstrated that, under certain assumptions, this is equivalent to the channel density N scaling linearly with the growth rate $\partial h/\partial t$, which has previously been observed in experiments (Wakatsuchi and Saito, 1985; Tison and Verbeke, 2001).

In § 5.2 I investigated the effect of varying the concentration ratio, $\mathscr{C}$. As in § 5.1, I found that the onset of convection is typically controlled by the porosity of the mushy layer. In this case the porosity increases with $\mathscr{C}$, and therefore the critical mush-layer thickness decreases with $\mathscr{C}$. However this trend does not continue indefinitely. For $\mathscr{C}$ greater than some value $\mathscr{C}^*$ the critical thickness begins to increase with $\mathscr{C}$ in a manner consistent with the predictions of weakly nonlinear stability analyses (Amberg and Homsy, 1993). Following the onset of convection, there are clear qualitative differences as $\mathscr{C}$ is varied. In systems with low $\mathscr{C}$, channels have a higher density and are confined to the region of high porosity near the mush-liquid interface. For $\mathscr{C} \gtrapprox 1$, convection persists throughout the full depth of the mushy-layer. Channels move horizontally through the mushy-layer in both cases. On average, horizontal movement increases with $\mathscr{C}$, which may be due to the larger porosity in these cases. In all simulations the duration for which channels exist τ spans a range of times, with shorter durations being more common. The probability distribution of τ, $p(\tau)$, is consistent with a power law $p \sim \tau^{-1}$ which is also recovered from a simple probabilistic model of channel merging. The observation of an inverse power law is suggestive of a link to the phenomena of self-organized criticality, which has not been explored here but could be investigated in the future.

In both § 5.1 and § 5.2 I compared the observed salt fluxes with predictions from the steady state scalings found in chapter 4 for $\mathscr{C} \ll 1$. For both sets of transient simulations there was a reasonable qualitative agreement between the observed and predicted fluxes. For sea ice growth in § 5.1 I also found good quantitative agreement between the magnitude of the predicted and observed salt fluxes. This builds on the results of chapter 4, where I found that the steady state scalings were consistent with

experimental observations of salt fluxes from growing sea ice, and suggests that they may be a useful tool for understanding this process.

In 3-D simulations (§ 5.3), with otherwise equivalent dimensionless parameters to 2-D, convection tends to be stronger resulting in a greater flux of solute out of the mushy layer. Convection cells form in a square arrangement, with downwelling at the edges of the squares leading to the formation of shallow ridges at the mush-liquid interface. Channels are located at, or close to, the corners of the square convection cells and tend not to penetrate as far into the mushy layer as in 2-D simulations. The channel density in 3-D, N_3, is related to the density in 2-D, N_2, by $N_3 \sim N_2^2$ which is consistent with the additional dimension. In both 2-D and 3-D the evolution of the channel density with the mushy-layer growth rate $\dot{h}$ scales like $N \sim \dot{h}^{D-1}$, which is consistent with previous experiments (Tison and Verbeke, 2001) and observations (Wakatsuchi and Saito, 1985).

The stronger convection in the 3-D simulation relative to 2-D has potentially significant consequences for the parametrisation of salt fluxes from sea ice and merits further investigation. In both 2-D and 3-D simulations I have modelled flow using Darcy's law. Whilst the results generally agree well with experiments and observations, it would be more physically realistic to use a Darcy-Brinkman equation and future work should consider using this approach if computational resources allow.

Another avenue for future investigation would be to explore the effect of the Hele-Shaw permeability K_c, which places a limit on the maximum permeability of the system. This was briefly considered in the 2-D simulations (§ 5.1.4), where I found that increasing K_c reduces the stability of a growing mushy layer. However, the effect of K_c on the convective mushy layer dynamics in 2-D or 3-D was not considered here. Instead, all the simulations of flow in mushy layers were conducted with the same choice of K_c which, if different, may have affected the results. Increasing K_c would increase the permeability in the free liquid and within the high porosity at the mush-liquid interface, which should permit a stronger flow in these regions. This may in turn result in stronger solute fluxes, though in states with $\mathscr{C} \ll 1$, where $\chi \ll 1$ away from the mush-liquid, the dynamics within the interior of the mushy layer should be relatively unaffected by K_c. Equally, if K_c had been smaller then the flow in the liquid and the high porosity region of the mushy layer would be weaker and the solute flux might be smaller.

6

Salt Release from Warming Sea Ice

Whilst multiyear sea ice is relatively fresh, with salinities typically below 5 g/kg (Cox and Weeks, 1974), newly formed sea ice can contain significant quantities of salt (Cox and Weeks, 1974; Notz and Worster, 2008). A significant fraction of the remaining salt trapped in first year ice typically drains into the ocean during summer due to flushing (Vancoppenolle et al., 2007), when snow melt percolates down through the ice replacing the brine inclusions with fresh water. However there have also been observations of intense salt plumes below sea ice following a period of warming where the surface remained frozen (Widell et al., 2006; Jardon et al., 2013; Peterson, 2018), which cannot be attributed to flushing.

It has been proposed that these observations of salt plumes are the result of gravity drainage (Jardon et al., 2013), enabled by an increase in the porosity of the ice as a result of the warming. Whilst the permeability of sea ice increases due to internal melting, the internal salinity gradients which drive convection are simultaneously weakened by the dilution of trapped brine. Nevertheless, Jardon et al. (2013) demonstrated theoretically that a suitably defined local mushy Rayleigh number can increase due to warming, potentially crossing a critical threshold and permitting convection. Using the local mushy Rayleigh number to parameterise convection, Jardon et al. (2013) found that a 1-D model could produce similar desalination events to those seen in observations in response to surface warming. Griewank and Notz (2013) also parameterised convection via a local mushy Rayleigh number in a 1-D model, and found that both surface warming and basal warming can trigger convection in previously convectively stable sea ice.

In contrast to desalination during ice growth, where convection is typically confined to the permeable layer at the base of the ice (Lake and Lewis, 1970), the 1-D modelling studies of Jardon et al. (2013) and Griewank and Notz (2013) found that in warming sea

ice the convection may penetrate throughout the full depth of the ice. This phenomenon may therefore provide a significant pathway for the transport of nutrients and dissolved gases within the ocean-ice-atmosphere system, with important consequences for sea ice ecology (Arrigo et al., 1997). Ice-ocean buoyancy fluxes are typically small in the spring (Sathiyamoorthy and Moore, 2002), as brine rejection is weak and ice melt has yet to begin, so intense desalination events may have important consequences for stratification and circulation in the polar oceans (Aagaard and Carmack, 1989). In the context of an Arctic where the fraction of first year ice is increasing (Meier et al., 2014), it is becoming increasingly important to understand this desalination process.

In this chapter, we investigate salt release from warming sea ice using a 2-D model. This approach offers a significant advantage over previous modelling studies, which were conducted in 1-D, as we can resolve the effect of convection and so do not need to parameterise it. We first simulate ice growth, providing an initial state with salt trapped in remnant brine channels. We then investigate the future evolution of the sea ice in response to either surface warming (§ 6.2) or basal warming (§ 6.3). In both cases, we find intense desalination events. In § 6.4 the results from our 2-D simulations are compared with previous observations and 1-D models. Finally, in § 6.5 we summarise our results and suggest directions for future work.

6.1 Experimental design

We will simulate the evolution of a layer of sea ice in a narrow Hele-Shaw cell, using the model described in chapter 2 and the numerical methods described in chapter 3. The domain is illustrated in fig. 6.1, and is horizontally periodic with a top boundary which is impermeable to fluid flow with a fixed temperature and bulk salinity. An open bottom boundary is enforced by a constant pressure condition which permits flow in and out of the domain. Material entering the domain has a prescribed temperature T_o and salinity S_o. The cell has a width 0.5 m, height 1 m. The physical parameters used in these simulations are as in table 2.1, with a Hele-Shaw gap width d which varies between 0.5 and 2 mm. The resultant dimensionless parameters are presented in table 6.1.

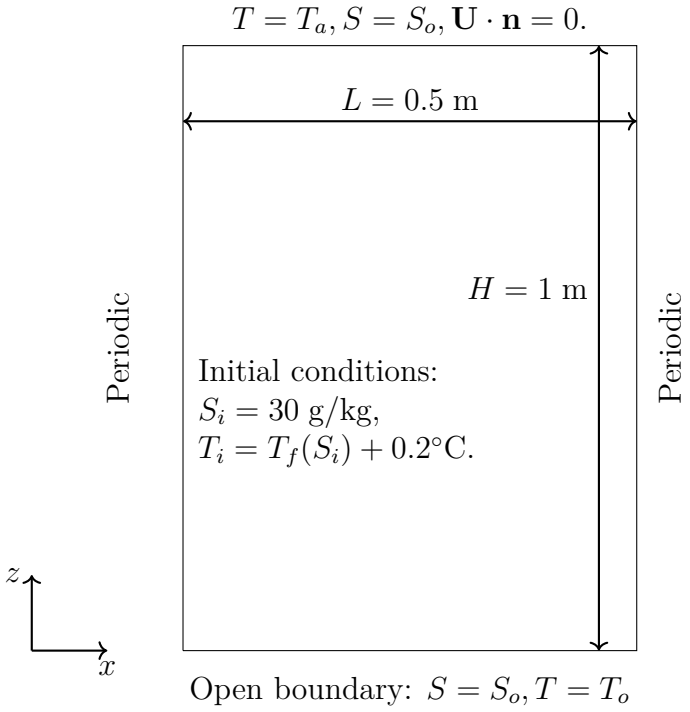


Figure 6.1: Domain for simulations considered in chapter 6. The atmospheric temperature T_a and ocean temperature T_o depend on whether we are considering the initial stage of ice growth (§ 6.1.1) or warming scenarios (§ 6.2, § 6.3). For numerical convenience, the bulk salinity is fixed at the top boundary which results in a small unphysical diffusive salt flux into/out of the domain when $\chi > 0$. Qualitatively, this does not appear to affect the results.

Dimensionless parameter		Value
Compositional Rayleigh number	Rm	8170
Thermal Rayleigh number	Rm_T	40.2
Concentration ratio	$\mathscr{C}$	0.15
Stefan number	$\mathscr{S}$	3.98
Hele-Shaw cell permeability	Π_c	20.8 – 333
Heat capacity ratio	c_p	0.505
Heat conductivity ratio	k	4.24

Table 6.1: Dimensionless parameters for sea ice simulations

6.1.1 Initial state

As noted by Griewank and Notz (2013), simulations of warming sea ice may be heavily dependent on the initial state used. Whilst there are observations of the vertical structure of first year ice (e.g. Notz and Worster, 2008; Nakawo and Sinha, 1981) the 2-D structure is relatively unconstrained. Therefore, we generate our initial state by simulating ice growth over a number of months.

The maximum stable timestep Δt during a simulation is limited by the CFL

condition (Courant et al., 1928), $\Delta t < \frac{\Delta x}{U}$, where Δx is the grid spacing and U is the maximum velocity. Given finite computational resources, we must limit the maximum fluid velocity U in order to integrate our model for several months of physical time with sufficient resolution to capture narrow brine channels. The Hele-Shaw plate separation d enforces a finite permeability $K_c = d^2/12$ on the fluid in the liquid phase. When $K_c \ll \mathcal{H}^2$, the momentum equation is well approximated by Darcy's law and the maximum possible fluid velocity is controlled by K_c. We find that with $d = 0.5$ mm, we can simulate 3 months of ice growth on a 128×256 mesh using 16 processors in ~ 1 week. This resolution is relatively coarse; the width of brine channels is typically of order a few grid cells, whilst ideally we would like to have $O(10)$ grid cells within a brine channel to be confident of having resolved the dynamics. However, we find that the simulated solute fluxes deviate by only around 5% from tests conducted over shorter timescales with a finer resolution of 512×512.

We start by considering an entirely liquid domain with salinity $S_i = 30$ g/kg and temperature $T_i = T_f(S_i) + 0.2°\text{C}$, where $T_f(S)$ is the freezing temperature for liquid of salinity S. For clarity we will describe the ocean temperature relative to the salinity dependent freezing temperature $T_f(S)$, as the assumed linear liquidus up to (T_E, S_E) means that the freezing point in our simulations can differ from reality by up to 1°C. We grow ice from a top boundary held at $T_a = -10°\text{C}$, which is in line with typical atmospheric temperature in the Arctic during spring, whilst fluid entering the bottom of the domain through the open boundary is set to the initial temperature and salinity. Ice is grown for ~ 2 months of physical time, by which point it has reached a depth of ~ 0.5 metres.

6.1.2 Spin up

During ice growth, convection in the liquid is dominated by the salty plumes sinking from the ice. Following basal melt, however, the salinity field will be stably stratified so any convection in the liquid would be driven by temperature differences. The effective porous medium Rayleigh number in the fluid is given by

$$Rm_T^{\text{liquid}} \approx Rm_T \Delta T^{\text{liquid}} h^{\text{liquid}} \Pi_c \approx \Pi_c, \tag{6.1}$$

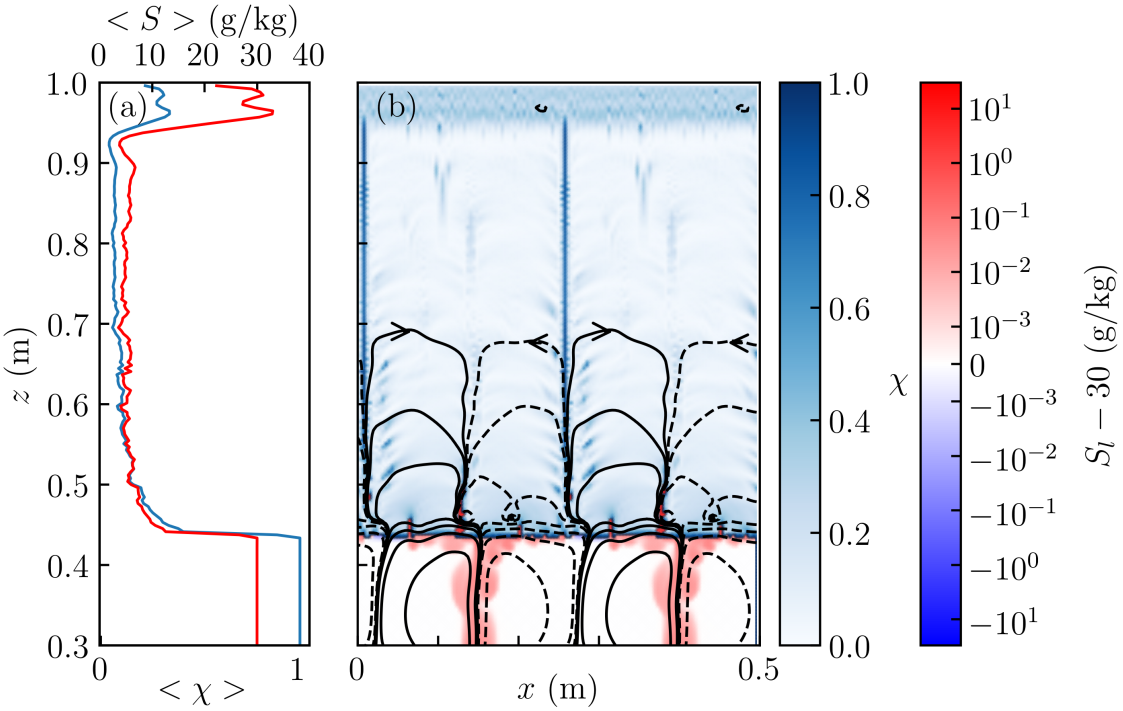


Figure 6.2: Initial state computed by simulating sea ice growth. (a) horizontally averaged profiles of the porosity $< \chi >$ (blue, bottom axis) and bulk salinity $< S >$ (red, top axis). (b) porosity χ and change in liquid salinity $S_l(x, z, t) - S_i$ (only plotted in the liquid, where $\chi = 1$). The porosity colour scale (white to blue) applies in the mushy layer (where $\chi < 1$), whilst the salinity colour scale (blue-white-red) applies in the pure liquid (where $\chi = 1$). The response of this state to atmospheric or oceanic warming is considered in this chapter.

where $\Delta T^{\text{liquid}} = 0.2$ is the dimensionless temperature difference across the liquid, $h^{\text{liquid}} \approx 0.5$ is the dimensionless liquid depth, and Rm_T is the global thermal Rayleigh number from table 6.1. With $d = 0.5$ mm, $Rm_T^{\text{liquid}} = 20.8$ which is below the critical value ($Ra_{\text{crit}} = 4\pi^2 = 39.5$) for convection (Horton and Rogers, 1945). This would artificially suppress thermal convection, which may be important in the case of basal melting. Therefore, following ice growth but before introducing warming, we increase the Hele-Shaw gap width to $d = 2$ mm such that the system is more permissive to flow and $Rm_T^{\text{liquid}} \approx \Pi_c = 333$. Simulations are then continued until initial transient effects have subsided, which takes approximately 8 days of physical time.

The sea ice state following this spin-up period is illustrated in fig. 6.2, which provides an initial condition for the experiment. This simulation is then continued for another month of physical time either with the original boundary conditions, which

provides a control run, or with an increased temperature at the top of the domain, T_a, or at the bottom of the domain T_o.

We will later find that a crucial feature of this initial state is the existence of remnant brine channels. In fig. 6.2 two such channels can be seen – narrow channels of relatively high porosity penetrating almost the full depth of the ice at $x \approx 0$ m and $x \approx 0.25$ m. These two channels are no longer actively convecting except at the base of the ice, but have retained a relatively high bulk salinity and therefore remain relatively unfrozen. There are around 6 further small brine channels at the base of the ice, which are actively draining solute from the high porosity layer which exists near the mush-liquid interface. Whilst the positions and distribution of the two long channels is clearly affected by the narrow domain width, the presence of multiple smaller channels at the base of the ice suggests that the domain size is not overly restrictive. Therefore we expect that we would find broadly similar dynamics in a wider domain.

6.1.3 Control run

In the control run, where the temperatures at the top and bottom of the domain are unchanged, ice continues to grow slowly whilst rejecting brine from a narrow layer at the base of the ice. In fig. 6.3 I plot the average vertical heat and salt fluxes over the open boundary at the bottom of the domain,

$$F_h = \frac{1}{L_x} \int \left(\rho_0 c_{p,l}\, \mathbf{u}\, T - k_l \nabla T\right)_{z=0} \cdot \hat{\mathbf{z}}\, dx, \tag{6.2}$$

$$F_s = \frac{1}{L_x} \int \left(\mathbf{u}\, S - D_l \nabla S\right)_{z=0} \cdot \hat{\mathbf{z}}\, dx, \tag{6.3}$$

where L_x is the domain width. Warming is introduced at a time $t = t_w$. Following the spin-up period (where $t - t_w < 0$) the salt and heat fluxes are roughly constant, with average values $\bar{F}_h = 44$ Wm^{-2}, $\bar{F}_s = -0.01 \times 10^{-5}$ g/kg ms^{-1}. The positive heat flux indicates a net flux of heat into the domain, whilst the negative solute flux indicates that salt is leaving the domain. In the simulations where warming in introduced, either at the surface or the base of the ice, I observe short-lived salt fluxes several orders of magnitude greater than those seen in the control run. I will describe these observations in more depth for the case of surface warming in § 6.2 and basal warming in § 6.3

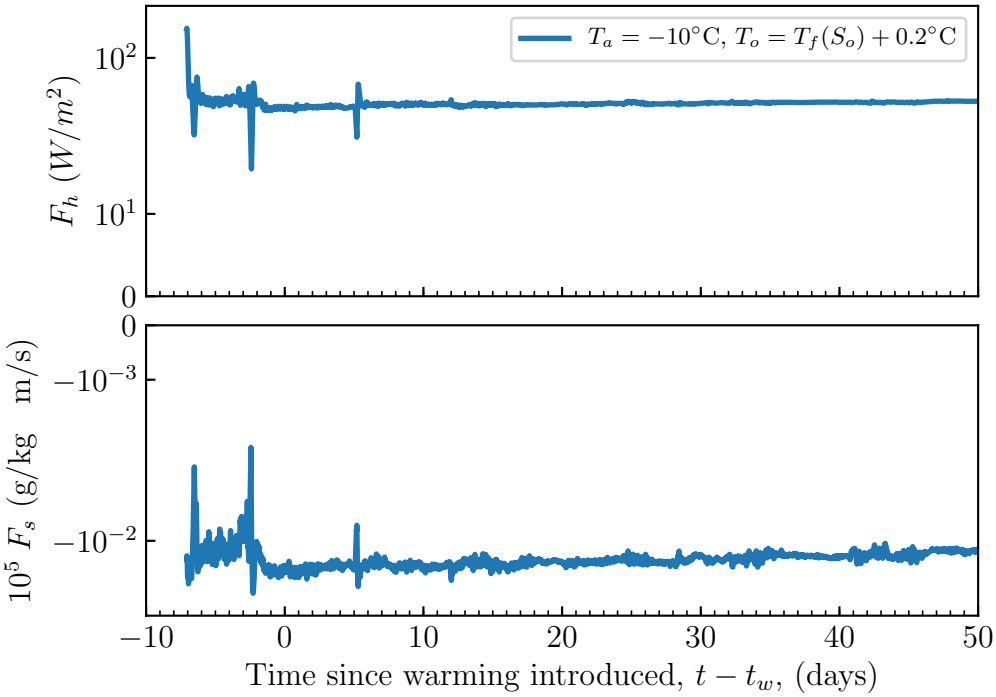


Figure 6.3: Heat flux F_h and salt flux F_s during the control run, where the atmospheric temperature $T_a = -10°C$ and oceanic temperature $T_o = T_f(S_o) + 0.2°C$. Times $t - t_w < 0$ correspond to the spin-up period following an increase in the Hele-Shaw gap width. High frequency variations in the solute flux (time scales of order hours) result from the combination of natural variations within the sea ice and the finite width of the domain. In a wider domain, we expect that these effects would average out.

6.2 Atmospheric warming

Following the initial sea ice growth described in § 6.1.1, and spin-up described in § 6.1.2, I next increased the atmospheric temperature T_a and investigated the response. In fig. 6.4 I plot the salt flux F_s and heat flux F_h for three different surface warming scenarios ($T_a = -2, -3, -5°C$), along with the control run ($T_a = -10°C$, blue). In all three warming cases the salt flux tends towards 0 over the course of the simulations, whilst for $T_a \geq -3°C$ there are intense desalination events (labelled in fig. 6.4). I discuss the dynamics in more detail below.

6.2.1 Response timescale

I expect that the timescale for the response to warming will be controlled by the diffusion of heat down through the ice. To test this, we can consider the diffusive

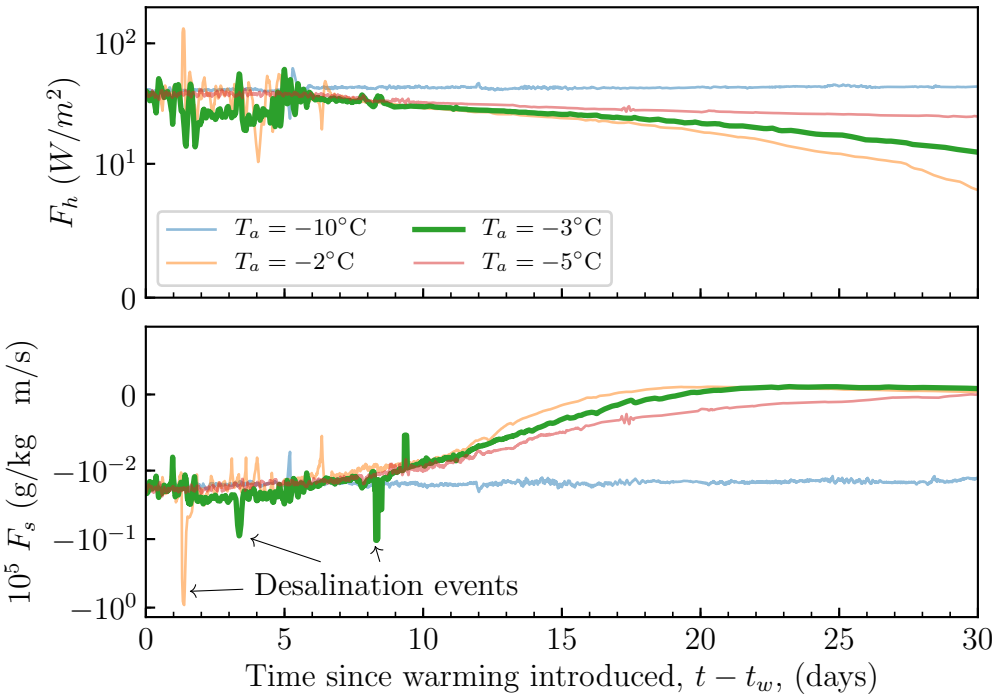


Figure 6.4: Ice-ocean heat flux F_h and salt flux F_s during the control run ($T_a = -10°C$) and following surface warming.

timescale τ_D for a depth of ice h, and compare this timescale with the observation that desalination events begin after a few days, whilst convection shuts down after around 15 days. The diffusive timescale is given by

$$\tau_D = \frac{h^2 \rho c_p}{k}, \tag{6.4}$$

where ρ is the density of the ice, c_p is the heat capacity, and k is the thermal conductivity. We have modelled the ice as a mushy layer, which has a thermal conductivity $\bar{k}$ and heat capacity $\bar{\rho c_p}$ given by the average over the solid and liquid phases,

$$\bar{k} = k_s\phi + k_l(1-\phi), \quad \bar{\rho c}_p = \rho_s\, c_{p,s}\phi + \rho_l\, c_{p,l}(1-\phi). \tag{6.5}$$

As the ice warms, internal melting will act as a heat sink and increase the effective heat capacity of the ice (see e.g. Worster and Rees Jones, 2015). To consider this

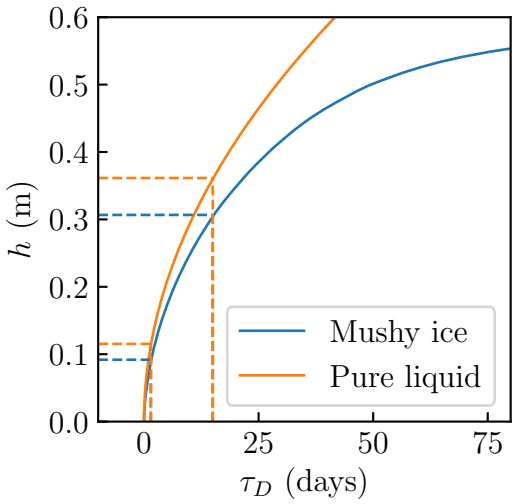


Figure 6.5: Effective diffusive length scale h in simulated sea ice as a function of time.

effect, we can replace $\bar{\rho}c_p$ with an effective heat capacity

$$\bar{\rho}c_{\text{eff}} = \bar{\rho}c_p + \rho_s L \frac{T_f(S)}{(T_f(S_i) - T)^2} \tag{6.6}$$

The enhanced effective heat capacity will slow the diffusion of heat through the ice according to

$$\tau_D^i = \frac{h^2 \bar{\rho} c_{\text{eff}}}{\bar{k}}. \tag{6.7}$$

Meanwhile, heat may also diffuse down through the remnant brine channels. Here the solid fraction is relatively small, so the thermal properties are well approximated by those of pure water and the diffusive timescale will be given by

$$\tau_D^l = \frac{h^2 \rho_l c_{p,l}}{k_l}. \tag{6.8}$$

In fig. 6.5 I plot the diffusive timescale as a function of ice depth h from the surface for mushy ice (τ_D^i, blue) and a pure liquid (τ_D^l, orange). To evaluate (6.7) I compute $c_{\text{eff}}(x, z)$ at each point in the ice for the initial state (fig. 6.2), horizontally average to

find $c_{\text{eff}}(z)$, then find the heat capacity over a depth h by considering the average

$$c_{\text{eff}}(h) = \frac{1}{h}\int_0^h c_{\text{eff}}(z)dz. \tag{6.9}$$

The difference between the diffusive timescale in mushy ice and in liquid channels increases with depth h, but is fairly modest over the range of times considered in the warming experiment ($t - t_w < 30$ days). Dashed lines in fig. 6.5 indicate the time t at which I first observe intense desalination events ($t \approx 1.5$) and at which the salt flux F_s starts to significantly decrease as convection is shut down ($t \approx 15$). The timescales in fig. 6.5 suggest that intense desalination events occur after the warming has penetrated the top ~ 10 cm of the ice. By this point the warming has passed the top of the remnant brine channels, though we cannot determine whether this is a necessary condition for desalination to occur or a coincidence. The shutdown of convection occurs once warming has penetrated over most of the ice depth, to around $\sim 30 - 40$ cm. No intense desalination events are observed in the simulation with $T_a = -5°$C despite the warming being sufficient to eventually shut down the background convection at late time. This suggests that the key factor in triggering intense desalination events is the magnitude of heating, which increases with the atmospheric temperature.

6.2.2 Sea ice response to warming

Whilst these simulations were conducted in 2-D, it is helpful to consider 1-D vertical profiles to study the transient evolution. At each vertical level z_i I compute the minimum vertical velocity $\min(U)$ (which corresponds to the greatest downwelling) and the change in the horizontally averaged porosity ($\Delta\chi$), bulk salinity (ΔS), and temperature (ΔT) relative to the initial state (fig. 6.2). The evolution of these 1-D vertical profiles over time is shown in fig. 6.6 for the experiment where the surface temperature was warmed to $T_a = -3°$C, which is the bold green line in fig. 6.4. The mush-liquid interface is indicated by a white (top panel) or black line (bottom panels).

Following the introduction of warming at the surface ($z = 1$ m), the warming signal propagates downwards through the ice (e.g. see fig. 6.6d), resulting in melting and an increase in porosity (positive $\Delta\chi$). However, close to the mush-liquid interface (within

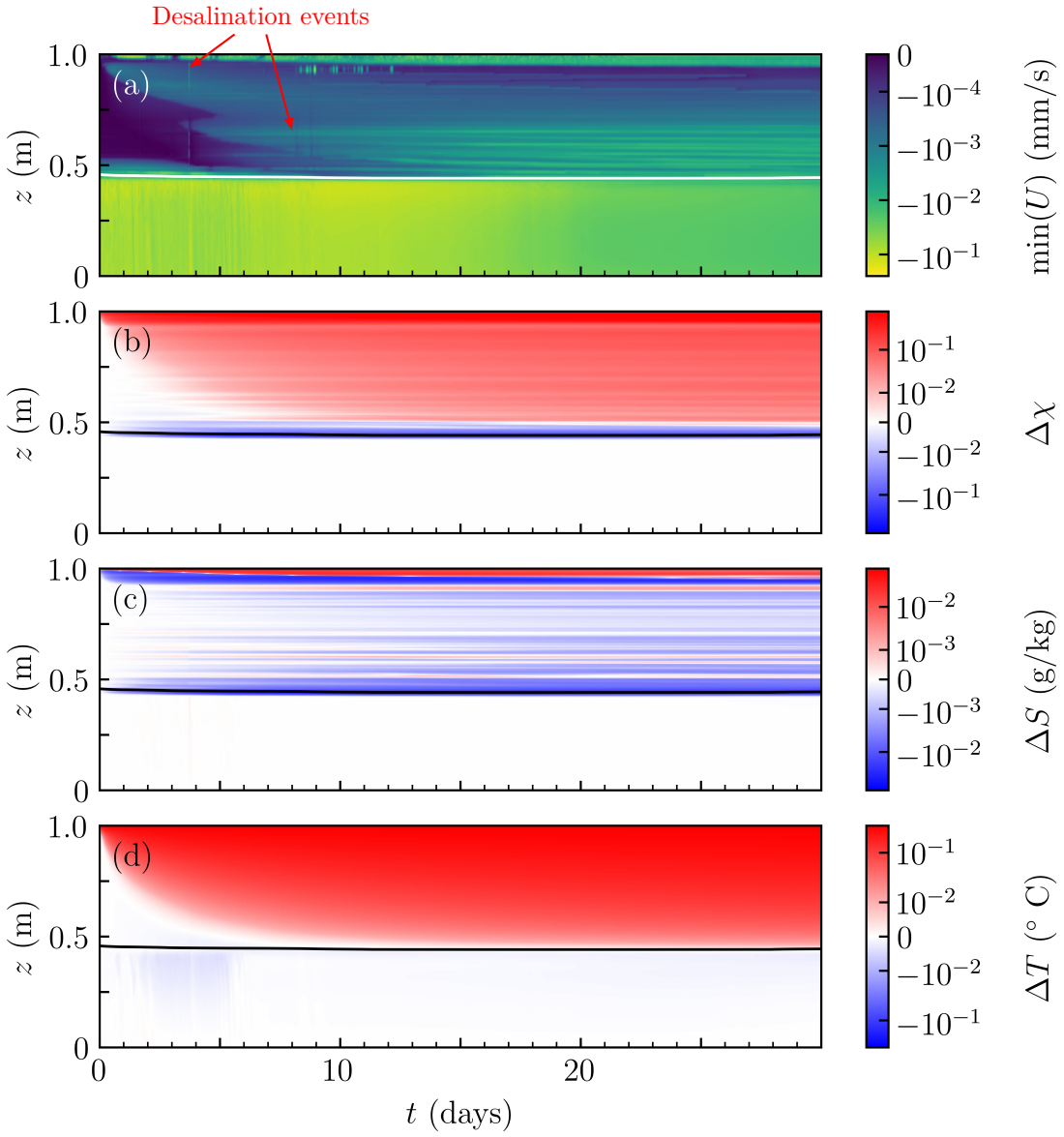


Figure 6.6: Vertical profiles following an increase in the surface temperature to $T_a = -3°\text{C}$. (a) minimum vertical velocity $\min(U)$, and (b-d) change in the horizontally averaged porosity $\Delta\chi$, bulk salinity ΔS and temperature T. The ice-ocean interface $h(z,t)$ is indicated by a white line (top panel) or black line (bottom panels). We use logarithmic colour scales as the quantities vary by several orders of magnitude. Where a quantity X may increase or decrease (i.e. b-d), we use a linear scale for $|\Delta X| < 10^{-2}$ and a logarithmic scale for $|\Delta X| \geq 10^{-2}$. The two desalination events seen in fig. 6.4 are very faintly visible in the velocity profiles, and have been highlighted.

~ 5 cm) brine rejection continues and the porosity decreases due to the rejection of solute (negative ΔS). The continued salt rejection is also evident in the velocity profiles, which show strong convection in both the lower layers of the ice and the underlying fluid at early times. When the warming signal (fig. 6.6d) approaches the mush-liquid interface the convection slows considerably (i.e. for time $\gtrapprox 15$ days). The shut down of convection is particularly evident in the velocity profile, where the flow in the underlying liquid reduces to around 10% of it's initial strength. Whilst warming increases the porosity of the ice, which might be expected to enable convection, the warmer ice has a weaker density stratification which ultimately inhibits convection. The salinity in the liquid phase, which determines the fluid density, is tied to the temperature according to the assumption of local thermodynamic equilibrium. As the temperature increases the salinity in the liquid decreases and the density stratification weakens.

During the first few days, the ice is relatively stagnant above the actively convecting layer at its base, as can be seen in the velocity profile. As the porosity increases at the top, a weak flow develops in the top layers of the ice whilst the middle section of ice, where $\Delta\chi \approx 0$ still, remains stagnant. After approximately 10 days the entire depth of ice warms sufficiently to permit a weak flow, although significant brine rejection has stopped by around 20 days. During the final $\sim$ 15 days of the simulation a weak flow persists within the lower half of the ice ($z \lesssim 0.7$ m), whilst above this level the flow strength is significantly smaller.

Previous authors (e.g. Notz and Worster, 2008; Griewank and Notz, 2013; Rees Jones and Worster, 2014) have suggested that tendency for convection within some region $h < z' < z$ of the mushy layer is controlled by an appropriately defined local Rayleigh number,

$$Rm(z,t) = \frac{g\rho_0\beta\left[S_l(z,t) - S_l(z=h)\right]K(z,t)\left[z - h(t)\right]}{\kappa\nu}, \tag{6.10}$$

where h is the depth of the ice-ocean interface and $K(z,t)$ characterizes permeability for the region $h < z' < z$.

A variety of possible definitions $K(z,t)$ have been employed by previous authors within 1-D models (Rees Jones and Worster, 2014), such as taking the lowest per-

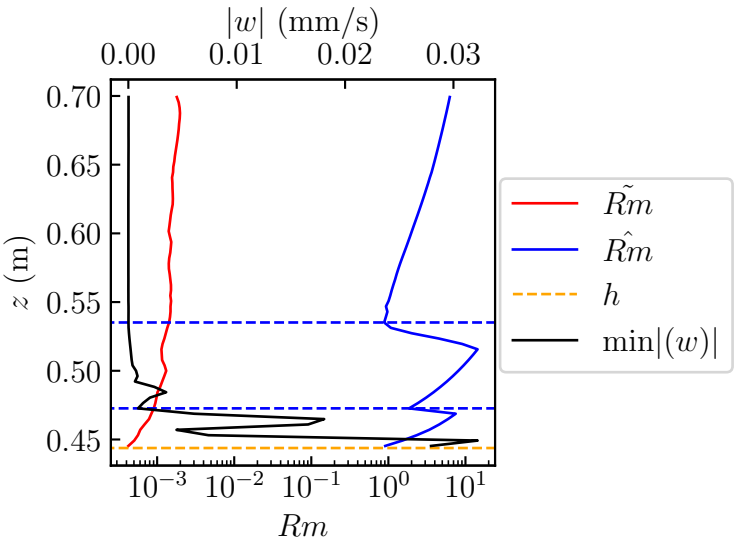


Figure 6.7: Profiles of two different definitions of the mushy Rayleigh number Rm (red/blue, bottom axis) and the absolute value of the minimum vertical velocity $|\min(w)|$ (black, top axis) within the bottom layer of sea ice at the start of warming simulations. The position of the ice-ocean interface h is indicated by the orange dashed line. The Rayleigh number is defined by (6.10), where the permeability (eq. 6.11) is computed using either the mean horizontal porosity ($\tilde{Rm}$, red) or the maximum horizontal porosity ($\hat{Rm}$, blue). There are two distinct dips in $\hat{Rm}$ (indicated by blue dashed lines), which could correspond to points where convection shuts down.

meability in the range $h < z' < z$ (e.g. Notz and Worster, 2008), or computing the harmonic mean permeability in the range $h < z' < z$ (e.g. Rees Jones and Worster, 2014). Meanwhile, to my knowledge, the problem of obtaining an appropriate definition in 2-D has not yet been approached.

I will consider two possible definitions for $K(z,t)$. In both cases, I will construct a 1-D profile $\bar{K}(z,t)$ of the permeability from my 2-D data and then, following Rees Jones and Worster (2014), take the harmonic average

$$K(z,t) = \left[\frac{1}{z-h(t)}\int_{z'=h}^{z'=z}\frac{1}{\bar{K}(z,t)}dz'\right]^{-1}. \tag{6.11}$$

In the first case, I will compute $\bar{K}(z,t)$ by taking the horizontal mean of the porosity, $\bar{\chi}(z,t)$, then compute the permeability from these values via (2.16). I will denote the resulting Rayleigh number in this case with a tilde, i.e. $\tilde{Rm}$. In the second case, I will take $\bar{K}(z,t)$ to be the maximum horizontal permeability at each z, with the resulting Rayleigh number identified by a hat: $\hat{Rm}$. The first case is likely to be more relevant

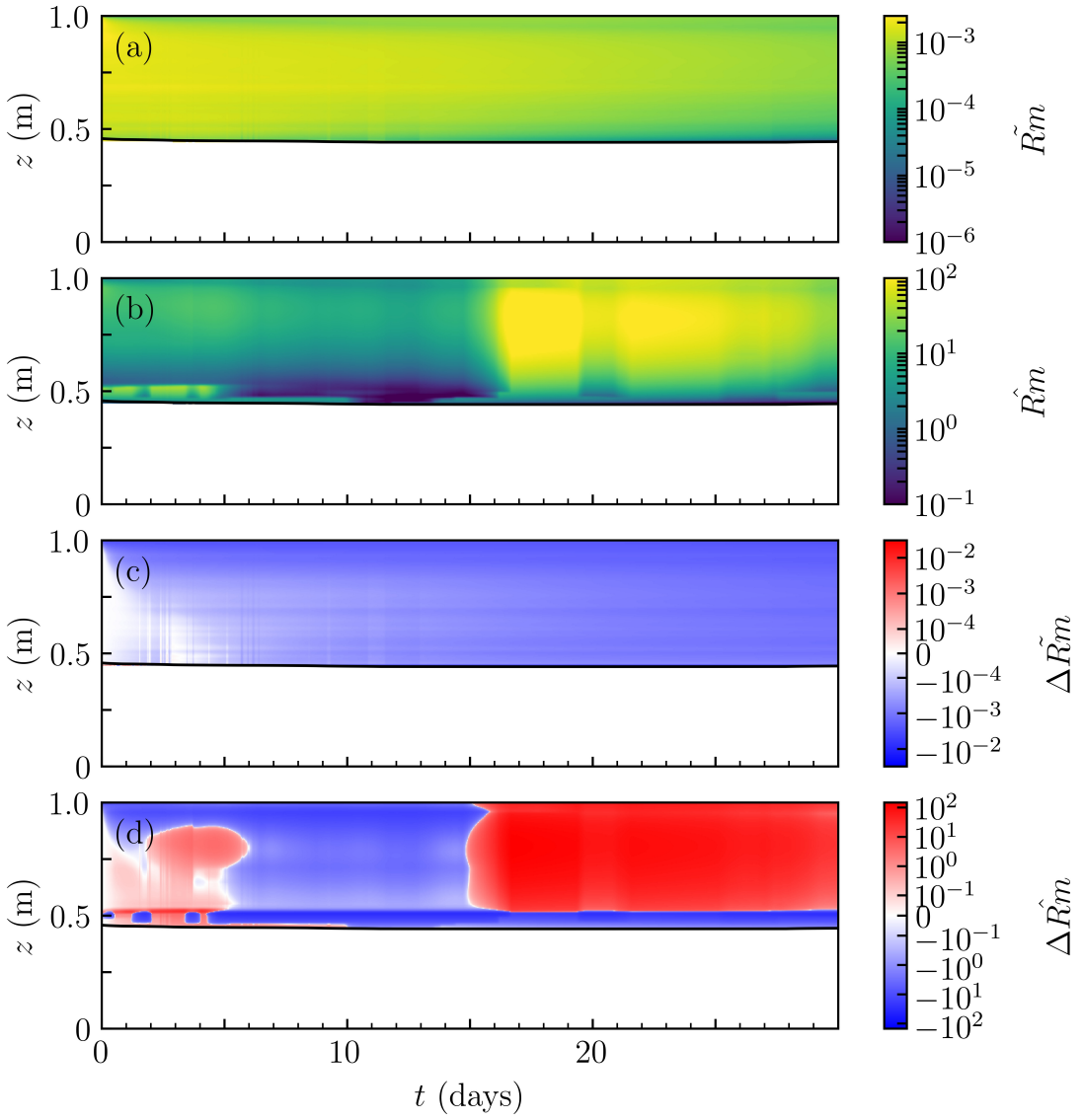


Figure 6.8: Vertical profiles of different measures of the Rayleigh number (a-b) and the change in these Rayleigh numbers (c-d) following an increase in the surface temperature to $T_a = -3°\text{C}$. Desalination events are observed in fig. 6.4 at $t \approx 3.5$ days and $t \approx 8$ days.

to observations such as ice cores, where the horizontal variations within the cores are averaged out by the sampling process, but may struggle to capture the heterogeneity introduced by narrow porous brine channels. This motivates the second choice, where we take the maximum horizontal permeability to highlight the impact of brine channels.

Due to the $(z-h)$ term, $Rm = 0$ at the mush-liquid interface. The salinity difference $S_l(z) - S_l(h)$ typically increases as z increases, increasing the tendency for convection, whilst the permeability typically decreases as z increases. $Rm(z,t)$ is a quantitative

measure of the balance between these effects, with larger values of Rm indicating an increased tendency for convection. It has been suggested that there is a critical Rayleigh number Rm_{crit} which Rm must exceed for convection to be possible (Wettlaufer et al., 1997a; Aussillous et al., 2006; Notz and Worster, 2008). Furthermore, if $Rm(z')$ drops below Rm_{crit} at some point then convection will be inhibited for $z > z'$ (Notz and Worster, 2008) which may determine the confinement of convection to the base of the ice.

To give an example of the $Rm(z)$ profiles which we see in our simulations, in fig. 6.7 I plot $\tilde{Rm}$ (red) and $\hat{Rm}$ (blue) for the initial state (fig. 6.2) to which we applied atmospheric warming.

The profile computed using the maximum permeability (blue) is several orders of magnitude larger than the profile computed using the mean horizontal permeability (red). Previous authors have found a critical Rayleigh number of $O(10)$, which is consistent with our computed $\hat{Rm}$ profile, but it may also be that our system has a different critical Rayleigh number due to the different geometry such as the use of a Hele-Shaw cell. What we are particularly interested in is the variation of these profiles with depth.

In both cases Rm initially increases as z increases, indicating an increasing tendency for convection. The value $\tilde{Rm}$ (red) based on mean porosity continues to increase approximately monotonically throughout the layer of sea ice, which would suggest that either the entire layer is convectively unstable (if at some point $\tilde{Rm}(z) > Rm_{crit}$), or that the entire layer is convectively stable (if $\tilde{Rm}(z) < Rm_{crit}$ for all z). Either way, this is qualitatively inconsistent with the velocity profile (black) which suggests that there is a strong confinement of flow to the lower ~ 5 cm of ice. The $\hat{Rm}(z)$ profile (blue), which was computed using the maximum horizontal permeability, reveals two distinct minima which are highlighted by horizontal dashed blue lines. Either one of these could correspond to $\hat{Rm}(z)$ dropping below the critical Rayleigh number, and therefore might be associated with the confinement of convection. There is a large decrease in the vertical velocity coincident with the lower spike (at $z \approx 0.474$ m), which provides some support for this hypothesis.

I have found that, for the initial state, $\tilde{Rm}$ does not appear to be a particularly relevant measure of the convective instability whilst $\hat{Rm}$ may be consistent with the

observed confinement of flow. I will now consider these metrics for the full simulation with atmospheric warming to $T_a = -3°\text{C}$. I am particularly interested in whether either of these formulations of Rm might have some ability to predict the observed flow through the full depth of the ice which we observe at $t \approx 4$ days.

In fig. 6.8 I plot each formulation of the Rayleigh number, $\tilde{Rm}$ and $\hat{Rm}$ (panels a-b), along with the change in each relative to the initial state (panels c-d). We see that the Rayleigh number computed from the mean porosity, $\tilde{Rm}$, decreases throughout the simulation (fig. 6.8c). This would suggest that the convective stability of the sea ice only increases, which is inconsistent with the observed periods of full depth convection. In contrast, the Rayleigh number computed from the maximum permeability, $\hat{Rm}$, initially increases throughout much of the ice (see fig. 6.8d for $t < 7$ days). This increase in $\hat{Rm}$ could push the system above the critical Rayleigh number and therefore explain why we see convection throughout regions of the mushy layer which were previously relatively stagnant. The decrease in $\hat{Rm}$ after around 7 days (negative regions in fig. 6.8d) may be the result of the full depth convection draining solute and therefore reducing the porosity in the brine channels. After around 15 days, $\hat{Rm}$ then increases again due to the imposed warming increasing the porosity of the mushy layer. However this increase does not trigger further convection. This may be due to the decrease in $\hat{Rm}$ in the lower levels of the ice preventing any flow, or it may indicate that whilst $\hat{Rm}$ is a faithful measure of convective stability early in the simulation, it is no longer relevant at later times.

The applicability of different formulations of Rm to describing the tendency for convection has important implications for parametrising this effect in global circulation models and for interpreting observational results, which will be discussed further in § 6.5.

6.2.3 Dynamics of full depth convection

Two intense desalination events were identified in fig. 6.4 for this simulation, one at ≈ 3.5 days and one at ≈ 7 days after the introduction of warming. Desalination events are associated with intense downward flow through the ice, and therefore we would expect to be able to see some indication of these events in the velocity profiles. There is a clear spike in the vertical velocity coincident with the first desalination event (labelled

in figure), whilst the second event is less clear. The lack of a clear signal during the second event may be due to the frequency with which data is output from the simulation relative to the brevity of the desalination events. Diagnostics such as the salt flux are output at each timestep but it is unfeasible to do the same with the full 2-D solution due to storage constraints, and therefore the brief desalination events may be missed.

Focussing on the first desalination event, the vertical velocity profile reveals that there is significant flow throughout the full depth of the mushy layer, including through a region of otherwise stagnant ice where $\min(U) = 0$ both before and afterwards. To build some understanding into the mechanism, in fig. 6.9 I plot the porosity χ and vertical fluid velocity w at $t \approx 1$ day (panels a-b), along with the change in porosity and change in w by $t = 5$ days (panels c-d). In panel (c) we can see that the porosity increases most significantly in regions where the porosity was already relatively high – in the remnant brine channels and at the top of the ice. Following the increase in porosity we see in panel (d) that the brine channels provide a pathway for fluid flow. Whilst most of the ice remains relatively impermeable, there can be significant flow throughout the depth of the ice.

For there to be flow down through the ice, there must also be a return flow to conserve mass. In the relatively porous region at the base of the ice, we can see (e.g. fig. 6.9b) that there is upwelling (red regions) across broad regions between the active brine channels. In the interior of the ice the porosity is too low for a similar return flow to be possible. Instead, downwelling through the two channels which penetrate the full ice depth is compensated by a return flow in the narrow highly porous region which surrounds each channel. The width of this highly porous region is commensurate with the channel width. Downwelling (negative w - blue) occurs in the centre of the channel, whilst upwelling (positive w - red) occurs simultaneously at the edges. Bidirectional flow inside brine channels has previously been observed in experiments by Niedrauer and Martin (1979), though it is not clear if this is the same mechanism that we see here. There are also hints of this type of behaviour in the steady state simulations described in chapter 4, where we found that for small $\mathscr{C}$ and large Rm there was significant upwelling in the vicinity of the channels. It should be noted that the channels in these simulations are unlikely to be fully resolved – there are

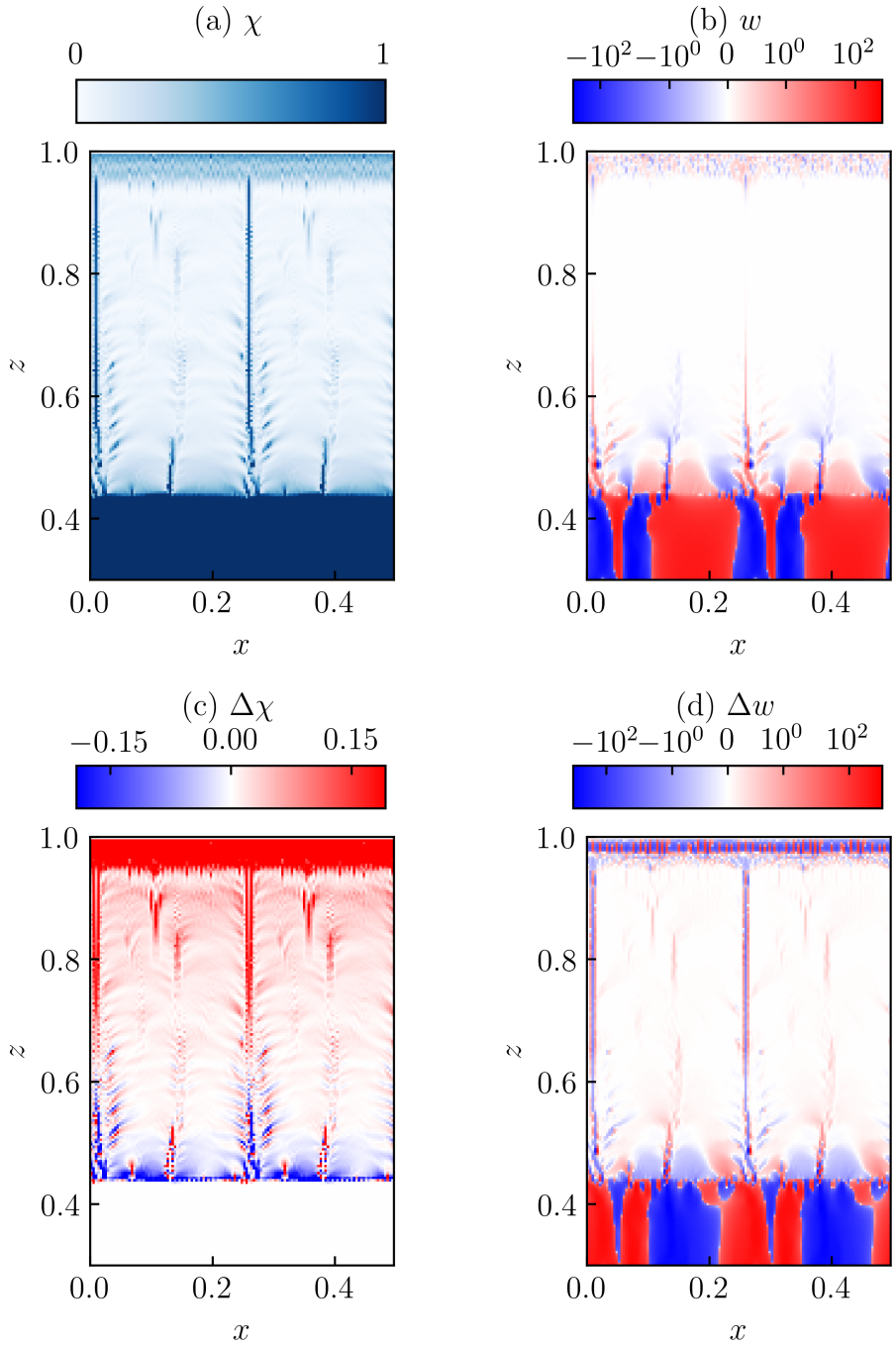


Figure 6.9: (a) porosity and (b) vertical fluid velocity just before the intense desalination event highlighted in fig. 6.6 for sea ice which has been warmed from above. (c) change in porosity and (d) change in vertical fluid velocity following the desalination event. Some grid scale size noise is visible at edges of the remnant channels and at the very top of the ice, which may influence the solution, though the simulation remained numerically stable.

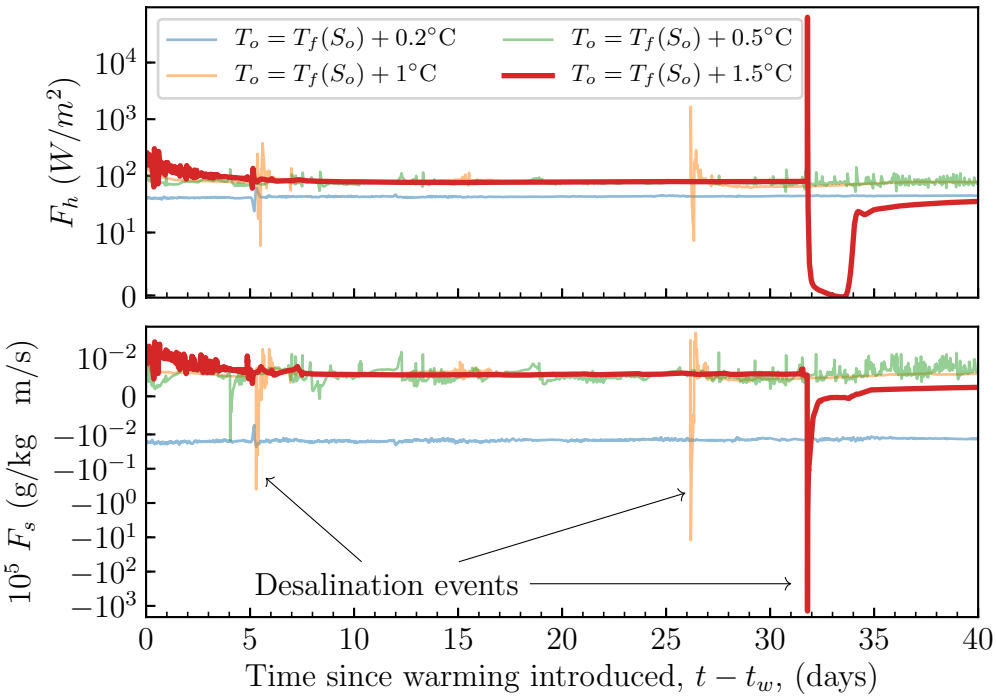


Figure 6.10: Heat flux F_h and salt flux F_s at the base of the domain ($z = 0$) during the control run ($T_a = -10°C$) and following ocean warming.

around 5 grid cells spanning the region of strong flow – and therefore some caution should be exercised over the confidence in this mechanism.

6.3 Ocean warming

In this section I will consider a set of experiments where, following the initial sea ice growth and spin-up period described in § 6.1, the temperature at the bottom boundary of the domain was increased to simulate ocean warming. The ocean temperature will be increased to $T_o = T_f(S_o) + \Delta T$, where $T_f(S_o)$ is the salinity dependent freezing point and $\Delta T = 0.5°C, 1°C$ or $1.5°C$.

In fig. 6.10 I plot the ice-ocean heat flux F_h and salt flux F_s for the simulations with ocean warming, alongside the control run (blue). Whilst in the case of atmospheric warming (§ 6.2) the flux of salt into the ocean gradually decreased, following ocean warming the ice-ocean interface begins to melt almost immediately and hence the salt flux is positive: the ocean becomes fresher. This trend is interrupted by several

significant desalination events (labelled in fig. 6.10), where the salt flux is negative and significantly larger than in the control run

The heat flux is positive in both the control run (blue line) and the warming scenarios due to flow of relatively warm fluid into the domain, but is significantly larger where the ocean temperature has been increased. Desalination events result in cold salty plumes sinking out of the domain, which are identified by large positive spikes in the heat flux and coincident negative spikes in salt flux. Such events are usually followed by a heat flux spike in the opposite direction (though the flux remains positive) as the plumes also cool the underlying liquid, reducing the upward heat flux. Usually this colder fluid is quickly circulated out of the domain and the status quo is recovered, however in the case of the particularly large desalination event at $t \approx 32$ days the signal remains until the end of the simulation. In all cases where warming has been applied, the average heat and salt fluxes are approximately the same independent of the size of the applied warming.

6.3.1 Initial warming

At the start of each simulation $t = t_w$, the warm water introduced at the base of the domain rapidly mixes upwards (e.g. see Δt in fig. 6.11, which increases almost instantaneously in the pure liquid) and begins to melt the base of the ice. Given an ocean warming temperature $T_o = T_f(S_o) + \Delta T$, and a Hele-Shaw cell of gap width $d = 2$ mm, a first approximation to the fluid velocity can be found from Darcy's law,

$$U = \frac{K_c}{\eta}(\nabla p - \rho_l \mathbf{g}) \sim \frac{d^2}{12}\frac{1}{\eta}\rho_l \, g \, \alpha \, \Delta T \sim 0.5 \text{ mm/s}. \tag{6.12}$$

where we have assumed that the convection in the liquid is thermally driven and parameter values are given by table 2.1. The estimated U is in agreement with the observed magnitude of velocities seen in fig. 6.11. The advective timescale for flow in liquid of depth $D \approx 0.5$ m is then $T = D/U \sim 15$ minutes. This is far shorter than the timescale considered in fig. 6.10, which is consistent with the apparently instantaneous jump in the heat and salt fluxes at $t - t_w = 0$.

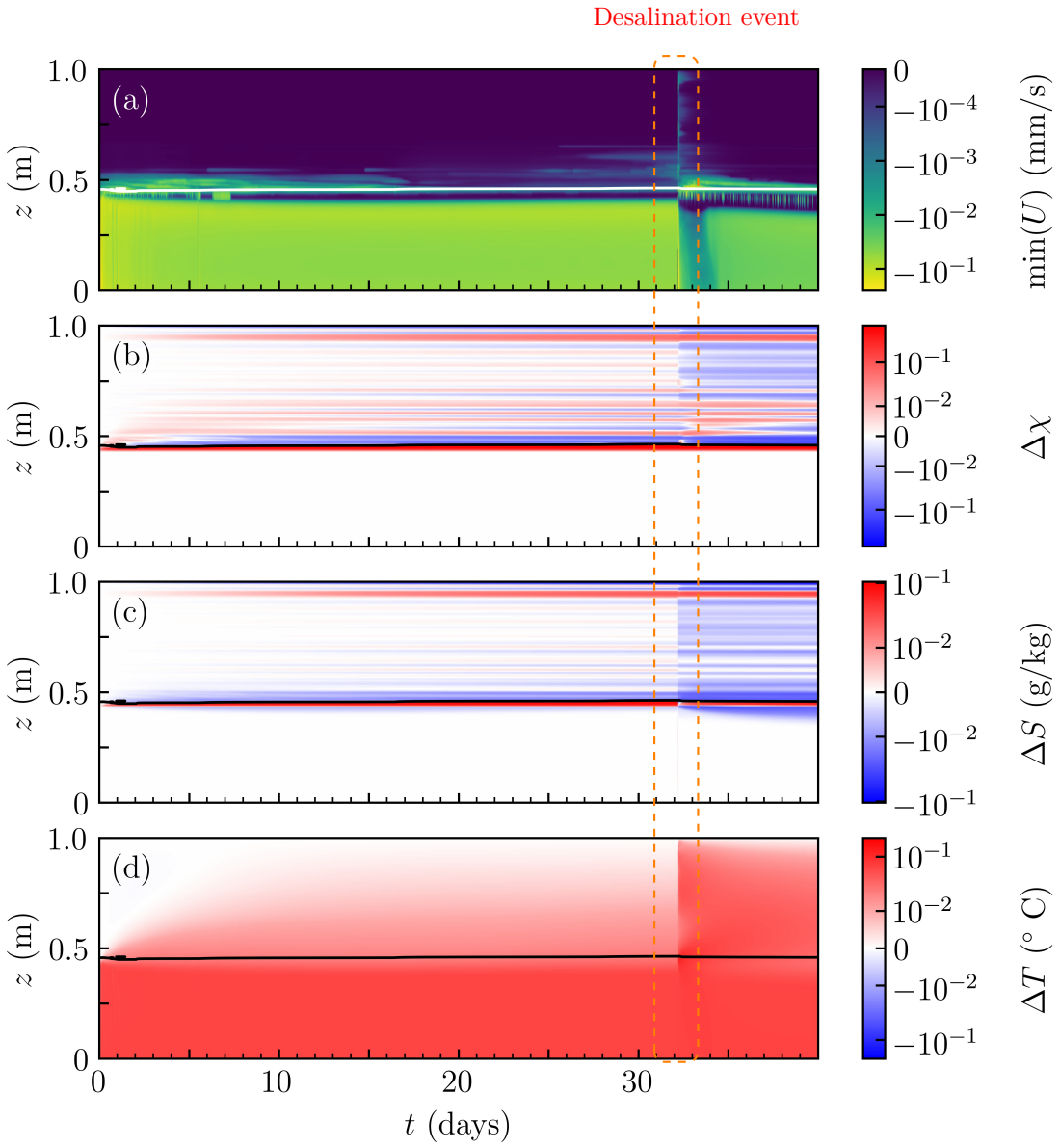


Figure 6.11: Vertical profiles of the minimum vertical velocity $\min(U)$, change in horizontally averaged porosity $\Delta\chi$ and change in horizontally averaged bulk salinity ΔS following an increase in the ocean temperature to $T_o = T_f(S_o) + 1.5°\text{C}$. The increase in salinity (positive ΔS) towards the top of the ice is curious, and possibly due to an increase in salinity at the top of the narrow channels. We are confident that this feature is not closely related to the desalination event at $t \approx 32$ days as the salinity anomaly in this region is relatively unaffected by the desalination.

6.3.2 Consequences of ice melt

Before the change in ocean temperature, the ice was in a state of growth. Increasing the temperature of the liquid alters the energy balance at the mush-liquid interface, and in all three warming scenarios leads to melting. Due to the previous salt rejection, the ice has a lower bulk salinity than the underlying liquid (e.g. see fig. 6.2) so ice melt is relatively fresh and buoyant. Therefore ice melt leads to the formation of a layer of fresh water at the base of the ice, which has several important consequences.

In fig. 6.12 I plot the porosity χ within the ice and the liquid salinity S_l in the pure liquid during the simulation with $T_o = T_f(S_o) + 1.5°\text{C}$. The fresh water layer is clearly evident as the blue region with negative salinity anomaly immediately below the ice.

Within the ice convection continues, rejecting salt into the underlying liquid. The ice-ocean salt flux due to brine rejection F_b is difficult to measure, but is likely somewhat weaker than in the control run, where F_b is of order 10^{-7} g/kg m/s. Salt which is rejected from the ice will increase the salinity of the fresh water layer, whilst the fresh water flux from melting ice F_m will reduce the salinity. The continued existence of a fresh water layer throughout the simulation (e.g. see fig. 6.12) is evidence that, in general, the fresh water flux due to ice melt is larger than the flux due to salt rejection: $|F_m| > |F_b|$. We can obtain a scaling estimate for the fresh water flux,

$$F_m = (S_i - S_o)\frac{\partial h}{\partial t}, \tag{6.13}$$

for ice melting at rate $\partial h/\partial t$ and ice salinity S_i observed in our numerical simulations. We find that $\partial h/\partial t \sim 10^{-8}$ m/s whilst $S_i \approx 10$, so $F_m \approx 10^{-7}$ g/kg m/s which is of the same order of magnitude as F_b. This suggests that the ocean warming in our simulations is just sufficient to form a fresh water layer under the ice. With weaker warming, we expect that the salt flux from the ice might exceed the fresh water flux.

Whilst the gradual warming tends to increase the porosity of the ice, the removal of salt due to convection has a stronger effect and the porosity in the lower layers of the ice decreases. We can see this in the vertical profiles (fig. 6.11) where the porosity generally increases within the ice except near the mush-liquid boundary (black line) until the desalination event at $t \approx 32$ days. In the lower layers of the ice

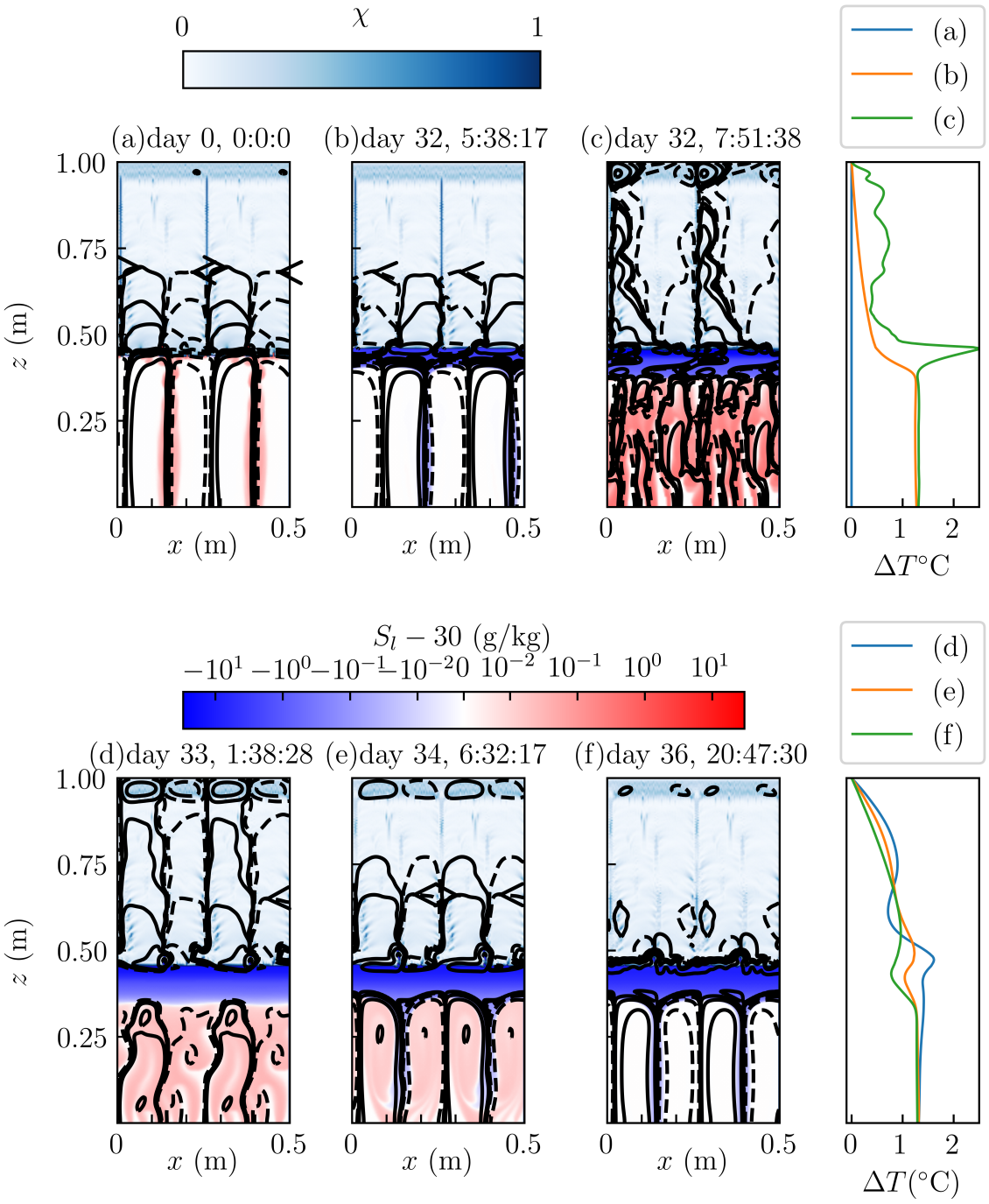


Figure 6.12: Porosity χ in the ice (upper colour scale), salinity S_l in the underlying liquid (lower colour scale), and streamfunction (solid black logarithmically spaced contours: CW, dashed: ACW) during ocean melting at 6 successive times. In the far right panel of each row I plot the change in the horizontally averaged temperature ΔT relative to the initial state. Remnant brine channels are visible throughout the ice during initial growth in (a). Subsequently the ocean temperature is increased to $T_o = T_f(S_o) + 1.5°\text{C}$ and a layer of buoyant water forms due to ocean melting, whilst internal melting within the ice gradually increases the porosity. After 32 days a period of strong convection is initiated throughout the ice. Melt water rises through previously active brine channels and sinks through the rest of the ice.

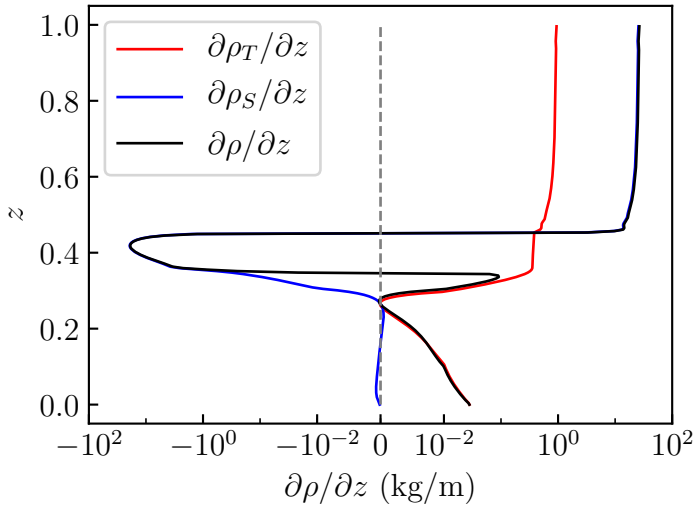


Figure 6.13: Horizontally averaged fluid density gradients due to thermal effects (red), salinity (blue) and the sum of both (black) for the state illustrated in fig. 6.11f. Where $\partial\rho/\partial z < 0$, the density decreases with increasing z so the liquid is stably stratified. When $\partial\rho/\partial z > 0$, convection is possible. In the ice ($z \gtrsim 0.45$) buoyancy is primarily determined by the liquid salinity and the black and blue lines are indistinguishable. In the liquid, the salinity is well mixed so thermal effects dominate the buoyancy stratification. The horizontal scale is logarithmic for $|\partial\rho/\partial z| > 10^{-2}$, and linear in between.

($0.45 \lesssim z \lesssim 0.5$ m), the decrease in porosity over time inhibits convection. We can see this in the vertical velocity profiles (fig. 6.11a) around the mush-liquid interface (white line), which decreases over time until, after around 18 days, the ice has become almost entirely impermeable to convection.

In fig. 6.13 I plot the horizontally averaged fluid density gradients due to thermal effects (red), salinity effects (blue) and both (black) for the state plotted in fig. 6.11f. Convection is only possible where the sum of these two contributions (black line) is positive, which is the case everywhere except the fresh water layer below the ice (where $0.35 \lesssim z \lesssim 0.45$). Above the fresh water layer, convection is primarily driven by salinity effects. Below the fresh water layer, in the pure liquid, the salinity is approximately vertically uniform and thermally driven convection mixes this cold fresh water with the warm relatively saline fluid from the base of the domain.

This thermal circulation is clearly illustrated in fig. 6.12 (panels a,b,e and f), and contrasts with salinity driven convection in the fluid (panels c-d). The compositional convection is unsteady, whilst the thermally driven convection forms into four steady

convection cells which is consistent with the thermal Rayleigh number being around 200 times smaller than in the compositional case.

6.3.3 Full depth convection

The simulation with $T_o = T_f(S_o) + 1.5°\text{C}$ features an intense desalination event at around 32 days, which I will now discuss further. Whilst convection in the lower layers of ice stops at around 18 days, after 32 days we can see in the vertical profiles (fig. 6.11) that there is flow throughout the full depth of the ice, coincident with the large salt flux seen in fig. 6.10. We can also see from fig. 6.11 that this event drains a significant quantity of salt from the ice, whilst reducing the porosity in the upper layers of the ice.

Some of the dynamics of this desalination event are illustrated in fig. 6.12. In fig. 6.12(c-d), we see that flow penetrates the full depth of the ice. The flow is strongest in the remnant brine channel (streamlines are closer spaced) but there is also significant flow through the adjacent relatively low-porosity ice. The ice at the very top of the domain has a high bulk salinity S and low porosity (see fig. 6.2) and therefore the salinity in the liquid phase is also large (approximately given by $S_l = S/\chi$). The streamlines in fig. 6.12(c-d) reveal that flow provides a pathway for this highly saline fluid to drain into the underlying ocean, which may contribute towards the intense salt fluxes observed below the ice.

To further illustrate the key features, in fig. 6.14 I compare the states presented in fig. 6.12b (which is just before the desalination event) and fig. 6.12c (which is during the desalination event). In fig. 6.14(a-b) I plot the porosity (a), vertical velocity (b), and horizontally averaged vertical density gradient (c), just before the desalination event. In (d) I plot the change in porosity between the two states. Finally, I plot the vertical velocity (e) and horizontally averaged density gradient (f) during the later state where desalination is actively occurring (fig. 6.12c).

Just before the desalination event (a-b) the flow is separated into two distinct regions separated by the stagnant layer of fresh melt water. Below the fresh melt water layer ($z \lesssim 0.4$), strong thermally driven convection is clearly visible in fig. 6.14b. There is also weak flow at the mush-liquid interface, where buoyant melt water rises before cooling and then sinking. The ice typically has a low porosity, even very

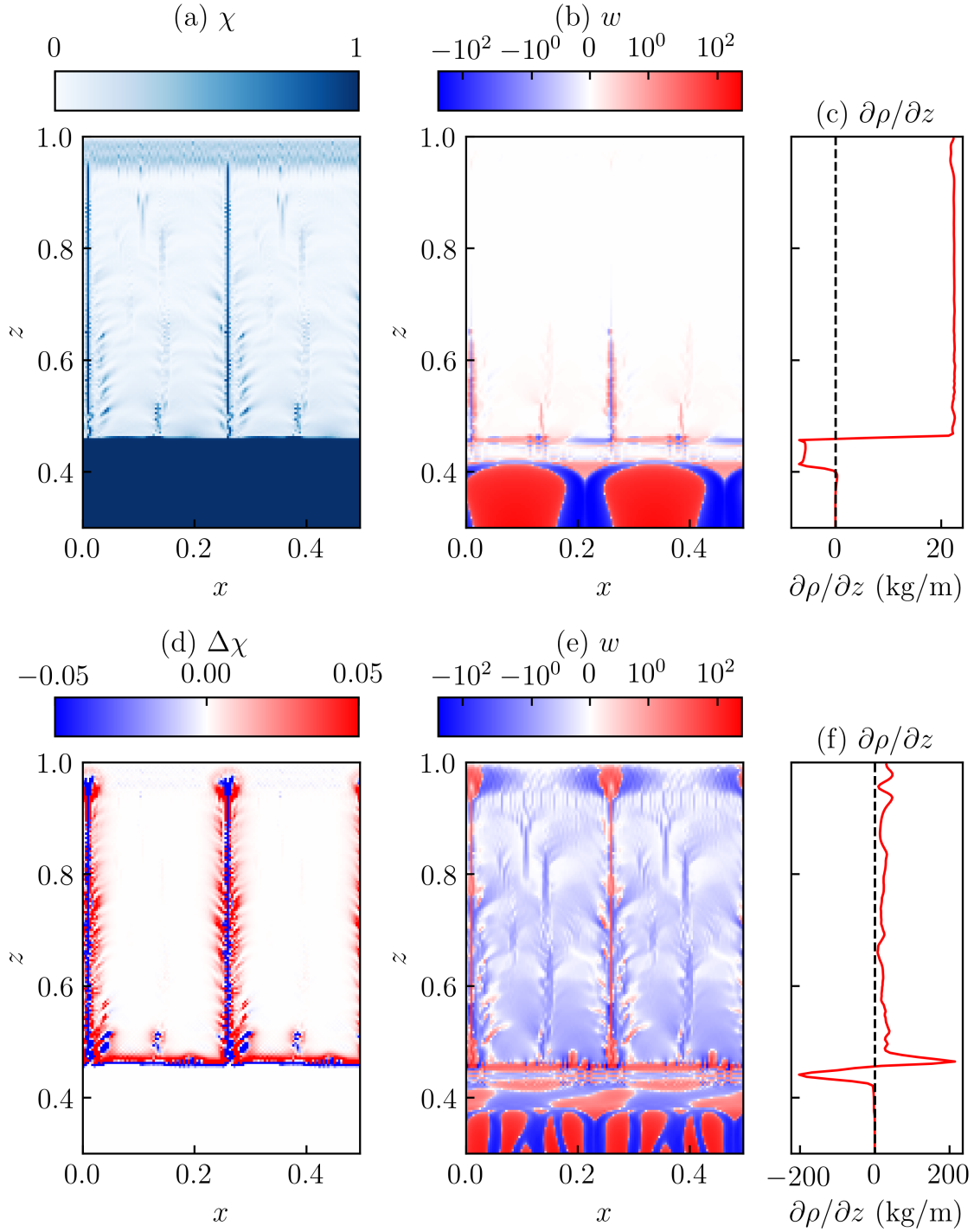


Figure 6.14: Top row: (a) porosity, (b) vertical fluid velocity and (c) density gradient $\partial\rho/\partial z$ for the state presented in fig. 6.12b, which is just before the intense desalination event. Bottom row: (d) difference in porosity between the fig. 6.12c (during the desalination event) and fig. 6.12b (just before the desalination), (e) vertical velocity and (f) density gradient during the desalination event (fig. 6.12c). Just below the ice, $\partial\rho/\partial z < 0$ indicating that in this region the system is convectively stable.

close to the mush-liquid interface, and therefore the flow is confined to the brine channels and a narrow layer spanning the entire base of the ice where the porosity remains relatively high (see fig. 6.14b).

Just a few hours after the state shown in fig. 6.14(a-b), the ice undergoes a period of intense convection. Usually, convection in sea ice involves downwelling through the narrow channels and a weaker upwelling through the rest of the mushy ice. However here we see the opposite picture. Buoyant melt water rises rapidly through the remnant brine channels and sinks through the porous ice to return to the base of the ice (fig. 6.14e). The sinking fluid is solute-rich, and in some cases is sufficiently dense to break through the fresh water layer and sink out of the domain, resulting in the large negative salt fluxes observed in fig. 6.10.

The relatively fresh melt water freezes rapidly within the channel, whilst the downwelling solute-rich fluid causes dissolution in the fringes of the channel and at the mush-liquid interface (see fig. 6.14c). The net contribution of these contrasting effects to the horizontally averaged porosity varies with depth (see fig. 6.11b). In the lower layers of the ice ($0.45 \lesssim z \lesssim 0.7$) the horizontally averaged porosity tends to increase following the desalination event, whilst in the upper layers ($z \gtrsim 0.7$) the average porosity tends to decrease. In contrast to convection where salty fluid sinks through the channels, maintaining high porosity in those regions, this mode of convection is not sustainable. The fresh fluid rising through the channels causes them freeze up, and after a few days the ice returns to a relatively stagnant state for $z \gtrsim 0.5$ m.

It is difficult to identify a particular trigger for the convective episode, and it is likely that a combination of multiple factors enabled this event. The warming of the ice and consequent increase in permeability, particularly within the remnant brine channels, will have reduced the resistance to convection within the ice. However the ice is typically less porous here than in the simulations where warming was applied from above, and flow in those cases was restricted to the brine channels. In contrast to warming from above, where the salinity stratification was weakened, during basal warming the salinity stratification is enhanced. This provides a stronger driving force, which may explain the differences between the two cases.

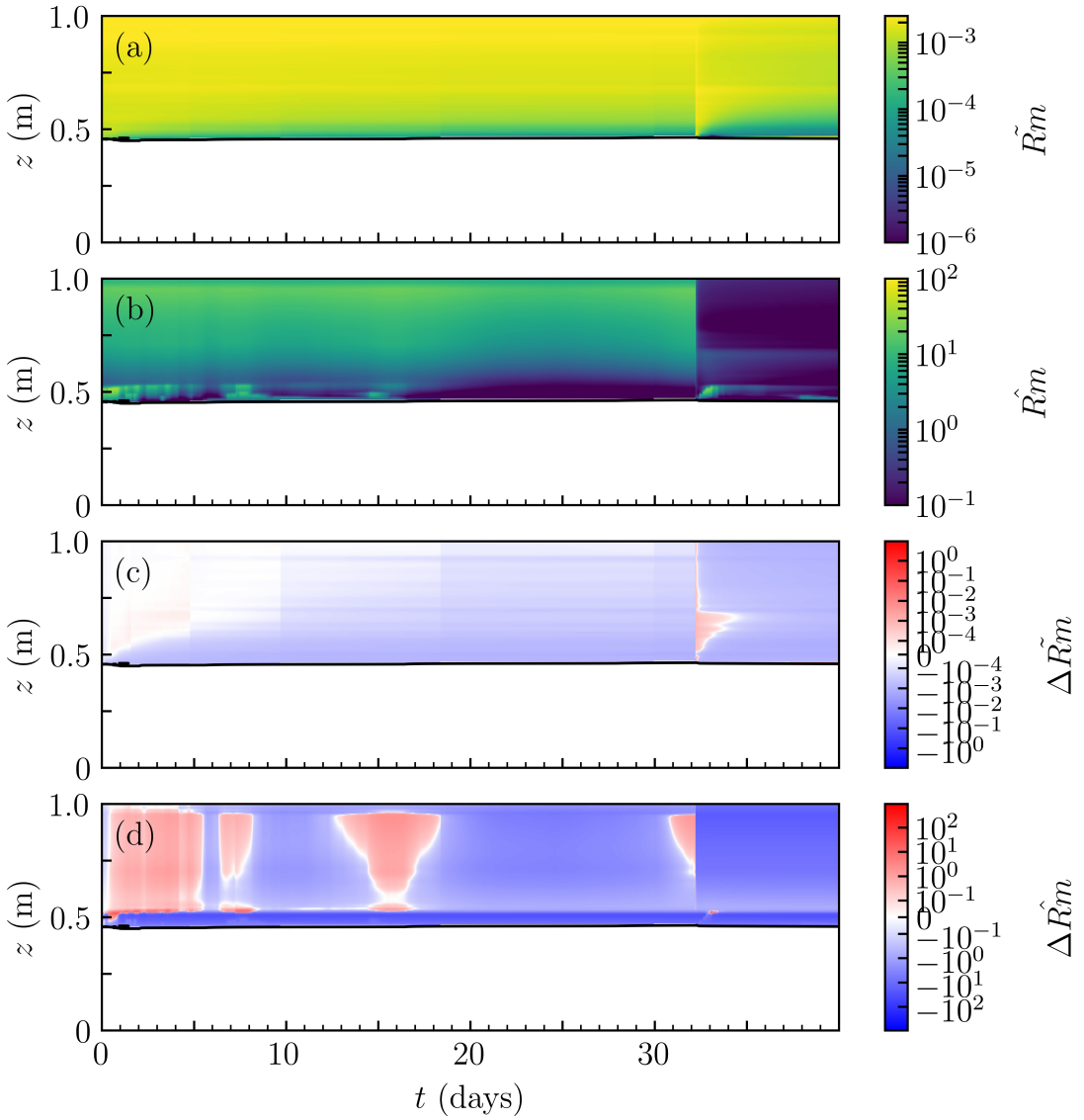


Figure 6.15: Vertical profiles of different measures of the Rayleigh number (a-b) and the change in these Rayleigh numbers (c-d) following an increase in the ocean temperature to $T_o = T_f(S_o) + 1.5°\text{C}$.

To try and understand why we see full depth convection, in fig. 6.15 I compute the same measures of the local Rayleigh number as in § 6.2.2. $\tilde{Rm}$ is computed using the horizontally averaged porosity, whilst $\hat{Rm}$ is computed using the maximum horizontal permeability at each vertical level. As before, the changes in each metric (fig. 6.15(c-d)) are relative to their initial values (at $t = 0$ days). There is a near instantaneous increase in $\hat{Rm}$, which is due to melting at the mush-liquid interface which increases the relative density difference between the mush-liquid interface and

the saline fluid within the ice (c.f. (6.10)). The same effect is present in $\tilde{Rm}$, but is far weaker. As in the case of atmospheric warming (fig. 6.15), $\tilde{Rm}$ appears to be a poor indicator of the tendency for convection. In fact, $\tilde{Rm}$ decreases throughout the simulation, suggesting that convection would be less achievable, until after the desalination event at which point it increases momentarily. Meanwhile, $\hat{Rm}$ increases just before the desalination event (at $t \approx 32$ days) indicating an increased tendency for convection which is consistent with the observed onset of full depth convection. However, interestingly, there are several other significant periods of increased $\hat{Rm}$ (at $t < 5$ days, $6 < t < 8$ days and $13 < t < 17$ days) which do not correspond to desalination events seen in fig. 6.10. It is not clear why the final period of enhanced $\hat{Rm}$ ($30 < t < 32$ days) triggers convection, but the others do not.

Whilst we have focussed on the desalination event observed in the simulation with $T_o = T_f(S_o) + 1.5°\text{C}$, the same mechanism is observed for the second desalination event in the simulation with $T_o = T_f(S_o) + 1.0°\text{C}$. However in that case the flow is confined to the bottom half of the ice, which possibly explains why the resultant salt flux is around an order of magnitude smaller. The first desalination event for $T_o = T_f(S_o) + 1.0°\text{C}$ proceeds via the same mechanism described in § 6.2, with bidirectional flow within the remnant brine channels. However, the flow is confined to the bottom 20 cm of the ice.

6.4 Comparison with other studies

So far we have seen that, in our 2-D model, either atmospheric or oceanic warming can lead to intense desalination events. In this section I will consider these results in the context of the observed salt fluxes which motivated this study, and draw comparisons with previous theoretical work.

6.4.1 Observations

Observations provide an important constraint for salt fluxes from sea ice, whilst leaving the internal dynamics within the ice relatively unknown.Widell et al. (2006) measured salt fluxes at 1m below ~ 1.2 m thick land-fast sea ice during March in Mijenfjorden, Svalbard. They observed large salt fluxes coincident with an increase in the atmospheric

Study	Range of F_s 10^5 (g/kg m/s)	Delay before desalination	Duration of desalination events
Widell et al. (2006)	0.2 – 4.0	$\sim 1-3$ days	$\gtrsim 7$ days
Peterson (2018)	1.0 – 15.0	~ 1 day	$\gtrsim 7$ days
Simulated atmospheric warming (§ 6.2)	0.1 – 1.0	1.2 – 3 days	~ 7 days
Simulated basal warming (§ 6.3)	1.0 – 100.0	4 – 32 days	~ 30 days

Table 6.2: Summary of key properties of observed and simulated desalination events.

temperature from $T_a \sim -20°\text{C}$ to $T_a \sim -2°\text{C}$, and an increase in ocean temperature from $T_o \sim T_f(S_o)$ to $T_o \sim T_f(S_o) + 0.1°\text{C}$. Peterson (2018) took measurements at 1 m below drifting ice just north of Svalbard in June. Large salt fluxes were measured following a passing storm, with atmospheric temperatures peaking at $T_a = 1.6°\text{C}$ and ocean temperatures peaking at $T_o \approx T_f(S_o) + 2°\text{C}$. The particularly warm ocean temperatures in the Peterson (2018) study resulted in significant basal melting, with the ice thickness decreasing from $\sim$ 1.5 m to $\sim$ 0.8 m in 1 week. In both studies the measurements were made using instruments which measured the eddy covariance (i.e. the instantaneous deviations of heat and salt fluxes from the mean values) and were suspended from the ice via a wire.

The timing and magnitude of the salt fluxes observed by Widell et al. (2006) and Peterson (2018) are summarised in table 6.2, along with the results from the simulations described in this chapter. It should be remembered when comparing these studies with our own that there are a number of notable differences. Firstly, our model makes a number of approximations which may not be physically realistic. We have considered sea ice dynamics in a narrow Hele-Shaw cell, where the flow beneath the ice is modelled using Darcy's law rather than the Navier-Stokes equation - a difference we will return to soon. Our simulations are also conducted in 2-D whilst in reality sea ice is 3-D, though in § 5.3 we found that this difference may only have a moderate effect on the dynamics of our model. The permeability of sea ice is not well constrained (as discussed in § 2.1.5), but can have a large effect on the modelled desalination of sea ice (e.g. see fig. 5.8). In this chapter we have chosen a sea ice permeability scale $K_0 = 10^{-9}\,\text{m}^2$ which is consistent with previous studies (e.g. Rees Jones and Worster, 2014), but different values may lead to different results. I also note that

in the observations, where the domain considered was notably wider than in these simulations, around 100 plumes were detected whilst only a handful were seen in the simulations here. Therefore the fluxes and timings reported for the simulations will have significant uncertainties attached to them.

Despite all these differences, both the simulated basal warming and simulated atmospheric warming result in salt fluxes which are of a magnitude consistent with the observations. This is perhaps slightly surprising. The salt flux F_s (6.3) is dominated by the advective part,

$$F_s \sim \frac{1}{L}\int_0^L wS_l\,dx \tag{6.14}$$

whilst the vertical velocity w is restricted in these simulations by the use of a Hele-Shaw cell to $w \sim 1$ mm/s. In the ocean, dense salty plumes typically have a vertical velocity in the range $10-60$ mm/s (Widell et al., 2006; Peterson, 2018) and therefore one might expect the salt fluxes to correspondingly smaller in these simulations compared to observations. However it appears that salinity of the brine plumes in these simulations is significantly greater than in the observations, which offsets the reduced speed of the plume to give approximately equivalent salt fluxes. This suggests that the salt fluxes are primarily controlled by dynamics in the mushy sea ice, where the physics in our model is a more faithful approximation to reality. Whilst the dynamics of brine plumes can be highly complicated, with turbulent flow and mixing affecting their speed, the net buoyancy flux is conserved. Therefore an accurate model of the brine plumes may not be essential for capturing the leading order behaviour of this process.

I also compare the timing of the desalination events. In the penultimate column of table 6.2 I report the delay between the introduction of warming and the first desalination event. With the simulations it is straightforward to measure this delay. It is less clear how to measure the delay in the case of the observational data, as the warming does not occur instantaneously at a well defined point in time, but in both cases the timescale appears to be O(days) which is consistent with the simulations.

Given our simulations, it therefore seems that the observed salt fluxes could be consistent with either basal or atmospheric warming of the sea ice. Both Widell et al.

(2006) and Peterson (2018) observed significant basal heat fluxes coincident with the desalination events, which would be expected to result in melting at the ice-ocean interface. Widell et al. (2006) reported atmospheric temperatures in the range $-10°C$ to $0°C$, whilst Peterson (2018) reported temperatures in the range $-2°C$ to $+2°C$. Therefore both basal and atmospheric warming are likely to have occurred, and it may be that the observed salt fluxes are a response to both effects.

A key difference between basal warming and atmospheric warming identified in our simulations is that following atmospheric warming convection shuts down once the warming has reached the base of the ice. The data reported by both Widell et al. (2006) and Peterson (2018) demonstrates the existence of brine plumes up until the end of the observational period, which is unfortunately around 7 days after the onset of desalination in both cases and commensurate with our estimated shutdown timescale. Therefore we cannot determine if the warming of the ice from above, and consequent reduction of the salinity stratification, would eventually prevent convection as found in our simulations.

6.4.2 Theory and 1-D models

Salt fluxes from warming sea ice have previously been predicted using 1-D models of sea ice (Jardon et al., 2013; Griewank and Notz, 2013). In a 1-D model, it is necessary to parametrize convection. Jardon et al. (2013) used the LIM1D model (Vancoppenolle et al., 2010) whilst the Griewank and Notz (2013) used the SAMSIM model. Both models solve for the thermodynamic growth of sea ice. Meanwhile, convection is parametrised on the basis of a local Rayleigh number, like the one introduced earlier in this chapter (6.10), which is calculated from the computed porosity and liquid salinity profiles. Jardon et al. (2013) emulate convection by increasing the solute diffusivity by several orders of magnitude when $Ra(z)$ exceeds some critical value Ra_{crit}. Griewank and Notz (2013) take a different approach by specifying a vertical fluid velocity at each vertical layer which is linearly proportional to $\max[Ra(z) - Ra_{crit}, 0]$. Both these approaches were motivated by the standard mechanism for convection during ice growth, where dense salty fluid sinks through narrow channels whilst relatively fresh cold water rises between the channels.

The results found in this chapter highlight two possible shortcomings of these types of parametrisation schemes. Firstly, I have found that in a 2-D model brine transport in warming sea ice may occur through different mechanisms to the standard picture of convection in sea ice during early growth. In § 6.2 I found bi-directional flow in the narrow channels, and in § 6.3 I found upwelling in the channels coupled with downwelling in the surrounding mushy ice. Secondly, I have found that a local Rayleigh number computed from the horizontally averaged porosity, $\tilde{Rm}$, is not consistent with the observed patterns of convection. As the horizontally averaged porosity will behave similarly to the thermodynamically determined porosity which 1-D models use to compute Rm, this suggests that such 1-D models may struggle to accurately predict the onset of convection in warming sea ice.

During ice growth, brine rejection occurs within an actively convecting region which has a relatively high porosity and is continually growing down into the ocean. In contrast, the simulations conducted here reveal that the remnant brine channels play a key role. Remnant brine channels introduce significant heterogeneity in the horizontal dimension which are a challenge to represent in 1-D models. In a 1-D model the permeability is assumed to vary only in the vertical direction, and convection is confined to the region where the permeability is sufficiently high that the local Rayleigh number (6.10) is above some critical value. However we have seen that convection, along with brine rejection, can be confined horizontally to narrow remnant brine channels whilst the adjacent mushy ice is stagnant (e.g. in § 6.2.3). The horizontally averaged permeability is too low in these cases to support flow throughout the ice, as demonstrated by the local Rayleigh number which was computed from the horizontally averaged porosity $\tilde{Rm}$ (plotted in fig. 6.15 and fig. 6.8). Therefore according to a parametrisation based on these definitions of the local Rayleigh number there would be no flow. A revised definition for the local Rayleigh number which uses the maximum horizontal permeability, $\hat{Rm}$, was a more useful predictor of the onset of full depth convection. This suggests that desalination like we see is made possible by the pre-existing arrangement of remnant brine channels, which themselves are a consequence of the conditions under which the ice was grown. To predict this behaviour in a 1-D model will require an understanding of the distribution, salinity, and porosity

of remnant brine channels under different growth conditions to be introduced to the existing parametrisations of brine rejection.

6.5 Summary

In this chapter I have investigated the response of a layer of sea ice to atmospheric or oceanic warming using a 2-D model. By first modelling sea ice growth, we computed an initial condition which consisted of a ~ 0.5 m thick layer of mushy sea ice which featured heterogeneous salinity and porosity fields including remnant brine channels. This layer of sea ice was then subjected to warming either at the surface or the base. In response to this warming we found intense desalination events where the salt flux at 0.5 m below the ice was orders of magnitude larger than in the cases where no warming was applied.

In the case of atmospheric warming (§ 6.2) we found that intense desalination events began $O(1$ day) after the introduction of warming and continued for around 7 days. During intense desalination events the flow was confined to the remnant brine channels, which span the full depth of the ice and warm quicker than the surrounding ice due to their lower solid fraction. Convection stops when the warming has penetrated through towards the base of the ice, and the internal melting of ice had weakened the density stratification to the point where convection was no longer possible despite the increased ice permeability.

Following ocean warming (§ 6.3), the base of the ice begins to melt creating a layer of relatively fresh water. Convection continues within the lower layers of the ice, but the salt flux due to brine rejection is weaker than the fresh water flux from melting ice and hence the fresh water layer persists. Gradually the ice warms and becomes more permeable, until after around 20-30 days full depth convection events occur in simulations with $T_o = T_f(S_o) + 1°\text{C}$ and $T_o = T_f(S_o) + 1.5°\text{C}$. However in contrast to the convection seen during ice growth, here there is upward flow of relatively fresh melt water in the narrow brine channels coupled with downwelling through the mushy ice.

In § 6.4, we saw that the magnitude and timings of the salt fluxes in these 2-D simulations are consistent with the scale seen in observations. This suggests that the mechanisms we have described may be active in sea ice during warming conditions.

We have demonstrated that a suitably defined local Rayleigh number can be a good predictor of the onset of convection, but only if defined in terms of the maximum horizontal permeability of the sea ice. This is because the dynamics are highly sensitive to the narrow highly permeable remnant brine channels, within which the flow is often confined. In contrast a Rayleigh number computed from the horizontally averaged porosity, which is akin to the porosity predicted by a 1-D thermodynamic sea ice model, is a poor predictor of the onset of convection in our simulations. Therefore it is unlikely that these processes will be well represented by current 1-D parametrisations of mushy-layer convection. We suggest that future work should attempt to constrain the distribution and properties of remnant brine channels, and then incorporate these features into 1-D models.

Our results also have important implications for the interpretation of observations. Profiles of the salinity and porosity within sea ice from ice cores will naturally be horizontally averaged over the cross sectional area of the core, which is typically much larger than the width of a brine channel. Such profiles may not capture the localised regions of high permeability which result from brine channels. Therefore, local Rayleigh numbers computed from such profiles may predict that the ice is convectively stable when in fact there could be a notable flux of salt and other nutrients through the full depth of the ice.

Flow through the full depth of the ice may have significant biogeochemical consequences. The interstitial fluid within the ice contains a range of dissolved chemicals beyond NaCl, including iron (Lannuzel et al., 2007), CO_2 (Loose et al., 2011) and methane (Damm et al., 2015). Microorganisms live in the ice which rely on some of these chemicals, along with suitable levels of light, for survival (Thomas and Dieckmann, 2002). Our simulations suggest that remnant brine channels may offer a pathway for the transport of nutrients and microorganisms through the full depth of sea ice. Following surface warming we found that flow was focussed in the high porosity regions - the narrow remnant brine channels and the base of the ice. The observed mechanism for full depth convection in the case of basal melt, where sinking fluid passes through the relatively low porosity mushy ice, may have different biogeochemical consequences from the canonical mechanism where downwelling is confined to narrow brine channels.

Our understanding of the biogeochemistry within sea ice would certainly benefit from the coupling of a 2-D model with a biogeochemical component.

Our modelling approach has involved a range of approximations, which we have discussed to some extent in § 6.4.1. Whilst the dynamics within the sea ice are reasonably robust, the flow in the underlying liquid is less realistic as we are modelling flow in a narrow Hele-Shaw cell. Future studies may attempt to relax this assumption, or at least constrain the effect it has on our results. For example, in the case of ocean warming (§ 6.3), we found that the fresh layer of melt water below the ice played an important role in the dynamics by enhancing the salinity stratification within the ice. In a model with more realistic dynamics in the pure fluid, such as ocean turbulence or a shear flow, this fresh water layer may be partially eroded reducing the likelihood of convection within the ice. We also found that the intense desalination events observed in the simulations in this chapter are highly dependent on the initial condition to which warming was applied. Therefore it would be interesting for future studies to consider warming with different initial conditions, which could be found by modelling ice growth under different conditions.

7

Discussion and conclusions

When the ocean freezes it forms sea ice, a reactive porous mixture of solid ice crystals and salty liquid brine known as a mushy layer. Flow within the pore space allows the dense brine to drain into the underlying ocean, where it provides a buoyancy force on the ocean, and transports biogeochemically relevant substances through the ice. Meanwhile, the porous ice mediates the fluxes of heat and other dissolved chemicals between the ocean and the atmosphere. The feedbacks between flow, solidification, and dissolution result in highly nonlinear dynamics across multiple scales. Notably, downwelling highly saline fluid leads to formation of narrow liquid brine channels through which the flow is focussed.

Convection within sea ice can occur when the buoyancy forces which drive flow are sufficiently large relative to the dissipative forces of thermal diffusion and viscous drag on the pore scale. This ratio is characterised by the dimensionless mushy Rayleigh number, $Rm = (g\beta\Delta S\, K_0\, h)/(\eta\kappa_l)$. Convection is possible when Rm exceeds some critical value, Rm_{crit}, which depends on the geometry and other material properties.

In this thesis, I have set out to build insight into the nonlinear convection which occurs within sea ice. To achieve this, I first developed a new numerical method capable of resolving the narrow brine channels which are an inherent feature of convection within sea ice. I then studied convection within a variety of settings. Firstly, I considered steady-state convection through a periodic array of channels leading to the development of new scaling laws in a dynamical regime which is particularly relevant to sea ice. I then simulated transient sea ice growth from a fixed boundary, where channels were free to develop spontaneously and interact with each other leading to rich nonlinear behaviour. Finally, I investigated the possibility for convection within a thick layer of ice in response to warming.

Throughout this thesis, a key focus has been on considering mushy layer systems in the *far-from eutectic* limit. This corresponds to situations where the dimensionless concentration ratio $\mathscr{C} \ll 1$, with the concentration defined via $\mathscr{C} = (S_i - S_S)(S_E - S_i)$, where S_i is the initial salinity of the fluid, S_E is the eutectic salinity, and S_S is salinity in the solid phase. In the far-from eutectic limit the initial salinity, which determines the availability of solute within the system, is small relative to the changes in salinity which occur as the system undergoes solidification. Whilst the presence of solute in sea water prevents sea ice from freezing completely solid for temperatures $T_L < T < 0°\mathrm{C}$, the relatively small value of the concentration ratio ($\mathscr{C} \approx 0.15$) means that the interior of sea ice has a relatively high solid fraction. Hence, the interior of sea ice is typically relatively impermeable to flow, confining convection to a narrow porous layer at the base of the ice.

I below summarise the main new results of this thesis and discuss the geophysical implications (§ 7.1), before identifying potential opportunities for future work building on these results (§ 7.2).

7.1 Key results and their implications

7.1.1 Modelling mushy layer convection with Adaptive Mesh Refinement

Convection in mushy layers can be modelled using a set of mesoscopic conservation equations (chapter 2). These equations are coupled, multi-scale, and, in the limit $\mathscr{C} \ll 1$, highly nonlinear. The solution of these equations poses a significant challenge.

In chapter 3 I developed and implemented a new algorithm for solving this model using Adaptive Mesh Refinement (AMR). In contrast to previous approaches, I used a finite volume discretisation which scales well on large numbers of processors and permits the use of *subcycling* in time. The method extended a previous algorithm for the incompressible Navier-Stokes equations (Martin et al., 2008), with additional terms to account for flow in a porous material and the conservation of heat and solute during the solidification of a binary alloy. The algorithm was implemented using the Chombo AMR library, which had pre-existing support for solving hyperbolic and linear elliptic

equations. To solve the coupled equations for heat and solute, I implemented a new nonlinear multigrid scheme in Chombo . Subcycling in time allows us to advance coarser meshes by larger timesteps according to the CFL condition improving efficiency, but requires a series of synchronisation steps to ensure approximate conservation properties at the interface between coarse and fine meshes. Existing strategies for *refluxing*, where mismatches in the flux of heat and salt are accounted for, were modified to account for the highly nonlinear behaviour of this system. I also derived a new condition on the stability of the freestream correction step which ensures approximate mass conservation.

In § 3.3 I demonstrated that this new scheme is both accurate and computationally efficient. Due to the time investment required to implement the AMR functionality, simulations in the remainder of the thesis were conducted using a uniform mesh. Had the AMR code been available earlier, it is likely that a similar series of studies would have been pursued but with calculations performed at a higher resolution. This would have been particularly helpful in chapter 6, where in some cases it is unlikely that the channels were fully resolved. In § 7.2 I will explore some of the possible opportunities that the ability to use AMR could offer for future studies.

7.1.2 Steady state convection

Our first steps into the world of mushy layer convection began in chapter 4, where we considered the simplified geometry of steady state convection through a periodic array of channels. This setting has previously been studied by various authors (e.g. Schulze and Worster, 1998; Chung and Worster, 2002; Wells et al., 2013), but not in the *far-from-eutectic* limit which is most applicable to sea ice. The bulk of this chapter focussed on understanding the effects of convective confinement on mushy layer dynamics in the limit $\mathscr{C} \ll 1$.

Using an optimal flux hypothesis (Wells et al., 2010) to determine the spacing of channels, steady state solutions were computed for $0.01 < \mathscr{C} < 20$ and $Rm_{crit} < Rm < O(10Rm_{crit})$. When $\mathscr{C} \ll 1$, we observed the confinement of convection to a narrow porous layer at the base of the ice. Meanwhile, the optimal solute flux between the mushy layer and underlying liquid F_O increased sublinearly with Rm, in contrast to the linear scaling $F_0 \sim Rm$ found by Wells et al. (2013) in the limit $\mathscr{C} \sim O(Rm)$.

Motivated by these numerical results, new scaling laws were found which described flow through channels confined to the porous layer at the base of the ice. These scaling laws were shown to be consistent with both the present numerical results and previous experimental studies (Wettlaufer et al., 1997b). The new scaling laws describe how, in the limit $\mathscr{C} \ll 1$, the fluid flow through the mushy layer is generally weak and therefore the diffusive temperature and porosity profiles remain good approximations to the full nonlinear dynamics. The porosity is small except for a narrow high porosity layer at the mush-liquid interface, within which convection is confined. The depth of this porous layer h_χ changes in response to the flow. As the mushy layer Rayleigh number Rm increases, the flow becomes stronger and removes more solute from the mushy layer. This reduces the porosity, decreasing h_χ. By considering the flow out of the liquid channels, our scalings predicted a solute flux $F_O \sim \mathscr{C}^{7/6} Rm^{5/6}$. This scaling predicts desalination consistent with that in laboratory sea ice growth, although unfortunately the data cannot distinguish this scaling from a previous scaling (Wells et al., 2011) that is linear in Rm.

The insights gained from these numerical and theoretical results may have important implications for our understanding of sea ice. A key feature of these scaling laws and numerical simulations is the presence of a high porosity layer at the ice-ocean interface, within which convection is confined. This region closely resembles the skeletal layer observed in sea ice (Reeburgh, 1984), which is an important biological habitat in the polar environment (Krembs et al., 2001). Our results may help understand how the geometry, porosity, and fluid transport in this region may evolve within growing sea ice, with important implications for polar biology. The prediction of a sublinear solute flux scaling may also have consequences for parametrising the fine-scale process of gravity drainage from sea ice in large-scale global circulation models. Ice-ocean solute fluxes provide an important buoyancy forcing for the polar oceans, but must be parametrised in such models. The most modern approaches to this problem compute solute fluxes from estimations of the Rayleigh number Rm in 1-D sea ice models. Until now, the best estimate of the solute flux dependence on Rm was the linear scaling found by Wells et al. (2013). The scaling found here ($F_O \sim \mathscr{C}^{7/6} Rm^{5/6}$) is only subtly different, and in fact both our scalings and those of Wells et al. (2013) predict a vertical velocity in the

brine channels which scales linearly with Rm. Therefore models which predict vertical flow in the mushy layer that is proportional to Rm (e.g. Griewank and Notz, 2013; Rees Jones and Worster, 2014) may not require modification in light of our results. Rather, our scalings build confidence in the faithfulness of these parametrisations. The predicted depth of the high porosity layer, within which convection is most active, may help inform the choice of vertical resolution in sea ice models. Our scalings suggest that it may be beneficial for resolution to be focussed on the base of the ice. Discrepancies between the predictions made in this section and the dynamics of sea ice may arise due the approximations made within the Darcy flow model. Most notably, I have considered flow in a narrow quasi 2-D Hele-Shaw cell where the flow in the pure liquid is slower and less turbulent than in reality. There is also considerable uncertainty over the appropriate choice of the permeability function $K(\chi)$ (§ 2.1.5). The model does describe the physics of the mushy layer in a faithful manner, and therefore I expect that the dynamics within the mushy layer will be a good approximation to those found within sea ice. This may explain why the predicted solute flux is consistent with experiments in spite of the model's deficiencies.

The latter part of this chapter relaxed the assumption that flow was confined within a narrow Hele-Shaw cell and instead applied a Darcy-Brinkman model. Focussing on the dynamics of the brine channels, we considered the effect of solute diffusion by varying the Lewis number $Le = \kappa_l/D_l$. Numerical simulations supported the prediction from theoretical scaling arguments that solute diffusion is only important if $Le \lesssim O(1)$ for the Darcy-Brinkman system, which is far smaller than found in typical systems (e.g. for sea ice, $Le \sim 200$). In contrast, the scalings for flow in a narrow Hele-Shaw cell found that solute diffusion was a key physical process within the narrow channels. This result serves as a reminder that the two cases are not identical, and suggests that the Le dependence found in § 4.1 may not be observed in sea ice growth which isn't constrained by a narrow Hele-Shaw cell.

7.1.3 Convection during transient growth

In chapter 5 I moved from steady-state growth to transient solidification from a fixed boundary. This setting is particularly relevant to sea ice growth on Earth, where the

atmosphere-ocean boundary is approximately fixed. In this chapter we considered a wider domain than in chapter 4, allowing channels to form and interact spontaneously.

I began in § 5.1 by considering sea ice growth in response to three different atmospheric temperatures: $T_a = -10°\text{C}, -15°\text{C}, -20°\text{C}$. The modelled sea ice growth was qualitatively consistent with previous experimental studies (e.g. Wettlaufer et al., 1997b) and theoretical predictions (e.g. Worster and Rees Jones, 2015), where growth was also from a boundary held at a fixed temperature. For sea ice formation in the ocean, the variability of the atmospheric temperature which I have neglected may lead to modest differences which are left for future studies to investigate. I found that the onset of convection was delayed until the ice had grown to a critical depth, which varied with T_a in a manner consistent with the hypothesis that convection requires the local Rayleigh number to exceed some critical value (Wettlaufer et al., 1997a). For smaller T_a, the mushy layer is colder and less porous, requiring a greater depth to generate the sufficiently unstable buoyancy stratification for convection. This was also shown to be consistent with experimental results (Wettlaufer et al., 1997b). Following the onset of convection, the transiently evolving mushy-layer porosity, channel spacing, and mush-liquid solute flux was found to follow scaling behaviour commensurate with the scalings obtained in chapter 4 for steady state growth.

The average spacing between brine channels $\bar{L}$ increases over time as the mushy layer depth h increases, and decreases as the atmospheric temperature decreases. This is consistent with a number of previous studies (e.g. Tait and Jaupart, 1992; Katz and Worster, 2008). Growth from a colder boundary results in a closer channel spacing for the same ice depth. I found that a scaling $\bar{L} \sim h\bar{\chi}$ describes the time evolution of the channel spacing well in all 3 simulations, and showed that this is consistent with the observation made by previous authors (e.g. Tison and Verbeke, 2001) that the channel density $n \sim 1/\bar{L}$ is proportional to the ice growth rate. I also demonstrated that this empirical scaling is consistent with our steady state scalings, where we found that the ratio of the depth of the high porosity region at the base of the mushy layer to the channel spacing, h_χ/λ, is independent of the length scale.

Amongst all of this, it is still not clear what physical processes determine the channel spacing. The scaling arguments we derived in chapter 4 made no assumptions

of the channel spacing, but nevertheless were found to be consistent with our transient simulations where the channel spacing was allowed to develop naturally within the limits of the finite domain. Meanwhile, we showed that the variation of the channel spacing with the mush depth and porosity in our transient simulations was consistent with that found experimentally by previous authors in experiments (e.g. see Tison and Verbeke, 2001). The agreement between these different studies suggests that the scalings found in chapter 4 may apply in a wide range of physical settings. Therefore it is particularly interesting that these scalings were also found to be consistent with the numerical calculations in chapter 4, where the channel spacing was calculated according to an optimal flux hypothesis (Wells et al., 2010). By extension, it is plausible that the optimal flux hypothesis, which states that the channel spacing adjusts dynamically to maximise the drainage of potential energy from the mushy layer, does indeed control the spacing of brine channels. At any rate, the results in chapter 4 and chapter 5 are consistent with this hypothesis. The narrow brine channels within sea ice pose a significant challenge to model developers. They are far too small to be described explicitly but, as we saw in chapter 6, it can be difficult to accurately predict salt fluxes without knowing the properties and distribution of the channels. The scalings found here may provide a useful tool for understanding their behaviour. Therefore there is a need for more robust tests of these scaling arguments, and more generally of the optimal flux hypothesis, which I will discuss further in § 7.2.

Whilst $\mathscr{C} \ll 1$ for sea ice, there are other mushy layers of geophysical and industrial interest which are often characterised by different values of $\mathscr{C}$. Therefore, in the second section of chapter 5 I considered the effect of the concentration ratio on the transient growth of mushy layers. As in § 5.1, I found that for all $\mathscr{C}$ the onset of convection is delayed until the mushy layer reaches a critical depth. For small $\mathscr{C} \lesssim O(1)$ the critical depth decreases as $\mathscr{C}$ increases due to the increased porosity of the mushy layer, but for larger $\mathscr{C}$ the critical depth begins to increase again. This variation, which had previously not been seen in experimental or numerical studies, was broadly consistent with the predictions of weakly nonlinear stability analyses (Amberg and Homsy, 1993) to within some minor quantitative differences. Following the onset of convection, flow with $\mathscr{C} \ll 1$ was confined to a small fraction of the mushy layer close to the mush-liquid

interface, where the porosity was higher. For $\mathscr{C} \gtrsim O(1)$, flow penetrated the full depth of the mushy-layer. Whilst in general these simulations evolve transiently, after a dimensionless time $t \approx 1$, many of the properties appear to tend towards a constant value. In § 5.2.4 I found that the mushy-layer properties at this time were broadly consistent with the scalings identified in chapter 4. Most notably, the decrease in the bulk solute concentration within the mushy layer was in close agreement with the predictions of the solute flux found in chapter 4.

As in § 5.1, the channels were not stationary in these simulations but moved horizontally through the mushy layer resulting in highly nonlinear behaviour including channel merging and the spontaneous formation of new channels. By tracking the position of channels at the mush-liquid interface, I computed the trajectory of channels over time allowing for a quantitative analysis of their behaviour (§ 5.2.5). In some ways the channel dynamics vary significantly with $\mathscr{C}$. Simulations with smaller values of $\mathscr{C}$ typically feature more channels which are closer spaced and less horizontally mobile. However, if we compare the distribution $f(\tau)$ of channel durations τ - that is, the time between a channel forming and then merging - we find that in all our simulations there is an inverse power law relationship $f(\tau) \sim \tau^{-1}$. The discovery of a relationship which applies independent of the system parameters may indicate the existence of self organized criticality. This a phenomena which can occur when a dynamical system has an attractor which is also a critical point, and hence evolves in a similar way for a wide range of parameters (e.g. see Jensen and Magnasco, 1999). I also found that the same power law relationship could be recovered from a simple statistical model which neglects the more complicated nonlinear physics present in the full mushy layer model by treating the horizontal movement of channels through the mushy layer as a random walk.

The results in § 5.2.5 are particularly interesting and warrant further investigation. If some of the channel dynamics are indeed the result of self-organized criticality then there could be an alternative explanation for the spacing of channels. We observe this behaviour across a wide range of $\mathscr{C}$, and therefore this may have important implications not just for sea ice modelling, but also for understanding a wide range of mushy layers.

In the final part of this chapter (§ 5.3), I briefly considered mushy layer convection in a 3-D model. Due to the computational expense of running simulations in 3-D, a

single 3-D simulation was compared to its 2-D equivalent. The two were found to be broadly consistent, though in 3-D the fluid flow was slightly stronger which resulted in greater desalination of the ice. In 3-D, we found sheets of downwelling within the mushy layer arranged in a square array pattern. At the mush-liquid interface, regions of downwelling at the edges of the squares resulted in dissolution, with brine channels (i.e. regions of maximum dissolution) occurring at the vertices of the squares. This is similar to the (albeit hexagonal) patterns seen in ammonimum chloride by Tait et al. (1992). For consistency with our 2-D simulations, which were conducted in a narrow Hele-Shaw cell, in our 3-D simulations we modelled the flow in the underlying pure fluid using Darcy's law. This is not physically justifiable for the case of sea ice, and future work should aim to improve on this assumption by using larger computational resources to exploit the Darcy-Brinkman version of the code. The spacing of channels in 3-D was found to be approximately commensurate with the spacing seen in 2-D simulations after accounting for geometric factors relating to the difference in dimensions. The variation of the channel spacing with the mush depth is also consistent with the statistical scaling seen in experiments (Tison and Verbeke, 2001) and observations (Wakatsuchi and Saito, 1985). It is plausible that the channel spacing is primarily controlled by dynamics within the mushy layer, which are described well by our model, and therefore that it is not essential to accurately model flow in the liquid region in order to understand flow and solidification within the mushy layer in 3-D. If true, this would be particularly convenient for future modelling studies.

7.1.4 Convection in warming sea ice

In the earlier chapters, the focus has been on flow and solidification during ice growth. Motivated by observations of intense brine plumes below warming sea ice (e.g. Widell et al., 2006; Peterson, 2018), in chapter 6 I investigated the response of a layer of sea ice to a sudden increase in the atmospheric (§ 6.2) or oceanic (§ 6.3) temperature.

In contrast to previous studies (e.g. Jardon et al., 2013; Griewank and Notz, 2013), which have used 1-D models to suggest that such warming may trigger convection in previously stagnant ice, our 2-D model allows for spatial heterogeneity within the ice. In particular our initial state, which was found by simulation ice growth for several

months, contains several remnant brine channels - narrow highly permeable regions that were previously active brine channels but have since frozen over.

I found that either atmospheric or oceanic warming could trigger intense desalination events in the 2-D model. In both cases, the remnant brine channels play a key role in the dynamics. Following atmospheric warming to $T_a = -3°\text{C}$ I found that intense flow through the full depth of the ice was focussed in the remnant brine channels with relatively little penetration into the surrounding ice. Increasing the ocean temperature to 1.5°C above its freezing temperature was found to trigger a particularly intense desalination event, where relatively fresh melt water rose through the remnant brine channels before sinking through the adjacent relatively low-porosity ice. It is possible that different warming scenarios may lead to a different response, and this is an area that could be explored in the future. For example, here I considered a sudden increase in temperature but in reality warming is likely to occur over a finite time period, or may vary nonmonotonically - perhaps due to the diurnal cycle.

Previous authors have suggested that the tendency for convection within a layer of sea ice (or some other mushy layer) is controlled by a local Rayleigh number (Wettlaufer et al., 1997a; Aussillous et al., 2006; Notz and Worster, 2008, e.g.). This has been used as the basis for parametrising convection within a number of 1-D sea ice models (e.g. Turner et al., 2013; Griewank and Notz, 2013; Rees Jones and Worster, 2014). These models typically solve numerically for diffusive growth of the ice, then use the computed porosity and salinity profiles to define the local Rayleigh number and hence estimate the strength of convection. I compared two possible formulations of the local Rayleigh number with my 2-D numerical simulations. First I computed $\tilde{Rm}$ from the horizontally averaged porosity, then I computed $\hat{Rm}$ from the horizontal maximum of permeability at each vertical level. The horizontally averaged porosity is relatively insensitive to the presence of narrow brine channels, being most consistent with the diffusive porosity profile which would be computed in 1-D simulations. Meanwhile the horizontal maximum of permeability will be dominated by the presence of highly permeable brine channels (or remnant brine channels). I found that a criteria based on $\tilde{Rm}$ was inconsistent with convective onset in my 2-D simulations; the horizontally

averaged properties of the ice were too impermeable to predict flow. In contrast, $\hat{Rm}$ was a far better indicator of the tendency of the ice to undergo full depth convection.

These results, particularly the discovery that $\tilde{Rm}$ is inconsistent with the observed convection within sea ice, suggest that current sea ice models may struggle to accurately model these processes. Specifically, our results highlight the possibility that convection may occur within a layer of sea ice in situations where current parametrisations based on $\tilde{Rm}$ predict that there would be no flow. The desalination events we observed featured strong flow throughout the full depth of the ice, which would transport not just salt but a wide range of solutes including nutrients and dissolved gases. These processes could have important biogeochemical consequences for the polar regions, such as increasing the transport of iron between the ice and the ocean which can enhance primary productivity (Lannuzel et al., 2007) or releasing dissolved gases from the ocean into the atmosphere (e.g. Damm et al., 2015). Within the sea ice, our simulations reveal that flow, and hence the presence the of dissolved chemicals, is highly localised within the regions of high porosity. The remnant brine channels and the high porosity layer at the base of the ice may feature particularly high concentrations of solute and nutrients, allowing organisms to thrive in these environments (Thomas and Dieckmann, 2002). Future studies should investigate options for better representing the diverse heterogeneity of brine channels into 1-D models of sea ice.

7.2 Opportunities for further investigation

The work presented in this thesis provides a wide range of opportunities for future studies. A common approximation made throughout this thesis is to model sea ice in a narrow Hele-Shaw cell, where flow in the liquid phase is described by Darcy's law. Models with a more faithful representation of flow in the underlying pure liquid, such as using a Darcy-Brinkman equation, could be used to constrain the applicability of our results to physical settings such as sea ice growth. Our numerical method provides a possible tool for tackling this problem. In § 5.3 I briefly considered sea ice growth in 3-D, but there is significant scope for further investigation of these, particularly with the use of a more realistic Darcy-Brinkman equation. Such studies would require significant

computational resource, as the improved fidelity of the Darcy-Brinkman model comes at a high computational cost. The Darcy-Brinkman model results in stronger flow within the liquid than the Hele-Shaw model, which can be turbulent and requires far shorter timesteps than would otherwise be needed to model flow in the mushy layer.

Many of the results found in this thesis raise interesting physical questions, which could be explored in the future. Our results are broadly consistent with the hypothesis that the spacing of brine channels during mushy layer growth is determined by an optimal flux condition (Wells et al., 2010), though the comparison with the solute flux observed in simulations of transient sea ice growth is less convincing. Further attempts to prove or disprove this hypothesis are necessary. One possible option would be to consider directional solidification in a sufficiently wide domain that the channel spacing was determined dynamically, and then directly compare these simulations with our calculations of the optimal state. Such a study could be pursued using the numerical method we have developed. I also found hints of self-organized criticality in the dynamics of brine channels during transient growth, which may offer a new route to understanding their behaviour.

In chapter 6 I found that accurately describing remnant brine channels was crucial to predicting fluid flow in warming sea ice, which should motivate future work to understand these features and include them in a more realistic way within future 1-D sea ice models. This highlights the importance of understanding the factors controlling the spacing of brine channels, so that we can predict their distribution within sea ice. A thorough comparison between the results of 2-D simulations and state-of-the-art 1-D parametrisations would be useful for highlighting areas where the differences between the two are most pronounced.

Finally, I should emphasise that the numerical method developed in chapter 3 has a wide range of possible applications which have only briefly been explored here. Whilst we have focussed on terrestrial sea ice growth, there is growing interest in ice on other planetary bodies (e.g. Enceladus, Spencer and Nimmo, 2013) which might also behave like a mushy layer and is a potential habitat for life. Other examples of mushy layers which may be modelled using our method include the molten mixture of materials within the Earth's core (Fearn et al., 1981), where other physical processes such as

compaction of the solid are also relevant, and the solidification of binary alloys during metal casting (Copley et al., 1970). The AMR capabilities of our numerical method have not been exploited in full in this thesis, primarily due to chronology, but may allow future studies to investigate multiscale problems where the computational expense is otherwise prohibitive. AMR should be particularly beneficial for considering problems in 3-D, where the 1-D brine channels occupy a smaller fraction of the domain than in 2-D simulations. Future work may also benefit from the model features described in § 3.4, which have not been used in this thesis, such as the ability to simulate tracer transport, apply more complicated boundary conditions, or allow for a variable fluid viscosity. In particular, the ability to model tracer transport could enable more detailed numerical studies of sea ice biogeochemistry. This may help to improve our understanding of observations, which are often sparse and can have large uncertainties due to the challenges of measuring such processes.

Bibliography

K. Aagaard and E. C. Carmack. The role of sea ice and other fresh water in the Arctic circulation. *Journal of Geophysical Research: Oceans*, 94(C10):14485–14498, 1989. doi: 10.1029/JC094iC10p14485.

K. Aagaard and R. A. Woodgate. Some thoughts on the freezing and melting of sea ice and their effects on the ocean. *Ocean Modelling*, 2001. ISSN 14635003. doi: 10.1016/S1463-5003(01)00005-1.

Ryan P. Abernathey, Ivana Cerovecki, Paul R. Holland, Emily Newsom, Matt Mazloff, and Lynne D. Talley. Water-mass transformation by sea ice in the upper branch of the Southern Ocean overturning. *Nature Geoscience*, 2016. ISSN 1752-0894. doi: 10.1038/ngeo2749.

M. Adams, P. Colella, D. T. Graves, J. N. Johnson, N. D. Keen, T. J. Ligocki, D. F. Martin, P. W. McCorquodale, D. Modiano, P. O. Schwartz, T. D. Sternberg, and B. Van Straalen. Chombo Software Package for AMR Applications - Design Document, 2016.

A. Aitta, H. E. Huppert, and M. G. Worster. *Solidification in Ternary Systems*, pages 113–122. Springer Netherlands, Dordrecht, 2001. ISBN 978-94-015-9807-1. doi: 10.1007/978-94-015-9807-1_14.

V. Alexiades and A.D. Solomon. *Mathematical Modelling of Melting and Freezing Processes*. Hemisphere Publishing Corporation, 1993.

A. S. Almgren, John B. Bell, Phillip Colella, Louis H. Howell, and Michael L. Welcome. A Conservative Adaptive Projection Method for the Variable Density Incompressible Navier-Stokes Equations. *Journal of Computational Physics*, 142(1):1–46, 1998. ISSN 00219991. doi: 10.1006/jcph.1998.5890.

Gustav Amberg and G. M. Homsy. Nonlinear-Analysis Of Buoyant Convection In Binary Solidification with Application To Channel Formation. *Journal of Fluid Mechanics*, 252:79–98, 1993. doi: Doi10.1017/S0022112093003672.

D. M. Anderson and M. G. Worster. Weakly nonlinear analysis of convection in mushy layers during the solidification of binary alloys. *Journal of Fluid Mechanics*, 302:307–331, 1995.

D. M. Anderson and M. Grae Worster. A new oscillatory instability in a mushy layer during the solidification of binary alloys. *Journal of Fluid Mechanics*, 307:245–267, 1996. ISSN 00221120. doi: 10.1017/S0022112096000110.

Daniel M. Anderson and Peter Guba. Convective Phenomena in Mushy Layers. *Annual Review of Fluid Mechanics*, 52(1):93–119, 2020. doi: 10.1146/annurev-fluid-010719-060332.

Kevin R. Arrigo, Denise L. Worthen, Michael P. Lizotte, Paul Dixon, and Gerhard Dieckmann. Primary Production in Antarctic Sea Ice. *Science*, 276:394–397, 1997. doi: 10.1126/science.276.5311.394.

Andrew Assur. Composition of Sea Ice and its Tensile Strength. *SIPRE Research Report*, 44:54, 1960.

Pascale Aussillous, Andrew J. Sederman, Lynn F. Gladden, Herbert E. Huppert, and M. G. Worster. Magnetic resonance imaging of structure and convection in solidifying mushy layers. *Journal of Fluid Mechanics*, 552:99–125, 2006. ISSN 0022-1120. doi: 10.1017/S0022112005008451.

Jan O. Backhaus, Hermann Fohrmann, Jochen Kämpf, and Angelo Rubino. Formation and export of water masses produced in Arctic shelf polynyas – process studies of oceanic convection. *ICES J. Marine Science*, 54:366–382, 1997. ISSN 10543139. doi: 10.1006/jmsc.1997.0230.

Lars G. E. Backstrom and Hajo Eicken. Capacitance probe measurements of brine volume and bulk salinity in first-year sea ice. *Cold Regions Science and Technology*, 46:167–180, 2006. doi: 10.1016/j.coldregions.2006.08.018.

J. Bear. *Dynamics of Fluids in Porous Media*. Dover Civil and Mechanical Engineering Series. Dover, 1972. ISBN 9780486656755.

C. Beckermann, H. J. Diepers, I. Steinbach, A. Karma, and X. Tong. Modeling Melt Convection in Phase-Field Simulations of Solidification. *Journal of Computational Physics*, 154(2):468–496, 1999. ISSN 00219991. doi: 10.1006/jcph.1999.6323.

Kenneth O. Bennington. Desalination Features in Natural Sea Ice. *Journal of Glaciology*, 6 (48):845–857, 1967.

M. J. Berger and P. Colella. Local adaptive mesh refinement for shock hydrodynamics. *Journal of Computational Physics*, 82(1):64–84, 1989. ISSN 10902716. doi: 10.1016/0021-9991(89)90035-1.

Marsha J. Berger and Joseph Oliger. Adaptive mesh refinement for hyperbolic partial differential equations. *Journal of Computational Physics*, 53(3):484–512, 1984. ISSN 10902716. doi: 10.1016/0021-9991(84)90073-1.

Michael I. Bergman and David R. Fearn. Chimneys on the Earth's Inner-Outer Core Boundary? *Geophysical Research Letters*, 21(6):477–480, 1994.

Michael I. Bergman, David R. Fearn, Jeremy Bloxham, and Margarita C Shannon. Convection and channel formation in solidifying Pb-Sn alloys. *Metallurgical and Materials Transactions A*, 28(March):859–866, 1997. ISSN 1073-5623. doi: 10.1007/s11661-997-0073-y.

C. M. Bitz and William H. Lipscomb. An energy-conserving thermodynamic model of sea ice. *Journal of Geophysical Research: Oceans*, 104(C7):15669–15677, 1999. doi: 10.1029/1999jc900100.

William L Briggs, Steve F McCormick, and Van E Henson. *A multigrid tutorial*. Society for Industrial and Applied Mathematics, 2000. ISBN 9780898714623.

P. C. Carman. Fluid flow through granular beds. *Transactions-Institution of Chemical Engineeres*, 15:150–166, 1937. ISSN 02638762. doi: 10.1016/S0263-8762(97)80003-2.

D. J. Cavalieri and C. L. Parkinson. Arctic sea ice variability and trends, 1979–2010. *The Cryosphere*, 6:881–889, 2012. doi: 10.5194/tc-6-881-2012.

C. F. Chen. Experimental Study of Convection in a Mushy Layer During Directional Solidification. *Journal of Fluid Mechanics*, 293:81–98, 1995. ISSN 14697645. doi: 10.1017/S0022112095001649.

C. F. Chen and Falin Chen. Experimental study of directional solidification of aqueous ammonium chloride solution. *Journal of Fluid Mechanics*, 227:567–586, 1991. doi: 10.1017/S0022112091000253.

A. O. P. Chiareli and M.Grae Worster. On measurement and prediction of the solid fraction within mushy layers. *Journal of Crystal Growth*, 125(3-4):487–494, dec 1992. ISSN 0022-0248. doi: 10.1016/0022-0248(92)90288-T.

A. O. P. Chiareli, Herbert E. Huppert, and M. G. Worster. Segregation and flow during the solidification of alloys. *Journal of Crystal Growth*, 139(1-2):134–146, 1994. ISSN 00220248. doi: 10.1016/0022-0248(94)90038-8.

C. A. Chung and Falin Chen. Onset of plume convection in mushy layers. *Journal of Fluid Mechanics*, 408:53–82, 2000. ISSN 00221120. doi: 10.1017/S0022112099007429.

C. A. Chung and M. Grae Worster. Steady-state chimneys in a mushy layer. *Journal of Fluid Mechanics*, 455:387–411, 2002. ISSN 0022-1120. doi: 10.1017/S0022112001007558.

L. K. Coachman and K. Aagaard. Physical Oceanography of Arctic and Subarctic Seas. In Yvonne Herman, editor, *Marine Geology and Oceanography of the Arctic Seas*, pages 1–72, Berlin, Heidelberg, 1974. Springer Berlin Heidelberg. ISBN 978-3-642-87411-6.

Yossi Cohen, Olivier Devauchelle, Hansjörg F. Seybold, Robert S. Yi, Piotr Szymczak, and Daniel H. Rothman. Path selection in the growth of rivers. *Proceedings of the National Academy of Sciences*, 112(46):14132–14137, 2015. ISSN 0027-8424. doi: 10.1073/pnas.1413883112.

P. Colella, D. T. Graves, T. J. Ligocki, and B. Van Straalen. Godunov unsplit algorithm and implementation. Technical report, 2008.

Phillip Colella. Multidimensional Upwind for Hyperbolic Conservation Laws. *Journal of Computational Physics*, 200:171–200, 1990.

S. M. Copley, A. F. Giamei, S. M. Johnson, and M. F. Hornbecker. The origin of freckles in unidirectionally solidified castings. *Metallurgical Transactions*, 1(8):2193–2204, 1970. ISSN 1543-1916. doi: 10.1007/BF02643435.

Stephen L. Cornford, D. F. Martin, Daniel T. Graves, Douglas F. Ranken, Anne M. Le Brocq, Rupert M. Gladstone, Antony J. Payne, Esmond G. Ng, and William H. Lipscomb. Adaptive mesh, finite volume modeling of marine ice sheets. *Journal of Computational Physics*, 232(1):529–549, 2013. ISSN 00219991. doi: 10.1016/j.jcp.2012.08.037.

F. R. Cottier, F. Nilsen, M E Inall, S. Gerland, V. Tverberg, H. Svendsen, M. E. Enall, S. Gerland, V. Tverberg, and H. Svendsen. Wintertime warming of an Arctic shelf in response to large-scale atmospheric circulation. *Geophysical Research Letters*, 34(10):1–5, 2007. ISSN 00948276. doi: 10.1029/2007GL029948.

Finlo Cottier and P. Wadhams. Linkages between salinity and brine channel distribution in young sea ice. *Polar Research*, 104:859–871, 1999.

R. Courant, K. Friedrichs, and H. Lewy. Uber die partiellen Differenzengleichungen der mathematischen Physik. *Math. Ann.*, 100:32–74, 1928. ISSN 0025-5831; 1432-1807/e. doi: 10.1007/BF01448839.

G. F. N. Cox and W. F. Weeks. Salinity Variations in Sea Ice. *Journal of Glaciology*, 13(67): 109–120, 1974. ISSN 0022-1430. doi: 10.1017/s0022143000023418.

G. F. N. Cox and W. F. Weeks. Brine Drainage and Initial Salt Entrapment in Sodium Chloride Ice Cold Regions Research and Engineering Laboratory. *CRREL Res. Rep. 345, Cold Reg. Res. and Eng. Lab., Hanover, N. H*, 1975.

G. F. N. Cox and W. F. Weeks. Numerical simulations of the profile properties of undeformed first-year sea ice during the growth season. *Journal of Geophysical Research*, 93(C10):12449, 1988. ISSN 0148-0227. doi: 10.1029/JC093iC10p12449.

Judith A. Curry, Julie L. Schramm, and Elizabeth E. Ebert. Sea Ice-Albedo Climate Feedback Mechanism. *Journal of Climate*, 8:240–247, 1995. doi: 10.1175/1520-0442(1995)008<0240:SIACFM>2.0.CO;2.

E. Damm, B. Rudels, U. Schauer, S. Mau, and G. Dieckmann. Methane excess in Arctic surface water-triggered by sea ice formation and melting. *Scientific Reports*, 5:1–9, 2015. ISSN 20452322. doi: 10.1038/srep16179.

L. Diachin, R. Hornung, P. Plassman, and A. Wissink. Parallel Adaptive Mesh Refinement. In Michael A Heroux, Padma Raghavan, and Horst D Simon, editors, *Parallel Processing for Scientific Computing*, pages 143–162. SIAM, 2006.

Guang-Yu Ding, Andrew J. Wells, and Jin-Qiang Zhong. Solidification of binary aqueous solutions under periodic cooling. Part 1. Dynamics of mushy-layer growth. *Journal of Fluid Mechanics*, 870:121–146, 2019a. ISSN 0022-1120. doi: 10.1017/jfm.2019.256.

Guang-Yu Ding, Andrew J. Wells, and Jin-Qiang Zhong. Solidification of binary aqueous solutions under periodic cooling. Part 2. Distribution of solid fraction. *Journal of Fluid Mechanics*, 870:147–174, 2019b. ISSN 0022-1120. doi: 10.1017/jfm.2019.257.

P.B. Duffy, M. Eby, and A.J. Weaver. Effects of sinking of salt rejected during formation of sea ice on. *Geophysical Research Letters*, 26(12):1739–1742, 1999. ISSN 1944-8007. doi: 10.1029/1999GL900286.

H. Eicken, C. Bock, R. Wittig, H. Miller, and H. O. Poertner. Magnetic resonance imaging of sea-ice pore fluids: Methods and thermal evolution of pore microstructure. *Cold Regions Science and Technology*, 31(3):207–225, 2000. ISSN 0165232X. doi: 10.1016/S0165-232X(00)00016-1.

Hajo Eicken. Salinity Profiles of Antractic Sea Ice: Field Data and Model Results. *Journal of Geophysical Research*, 97(C10):15545–15557, 1992.

Lars Ingolf Eide and Seelye Martin. The formation of brine drainage features in young sea ice. *Journal of Glaciology*, 14(70):137–154, 1975. ISSN 0022-1430.

La Kenya Evans and Jun Nishioka. Accumulation processes of trace metals into Arctic sea ice: distribution of Fe, Mn and Cd associated with ice structure. *Marine Chemistry*, 209: 36–47, 2018. ISSN 0304-4203. doi: 10.1016/j.marchem.2018.11.011.

David R. Fearn, David E. Loper, and Paul H. Roberts. Structure of the Earth's inner core. *Nature*, 292:232–233, 1981.

S. D. Felicelli, J. C. Heinrich, and D. R. Poirier. Finite element analysis of directional solidification of multicomponent alloys. *International Journal for Numerical Methods in Fluids*, 27(1-4):207–227, 1998. ISSN 02712091. doi: 10.1002/(SICI)1097-0363(199801)27:1/4<207::AID-FLD660>3.0.CO;2-X.

Sergio D Felicelli, Juan C Heinrich, and David R Poirier. Numerical Simulation of Freckle Formation in Directional Solidification of Binary Alloys. pages 433–441, 1992.

D. L. Feltham, N. Untersteiner, J. S. Wettlaufer, and M. G. Worster. Sea ice is a mushy layer. *Geophysical Research Letters*, 33(14):L14501, 2006. ISSN 0094-8276. doi: 10.1029/2006GL026290.

Daniel L. Feltham. The influence of ocean flow on newly forming sea ice. *Journal of Geophysical Research*, 107(C2):3009, 2002. ISSN 0148-0227. doi: 10.1029/2000JC000559.

Daniel L. Feltham. Sea Ice Rheology. *Annual Review of Fluid Mechanics*, 40(1):91–112, 2008. ISSN 0066-4189. doi: 10.1146/annurev.fluid.40.111406.102151.

F. Fetterer, Knowles K, W. Meier, and M. Savoie. Sea Ice Index, Version 2. Digital media, 2017.

Arne Foldvik and Tor Gammelsrød. Notes on Southern Ocean hydrography, sea-ice and bottom water formation. *Palaeogeography, Palaeoclimatology, Palaeoecology*, 67(1-2):3–17, 1988. ISSN 00310182. doi: 10.1016/0031-0182(88)90119-8.

A C Fowler. The formation of freckles in binary alloys. *IMA Journal of Applied Mathematics*, 35(June):159–174, 1985. ISSN 02724960. doi: 10.1093/imamat/35.2.159.

Johannes Freitag. The hydraulic properties of Arctic Sea-Ice - Implications for the small scale particle transport. *Ber. Polarforsch*, 325:1–170, 1999.

Johannes Freitag and Hajo Eicken. Meltwater circulation and permeability of Arctic summer sea ice derived from hydrological field experiments. *Journal of Glaciology*, 49(166):349–358, 2003. ISSN 00221430. doi: 10.3189/172756503781830601.

R. J. Galley, B. G T Else, N. X. Geilfus, A. A. Hare, D. Isleifson, D. G. Barber, and S. Rysgaard. Imaged brine inclusions in young sea ice-Shape, distribution and formation timing. *Cold Regions Science and Technology*, 111:39–48, 2015. ISSN 0165232X. doi: 10.1016/j.coldregions.2014.12.011.

N. X. Geilfus, K. M. Munson, J. Sousa, Y. Germanov, S. Bhugaloo, D. Babb, and F. Wang. Distribution and impacts of microplastic incorporation within sea ice. *Marine Pollution Bulletin*, 145:463–473, 2019. ISSN 18793363. doi: 10.1016/j.marpolbul.2019.06.029.

Nicholas R Gewecke and T. P. Schulze. The rapid advance and slow retreat of a mushy zone. *Journal of Fluid Mechanics*, 674:1–17, 2011. ISSN 0022-1120. doi: 10.1017/S0022112011000103.

A. L. Gordon. Bottom Water Formation. *Encyclopedia of Ocean Sciences*, 2001. doi: 10.1016/B978-012374473-9.00006-0.

Margaux Gourdal, Odile Crabeck, Martine Lizotte, Virginie Galindo, and Michel Gosselin. Upward transport of bottom-ice dimethyl sulfide during advanced melting of arctic first-year sea ice. *Elem. Sci. Anth.*, 7, 2019. doi: https://doi.org/10.1525/elementa.370.

Philipp J. Griewank and D. Notz. Insights into brine dynamics and sea ice desalination from a 1-D model study of gravity drainage. *Journal of Geophysical Research: Oceans*, 118(7): 3370–3386, 2013. ISSN 21699291. doi: 10.1002/jgrc.20247.

Peter Guba and M. G. Worster. Interactions between steady and oscillatory convection in mushy layers. *Journal of Fluid Mechanics*, 645:411–434, 2010. doi: 10.1017/S0022112009992709.

Peter Guba and M. Grae Worster. Nonlinear oscillatory convection in mushy layers. *Journal of Fluid Mechanics*, 553:419–443, 2006. doi: 10.1017/S0022112006009098.

Christian Haas. Dynamics Versus Thermodynamics: The Sea Ice Thickness Distribution. In Gerhard Dieckmann and David Thomas, editors, *Sea Ice*, chapter 4, pages 113–151. Wiley-Blackwell, 2 edition, 2010. ISBN 9781405185806. doi: 10.1002/9781444317145.ch4.

A. Hellawell, J. Sarazin, and Ronald Steube. Channel Convection in Partly Solidified Systems. *Philosophical Transactions of The Royal Society A Mathematical Physical and Engineering Sciences*, 345, 1993. doi: 10.1098/rsta.1993.0143.

D. R. Hewitt, Jerome A. Neufeld, and John R. Lister. High Rayleigh number convection in a three-dimensional porous medium. pages 879–895, 2014. doi: 10.1017/jfm.2014.216.

Joseph Hitchen. *Understanding the growth and convective instability of mushy layers, with application to young sea ice*. PhD thesis, University of Oxford, 2017.

Joseph Hitchen and Andrew J. Wells. The impact of imperfect heat transfer on the convective instability of a thermal boundary layer in a porous media. *Journal of Fluid Mechanics*, 794:154–174, 2016. ISSN 0022-1120. doi: 10.1017/jfm.2016.149.

C. W. Horton and F. T. Rogers. Convection currents in a porous medium. *J. Appl. Phys.*, 16:367–370, 1945.

Ludovic Huguet, Thierry Alboussiére, Michael I. Bergman, Renaud Deguen, Stephane Labrosse, and Germain Lesoeur. Structure of a mushy layer under hypergravity with implications for Earth's inner core. *Geophysical Journal International*, 204(3):1729–1755, 2016. ISSN 1365246X. doi: 10.1093/gji/ggv554.

E. C. Hunke, D. Notz, A. K. Turner, and M. Vancoppenolle. The multiphase physics of sea ice: a review for model developers. *The Cryosphere*, 5(4):989–1009, 2011. ISSN 1994-0424. doi: 10.5194/tc-5-989-2011.

In Gook Hwang. Stability analysis of compositional convection in a mushy layer in the time-dependent solidification system. *Korean Journal of Chemical Engineering*, 30(5): 1023–1028, 2013. ISSN 02561115. doi: 10.1007/s11814-013-0013-z.

D.T. Jamieson, J.S. Tudhope, R. Morris, and G. Cartwright. Physical properties of sea water solutions: heat capacity. *Desalination*, 7(1):23–30, 1969. ISSN 00119164. doi: 10.1016/S0011-9164(00)80271-4.

F. P. Jardon, F. Vivier, M. Vancoppenolle, a. Lourenço, P. Bouruet-Aubertot, and Y. Cuypers. Full-depth desalination of warm sea ice. *Journal of Geophysical Research: Oceans*, 118(1): 435–447, 2013. ISSN 21699275. doi: 10.1029/2012JC007962.

Adrian Jenkins. Convection-driven melting near the grounding lines of ice shelves and tidewater glaciers. *Journal of Physical Oceanography*, 41(12):2279–2294, 2011. ISSN 0022-3670. doi: 10.1175/JPO-D-11-03.1.

Henrik Jensen and Marcelo Magnasco. Self-Organized Criticality: Emergent Complex Behavior in Physical and Biological Systems. *Physics Today - PHYS TODAY*, 52, 1999. doi: 10.1063/1.882869.

Th U. Kaempfer and M. Rappaz. Modelling of macrosegregation during solidification processes using an adaptive domain decomposition method. *Modelling and Simulation in Materials Science and Engineering*, 11(4):575–597, 2003. ISSN 09650393. doi: 10.1088/0965-0393/11/4/310.

Richard F. Katz and M. Grae Worster. Simulation of directional solidification, thermochemical convection, and chimney formation in a Hele-Shaw cell. *Journal of Computational Physics*, 227(23):9823–9840, 2008. ISSN 00219991. doi: 10.1016/j.jcp.2008.06.039.

T. Kawamura, M. Ishikawa, T. Takatsuka, S. Kojima, and K. Shirasawa. Measurements of permeability of sea ice. In *Proceedings of the 18th IAHR International Symposium on Ice*, pages 105–122, 2006.

Shane R. Keating, E. A. Spiegel, and M. G. Worster. Patterns of convection in solidifying binary solutions. *Geophysical and Astrophysical Fluid Dynamics*, 105(2-3):304–328, 2011. ISSN 03091929. doi: 10.1080/03091929.2010.545405.

Ross C. Kerr, Andrew W. Woods, M. Grae Worster, and Herbert E. Huppert. Solidification of an alloy cooled from above Part 1. Equilibrium growth. *Journal of Fluid Mechanics*, 216:323–342, 1990a.

Ross C. Kerr, Andrew W. Woods, M. Grae Worster, and Herbert E. Huppert. Solidification of an alloy cooled from above Part 2. Non-equilibrium interfacial kinetics. *Journal of Fluid Mechanics*, 216:323–342, 1990b.

J Kozeny. Uber kapillare Leitung des Wassers im Boden. *Akad. Wiss. Wien*, 136:271–306, 1927.

C. Krembs, T. Mock, and R. Gradinger. A mesocosm study of physical-biological interactions in artificial sea ice: Effects of brine channel surface evolution and brine movement on algal biomass. *Polar Biology*, 24(5):356–364, 2001. ISSN 07224060. doi: 10.1007/s003000000219.

Pijush K. Kundu, Ira M. Cohen, and David R. Dowling. Chapter 4 - Conservation Laws. In Pijush K Kundu, Ira M Cohen, and David R Dowling, editors, *Fluid Mechanics (Fifth Edition)*, pages 95–169. Academic Press, Boston, 2012. ISBN 978-0-12-382100-3. doi: https://doi.org/10.1016/B978-0-12-382100-3.10004-6.

R A Lake and E L Lewis. Salt Rejection by Sea Ice during Growth. *Journal of Geophysical Research*, 75(3):583, 1970. ISSN 01480227. doi: 10.1029/JC075i003p00583.

C. Lancelot, A. De Montety, H. Goosse, S. Becquevort, V. Schoemann, B. Pasquer, and M. Vancoppenolle. Spatial distribution of the iron supply to phytoplankton in the Southern Ocean: A model study. *Biogeosciences*, 6(12):2861–2878, 2009. ISSN 17264189. doi: 10.5194/bg-6-2861-2009.

Delphine Lannuzel, Véronique Schoemann, Jeroen de Jong, Jean Louis Tison, and Lei Chou. Distribution and biogeochemical behaviour of iron in the East Antarctic sea ice. *Marine Chemistry*, 106(1-2 SPEC. ISS.):18–32, 2007. ISSN 03044203. doi: 10.1016/j.marchem.2006.06.010.

Michael Le Bars and M. G. Worster. Interfacial conditions between a pure fluid and a porous medium: implications for binary alloy solidification. *Journal of Fluid Mechanics*, 550(-1): 149, 2006a. ISSN 0022-1120. doi: 10.1017/S0022112005007998.

Michael Le Bars and M. G. Worster. Solidification of a binary alloy: Finite-element, single-domain simulation and new benchmark solutions. *Journal of Computational Physics*, 216 (1):247–263, 2006b. ISSN 00219991. doi: 10.1016/j.jcp.2005.12.002.

Randall J LeVeque. *Finite difference methods for ordinary and partial differential equations: steady-state and time-dependent problems*, volume 98. Siam, 2007.

R. M. Lieb-Lappen and R. W. Obbard. The role of blowing snow in the activation of bromine over first-year Antarctic sea ice. *Atmospheric Chemistry and Physics*, 15(13):7537–7545, 2015. ISSN 1680-7324. doi: 10.5194/acp-15-7537-2015.

Weitao Liu, Changchuan Xie, Michel Bellet, and Hervé Combeau. 2-Dimensional FEM modeling of macrosegregation in the directional solidification with mesh adaptation. *Acta Metallurgica Sinica (English Letters)*, 22(3):233–240, jun 2009. ISSN 1006-7191. doi: 10.1016/S1006-7191(08)60094-0.

Rainald Löhner. An adaptive finite element scheme for transient problems in CFD. *Computer Methods in Applied Mechanics and Engineering*, 61(3):323–338, 1987. ISSN 00457825. doi: 10.1016/0045-7825(87)90098-3.

B. Loose, L.A. A Miller, S Elliott, and T Papakyriakou. Sea ice biogeochemistry and material transport across the frozen interface. *Oceanography*, 24(3):202–218, 2011. ISSN 10428275. doi: 10.5670/oceanog.2011.65.

Jay W. Lu and Falin Chen. Instability-mode competition due to change of partition coefficient of binary alloy unidirectionally solidified from below. *Journal of Crystal Growth*, 140(1-2): 182–190, jun 1994. ISSN 00220248. doi: 10.1016/0022-0248(94)90512-6.

T. Maksym and M. O. Jeffries. Phase and compositional evolution of the flooded layer during snow-ice formation on Antartic sea ice. *Annals of Glaciology*, 33(3):37–44, 2001. ISSN 02603055.

D. F. Martin and Phillip Colella. A cell-centered adaptive projection method for the incompressible Euler equations. *Journal of Computational Physics*, 163(2):271–312, 2000. ISSN 00219991. doi: 10.1006/jcph.2000.6575.

D. F. Martin, Phillip Colella, and Daniel Graves. A cell-centered adaptive projection method for the incompressible Navier-Stokes equations in three dimensions. *Journal of Computational Physics*, 227(3):1863–1886, 2008. ISSN 00219991. doi: 10.1016/j.jcp.2007.09.032.

Seelye Martin. Frazil ice in rivers and oceans. *Ann. Rev. Fluid Mech.*, 13:379–397, 1981.

Gary A. Maykut. Energy exchange over young sea ice in the central Arctic. *Journal of Geophysical Research*, 83(C7):3646, 1978. ISSN 0148-0227. doi: 10.1029/jc083ic07p03646.

Gary A. Maykut and Norbert Untersteiner. Some results from a time-dependent thermodynamic model of sea ice. *Journal of Geophysical Research*, 76(6):1550–1575, 1971. doi: 10.1029/jc076i006p01550.

Walter N. Meier, Greta K. Hovelsrud, Bob E .H. van Oort, Jeffrey R. Key, Kit M. Kovacs, Christine Michel, Christian Haas, Mats A. Granskog, Sebastian Gerland, Donald K. Perovich, Alexander Makshtas, and James D. Reist. Arctic sea ice in transformation: A review of recent observed changes and impacts on biology and human activity. *Reviews of Geophysics*, 52(3):185–217, 2014. doi: 10.1002/2013RG000431.

George L Mellor. An Ice-Ocean Coupled Model. *Journal of Geophysical Research*, 94(89): 937–954, 1989.

C. A. Middleton, C. Thomas, A. De Wit, and J.-L. Tison. Visualizing brine channel development and convective processes during artificial sea-ice growth using Schlieren optical methods. *Journal of Glaciology*, 62(231):1–17, 2016. ISSN 0022-1430. doi: 10.1017/jog.2015.1.

W. Moon and J. S. Wettlaufer. A low-order theory of Arctic sea ice stability. *EPL (Europhysics Letters)*, 96(3):39001, 2011. ISSN 0295-5075. doi: 10.1209/0295-5075/96/39001.

M. A. Morales Maqueda, A. J. Willmott, and N. R.T. Biggs. Polynya dynamics: A review of observations and modeling. *Reviews of Geophysics*, 42(1), 2004. ISSN 87551209. doi: 10.1029/2002RG000116.

W. W. Mullins and R. F. Sekerka. Stability of a planar interface during solidification of a dilute binary alloy. *Journal of Applied Physics*, 35(2):444–451, 1964. ISSN 00218979. doi: 10.1063/1.1713333.

M. Nakawo and N. K. Sinha. Growth rate and salinity profile of first-year sea ice in the high arctic. *Journal of Glaciology*, 27(96), 1981.

Kishor G. Nayar, Mostafa H. Sharqawy, Leonardo D. Banchik, and John H. Lienhard V. Thermophysical properties of seawater: A review and new correlations that include pressure dependence. *Desalination*, 390:1–24, 2016. ISSN 00119164. doi: 10.1016/j.desal.2016.02.024.

Jerome A. Neufeld and J. S. Wettlaufer. Shear-enhanced convection in a mushy layer. *Journal of Fluid Mechanics*, 612:339–361, 2008a. ISSN 00221120. doi: 10.1017/S0022112008002991.

Jerome A. Neufeld and J. S. Wettlaufer. An experimental study of shear-enhanced convection in a mushy layer. *Journal of Fluid Mechanics*, 612:363–385, oct 2008b. ISSN 0022-1120. doi: 10.1017/S0022112008003339.

A. T. Nguyen, D. Menemenlis, and R. Kwok. Improved modeling of the arctic halocline with a subgrid-scale brine rejection parameterization. *Journal of Geophysical Research: Oceans*, 114(11):1–12, 2009. ISSN 21699291. doi: 10.1029/2008JC005121.

Terren M. Niedrauer and Seelye Martin. An experimental study of brine drainage and convection young sea ice. *Journal of Geophysical Research*, 84(8):1176, 1979. ISSN 0148-0227. doi: 10.1029/JC084iC03p01176.

P. Nithiarasu, K. N. Seetharamu, and T. Sundararajan. Natural convective heat transfer in a fluid saturated variable porosity medium. *International Journal of Heat and Mass Transfer*, 40(16):3955–3967, 1997. ISSN 00179310. doi: 10.1016/S0017-9310(97)00008-2.

D. Notz. *Thermodynamic and fluid-dynamical processes in sea ice*. PhD thesis, University of Cambridge, 2005.

D. Notz and M. G. Worster. A one-dimensional enthalpy model of sea ice. *Annals of Glaciology*, 44:123–128, 2006. ISSN 02603055. doi: 10.3189/172756406781811196.

D. Notz and M. G. Worster. In situ measurements of the evolution of young sea ice. *Journal of Geophysical Research: Oceans*, 113(3), 2008. ISSN 21699291. doi: 10.1029/2007JC004333.

D. Notz and M. G. Worster. Desalination processes of sea ice revisited. *Journal of Geophysical Research*, 114(C5):C05006, 2009. ISSN 0148-0227. doi: 10.1029/2008JC004885.

Annette B. Oertling and Robert G. Watts. Growth of and brine drainage from NaClH2O freezing: A simulation of young sea ice. *Journal of Geophysical Research C: Oceans*, 109 (4):1–10, 2004. ISSN 01480227. doi: 10.1029/2001JC001109.

Kay I. Ohshima, Sohey Nihashi, and Katsushi Iwamoto. Global view of sea-ice production in polynyas and its linkage to dense/bottom water formation. *Geoscience Letters*, 3(1), 2016. ISSN 21964092. doi: 10.1186/s40562-016-0045-4.

J. G. O'Rourke, A. J. E. Riggs, C. A. Guertler, P. W. Miller, C. M. Padhi, M. M. Popelka, A. J. Wells, A. C. West, J.-Q. Zhong, and J. S. Wettlaufer. Mushy-layer dynamics in micro and hyper gravity. *Physics of Fluids*, 24(10), 2012. ISSN 10706631. doi: 10.1063/1.4760256.

Irina Overeem. *Sea Ice: An Introduction to Its Physics*, volume 35. jul 2006. ISBN Dieckmann, G. (2003) Sea ice : an introduction to its physics, chemistry, biology, and geology / D. Thomas (editor) , Oxford [u.a.] : Blackwell Science, 402 p., ISBN: 0-632-05808-0 . hdl:10013/epic.18436. doi: 10.1657/1523-0430(2003)035[0542:br]2.0.co;2.

Tim Palmer. Climate forecasting: Build high-resolution global climate models. *Nature*, 515 (7527):338–339, 2014. ISSN 14764687. doi: 10.1038/515338a.

James R G Parkinson, Daniel F. Martin, Andrew J. Wells, and Richard F. Katz. Modelling binary alloy solidification with Adaptive Mesh Refinement. *Journal of Computational Physics*, submitted, 2019.

S. S. L. Peppin, P. Aussillous, Herbert E. Huppert, and M. G. Worster. Steady-state mushy layers: Experiments and theory. *Journal of Fluid Mechanics*, 570:69–77, 2007. ISSN 00221120. doi: 10.1017/S0022112006003028.

S. S. L. Peppin, Herbert E. Huppert, and M. G. Worster. Steady-state solidification of aqueous ammonium chloride. *Journal of Fluid Mechanics*, 599:465–476, 2008. ISSN 00221120. doi: 10.1017/S0022112008000219.

Algot K. Peterson. Observations of brine plumes below Arctic sea ice. *Ocean Science Discussions*, pages 1–18, 2018. ISSN 1812-0822. doi: 10.5194/os-2017-27.

C Petrich and Hajo Eicken. Growth, Structure and Properties of Sea Ice. In D N Thomas and G S Dieckmann, editors, *Sea Ice*, pages 23–78. Wiley-Blackwell, 2010. ISBN 9781405185806. doi: 10.1002/9781444317145.ch2.

Chris Petrich, Pat J. Langhorne, and Zhifa Sun. Numerical simulation of sea ice growth and desalinition. In *Proceedings of the 17th IAHR International Symposium on Ice*, volume 3, pages 68–75, St Petersburg, Russia, 2004.

M E Q Pilson. *An Introduction to the Chemistry of the Sea.* Cambridge University Press, 2013. ISBN 9780521887076.

Frans Pretorius and Matthew W. Choptuik. Adaptive mesh refinement for coupled elliptic-hyperbolic systems. *Journal of Computational Physics*, 218(1):246–274, 2006. ISSN 00219991. doi: 10.1016/j.jcp.2006.02.011.

N. Provatas, N. Goldenfeld, and J. Dantzig. Efficient computation of dendritic microstructures using adaptive mesh refinement. *Physical Review Letters*, 80(15):3308–3311, 1998. ISSN 0031-9007. doi: 10.1103/PhysRevLett.80.3308.

Nikolas Provatas, Quanyong Wang, Mikko Haataja, and Martin Grant. Seaweed to dendrite transition in directional solidification. *Physical Review Letters*, 91(15):1–4, 2003. ISSN 10797114. doi: 10.1103/PhysRevLett.91.155502.

W. S. Reeburgh. Fluxes associated with brine motion in growing sea ice. *Polar Biology*, 3(1): 29–33, 1984. ISSN 07224060. doi: 10.1007/BF00265564.

D. W. Rees Jones and M. G. Worster. Fluxes through steady chimneys in a mushy layer during binary alloy solidification. *Journal of Fluid Mechanics*, 714:127–151, 2013. ISSN 0022-1120. doi: 10.1017/jfm.2012.462.

D. W. Rees Jones and M. G. Worster. A physically based parameterization of gravity drainage for sea-ice modeling. *Journal of Geophysical Research: Oceans*, 119:5599–5621, 2014. ISSN 21699275. doi: 10.1002/2014JC010066.Received.

C Richardson. Phase relationships in sea ice as a function of temperature. *Journal of Glaciology*, 17(77):507–519, 1976. doi: https://doi.org/10.3198/1976JoG17-77-507-519.

S. M. Roper, S. H. Davis, and P. W. Voorhees. An analysis of convection in a mushy layer with a deformable permeable interface. *Journal of Fluid Mechanics*, 596:333–352, 2008. ISSN 00221120. doi: 10.1017/S0022112007009469.

Bert Rudels, E. Peter Jones, Ursula Schauer, and Patrick Eriksson. Atlantic sources of the Arctic Ocean surface and halocline waters. *Polar Research*, 23(2):181–208, 2004. ISSN 08000395. doi: 10.3402/polar.v23i2.6278.

H. Saeki, T. Takeuchi, and E. Suenaga. Experimental study on permeability coefficient of sea ice. In T.K. S. Murthy, J. J. Connor, and C. A. Springer-Verlag Brebbia, editors, *IceTechnology. 1st International Conference, June 1986, Cambridge, Massachusetts. Proceedings.*, pages 237–246. Springer-Verlag, 1986.

Udaya K. Sajja and Sergio D. Felicelli. Modeling freckle segregation with mesh adaptation. *Metallurgical and Materials Transactions B: Process Metallurgy and Materials Processing Science*, 42(6):1118–1129, 2011. ISSN 10735615. doi: 10.1007/s11663-011-9565-7.

Jeff Saltzman. An unsplit 3D upwind method for hyperbolic conservation laws. *Journal of Computational Physics*, 115(1):153–168, 1994. ISSN 00219991. doi: 10.1006/jcph.1994.1184.

J. Sarazin and A. Hellawell. Channel formation in Pb-Sn, Pb-Sb, and Pb-Sn-Sb alloy ingots and comparison with the system NH4CI-H2O. *Metallurgical and Materials Transactions A*, 19:1861–1871, 1988. doi: 10.1007/BF02645156.

S. Sathiyamoorthy and G. W. K. Moore. Buoyancy Flux at Ocean Weather Station Bravo. *Journal of Physical Oceanography*, 32(2):458–474, 2002. ISSN 0022-3670. doi: 10.1175/1520-0485(2002)032<0458:bfaows>2.0.co;2.

W. J. Schmitz Jr. On the interbasin-scale thermohaline circulation. *Reviews of Geophysics*, 33(95):151–173, 1995.

T. P. Schulze and M. G. Worster. A numerical investigation of steady convection in mushy layers during the directional solidification of binary alloys. *Journal of Fluid Mechanics*, 356:199–220, 1998. ISSN 00221120. doi: 10.1017/S0022112097007878.

T. P. Schulze and M. G. Worster. Weak convection, liquid inclusions and the formation of chimneys in mushy layers. *Journal of Fluid Mechanics*, 388:197–215, 1999. ISSN 00221120. doi: 10.1017/S0022112099004589.

Florian Sévellec, Alexey V. Fedorov, and Wei Liu. Arctic sea-ice decline weakens the Atlantic Meridional Overturning Circulation. *Nature Climate Change*, 7(8):604–610, 2017. ISSN 1758-678X. doi: 10.1038/nclimate3353.

Mostafa H. Sharqawy, John H. Lienhard V, and Syed M. Zubair. Erratum to Thermophysical properties of seawater: A review of existing correlations and data. *Desalination and Water Treatment*, 29(1-3):355, 2011. ISSN 1944-3994. doi: 10.5004/dwt.2011.2947.

Andrey Y. Shcherbina, Lynne D. Talley, and Daniel L. Rudnick. Direct observations of North Pacific ventilation: brine rejection in the Okhotsk Sea. *Science*, 302(5652):1952–1955, 2003. ISSN 0036-8075. doi: 10.1126/science.1088692.

Wei Shyy, S. S. Thakur, H. Ouyang, J. Liu, and E. Blosch. Multiblock Methods. In *Computational Techniques for Complex Transport Phenomena*, pages 122–162. Cambridge University Press, 1997. doi: 10.1017/CBO9780511665462.005.

L. C. Skinner, S. Fallon, C. Waelbroeck, E. Michel, and S. Barker. Ventilation of the Deep Southern Ocean and Deglacial CO2 Rise. *Science*, 328(5982):1147 LP – 1151, may 2010. doi: 10.1126/science.1183627.

John Joseph Charles Smith. Improvement in clay moulds for casting metals, 1868.

T. H. Solomon and R. R. Hartley. Measurements of the temperature field of mushy and liquid regions during solidification of aqueous ammonium chloride. *Journal of Fluid Mechanics*, 358:87–106, 1998. ISSN 00221120. doi: 10.1017/S0022112097008264.

John R. Spencer and Francis Nimmo. Enceladus: An Active Ice World in the Saturn System. *Annual Review of Earth and Planetary Sciences*, 41(1):693–717, 2013. ISSN 0084-6597. doi: 10.1146/annurev-earth-050212-124025.

J Stefan. Ueber die Theorie der Eisbildung, insbesondere über die Eisbildung im Polarmeere. *Annalen der Physik*, 278(2):269–286, 1891. doi: 10.1002/andp.18912780206.

Julienne Stroeve and W. Meier. Sea Ice Trends and Climatologies from SMMR and SSM/I-SSMIS, Version 2. Technical report, NASA National Snow and Ice Data Center Distributed Active Archive Center, Boulder, Colorado USA, 2017.

H. Struthers, A. M L Ekman, P. Glantz, T. Iversen, A. Kirkevåg, E. M. Mårtensson, Seland, E. D. Nilsson, A Kirkev, A. Kirkevåg, E. M. Mårtensson, Seland, and E. D. Nilsson. The effect of sea ice loss on sea salt aerosol concentrations and the radiative balance in the Arctic. *Atmospheric Chemistry and Physics*, 11(7):3459–3477, 2011. ISSN 16807316. doi: 10.5194/acp-11-3459-2011.

Stephen Tait and Claude Jaupart. Compositional convection in a reactive crystalline mush and melt differentiation. *Journal of Geophysical Research*, 97(B5):6735–6756, 1992. ISSN 0148-0227. doi: 10.1029/92JB00016.

Stephen Tait, Katia Jahrling, and Claude Jaupart. The planform of compositional convection and chimney formation in a mushy layer. *Letters to Nature*, 359, 1992.

Lynne D. Talley, V. Lobanov, V. Ponomarev, A. Salyuk, P. Tishchenko, I. Zhabin, and S. Riser. Deep convection and brine rejection in the Japan Sea. *Geophysical Research Letters*, 30(4):1159, 2003. ISSN 1944-8007. doi: 10.1029/2002GL016451.

D. N. Thomas and G. S. Dieckmann. Antarctic sea ice - A habitat for extremophiles. *Science*, 295(5555):641–644, 2002. ISSN 00368075. doi: 10.1126/science.1063391.

M. L. Timmermans. The impact of stored solar heat on Arctic sea ice growth. *Geophysical Research Letters*, 42(15):6399–6406, 2015. ISSN 19448007. doi: 10.1002/2015GL064541.

J.-L. Tison and V. Verbeke. Chlorinity/salinity distribution patterns in experimental granular sea ice. *Annals of Glaciology*, 33:13–20, 2001. ISSN 0260-3055. doi: 10.3189/172756401781818211.

A. K. Turner, Elizabeth C. Hunke, and Cecilia M. Bitz. Two modes of sea-ice gravity drainage: A parameterization for large-scale modeling. *Journal of Geophysical Research: Oceans*, 118 (5):2279–2294, 2013. ISSN 21699291. doi: 10.1002/jgrc.20171.

N. Untersteiner. Natural desalination and equilibrium salinity profile of perennial sea ice. *Journal of Geophysical Research*, 73(4):1251–1257, 1968. ISSN 01480227. doi: 10.1029/JB073i004p01251.

Erwin P. Van Der Poel, Richard J.A.M. Stevens, and Detlef Lohse. Comparison between two-and three-dimensional Rayleigh-Bénard convection. *Journal of Fluid Mechanics*, 736: 177–194, 2013. ISSN 14697645. doi: 10.1017/jfm.2013.488.

Brian Van Straalen, John Shalf, Terry Ligocki, Noel Keen, and Woo Sun Yang. Scalability challenges for massively parallel AMR applications. *IPDPS 2009 - Proceedings of the 2009 IEEE International Parallel and Distributed Processing Symposium*, 2009. ISSN 1530-2075. doi: 10.1109/IPDPS.2009.5161014.

M. Vancoppenolle, Cecilia M. Bitz, and Thierry Fichefet. Summer landfast sea ice desalination at Point Barrow, Alaska: Modeling and observations. *Journal of Geophysical Research: Oceans*, 112(4):1–20, 2007. ISSN 21699291. doi: 10.1029/2006JC003493.

M. Vancoppenolle, Thierry Fichefet, Hugues Goosse, Sylvain Bouillon, Gurvan Madec, and Miguel Angel Morales Maqueda. Simulating the mass balance and salinity of Arctic and Antarctic sea ice. 1. Model description and validation. *Ocean Modelling*, 27(1-2):33–53, 2009. ISSN 14635003. doi: 10.1016/j.ocemod.2008.10.005.

M. Vancoppenolle, Hugues Goosse, Anne De Montety, Thierry Fichefet, Bruno Tremblay, and Jean Louis Tison. Modeling brine and nutrient dynamics in Antarctic sea ice: The case of dissolved silica. *Journal of Geophysical Research: Oceans*, 115(2):1–18, 2010. ISSN 21699291. doi: 10.1029/2009JC005369.

Martin Vancoppenolle, Klaus M. Meiners, Christine Michel, Laurent Bopp, Frédéric Brabant, Gauthier Carnat, Bruno Delille, Delphine Lannuzel, Gurvan Madec, Sébastien Moreau, Jean Louis Tison, and Pier van der Merwe. Role of sea ice in global biogeochemical cycles: Emerging views and challenges. *Quaternary Science Reviews*, 2013. ISSN 02773791. doi: 10.1016/j.quascirev.2013.04.011.

Martin Vancoppenolle, Gurvan Madec, Max Thomas, and Trevor J. McDougall. Thermodynamics of Sea Ice Phase Composition Revisited. *Journal of Geophysical Research: Oceans*, 124(1):615–634, 2019. ISSN 21699291. doi: 10.1029/2018JC014611.

Timo Vihma. *Effects of Arctic Sea Ice Decline on Weather and Climate : A Review*, volume 35. 2014. ISBN 1071201492. doi: 10.1007/s10712-014-9284-0.

Masaaki Wakatsuchi and Nobuo Ono. Measurements of salinity and volume of brine excluded from growing sea ice. *Journal of Geophysical Research*, 88(2):2943–2951, 1983. ISSN 0148-0227. doi: 10.1029/JC088iC05p02943.

Masaaki Wakatsuchi and T. Saito. On brine drainage channels of young sea ice. *Annals of Glaciology*, 6:200–202, 1985.

Andrew J. Wells, J. S. Wettlaufer, and S. A. Orszag. Maximal potential energy transport: a variational principle for solidification problems. *Physical Review Letters*, 105, 2010. doi: 10.1103/PhysRevLett.105.254502.

Andrew J. Wells, J. S. Wettlaufer, and S. A. Orszag. Brine fluxes from growing sea ice. *Geophysical Research Letters*, 38(4):1–5, 2011. ISSN 00948276. doi: 10.1029/2010GL046288.

Andrew J. Wells, J. S. Wettlaufer, and S. A. Orszag. Nonlinear mushy-layer convection with chimneys: stability and optimal solute fluxes. *Journal of Fluid Mechanics*, 716:203–227, 2013. doi: 10.1017/jfm.2012.541.

Andrew J. Wells, Joseph Hitchen, and James R. G. Parkinson. Mushy-layer growth and convection, with application to sea ice. *Philosophical Transactions of the Royal Society A: Mathematical, Physical and Engineering Sciences*, 377(2146):20180165, 2019. ISSN 1364-503X. doi: 10.1098/rsta.2018.0165.

M. G. Wells and J. S. Wettlaufer. The long-term circulation driven by density currents in a two-layer stratified basin. *Journal of Fluid Mechanics*, 572(June 2014):37–58, 2007. ISSN 00221120. doi: 10.1017/S0022112006003478.

J. S. Wettlaufer, M. G. Worster, and Herbert E. Huppert. The phase evolution of young sea ice. *Geophysical Research Letters*, 24(10):1251, 1997a. ISSN 0094-8276. doi: 10.1029/97GL00877.

J. S. Wettlaufer, M. G. Worster, and Herbert E. Huppert. Natural convection during solidification of an alloy from above with application to the evolution of sea ice. *Journal of Fluid Mechanics*, 344:291–316, 1997b. ISSN 00221120. doi: 10.1017/S0022112097006022.

J. S. Wettlaufer, M. G. Worster, and H. E. Huppert. The solidification of leads: theory, experiment and Field observations. *Journal of Geophysical Research*, 105:1123–1134, 2000.

S. H. Whiteoak, Herbert E. Huppert, and M. G. Worster. Conditions for defect-free solidification of aqueous ammonium chloride in a quasi two-dimensional directional solidification facility. *Journal of Crystal Growth*, 310(15):3545–3551, 2008. ISSN 00220248. doi: 10.1016/j.jcrysgro.2008.04.046.

Karolina Widell, Ilker Fer, and Peter M. Haugan. Salt release from warming sea ice. *Geophysical Research Letters*, 33(12):1–5, 2006. ISSN 00948276. doi: 10.1029/2006GL026262.

M. G. Worster. *Convective Flow Problems in Geological Fluid Mechanics*. PhD thesis, Cambridge University, 1983.

M. G. Worster. Solidification of an alloy from a cooled boundary. *Journal of Fluid Mechanics*, 167:481–501, 1986.

M. G. Worster. Natural convection in a mushy layer. *Journal of Fluid Mechanics*, 224: 335–359, 1991. ISSN 0022-1120. doi: 10.1017/S0022112091001787.

M. G. Worster. The Dynamics of Mushy Layers. In S. H. Davis, H. E. Huppert, U. Müller, and M. G. Worster, editors, *Interactive Dynamics of Convection and Solidification*, pages 112–138. Kluwer Academic Publishers, 1992a.

M. G. Worster. Instabilities of the Liquid and Mushy Regions During Solidification of Alloys. *Journal of Fluid Mechanics*, 237:649–669, 1992b. ISSN 0022-1120. doi: 10.1017/S0022112092003562.

M. G. Worster. Convection in mushy layers. *Annu. Rev. Fluid Mech.*, 29:91–122, 1997.

M. G. Worster. Solidification of Fluids. In G. K. Batchelor, H. K. Moffat, and M. G. Worster, editors, *Perspectives in Fluid Dynamics*, chapter 8, pages 393–446. Cambridge University Press, 2000.

M. G. Worster and D. W. Rees Jones. Sea-ice thermodynamics and brine drainage. *Philosophical Transactions of the Royal Society A: Mathematical, Physical and Engineering Sciences*, 373(2045):20140166, 2015. ISSN 1471-2962. doi: 10.1098/rsta.2014.0166.

M. G. Worster and J. S. Wettlaufer. Natural convection, solute trapping, and channel formation during solidification of saltwater. *Journal of Physical Chemistry B*, 101(32): 6132–6136, 1997. ISSN 10895647. doi: 10.1021/jp9632448.

Ridha Ben Yedder and Fouad Erchiqui. Convective flow and heat transfer in a tall porous cavity side-cooled with temperature profile. *International Journal of Heat and Mass Transfer*, 52 (25-26):5712–5718, 2009. ISSN 00179310. doi: 10.1016/j.ijheatmasstransfer.2009.08.016.

J.-Q. Zhong, A. T. Fragoso, A. J. Wells, and J. S. Wettlaufer. Finite-sample-size effects on convection in mushy layers. *Journal of Fluid Mechanics*, 704:89–108, jul 2012. ISSN 0022-1120. doi: 10.1017/jfm.2012.219.

Jiayun Zhou, Bruno Delille, Hajo Eicken, M. Vancoppenolle, Frédéric Brabant, Gauthier Carnat, Nicolas Xavier Geilfus, Tim Papakyriakou, Bernard Heinesch, and Jean Louis Tison. Physical and biogeochemical properties in landfast sea ice (Barrow, Alaska): Insights on brine and gas dynamics across seasons. *Journal of Geophysical Research: Oceans*, 118 (6):3172–3189, 2013. ISSN 21699291. doi: 10.1002/jgrc.20232.